



Ab initio description of doubly-open shell nuclei via a novel resolution method of the quantum many-body problem

Mikael Frosini

► To cite this version:

Mikael Frosini. Ab initio description of doubly-open shell nuclei via a novel resolution method of the quantum many-body problem. Nuclear Theory [nucl-th]. Université Paris-Saclay, 2021. English. NNT : 2021UPASP078 . tel-03374323

HAL Id: tel-03374323

<https://theses.hal.science/tel-03374323v1>

Submitted on 12 Oct 2021

HAL is a multi-disciplinary open access archive for the deposit and dissemination of scientific research documents, whether they are published or not. The documents may come from teaching and research institutions in France or abroad, or from public or private research centers.

L'archive ouverte pluridisciplinaire **HAL**, est destinée au dépôt et à la diffusion de documents scientifiques de niveau recherche, publiés ou non, émanant des établissements d'enseignement et de recherche français ou étrangers, des laboratoires publics ou privés.

Ab initio description of doubly-open shell nuclei
via a novel resolution method of the quantum
many-body problem

*Description ab initio des noyaux à double couches
ouvertes via une nouvelle méthode de résolution du
problème quantique à N corps*

Thèse de doctorat de l'université Paris-Saclay

École doctorale n° 576
Particules, Hadrons, Énergie et Noyau : Instrumentation, Imagerie,
Cosmos et Simulation (PHENIICS)
Spécialité de doctorat : Structure et réactions nucléaires
Unité de recherche : Université Paris-Saclay, CEA, Département de Physique
Nucléaire, 91191, Gif-sur-Yvette, France
Référént : Faculté des sciences d'Orsay

Thèse présentée et soutenue à Gif-sur-Yvette, le 21 septembre 2021, par

Mikael FROSINI

Composition du jury :

Andreas EKSTRÖM

Professeur associé, Université Technologique de Chalmers

Heiko HERGERT

Professeur associé, Université d'État du Michigan

Pierre-François LOOS

Chargé de Recherche (HDR), Université de Toulouse, CNRS

Président

Rapporteur & Examineur

Rapporteur & Examineur

Direction de la thèse :

Thomas DUGUET

Ingénieur de recherche, professeur, CEA Saclay, IRFU, KU Leuven

Vittorio SOMA

Ingénieur de recherche, CEA Saclay, IRFU

Jean-Paul EBRAN

Ingénieur de recherche, CEA, DAM, DIF

Directeur de thèse

Co-encadrant

Co-encadrant

Acknowledgements

Here we are, about to turn a page. Before closing this chapter for good, a few words are due to thank all of those who made this possible and helped me walk my way around these three years.

First, let me thank warmly Andreas Ekström, Heiko Hergert and Pierre-François Loos for accepting taking part as jury members. I am grateful for your patience and dedication reading and improving the document. From remarks and corrections to numerous suggestions that could be further discussed during the defense, it will probably keep me (and others) busy for the years to come, this was very constructive. Sadly, the situation prevented us to be in the same room to discuss it in person - but as we say in french, *ce n'est que partie remise*.

Restons donc en français, pour rappeler (si certains en doutaient), que j'ai eu la chance de travailler avec les meilleurs. Pas sûr que j'arrive à exprimer comme il se doit ma reconnaissance envers Thomas, Vittorio et Jean-Paul, qui m'ont fait confiance en premier lieu puis m'ont guidé dans le monde de la physique nucléaire. Merci de m'avoir donné l'opportunité de travailler avec vous et d'ajouter mon petit caillou à l'édifice.

Thomas, je vais essayer de le dire simplement. Merci, merci de toujours m'avoir poussé à donner le meilleur possible. On en a déjà parlé, mais tu sais combien j'apprécie l'importance que tu donnes aux détails, et au fait qu'au delà des chiffres et des formules, ton intérêt premier est et reste le tableau général - car c'est bien ça qui nous intéresse. Dans tous les cas, sache que ta recherche permanente du mieux restera un exemple pour moi.

Et pourtant, il n'aurait sans doute pas été possible de tenir le cap sans le soutien constant de Vittorio. Ta porte est toujours ouverte, et quelque part on sait que quand on a besoin, tu trouves toujours le temps de porter une oreille attentive à tes étudiants. Ta gentillesse, ta patience, sont des qualités inestimables, et je te suis reconnaissant de tous ces moments où tu as pris le temps de me réexpliquer la même chose encore ou encore, ou bien de me rassurer sur les doutes existentiels qui peuvent apparaître au cours d'une thèse.

Jean-Paul, j'ai eu beaucoup de chance que nos routes se soient croisées, et que la thèse ait pris ce chemin. Grâce à toi, on a pu passer de la théorie générale à l'application concrète, et ainsi faire un travail vraiment complet. Ton enthousiasme constant, la passion sans limite que tu communique autour de toi au sujet de tous les domaines de la physique (du plus phénoménologique au plus abstrait) sont de vraies motivations. Merci pour la confiance que tu m'as faite pour me permettre d'utiliser le code HFB. Je te suis d'autant plus reconnaissant que c'est grâce à toi que je vais pouvoir continuer avec ces développements et à collaborer avec vous trois, merci merci merci.

Comment décide-t-on de faire une thèse? Dans mon cas, je pense avoir rencontré les bonnes personnes, à un moment ou à un autre du parcours. De M. Gouillon à M. Lefranc au collège, jusqu'à M. Brion et M. Ansaldi au lycée, des rencontres, des questionnements et des discussions m'ont poussé à quitter la pinède et le soleil pour le béton et le brouillard de la capitale. Si mon stage en entreprise n'est pas probablement pour rien dans ma décision de m'engager dans la voie de la recherche, je pense que c'est surtout l'accueil chaleureux de Denis, au LLR, puis d'Alexandre et Olivier au CERN, qui ont fini de me décider. J'allais

faire une thèse.

The first year, i had to learn a lot from scratch, so let me thank warmly Alex, that introduced us to the numerous questions surrounding perturbation theory. Pepijn, sadly we couldn't see much of you the last years with the endless confinements, I wish you the best luck with the rest of your thesis! Au final, c'est bien Julien qui m'a pris sous son aile, et s'il m'a fallu un an de plus pour vraiment comprendre le sujet de ta thèse, sache qu'elle est restée sur mon bureau (et sur mon navigateur) pendant les deux ans qui ont suivi ton départ.

Cette section serait incomplète sans dédier son propre paragraphe à Benjamin. Sans ton aide, il aurait sûrement été impossible de comprendre en profondeur les méthodes développées ici (en particulier leur implémentation pratique). Le temps que tu as pris à m'aider quand j'en avais besoin, ou qu'il fallait tester le code, tu l'as donné sans te poser de question, juste par altruisme. Bref, merci.

Merci également aux autres doctorants des Précaires (en particulier à Zoé qui était toujours là pour tout organiser!), et aussi à Killian, Yann et Florian, qui forment le groupe très sélect des thésards de Jean-Paul! Surtout, un grand merci à Andrea pour ces cafés interminables, ces débats sans fin (et sans conclusion). Bonne chance pour les deux années qui te restent, dans tous les cas j'espère bien pouvoir revenir te taxer un café ou deux avant ta défense!

Je suis également reconnaissant envers Danielle et Isabelle, qui sont toujours là quand on a besoin d'elles et ont toujours un mot gentil. Merci pour votre patience et votre bonne humeur!

Merci à mes parents qui m'ont toujours soutenu et sans qui je ne serais pas là aujourd'hui. Merci enfin à Tatiana, qui m'a accompagné dans les épreuves de ces dernières années et me suivra dans la suite!

Contents

Acknowledgements	iii
List of Acronyms	ix
Introduction	1
1. Basic definitions and elements of Bogoliubov algebra	7
1.1. Operators in second quantized form	8
1.1.1. Operators definition	8
1.1.2. Density matrices	9
1.2. Bogoliubov algebra	9
1.2.1. Bogoliubov state	9
1.2.2. One-body density matrices	10
1.2.3. Normal-ordered operators	11
1.2.4. Constrained Hartree-Fock-Bogoliubov theory	11
1.2.5. Elementary excitations	13
1.2.6. Rotated Bogoliubov state	13
1.2.7. Overlap between Bogoliubov vacua	14
1.2.8. Transition Bogoliubov transformation	15
1.2.9. Similarity transformation	15
2. PGCM-PT formalism	19
2.1. Introduction	19
2.2. Formal perturbation theory	22
2.2.1. Set up	22
2.2.2. Perturbative expansion	23
2.2.3. Computable expression	24
2.2.4. Hylleraas functional	25
2.3. PGCM-PT	26
2.3.1. PGCM unperturbed state	26
2.3.2. Partitioning	29
2.3.3. Application to second order (PGCM-PT(2))	32
2.4. Discussion	38
3. Interlude: In-medium interactions	41
3.1. Introduction	41
3.2. Formalism	44
3.2.1. Definitions	44
3.2.2. Standard NOkB approximation	45
3.2.3. Generalized k -body approximation	46
3.3. Many-body methods and one-body density matrices	49
3.3.1. Many-body methods	49

3.3.2. Trial one-body density matrices	50
3.4. Results	51
3.4.1. Studied nuclei	51
3.4.2. Numerical setting	52
3.4.3. Measure of the systematic deviations	52
3.4.4. Ground-state binding energy	53
3.4.5. PHFB absolute energies and radii	59
3.4.6. Spectroscopy	64
3.4.7. Optimal one-body density matrix	70
3.5. Discussion	73
4. Results: PGCM	77
4.1. Introduction	77
4.2. Many-body calculations	78
4.2.1. Nuclear Hamiltonian	78
4.2.2. PGCM	79
4.2.3. IM-NCSM	82
4.3. Results	83
4.3.1. Model-space convergence	83
4.3.2. ^{20}Ne	86
4.3.3. Isotopic chain	93
4.4. Discussion	104
5. Results: PGCM-PT(2)	105
5.1. Introduction	105
5.2. Many-body calculations	107
5.2.1. VSRG pre-processing	107
5.2.2. VSRG+MR-IMSRG pre-processing	119
5.3. Discussion	128
Conclusions	129
A. Symmetry group	133
A.1. Unitary representation	133
A.2. Projection operators	135
B. Permutation operators	137
C. Similarity-transformed matrix elements	139
D. PGCM-PT(2) matrix elements	141
D.1. Type-1 matrix elements	141
D.2. Type-2 matrix elements	142
D.3. Type-3 matrix elements	144
E. Single-reference (Bogoliubov) Many-Body Perturbation Theory	145
E.1. Single-reference partitioning	145
E.1.1. BMBPT	145
E.1.2. MBPT	146

E.2. Second and third order BMBPT energy corrections	147
E.2.1. Second order	147
E.2.2. Third order	147
E.3. BMBPT transition density matrix	148
E.3.1. BCI state	148
E.3.2. Expression in quasi-particle space	148
E.3.3. Expression in one-particle space	149
E.3.4. One-body density matrix	150
E.3.5. BMBPT coefficients	150
F. Inverse tensor transformations	153
G. PGCM transition density matrix	155
G.1. Inputs	155
G.1.1. Off-diagonal one-body density matrix	155
G.2. Definition	155
G.3. Simplified expressions	156
G.3.1. Expanding the projectors	156
G.3.2. Spherical one-body basis	156
G.3.3. Special case of the one-body density matrix of a $J^\pi = 0^+$ state . . .	157
G.4. Anomalous transition one-body density matrix	158
G.4.1. PGCM anomalous density matrix	158
G.4.2. Spherical one-body basis	158
H. Error-function sampling	159
H.1. Error function	159
H.2. Random one-body density matrices	160
H.3. Spherical Hartree-Fock field	161
I. Charge density distribution	163
J. Linear redundancies in HWG	165
K. Memory optimization	167
K.1. J -coupling scheme	167
K.1.1. Contractions with one-body density matrices	168
K.2. Evaluation of the norm overlap	168
L. Anti-symmetry reduction	171
M. Solving the linear problem	173
M.1. Exact SVD-based solution	173
M.2. QLP decomposition	174
M.2.1. Pivoted QR	174
M.3. Pivoted QLP	175
M.3.1. Application	175
M.4. From QLP to MINRES-QLP algorithm	176
M.5. Preconditioning of the linear system	176
M.5.1. Matrix scaling	177
M.5.2. Incomplete Cholesky decomposition	177

M.5.3. Norm preconditioning	177
M.6. Error evaluation	178
M.7. Stopping condition of iterative solver	178
M.8. Illustration of iterative solvers	179
N. Complex shift	181
N.1. Motivations	181
N.2. Implementation in real arithmetic	181
N.3. Example	182
O. Discussion on numerics	185
O.1. Complexity	185
O.2. Complexity reduction in PGCM-PT(2)	187
O.2.1. Norm-based importance truncation	187
O.2.2. Hamiltonian-based importance truncation	187
O.2.3. Energy-based importance truncation	188
O.2.4. Incremental building of the basis	188
P. On the numerical implementation	189
Résumé en français	191
List of Figures	199
List of Tables	207

List of Acronyms

χ **EFT** Chiral Effective Field Theory.

BCC Bogoliubov Coupled Cluster.

BMBPT Bogoliubov Many-Body Perturbation Theory.

CC Coupled Cluster.

dHFB deformed Hartree-Fock-Bogoliubov.

EDF Energy Density Functional.

FCI Full Configuration Interaction.

GSCGF Gorkov Self-Consistent Green Function.

HF Hartree-Fock.

HFB Hartree-Fock-Bogoliubov.

IMSRG In-Medium Similarity Renormalization Group.

IR infrared.

LDM Liquid Drop Model.

MBPT Many-Body Perturbation Theory.

MCPT Multi-Configuration Perturbation Theory.

MR multi reference.

MR-CC Multi-Reference Coupled Cluster.

MR-IMSRG Multi-Reference IMSRG.

NCSM No-Core Shell Model.

NO2B Normal-Ordered 2-Body approximation.

PBCC Projected Bogoliubov Coupled Cluster.

PGCM Projected Generator Coordinate Method.

PGCM-PT PGCM Perturbation Theory.

PHFB Projected Hartree-Fock-Bogoliubov.

QCD Quantum Chromodynamics.

SCGF Self-Consistent Green Function.

sHFB spherical Hartree-Fock-Bogoliubov.

SR single reference.

SRG Similarity Renormalization Group.

UV ultraviolet.

Introduction

La folie n'est plus folle, dès qu'elle est collective.

Alain Damasio
La Horde du Contrevent

The nuclear many-body problem

The theoretical description of atomic nuclei is still an open challenge for several reasons. Even if the experimental study of the rich phenomenology of nuclear systems has been steadily progressing in the past few years, the construction of a unified model capable of giving a reliable and predictive description of the whole nuclear chart is still missing. As of today, the most promising route for a unified theory relies on a set of consistent effective (field) theories (EFT) appropriate to describing various energy scales. For low-energy nuclear systems, one of the most elementary version of such an EFT is chiral EFT (χ EFT) describing the self-bound nucleus as a collection of N point-like neutrons and Z point-like protons in strong interaction. In this context, the theoretical scheme eventually consists of solving the A -body Schrödinger's equation on the basis of a nuclear Hamiltonian systematically built through the χ EFT expansion.

Thus, the first difficulty to the solution of the nuclear many-body problem stems from the complexity of inter-nucleon interactions, themselves deriving from the residual interaction between the quarks and gluons composing the nucleons. The non perturbativeness of Quantum Chromodynamics (QCD) at low energy has long been believed to prevent any workable expansion of the nuclear interaction, and Lattice QCD calculations have not yet been able to provide physically relevant results yet [1, 2, 3]. On top of that, the short-range repulsion of inter-nucleon interaction generates ultraviolet (UV) divergences, while the weakly-bound deuteron and the virtual di-neutron state are a source of infrared (IR) divergences, two fundamentally different phenomena that need to be dealt with to solve the nuclear problem. Last but not least, because nucleons are assumed to be point-like objects within χ EFT, their inner structure is at the source of two, three, four, ... up to A -body terms that would all need to be included in an exact solution of the many-body problem.

Besides the building of the Hamiltonian, the solution of the nuclear many-body problem presents a second challenge. Containing up to 300 hundred nucleons, the vast majority of nuclear systems are too large to allow an exact solution of the A -body Schrödinger's equation. Furthermore, the large variety of scales at play in a nucleus, ranging from short-range individual excitations responsible for absolute binding energies to long-range correlations associated with collective phenomena (at the origin of pairing, rotational and vibrational physics), not to mention phenomena like electroweak decays, make a unified description even harder to achieve. As of today, more than 3400 nuclei stable with

respect to the strong force have been observed [4] and thousands more have been predicted theoretically.

The first attempts to circumvent these difficulties advocated the use of macroscopic descriptions. For instance, semi-classical models of nuclei like Liquid Drop Model (LDM) [5], as crude as they may be, were and are still used for calculations in which fine structure mechanisms are not needed in first approximation. However, the inclusion of microscopic structure effects is mandatory as soon as one aims at a predictive and accurate description. Among microscopic approaches, Energy Density Functional (EDF) has managed, throughout the years, to achieve an empirical description of both long- and short-range correlations in all known (and still to be discovered) nuclei [6, 7]. Still, the phenomenological character of the effective interactions at play, that do not rely on a well-defined hierarchy between the various terms, lacks (as of today) a systematic character. Even with ever-increasing computational resources, this makes further improvement of this method problematic.

In this context, *ab initio* expansion techniques employed with χ EFT interactions and operators approximate the exact solution of A -body Schrödinger's equation through a truncated series, allowing to assess and propagate various sources of theoretical uncertainties through the calculation. *Ab initio* methods all share the following properties:

- Nucleons are considered as elementary structureless degrees of freedom. Consequently, collective nuclear phenomena must emerge from the complex correlations between the interacting nucleons.
- The Hamiltonian is derived consistently from the underlying theory, QCD. The current paradigm is to use Chiral Effective Field Theory (χ EFT) to expand the Hamiltonian matrix elements in a consistent sequence of successive approximations compatible with the symmetries of QCD [8, 9, 10].
- The solution of Schrödinger's equation is expanded in a systematic way, each truncation order correcting the previous one towards the exact solution.
- Errors coming from the various solution steps (Hamiltonian, expansion and numerical approximations) are to be eventually estimated and propagated to the computed observables.

Ab initio methods therefore differ inherently from more phenomenological approaches for which the error assessment is in the best case intricate if not impossible. Two decades ago, these methods were only implemented through quasi-exact approaches, e.g. Fadeev-Yakubovski [11, 12, 13], Green's function Monte Carlo [14, 15, 16] and No-Core Shell Model (NCSM) [17, 18, 19, 20, 21], and were consequently limited to light nuclei due to an exponential scaling with system size. Through the joint formalisation of preprocessing methods of the Hamiltonian removing the UV divergences [22], and of expansion methods for the solution of Schrödinger's equation, it has become possible in the past 15 years to develop polynomial methods to tackle medium-mass nuclear systems.

***Ab initio* expansion methods**

Expansion methods aim at adding correlations on top of a reference state suitably chosen such that it constitutes a good enough starting point towards the true solution. Although expansion methods capture by construction all correlations in their exact limit, they

tend, traditionally, to focus on short-range (dynamical) correlations, and usually fail to account correctly for residual strong (static) correlations arising in open-shell systems. This distinction between static and dynamical correlations, even if partly arbitrary, is very useful in practice and the coherent inclusion of both type of correlations is an important challenge for *ab initio* methods today.

Single-reference expansion methods in closed-shell systems

In closed-shell nuclei collective long-range effects are almost not necessary for the description of the ground state, such that it is sufficient to account for dynamical correlations. In such systems, expansions built on top of a single-determinantal (i.e. single reference (SR)) reference state, usually optimized via mean-field methods like Hartree-Fock (HF), account for dynamical correlations via particle-hole excitations. The wave function of the system $|\Psi\rangle$ is therefore written as a wave operator Ω acting on the reference state $|\Phi\rangle$

$$|\Psi\rangle \equiv \Omega|\Phi\rangle, \quad (0.1)$$

that correlates the mean-field ansatz towards the true solution. The first example is Many-Body Perturbation Theory (MBPT) [23, 24, 25], where Ω is expanded perturbatively. The method has gained a renewed interest in the last years thanks to the pre-processing of the interaction via Similarity Renormalization Group (SRG) transformations that make the expansion possibly convergent [26, 27, 28]. In parallel, non perturbative expansion methods have been developed as well. Coupled Cluster (CC) [29, 30, 31, 32, 33], In-Medium Similarity Renormalization Group (IMSRG) [34, 35, 36, 37] or Self-Consistent Green Function (SCGF) [38, 39, 40] methods all resum in their own way selected sets of perturbation theory contributions to infinite orders and therefore deliver higher accuracy at a given computational cost.

All those methods show a very good agreement with each other and with exact NCSM calculations, and have been able to extend the reach of *ab initio* calculations to systems containing up to $A \sim 130$ nucleons [41, 42].

Multi-reference approaches and static correlations

The application of expansion methods poses problems in open-shell systems, where single-determinantal expansions break down due to degeneracies with respect to elementary excitations. This difficulty is already known in the context of phenomenological EDFs, where the qualitative description within a symmetry-conserving mean-field scheme is quickly deteriorating away from doubly-magic nuclei. These degeneracies allow the development of strong long-range correlations near the Fermi level that can be safely captured by complexifying the reference state. Instead of sticking to a symmetry-conserving Slater determinant, an optimized linear combination of symmetry-breaking generalized product states is used as reference state.

In EDF approaches, this multi reference (MR) state is built in two separate steps. First, the symmetry-conserving determinant is replaced by a symmetry-breaking reference state [43]. This reference state is still a product state, but is allowed to be deformed or to break particle number symmetry. Since nuclei are mesoscopic quantum systems, however, true eigenstates of the Hamiltonian must carry good symmetry quantum numbers. Hence, in a second step, one needs to project the reference state onto good symmetry states via a linear combination involving all its symmetry-rotated partners, thus accounting for the

associated rotational (and/or pairing) physics. The vibrational physics is further addressed by additionally mixing projected states differing by the symmetry breaking content of the underlying product states, giving rise to the Projected Generator Coordinate Method (PGCM) method.

Following the same rationale, the unperturbed state at play in *ab initio* expansion methods can be allowed to break symmetries in order to lift unwanted degeneracies such that the expansion is performed on top of a symmetry-breaking unperturbed state. This approach has been implemented for particle-number symmetry through Bogoliubov Many-Body Perturbation Theory (BMBPT) [44, 45, 46, 47], Gorkov Self-Consistent Green Function (GSCGF) [48, 49, 50] and Bogoliubov Coupled Cluster (BCC), as well as for rotational symmetry through CC [51, 52]. The corresponding description of ground-state properties of medium mass nuclei competes with more phenomenological approaches. However, as for EDFs, symmetry breaking is only an intermediate step such that symmetries need to be eventually restored. The symmetry restoration becomes non-trivial in beyond mean-field methods and has been formulated only recently for both perturbative and non-perturbative expansions [53, 54]. Projected Bogoliubov Coupled Cluster (PBCC) has been implemented successfully for schematic Hamiltonians [55, 56], but no implementation with realistic nuclear interactions has been achieved yet and the first attempts in this direction have not been conclusive.

Another possible strategy is to add dynamical correlations on top of a multi-reference Ansatz that already incorporate static correlations. Following this idea, the Multi-Reference IMSRG (MR-IMSRG) has been developed in nuclear physics [37, 57], and Multi-Reference Coupled Cluster (MR-CC) in quantum chemistry [25], while Multi-Configuration Perturbation Theory (MCPT) perturbatively builds correlations on top of a NCSM reference state [28]. However, MR-IMSRG is not yet a solution method as such but acts more as a preprocessing of the Hamiltonian, while MCPT needs a preliminary NCSM reference state, which becomes out of reach beyond light nuclei. In quantum chemistry, another MR perturbation theory based on a non-orthogonal mixing of determinants has been recently proposed and implemented [58, 59], showing great success in systems with strong static correlations.

The present work has consisted in building on recent advances in quantum chemistry in order to

- Formalize a universal MR perturbation theory based on an unperturbed state mixing non-orthogonal Bogoliubov product states in order to consistently capture static and dynamical correlations within an *ab initio* context,
- Implement the first order of the formalism and use it to systematically investigate the low-lying spectroscopy in the neon chain,
- Implement the second order of the formalism in a restricted model space in order to assess the quality of the method with realistic nuclear Hamiltonians,
- Formalize, implement and benchmark a symmetry-conserving rank-reduction method of operators to efficiently reabsorb the effect of three-nucleon interactions (at the cost of introducing a controlled error in the end result) via the sole use of effective two-body operators.

The present thesis is structured as follows. Chapter 1 introduces the notations and the basic ingredients of the formalism used in the rest of the manuscript. Chapter 2 presents

the formalism of MR perturbation theory and discusses the role of the reference state in dynamical expansions. Chapter 3 describes the many-body reduction of the interaction, and carefully tests the approximation for three-body forces in a selected set of nuclei and many-body methods. Chapter 4 develops the first order of the theory that correspond to the linear mixing of projected mean-field calculations. Systematic results are shown for the neon chain and compared to other reference methods. Finally, Chapter 5 implements and shows the first original results of the new perturbation theory in restricted model spaces. Attention is put on total energies as well as spectroscopic quantities. Details on symmetry groups, derivations, similarity-transformed matrix elements and aspects of the numerical implementation are given in the appendices.

Chapter 1.

Basic definitions and elements of Bogoliubov algebra

Contents

1.1. Operators in second quantized form	8
1.1.1. Operators definition	8
1.1.2. Density matrices	9
1.2. Bogoliubov algebra	9
1.2.1. Bogoliubov state	9
1.2.2. One-body density matrices	10
1.2.3. Normal-ordered operators	11
1.2.4. Constrained Hartree-Fock-Bogoliubov theory	11
1.2.5. Elementary excitations	13
1.2.6. Rotated Bogoliubov state	13
1.2.7. Overlap between Bogoliubov vacua	14
1.2.8. Transition Bogoliubov transformation	15
1.2.9. Similarity transformation	15

Given the nuclear Hamiltonian H , *ab initio* nuclear structure calculations seek a solution of the A -body Schrödinger's eigenvalue equation

$$H|\Psi_\mu^\sigma\rangle = E_\mu^{\tilde{\sigma}} |\Psi_\mu^\sigma\rangle, \quad (1.1)$$

that is as accurate as possible for as many nuclei as possible. In Eq. (1.1), μ denotes a principal quantum number whereas $\sigma \equiv (JM\Pi NZ) \equiv (\tilde{\sigma}M)$ collects the set of symmetry quantum numbers labelling the many-body states, i.e. the angular momentum J and its projection M , the parity $\Pi = \pm 1$ as well as neutron N and proton Z numbers. The M -independence of the eigenenergies $E_\mu^{\tilde{\sigma}}$ and the symmetry quantum numbers carried by the eigenstates are a testimony of the symmetry group

$$G_H \equiv \{R(\theta), \theta \in D_G\} \quad (1.2)$$

of the Hamiltonian, i.e.,

$$[H, R(\theta)] = 0, \forall \theta, \quad (1.3)$$

which plays a key role in the present context¹. In the particular case of *ab initio* calculations, H is a realistic interaction and its matrix elements are derived consistently with the underlying physics within the framework of χ EFT.

To solve this equation, one must first define a many-body basis in which the problem is expressed prior to applying solution methods.

1.1. Operators in second quantized form

1.1.1. Operators definition

Given a basis $\mathcal{B}_1 \equiv \{|l\rangle\}$ of the one-body Hilbert space \mathcal{H}_1 whose associated set of particle creation and annihilation operators is denoted as $\{c_l^\dagger, c_l\}$, an arbitrary particle-number-conserving operator O is represented as

$$O \equiv \sum_{n=0}^r O^{nn}, \quad (1.4)$$

where each n -body component²

$$O^{nn} \equiv \frac{1}{n!} \frac{1}{n!} \sum_{\substack{a_1 \dots a_n \\ b_1 \dots b_n}} o_{b_1 \dots b_n}^{a_1 \dots a_n} C_{b_1 \dots b_n}^{a_1 \dots a_n}, \quad (1.5)$$

and

$$C_{b_1 \dots b_n}^{a_1 \dots a_n} \equiv c_{a_1}^\dagger \dots c_{a_n}^\dagger c_{b_n} \dots c_{b_1} \quad (1.6)$$

defines a string of n particle creation and n particle annihilation operators such that

$$\left(C_{b_1 \dots b_n}^{a_1 \dots a_n}\right)^\dagger = C_{a_1 \dots a_n}^{b_1 \dots b_n}. \quad (1.7)$$

The string is in normal order with respect to the particle vacuum $|0\rangle$

$$N(C_{b_1 \dots b_n}^{a_1 \dots a_n}) = C_{b_1 \dots b_n}^{a_1 \dots a_n}, \quad (1.8)$$

where $N(\dots)$ denotes the normal ordering with respect to $|0\rangle$, and it is anti-symmetric under the exchange of any pair of upper or lower indices, i.e.

$$C_{b_1 \dots b_n}^{a_1 \dots a_n} = \epsilon(\sigma_u) \epsilon(\sigma_l) C_{\sigma_l(b_1 \dots b_n)}^{\sigma_u(a_1 \dots a_n)}, \quad (1.9)$$

where $\epsilon(\sigma_u)$ ($\epsilon(\sigma_l)$) refers to the signature of the permutation $\sigma_u(\dots)$ ($\sigma_l(\dots)$) of the n upper (lower) indices.

In Eq. (1.5), the n -body matrix elements $\{o_{b_1 \dots b_n}^{a_1 \dots a_n}\}$ constitute a mode- $2n$ tensor, i.e. a data array carrying $2n$ indices, associated with the string they multiply. The n -body matrix elements are also fully anti-symmetric under the exchange of any pair of upper or lower indices, i.e.

$$o_{b_1 \dots b_n}^{a_1 \dots a_n} = \epsilon(\sigma_u) \epsilon(\sigma_l) o_{\sigma_l(b_1 \dots b_n)}^{\sigma_u(a_1 \dots a_n)}. \quad (1.10)$$

¹The characteristics of G_H and the definitions of the quantities associated with it that are used throughout the present work are detailed in App. A.

²The term O^{00} is a number.

1.1.2. Density matrices

The l -body density matrix associated with a many-body state $|\Theta\rangle$ constitutes a mode- $2l$ tensor defined through³

$$[\rho^{(l)\Theta}]_{a_1 \dots a_l}^{b_1 \dots b_l} \equiv \frac{\langle \Theta | C_{b_1 \dots b_l}^{a_1 \dots a_l} | \Theta \rangle}{\langle \Theta | \Theta \rangle}. \quad (1.11)$$

In the following, the superscripts l and Θ are omitted for $l = 1$ and when dealing with a generic density matrix, respectively. The elements of $\rho^{(l)\Theta}$ inherit from $C_{b_1 \dots b_l}^{a_1 \dots a_l}$ a full anti-symmetry under the exchange of any pair of upper or lower indices along with a hermitian character, i.e.

$$[\rho^{(l)\Theta}]_{a_1 \dots a_l}^{b_1 \dots b_l} = \left([\rho^{(l)\Theta}]_{b_1 \dots b_l}^{a_1 \dots a_l} \right)^*. \quad (1.12)$$

Given two density matrices $\rho^{(l)\Theta}$ and $\rho^{(k)\Psi}$, their tensor product

$$\rho^{(l)\Theta \otimes (k)\Psi} \equiv \rho^{(l)\Theta} \otimes \rho^{(k)\Psi} \quad (1.13)$$

defines a direct-product $(l+k)$ -body density matrix through the mode- $2(l+k)$ tensor whose elements are given by

$$[\rho^{(l)\Theta \otimes (k)\Psi}]_{a_1 \dots a_{l+k}}^{b_1 \dots b_{l+k}} \equiv [\rho^{(l)\Theta}]_{a_1 \dots a_l}^{b_1 \dots b_l} [\rho^{(k)\Psi}]_{a_{l+1} \dots a_{l+k}}^{b_{l+1} \dots b_{l+k}}, \quad (1.14)$$

and display the hermitian property characterized in Eq. (1.12). Because of the direct-product character of $\rho^{(l)\Theta \otimes (k)\Psi}$, its elements are only partially anti-symmetrized, i.e. they are anti-symmetric under the exchange of any pair of the first l (or last k) upper or lower indices.

In case one considers the m -fold tensor product of the same l -body density matrix $\rho^{(l)\Theta}$, the notation can be further simplified according to $\rho^{\otimes(m)l\Theta} \equiv \rho^{(l)\Theta} \otimes \dots \otimes \rho^{(l)\Theta}$. In particular, the m -fold tensor product of the generic one-body density matrix ρ defines a mode- $2m$ tensor whose elements are

$$[\rho^{\otimes(m)}]_{a_1 \dots a_m}^{b_1 \dots b_m} \equiv \rho_{a_1}^{b_1} \dots \rho_{a_m}^{b_m}. \quad (1.15)$$

Because of its pure direct-product character, the elements of $\rho^{\otimes(m)}$ display no property under the exchange of any pair of upper or lower indices but inherit the hermitian property characterized by Eq. (1.12).

1.2. Bogoliubov algebra

1.2.1. Bogoliubov state

Considering an arbitrary order parameter q , whose detailed significance will be specified later on, the linear Bogoliubov transformation $\mathcal{W}(q)$ connects the set of particle creation and annihilation operators $\{c, c^\dagger\}$ to a set of quasi-particles creation and annihilation operators $\{\beta(q), \beta^\dagger(q)\}$ obeying fermionic anti-commutation rules

$$\{\beta_k(q), \beta_l(q)\} = 0, \quad (1.16a)$$

$$\{\beta_k^\dagger(q), \beta_l^\dagger(q)\} = 0, \quad (1.16b)$$

³Conventionally, Eq. (1.11) is consistently extended to $l = 0$ via $\rho^{(0)\Theta} \equiv 1$.

$$\{\beta_k(q), \beta_l^\dagger(q)\} = \delta_{kl}. \quad (1.16c)$$

Formally the transformation reads [43]

$$\begin{pmatrix} \beta(q) \\ \beta^\dagger(q) \end{pmatrix} \equiv \mathcal{W}^\dagger(q) \begin{pmatrix} c \\ c^\dagger \end{pmatrix}, \quad (1.17)$$

with

$$\mathcal{W}(q) \equiv \begin{pmatrix} U(q) & V^*(q) \\ V(q) & U^*(q) \end{pmatrix}. \quad (1.18)$$

so that the Bogoliubov transformation in expanded form reads as

$$\beta_k(q) \equiv \sum_l U_{lk}^*(q) c_l + V_k^{*l}(q) c_l^\dagger, \quad (1.19a)$$

$$\beta_k^\dagger(q) \equiv \sum_l U^{lk}(q) c_l^\dagger + V_l^k(q) c_l. \quad (1.19b)$$

The anti-commutation rules (Eq. (1.16)) constrain $\mathcal{W}(q)$ to be unitary

$$\mathcal{W}^\dagger(q) \mathcal{W}(q) = \mathcal{W}(q) \mathcal{W}^\dagger(q) = 1, \quad (1.20)$$

which translates into

$$U^\dagger(q)U(q) + V^\dagger(q)V(q) = 1, \quad (1.21a)$$

$$V^T(q)U(q) + U^T(q)V(q) = 0, \quad (1.21b)$$

$$U(q)U^\dagger(q) + V^*(q)V^T(q) = 1, \quad (1.21c)$$

$$V(q)U^\dagger(q) + U^*(q)V^T(q) = 0. \quad (1.21d)$$

The normalized Bogoliubov product state $|\Phi(q)\rangle$ is defined, up to a phase, as the vacuum of the quasi-particle operators, i.e.

$$\beta_k(q)|\Phi(q)\rangle \equiv 0, \quad \forall k. \quad (1.22)$$

Contrary to Slater determinants, which constitute a subset of Bogoliubov states, the latter are not eigenstates of neutron and proton number operators in general.

1.2.2. One-body density matrices

The Bogoliubov vacuum is fully characterized by its normal $\rho(q)$ and anomalous $\kappa(q)$ one-body density matrices whose matrix elements are defined through

$$\rho_{l_2}^{l_1}(q) \equiv \langle \Phi(q) | c_{l_2}^\dagger c_{l_1} | \Phi(q) \rangle = V^*(q) V^T(q), \quad (1.23a)$$

$$\kappa^{l_1 l_2}(q) \equiv \langle \Phi(q) | c_{l_2} c_{l_1} | \Phi(q) \rangle = V^*(q) U^T(q), \quad (1.23b)$$

such that

$$\rho^\dagger(q) = \rho(q), \quad (1.24a)$$

$$\kappa^T(q) = -\kappa(q). \quad (1.24b)$$

1.2.3. Normal-ordered operators

It is eventually useful to normal order operators with respect to the Bogoliubov vacuum $|\Phi(q)\rangle$ and express them in terms of the associated quasi-particle operators. Applying the standard Wick's theorem leads to

$$O \equiv \sum_{n=0}^r \mathbf{O}^{[2n]}(q) \equiv \sum_{n=0}^r \sum_{\substack{i,j=0 \\ i+j=2n}}^{2r} \mathbf{O}^{ij}(q), \quad (1.25)$$

with⁴

$$\mathbf{O}^{ij}(q) \equiv \frac{1}{i!} \frac{1}{j!} \sum_{\substack{k_1 \dots k_i \\ l_1 \dots l_j}} \mathbf{o}_{l_1 \dots l_j}^{k_1 \dots k_i}(q) B_{l_1 \dots l_j}^{k_1 \dots k_i}(q), \quad (1.26)$$

where

$$B_{l_1 \dots l_j}^{k_1 \dots k_i}(q) \equiv \beta_{k_1}^\dagger(q) \dots \beta_{k_i}^\dagger(q) \beta_{l_1}(q) \dots \beta_{l_j}(q) \quad (1.27)$$

denotes a string of i quasi-particle creation and j quasi-particle annihilation operators such that

$$(B_{l_1 \dots l_j}^{k_1 \dots k_i}(q))^\dagger = B_{k_1 \dots k_i}^{l_1 \dots l_j}(q). \quad (1.28)$$

The string is in normal order with respect to the Bogoliubov state $|\Phi(q)\rangle$

$$: B_{l_1 \dots l_j}^{k_1 \dots k_i}(q) := B_{l_1 \dots l_j}^{k_1 \dots k_i}(q), \quad (1.29)$$

where $:\dots:$ denotes the normal ordering with respect to $|\Phi(q)\rangle$, and it is anti-symmetric under the exchange of any pair of upper or lower indices, i.e.

$$B_{l_1 \dots l_j}^{k_1 \dots k_i}(q) = \epsilon(\sigma_u) \epsilon(\sigma_l) B_{\sigma_l(l_1 \dots l_j)}^{\sigma_u(k_1 \dots k_i)}(q). \quad (1.30)$$

In Eq. (1.26), the matrix elements $\{\mathbf{o}_{l_1 \dots l_j}^{k_1 \dots k_i}(q)\}$ are fully anti-symmetric under the exchange of any pair of upper or lower indices, i.e.

$$\mathbf{o}_{l_1 \dots l_j}^{k_1 \dots k_i}(q) = \epsilon(\sigma_u) \epsilon(\sigma_l) \mathbf{o}_{\sigma_l(l_1 \dots l_j)}^{\sigma_u(k_1 \dots k_i)}(q), \quad (1.31)$$

and are functionals of the Bogoliubov matrices $(U(q), V(q))$ and of the matrix elements $\{o_{b_1 \dots b_n}^{a_1 \dots a_n}\}$ initially defining the operator O . As such, the content of each operator $\mathbf{O}^{ij}(q)$ depends on the rank r of O . For more details about the normal ordering procedure and for explicit expressions of the matrix elements up to $r = 3$, see Refs. [45, 46, 47, 53, 60, 61].

1.2.4. Constrained Hartree-Fock-Bogoliubov theory

The state $|\Phi(q)\rangle$ is obtained by minimizing its total energy under the constraints that it satisfies⁵

$$\langle \Phi(q) | A | \Phi(q) \rangle = A, \quad (1.32a)$$

$$\langle \Phi(q) | Q | \Phi(q) \rangle = q, \quad (1.32b)$$

where Q is a generic operator of interest. To do so, one considers the Routhian

$$R \equiv H - \lambda_A(A - A) - \lambda_q(Q - q) \quad (1.33a)$$

⁴The term $\mathbf{O}^{00}(q)$ is just a number.

⁵In our discussion A stands for either the neutron (N) or the proton (Z) number.

$$\equiv \Omega - \lambda_q(Q - q), \quad (1.33b)$$

where λ_A and λ_q denote two Lagrange parameters⁶. The Routhian reduces to the so-called grand potential Ω whenever $\lambda_q = 0$, i.e. when we perform unconstrained calculations with respect to the order parameter q . Minimizing⁷

$$R(q) \equiv \langle \Phi(q) | R | \Phi(q) \rangle = \mathbf{R}^{00}(q) \quad (1.34)$$

according to Ritz' variational principle, the Bogoliubov matrices ($U(q), V(q)$) are found as the solutions of the Hartree-Fock-Bogoliubov (HFB) eigenequation [43]

$$\begin{pmatrix} \bar{h}(q) & \bar{\Delta}(q) \\ -\bar{\Delta}^*(q) & -\bar{h}^*(q) \end{pmatrix} \begin{pmatrix} U(q) \\ V(q) \end{pmatrix}_k = E_k(q) \begin{pmatrix} U(q) \\ V(q) \end{pmatrix}_k, \quad (1.35)$$

where the eigenvalues $\{E_k(q)\}$ are referred to as quasi-particle energies. The constrained HFB Hamiltonian matrix

$$\mathcal{H}(q) \equiv \begin{pmatrix} \bar{h}(q) & \bar{\Delta}(q) \\ -\bar{\Delta}^*(q) & -\bar{h}^*(q) \end{pmatrix}, \quad (1.36)$$

is built out of the constrained one-body Hartree-Fock and Bogoliubov fields

$$\bar{h}_{l'}^l(q) \equiv \frac{\partial \mathbf{R}^{00}(q)}{\partial \rho_{l'}^{*l}(q)} \quad (1.37a)$$

$$\begin{aligned} &= \langle \Phi(q) | \{[c_l, R], c_{l'}^\dagger\} | \Phi(q) \rangle \\ &= f_{l'}^l[|\Phi(q)\rangle] - \lambda_q \frac{\partial \mathbf{Q}^{00}(q)}{\partial \rho_{l'}^{*l}(q)} - \lambda_A \delta_{ll'}, \end{aligned}$$

$$\bar{\Delta}_{ll'}(q) \equiv \frac{\partial \mathbf{R}^{00}(q)}{\partial \kappa_{ll'}^*(q)} \quad (1.37b)$$

$$\begin{aligned} &= \langle \Phi(q) | \{[c_l, R], c_{l'}\} | \Phi(q) \rangle \\ &= \frac{\partial \mathbf{H}^{00}(q)}{\partial \kappa_{ll'}^*(q)} - \lambda_q \frac{\partial \mathbf{Q}^{00}(q)}{\partial \kappa_{ll'}^*(q)}, \end{aligned}$$

where $f_{l'}^l[|\Phi(q)\rangle]$ denote the matrix elements of the one-body operator generically defined in Eq. (2.31) but presently computed from the normal one-body density matrix of $|\Phi(q)\rangle$.

At convergence where the constraints (Eq. (1.32)) are satisfied, the HFB energy is

$$\langle \Phi(q) | H | \Phi(q) \rangle = \mathbf{H}^{00}(q) = \mathbf{R}^{00}(q). \quad (1.38)$$

Furthermore, Eq. 1.35 implies that

$$\begin{aligned} \mathcal{W}^\dagger(q) \mathcal{H}(q) W(q) &= \begin{pmatrix} \mathbf{R}^{11}(q) & \mathbf{R}^{20}(q) \\ -\mathbf{R}^{20*}(q) & -\mathbf{R}^{11*}(q) \end{pmatrix} \\ &= \begin{pmatrix} E(q) & 0 \\ 0 & -E(q) \end{pmatrix}, \end{aligned}$$

⁶In actual applications, one Lagrange multiplier relates to constraining the neutron number N and one Lagrange multiplier is used to constrain the proton number Z .

⁷As alluded to in Sec. 1.2.3, the explicit functional form of $\mathbf{R}^{00}(q)$ depends on the initial rank of H and Q and can be found elsewhere for up to 3-body operators [45, 53, 61].

such that the properties

$$\mathbf{R}^{20}(q) = \mathbf{R}^{02}(q) = 0, \quad (1.39a)$$

$$\mathbf{R}^{11}(q) = \sum_k E_k(q) \beta_k^\dagger(q) \beta_k(q), \quad (1.39b)$$

are fulfilled at convergence.

1.2.5. Elementary excitations

Given the Bogoliubov state $|\Phi(q)\rangle$, a complete basis of Fock space \mathcal{F} is obtained by generating all its elementary excitations

$$|\Phi^{k_1 \dots k_i}(q)\rangle \equiv B^{k_1 \dots k_i}(q) |\Phi(q)\rangle. \quad (1.40)$$

where $B^{k_1 \dots k_i}(q)$ defines the subclass of strings defined in Eq. (1.27) that only contain quasi-particle creation operators.

It is interesting to note that each state defined through Eq. (1.40) is itself a Bogoliubov vacuum whose associated Bogoliubov transformation can be deduced from the one defining $|\Phi(q)\rangle$ (Eq. (1.19)). Writing as $K_n \equiv \{k_1 \dots k_n\}$ the n-tuple defining a given elementary excitation $|\Phi^{K_n}(q)\rangle$, the associated Bogoliubov transformation $(U(q, K_n), V(q, K_n))$ is given by the matrices

$$U^{lk}(q, K_n) \equiv U^{lk}(q) \text{ if } k \notin K_n, \quad (1.41a)$$

$$U^{lk}(q, K_n) \equiv V_l^{k*}(q) \text{ if } k \in K_n, \quad (1.41b)$$

$$V_k^l(q, K_n) \equiv V_k^l(q) \text{ if } k \notin K_n, \quad (1.41c)$$

$$V_k^l(q, K_n) \equiv U_{lk}^*(q) \text{ if } k \in K_n. \quad (1.41d)$$

Such a consideration can be exploited to eventually compute matrix elements of operators between two Bogoliubov states that may differ not only by the value of the collective coordinate q but also by the elementary excitation character. The idea of evaluating matrix elements by redefining each elementary excitation of an original Bogoliubov vacuum as a novel vacuum is a generalization of the so-called generalized Slater-Condon rules [62]. The present work follows a numerically more efficient route where quasi-particle excitation operators are explicitly processed in order to avoid the combinatorics associated with the redefinition of many Bogoliubov transformations through Eq. (1.41).

1.2.6. Rotated Bogoliubov state

Given the Bogoliubov state $|\Phi(q)\rangle$, its rotated partner

$$|\Phi(q; \theta)\rangle \equiv R(\theta) |\Phi(q)\rangle, \quad (1.42)$$

is also a Bogoliubov state whose associated quasi-particle operators $\{\beta(q; \theta), \beta^\dagger(q; \theta)\}$ are characterized by the Bogoliubov transformation

$$\begin{aligned} \mathcal{W}(q; \theta) &= \begin{pmatrix} r(\theta) & 0 \\ 0 & r(\theta)^\dagger \end{pmatrix} \mathcal{W}(q) \\ &\equiv \begin{pmatrix} U(q; \theta) & V^*(q; \theta) \\ V(q; \theta) & U^*(q; \theta) \end{pmatrix}, \end{aligned} \quad (1.43)$$

where $r(\theta)$ defines the matrix representation of $R(\theta)$ in the one-body Hilbert-space. Its matrix elements are

$$r_{l_2}^{l_1}(\theta) \equiv \langle l_1 | R(\theta) | l_2 \rangle. \quad (1.44)$$

Given that $\mathcal{W}(q; \theta)$ is a unitary Bogoliubov transformation, Eqs. (1.21) are also satisfied when substituting $(U(q), V(q))$ for $(U(q; \theta), V(q; \theta))$.

Because $R(\theta) \in G_H$, the energy of the rotated HFB state

$$\langle \Phi(q; \theta) | H | \Phi(q; \theta) \rangle = \mathbf{H}^{00}(q; \theta) \quad (1.45)$$

is in fact independent of the rotation angle; i.e. $\mathbf{H}^{00}(q; \theta) = \mathbf{H}^{00}(q)$ for all θ .

Elementary excitations of the rotated Bogoliubov state are given by

$$|\Phi^{k_1 \dots k_i}(q; \theta)\rangle \equiv B^{k_1 \dots k_i}(q; \theta) |\Phi(q; \theta)\rangle \quad (1.46)$$

where the rotated string reads as

$$\begin{aligned} B^{k_1 \dots k_i}(q; \theta) &\equiv R(\theta) B_{l_1 \dots l_j}^{k_1 \dots k_i}(q) R^\dagger(\theta) \\ &= \beta_{k_1}^\dagger(q; \theta) \dots \beta_{k_i}^\dagger(q; \theta) \beta_{l_j}(q; \theta) \dots \beta_{l_1}(q; \theta), \end{aligned} \quad (1.47)$$

such that they are nothing but the rotated elementary excitations

$$|\Phi^{k_1 \dots k_i}(q; \theta)\rangle \equiv R(\theta) |\Phi^{k_1 \dots k_i}(q)\rangle. \quad (1.48)$$

1.2.7. Overlap between Bogoliubov vacua

Given two Bogoliubov vacua $|\Phi(q, \theta)\rangle$ and $|\Phi(p)\rangle$, their overlap is a key ingredient to the calculation of the needed many-body matrix elements. To express the result, Bloch-Messiah-Zumino decompositions [43] of the Bogoliubov transformations $\mathcal{W}(p)$ and $\mathcal{W}(q)$ are invoked, e.g. the matrices defining $\mathcal{W}(p)$ are expressed as the product of unitary matrices $D(p)$ and $C(p)$ and special block-diagonal matrices $\bar{U}(p)$ and $\bar{V}(p)$ according to

$$U(p) \equiv D(p) \bar{U}(p) C(p), \quad (1.49a)$$

$$V(p) = D^*(p) \bar{V}(p) C(p). \quad (1.49b)$$

Further denoting by $v_k(p)$ the BCS-like coefficients making up $\bar{V}(p)$, the overlap eventually reads as [63]⁸

$$\langle \Phi(p) | \Phi(q; \theta) \rangle = (-1)^n \frac{\det(C^*(p)) \det(C(q))}{\prod_k^n v_k(p) v_k(q)} \text{pf} \left[\begin{pmatrix} V(p)^T U(p) & V^T(p) \mathbf{r}^T(\theta) V^*(q) \\ -V(q)^\dagger \mathbf{r}(\theta) V(p) & U^\dagger(q) V^*(q) \end{pmatrix} \right], \quad (1.50)$$

where $2n$ denotes the dimension of \mathcal{H}_1 and where the pfaffian of a symplectic matrix has been considered.

⁸There exists an alternative way to compute the overlap between any two Bogoliubov states without any phase ambiguity, see Ref. [64].

1.2.8. Transition Bogoliubov transformation

Given the Bogoliubov vacua $|\Phi(q, \theta)\rangle$ and $|\Phi(p)\rangle$, the two sets of quasi-particle operators are related via the Bogoliubov transformation

$$\begin{aligned} \begin{pmatrix} \beta(q; \theta) \\ \beta^\dagger(q; \theta) \end{pmatrix} &= \mathcal{W}^\dagger(q; \theta) \mathcal{W}(p) \begin{pmatrix} \beta(p) \\ \beta^\dagger(p) \end{pmatrix} \\ &\equiv \begin{pmatrix} D^\dagger(p, q; \theta) & E^\dagger(p, q; \theta) \\ E^T(p, q; \theta) & D^T(p, q; \theta) \end{pmatrix} \begin{pmatrix} \beta(p) \\ \beta^\dagger(p) \end{pmatrix} \\ &\equiv \mathcal{W}^\dagger(p, q; \theta) \begin{pmatrix} \beta(p) \\ \beta^\dagger(p) \end{pmatrix}, \end{aligned} \quad (1.51)$$

where

$$E(p, q; \theta) \equiv V^T(q)U(q; \theta) + U^T(q)V(q; \theta), \quad (1.52a)$$

$$D(p, q; \theta) \equiv U^\dagger(q)U(q; \theta) + V^\dagger(q)V(q; \theta). \quad (1.52b)$$

Given that $W(p, q; \theta)$ is a unitary Bogoliubov transformation, Eqs. (1.21) is also satisfied when substituting $(U(q), V(q))$ for $(D(p, q; \theta), E(p, q; \theta))$.

1.2.9. Similarity transformation

Thouless transformation

The two Bogoliubov vacua $|\Phi(q, \theta)\rangle$ and $|\Phi(p)\rangle$ can be connected via a non-unitary Thouless transformation

$$|\Phi(q; \theta)\rangle = \langle \Phi(p) | \Phi(q; \theta) \rangle \exp \left[\mathbf{Z}^{20}(p, q; \theta) \right] |\Phi(p)\rangle, \quad (1.53)$$

where matrix elements of the Thouless operator

$$\mathbf{Z}^{20}(p, q; \theta) \equiv \frac{1}{2} \sum_{k_1 k_2} \mathbf{z}^{k_1 k_2}(p, q; \theta) B^{k_1 k_2}(p). \quad (1.54)$$

are expressed in terms of the transition Bogoliubov transformation between both vacua (Eqs. (1.51)-(1.52)) according to

$$\mathbf{z}(p, q; \theta) = E^*(p, q; \theta) D^{*-1}(p, q; \theta). \quad (1.55)$$

Similarity-transformed operators

Given $|\Phi(p)\rangle$, $|\Phi(q, \theta)\rangle$ and an operator O , the similarity-transformed operator is introduced as

$${}^Z O \equiv e^{-\mathbf{Z}^{20}(p, q; \theta)} O e^{\mathbf{Z}^{20}(p, q; \theta)}, \quad (1.56)$$

which obviously depends on $(p, q; \theta)$ via $\mathbf{Z}^{20}(p, q; \theta)$. Because the similarity transformation is not unitary, ${}^Z O$ is not hermitian. Such similarity-transformed operators appear repeatedly in the PGCM-PT formalism developed in the present work.

Normal ordering O with respect to $|\Phi(p)\rangle$ according to Eqs. (1.25)-(1.26), ${}^Z O$ is obtained by simply replacing the quasi-particle operators $\{\beta_k^\dagger(p), \beta_k(p)\}$ by the similarity-transformed ones

$$\begin{pmatrix} {}^Z \beta(p) \\ {}^Z \beta^\dagger(p) \end{pmatrix} \equiv e^{-\mathbf{Z}^{20}(p, q; \theta)} \begin{pmatrix} \beta(p) \\ \beta^\dagger(p) \end{pmatrix} e^{\mathbf{Z}^{20}(p, q; \theta)}$$

$$\begin{aligned}
 &= \begin{pmatrix} 1 & \mathbf{z}(p, q; \theta) \\ 0 & 1 \end{pmatrix} \begin{pmatrix} \beta(p) \\ \beta^\dagger(p) \end{pmatrix} \\
 &\equiv {}^Z\mathcal{X}^\dagger(p, q; \theta) \begin{pmatrix} \beta(p) \\ \beta^\dagger(p) \end{pmatrix}.
 \end{aligned} \tag{1.57}$$

Expressing the result in terms of the initial set $\{\beta_k^\dagger(p), \beta_k(p)\}$ and applying Wick's theorem allows one to eventually express ZO in normal-ordered form with respect to $|\Phi(p)\rangle$, i.e. according to Eqs. (1.25)-(1.27), where the set of $(p, q; \theta)$ -dependent matrix elements are functions of the original set of matrix elements and of the matrix $\mathbf{z}(p, q; \theta)$. The explicit expressions of these matrix elements are provided in App. C for a two-body operator O , i.e. an operator with $r = 2$ in Eqs. (1.4)-(1.6) and/or Eqs. (1.25)-(1.27).

As made clear in App. D, one also needs the similarity transformation of a de-excitation operator $B_{l_1 \dots l_i}(p)$ acting on the corresponding vacuum bra $\langle \Phi(p)|$, i.e.

$$\begin{aligned}
 \langle \Phi(p)| {}^Z B_{l_1 \dots l_i}(p) &= \langle \Phi(p)| \prod_{n=i}^1 {}^Z \beta_{l_n}(p) \\
 &= \langle \Phi(p)| \prod_{n=i}^1 \left(\beta_{l_n}(p) + \sum_m \mathbf{z}^{l_i l_m} \beta_{l_m}^\dagger(p) \right),
 \end{aligned} \tag{1.58}$$

where the transformation (1.57) is used repeatedly and where the dependence of $\mathbf{z}(p, q; \theta)$ on $(p, q; \theta)$ is omitted for simplicity. This gives for a single de-excitation

$$\begin{aligned}
 \langle \Phi(p)| {}^Z B_{l_1 l_2}(p) &= \langle \Phi^{l_1 l_2}(p)| \\
 &\quad + \mathbf{z}^{l_1 l_2} \langle \Phi(p)|,
 \end{aligned} \tag{1.59}$$

and for a double de-excitation

$$\begin{aligned}
 \langle \Phi(p)| {}^Z B_{l_1 l_2 l_3 l_4}(p) &= \langle \Phi^{l_1 l_2 l_3 l_4}(p)| \\
 &\quad + P(l_1 l_2 / l_3 l_4) \mathbf{z}^{l_3 l_4} \langle \Phi^{l_1 l_2}(p)| \\
 &\quad + P(l_1 / l_3 l_4) \mathbf{z}^{l_1 l_2} \mathbf{z}^{l_3 l_4} \langle \Phi(p)|,
 \end{aligned} \tag{1.60}$$

where the final expressions are obtained by expanding the product of transformed quasi-particle operators, by applying Wick's theorem and by acting on the bra to eliminate many null terms. The definition of the needed permutation operators can be found in App. B. Interestingly, one observes that the excitation rank is not increased through the similarity transformation in Eqs. (1.59)-(1.60).

Rotated/similarity-transformed operators

Given $|\Phi(p)\rangle$, $|\Phi(q, \theta)\rangle$ and an operator O , the rotated/similarity-transformed operator is introduced as

$${}^Z O(\theta) \equiv e^{-\mathbf{Z}^{20}(p, q; \theta)} R(\theta) O R^\dagger(\theta) e^{\mathbf{Z}^{20}(p, q; \theta)}, \tag{1.61}$$

where the extra dependence in θ due to the additional rotation compared to O_Z defined in Eq. (1.56) is made apparent in the newly introduced notation ${}^Z O(\theta)$ such that ${}^Z O(0) = {}^Z O$.

Of course, the particular form used to express the initial operator O does not impact the actual content of ${}^Z O$ or ${}^Z O(\theta)$. In the PGCM-PT formalism of present interest, it happens that ${}^Z O$ and ${}^Z O(\theta)$ arise for operators O that are initially normal ordered

with respect to $|\Phi(p)\rangle$ and $|\Phi(q)\rangle$, respectively, and thus expressed in terms of quasi-particle operators $\{\beta_k^\dagger(p), \beta_k(p)\}$ and $\{\beta_k^\dagger(q), \beta_k(q)\}$, respectively. With this in mind, ${}^Z O(\theta)$ is obtained by simply replacing the quasi-particle operators $\{\beta_k^\dagger(q), \beta_k(q)\}$ by rotated/similarity-transformed ones

$$\begin{aligned} \begin{pmatrix} {}^Z \beta(q; \theta) \\ {}^Z \beta^\dagger(q; \theta) \end{pmatrix} &\equiv e^{-\mathbf{Z}^{20}(p, q; \theta)} R(\theta) \begin{pmatrix} \beta(q) \\ \beta^\dagger(q) \end{pmatrix} R^\dagger(\theta) e^{\mathbf{Z}^{20}(p, q; \theta)} \\ &\equiv e^{-\mathbf{Z}^{20}(p, q; \theta)} \begin{pmatrix} \beta(q; \theta) \\ \beta^\dagger(q; \theta) \end{pmatrix} e^{\mathbf{Z}^{20}(p, q; \theta)}. \end{aligned} \quad (1.62)$$

Eventually, the operator ${}^Z O(\theta)$ needs to be re-expressed in terms of the set $\{\beta_k^\dagger(p), \beta_k(p)\}$, the goal being to express all quantities involved in a many-body matrix element of interest in terms of a single set of quasi-particle operators. To do so, the rotated/similarity-transformed quasi-particle operators are written as

$$\begin{aligned} \begin{pmatrix} {}^Z \beta(q; \theta) \\ {}^Z \beta^\dagger(q; \theta) \end{pmatrix} &\equiv e^{-\mathbf{Z}^{20}(p, q; \theta)} \begin{pmatrix} \beta(q; \theta) \\ \beta^\dagger(q; \theta) \end{pmatrix} e^{\mathbf{Z}^{20}(p, q; \theta)} \\ &= \mathcal{W}^\dagger(p, q; \theta) {}^Z \mathcal{X}^\dagger(p, q; \theta) \begin{pmatrix} \beta(p) \\ \beta^\dagger(p) \end{pmatrix} \\ &\equiv {}^Z \mathcal{Y}^\dagger(p, q; \theta) \begin{pmatrix} \beta(p) \\ \beta^\dagger(p) \end{pmatrix}, \end{aligned} \quad (1.63)$$

with

$$\begin{aligned} {}^Z \mathcal{Y}^\dagger(p, q; \theta) &= \begin{pmatrix} D^\dagger(p, q; \theta) & D^\dagger(p, q; \theta) \mathbf{z}(p, q; \theta) + E^\dagger(p, q; \theta) \\ E^T(p, q; \theta) & E^T(p, q; \theta) \mathbf{z}(p, q; \theta) + D^T(p, q; \theta) \end{pmatrix} \\ &= \begin{pmatrix} D^\dagger(p, q; \theta) & 0 \\ E^T(p, q; \theta) & D^{*-1}(p, q; \theta) \end{pmatrix} \end{aligned} \quad (1.64)$$

where the second line is obtained by inserting Eq. (1.55) into the first one and utilizing Eqs. (1.21a) and (1.21b).

In the present context, and as made clear in App. D, one only needs to perform the rotation/similarity-transformation of an excitation operator $B^{k_1 \dots k_i}(q)$ acting on the vacuum $|\Phi(p)\rangle$

$$\begin{aligned} {}^Z B^{k_1 \dots k_j}(q; \theta) |\Phi(p)\rangle &= \prod_{n=1}^j {}^Z \beta_{k_n}^\dagger(q; \theta) |\Phi(p)\rangle \\ &= \prod_{n=1}^j \sum_{k_m} \left(E_{k_m}^{k_n} \beta_{k_m}(p) + D^{-1 \dagger k_m k_n} \beta_{k_m}^\dagger(p) \right) |\Phi(p)\rangle, \end{aligned} \quad (1.65)$$

where the transformation (1.62)-(1.64) has been used repeatedly and where the dependence of $E(p, q; \theta)$ and $D(p, q; \theta)$ on $(p, q; \theta)$ has been omitted for simplicity. This gives for a single excitation

$${}^Z B^{k_1 k_2}(q; \theta) |\Phi(p)\rangle = \sum_{j_1 j_2} D^{-1 \dagger j_1 k_1} D^{-1 \dagger j_2 k_2} |\Phi^{j_1 j_2}(p)\rangle$$

$$+ \sum_{j_1} E_{j_1}^{k_1} D^{-1\dagger j_1 k_2} |\Phi(p)\rangle, \quad (1.66)$$

and for a double excitation

$$\begin{aligned} {}^Z B^{k_1 k_2 k_3 k_4}(q; \theta) |\Phi(p)\rangle &= \sum_{j_1 j_2 j_3 j_4} D^{-1\dagger j_1 k_1} D^{-1\dagger j_2 k_2} D^{-1\dagger j_3 k_3} D^{-1\dagger j_4 k_4} |\Phi^{j_1 j_2 j_3 j_4}(p)\rangle \\ &+ P(k_1 k_2 / k_3 k_4) \sum_{j_1 j_2 j_4} D^{-1\dagger j_1 k_1} D^{-1\dagger j_2 k_2} E_{j_4}^{k_3} D^{-1\dagger j_4 k_4} |\Phi^{j_1 j_2}(p)\rangle \\ &+ P(k_1 / k_3 k_4) \sum_{j_2 j_4} E_{j_2}^{k_1} D^{-1\dagger j_2 k_2} E_{j_4}^{k_3} D^{-1\dagger j_4 k_4} |\Phi(p)\rangle, \end{aligned} \quad (1.67)$$

where the final expressions are obtained by expanding the product of transformed quasi-particle operators, applying Wick's theorem and acting on the ket to eliminate many vanishing terms. Interestingly, one observes that the excitation rank is *not increased* through the rotation and similarity transformation in Eqs. (1.66)-(1.67).

Chapter 2.

PGCM-PT formalism

Contents

2.1. Introduction	19
2.2. Formal perturbation theory	22
2.2.1. Set up	22
2.2.2. Perturbative expansion	23
2.2.3. Computable expression	24
2.2.4. Hylleraas functional	25
2.3. PGCM-PT	26
2.3.1. PGCM unperturbed state	26
2.3.2. Partitioning	29
2.3.3. Application to second order (PGCM-PT(2))	32
2.4. Discussion	38

Now that the necessary elements of formalism have been introduced, we can dive into the solution of Eq. (1.1). The present chapter is dedicated to the formulation of a generic multi-reference many-body perturbation theory applicable to all systems, regardless of their closed- or open-shell character.

2.1. Introduction

The breaking of ab initio calculations away from p-shell nuclei over the last fifteen years has essentially been due to the development and implementation of so-called *expansion many-body methods* to solve Eq. (1.1). Generically, these methods rely on a partitioning of the Hamiltonian

$$H = H_0 + H_1 \quad (2.1)$$

chosen such that (at least) one appropriate eigenstate $|\Theta_\mu^{\tilde{\sigma}M}\rangle$ of H_0 is known, i.e.

$$H_0|\Theta_\mu^{\tilde{\sigma}M}\rangle = E_\mu^{\tilde{\sigma}(0)}|\Theta_\mu^{\tilde{\sigma}M}\rangle. \quad (2.2)$$

Given this state, the so-called *unperturbed state*, expansion methods aim at finding an efficient way to connect it to a target eigenstate $|\Psi_\mu^\sigma\rangle$ of H . This connection is formally achieved via the so-called *wave operator*, i.e.

$$|\Psi_\mu^{\tilde{\sigma}M}\rangle \equiv \Omega_{[\tilde{\sigma},\mu,H_1]}|\Theta_\mu^{\tilde{\sigma}M}\rangle, \quad (2.3)$$

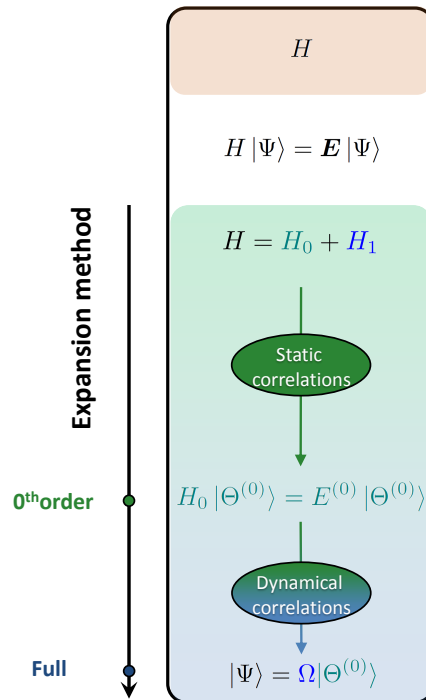


Figure 2.1. (color online) Schematic illustration of the workflow of expansion many-body methods based on a given input Hamiltonian H . While the unperturbed state must be capable of capturing so-called static correlations (if any), the expansion on top of it typically focuses on grasping so-called dynamical correlations (either perturbatively or non-perturbatively).

which is state specific and carries the complete effect of the residual interaction H_1 . This two-step procedure is schematically illustrated in Fig. 2.1.

Two ingredients characterize a given expansion method

1. the nature of the partitioning and the associated unperturbed state,
2. the rationale behind the construction, i.e the expansion and truncation, of the wave operator.

The construction of the wave operator is typically realized via either perturbative [60] or non-perturbative [41] techniques, i.e. by either expanding $\Omega_{[\tilde{\sigma}, \mu, H_1]}$ as a power series in H_1 or organizing the series as a more elaborate function of the residual interaction. Independently of this, the nature and the *reach* of the expansion is first and foremost determined by the type of unperturbed state used, which is itself governed by two main characteristics. The first feature relates to whether $|\Theta_\mu^{\tilde{\sigma}M}\rangle$ is a pure product state or a linear combination of product states. In the former case, the method is said to be of SR nature. In the latter case, the method is said to be of MR character. One typically needs to transition from the former to the latter whenever the system is (nearly) degenerate and displays strong static correlations, e.g. going from closed-shell to open-shell nuclei, thus making the SR expansion singular. Standard MR unperturbed states are linear combinations of orthonormal Slater determinants spanning a so-called valence/active space. This is indeed the case of the sole multi-reference method implemented to date in nuclear physics, i.e. MCPT [28]. In the present work, the goal is to generalize to the nuclear context the multi-reference perturbation theory developed in Ref. [65] in which the unperturbed state is built as a linear combination of *non-orthogonal* Slater determinants.

In addition to the SR or MR nature of the unperturbed state, a second, key feature relates to the symmetry conserving or non-conserving character of the partitioning, Eq. (2.1). While expansion methods typically build on a symmetry-conserving scheme [25] as implied by Eq. (2.2), a given SR expansion method can be generalized to a symmetry non-conserving formulation in which

$$[H_0, R(\theta)] \neq 0, \quad (2.4a)$$

$$[H_1, R(\theta)] \neq 0. \quad (2.4b)$$

As a result, the unperturbed state is said to be *symmetry breaking*, i.e. it loses (some of) the symmetry quantum numbers characterizing the eigenstates of H and rather carries a non-zero order parameter $\varrho \equiv qe^{i\theta}$ whose norm q quantifies the extent of the symmetry breaking. In this case, the unperturbed state is written as $|\Phi_\mu(q)\rangle$. Breaking symmetries is employed to capture strong static correlations *without* having to resort to MR methods that are typically formally and numerically more involved. While such a philosophy is indeed very powerful [45, 46, 47, 48, 49, 51, 66, 67, 68], it carries the loss of good symmetries over to the (approximation of) $|\Psi_\mu^{\tilde{\sigma}M}\rangle$ generated through the expansion method as soon as the wave operator is truncated in Eq. (2.3).

In this context, the natural question is whether broken symmetries can be restored¹ at any given truncation order whenever a symmetry-breaking SR partitioning is used. Doing so amounts to incorporating large amplitude fluctuations of the *phase* θ of the order parameter characterizing the broken symmetry. While it is indeed straightforward to do

¹While the full wave operator restores broken symmetries, it is always truncated in actual calculations such that the formal restoration obtained in the exact limit is of no practical help.

so for the unperturbed product state, i.e. at zeroth order in the many-body expansion, by acting with a symmetry projection operator [43], the generalization of symmetry-breaking SR expansion methods to restore the symmetries at any finite truncation order has only attracted serious attention recently, both for perturbation [53, 69, 70] and coupled cluster [53, 55, 69] theories². These approaches follow a philosophy that can be coined as "partition-project-and-expand" in which the action of the symmetry projector itself needs to be expanded and truncated as soon as one goes beyond zeroth order in the expansion of the wave operator. After showing promising results in the context of solvable/toy models [55, 56], these novel formalisms are now being implemented and tested within the frame of realistic nuclear structure calculations where the necessary approximation of the symmetry projector seems to constitute a challenge [80].

The present work wishes to promote an alternative strategy through a novel MR perturbation theory that, while building the unperturbed state out of symmetry-breaking product states, does rather follow a "project-partition-and-expand" philosophy, i.e. relies on a symmetry-conserving partitioning, such that symmetries are exactly maintained all throughout the expansion. Furthermore, the approach is not only capable of incorporating large amplitude fluctuations of the phase of ϱ into the unperturbed state, but also of including large amplitude fluctuations of its norm q , which constitutes an efficient asset to fully incorporate static correlations.

This chapter is organized as follows. Section 2.2 briefly summarizes formal Rayleigh-Schrödinger's perturbation theory [25] underlying the subsequent formulation of the multi-reference perturbation theory of present interest that is formulated in detail in Sec. 2.3. Section 2.4 is dedicated to discussions and conclusions. While the bulk of the chapter is restricted to the generic formulation of the many-body method, Apps. C, D and E provide all algebraic details necessary to the actual implementation of the approach.

2.2. Formal perturbation theory

2.2.1. Set up

The present work focuses on the perturbative expansion of the wave operator. Starting from Eqs. (2.1)-(2.2), the two projectors in direct sum³

$$\mathcal{P}_\mu^{\tilde{\sigma}} \equiv \sum_K |\Theta_\mu^{\tilde{\sigma}K}\rangle \langle \Theta_\mu^{\tilde{\sigma}K}|, \quad (2.5a)$$

$$\mathcal{Q}_\mu^{\tilde{\sigma}} \equiv 1 - \mathcal{P}_\mu^{\tilde{\sigma}}, \quad (2.5b)$$

are introduced. The operator $\mathcal{P}_\mu^{\tilde{\sigma}}$ projects on the eigen subspace of H_0 spanned by the unperturbed state along with the degenerate states obtained via symmetry transformations, i.e. belonging to the same irreducible representation (IRREP) of the symmetry group. This constitutes the so-called \mathcal{P} space. The operator $\mathcal{Q}_\mu^{\tilde{\sigma}}$ projects onto the complementary orthogonal subspace, the so-called \mathcal{Q} space. In the present context, the eigenstates of H_0 spanning the latter subspace are *not* assumed to be known explicitly.

²The insertion of a projector at second-order in perturbation theory was investigated at some point in nuclear physics [71, 72, 73, 74, 75] and quantum chemistry [76, 77, 78] but not pursued since. Those methods relied on Löwdin's representation of the spin projector [79], often approximating it to only remove the next highest spin.

³The two hermitian operators fulfill $(\mathcal{P}_\mu^{\tilde{\sigma}})^2 = \mathcal{P}_\mu^{\tilde{\sigma}}$, $(\mathcal{Q}_\mu^{\tilde{\sigma}})^2 = \mathcal{Q}_\mu^{\tilde{\sigma}}$ and $\mathcal{P}_\mu^{\tilde{\sigma}} \mathcal{Q}_\mu^{\tilde{\sigma}} = \mathcal{Q}_\mu^{\tilde{\sigma}} \mathcal{P}_\mu^{\tilde{\sigma}} = 0$ such that $\mathcal{P}_\mu^{\tilde{\sigma}} + \mathcal{Q}_\mu^{\tilde{\sigma}} = 1$.

While the ingredients introduced above are state specific and, as such, depend on the quantum numbers (μ, σ) , those labels are dropped for the time being to lighten the notations. Consequently, the targeted eigenstate and energy (of the full H) are written as $|\Psi\rangle$ and E , respectively, whereas the unperturbed state and energy are denoted as $|\Theta^{(0)}\rangle$ and $E^{(0)}$ to typify that they act as zeroth-order quantities in the perturbative expansion designed below. The projectors are simply denoted as \mathcal{P} and \mathcal{Q} .

The goal is to compute the perturbative corrections to both $|\Theta^{(0)}\rangle$ and $E^{(0)}$ such that

$$|\Psi\rangle \equiv \sum_{k=0}^{\infty} |\Theta^{(k)}\rangle, \quad (2.6a)$$

$$E \equiv \sum_{k=0}^{\infty} E^{(k)}, \quad (2.6b)$$

where the superscript k indicates that the corresponding quantity depends on the k^{th} power of H_1 . This expansion is defined using the so-called *intermediate normalization*, i.e.

$$\langle \Theta^{(0)} | \Theta^{(k)} \rangle = 0, \quad \forall k \geq 1, \quad (2.7)$$

such that

$$\langle \Theta^{(0)} | \Psi \rangle = 1. \quad (2.8)$$

2.2.2. Perturbative expansion

Rayleigh-Schrödinger perturbation theory [25] allows one to first expand the exact state and energy as

$$|\Psi\rangle \equiv \sum_{m=0}^{\infty} (X^{-1}Y)^m |\Theta^{(0)}\rangle, \quad (2.9a)$$

$$E - E^{(0)} \equiv \sum_{m=0}^{\infty} \langle \Theta^{(0)} | H_1 (X^{-1}Y)^m | \Theta^{(0)} \rangle, \quad (2.9b)$$

where

$$X \equiv \mathcal{Q} (H_0 - E^{(0)}) \mathcal{Q}, \quad (2.10a)$$

$$Y \equiv \mathcal{Q} (E - E^{(0)} - H_1) \mathcal{Q}. \quad (2.10b)$$

The two series do not yet provide the perturbative corrections to the unperturbed quantities because of the presence of $E - E^{(0)}$ on the right-hand side through Y . To identify each perturbative contribution, it is necessary to substitute Eq. (2.9b) for each $E - E^{(0)}$ in the right-hand-side of Eq. (2.9) iteratively and sort out the terms with equal powers of H_1 . This procedure leads to^{4,5}

$$|\Theta^{(1)}\rangle = -X^{-1} \mathcal{Q} H_1 |\Theta^{(0)}\rangle, \quad (2.11a)$$

⁴Starting with $|\Theta^{(3)}\rangle$ and $E^{(4)}$, so-called *renormalization terms* arise in addition to the *principal term* [25].

⁵The perturbative expansion of the wave operator formally introduced in Eq. (2.3) is thus obtained as

$$\begin{aligned} \Omega_{[\tilde{\sigma}, \mu, H_1]} &= 1 \\ &- (X_{\mu}^{\tilde{\sigma}})^{-1} \mathcal{Q}_{\mu}^{\tilde{\sigma}} H_1 \\ &+ (X_{\mu}^{\tilde{\sigma}})^{-1} \mathcal{Q}_{\mu}^{\tilde{\sigma}} \tilde{H}_1 \mathcal{Q}_{\mu}^{\tilde{\sigma}} (X_{\mu}^{\tilde{\sigma}})^{-1} \mathcal{Q}_{\mu}^{\tilde{\sigma}} H_1 \\ &+ \dots \end{aligned}$$

$$\begin{aligned} |\Theta^{(2)}\rangle &= +X^{-1}\mathcal{Q}\bar{H}_1\mathcal{Q}X^{-1}\mathcal{Q}H_1|\Theta^{(0)}\rangle, \\ &\vdots \end{aligned} \quad (2.11b)$$

and⁶

$$E^{(1)} = \langle \Theta^{(0)} | H_1 | \Theta^{(0)} \rangle, \quad (2.12a)$$

$$\begin{aligned} E^{(2)} &= \langle \Theta^{(0)} | H_1 \mathcal{Q} | \Theta^{(1)} \rangle \\ &= -\langle \Theta^{(0)} | H_1 \mathcal{Q} X^{-1} \mathcal{Q} H_1 | \Theta^{(0)} \rangle, \end{aligned} \quad (2.12b)$$

$$\begin{aligned} E^{(3)} &= \langle \Theta^{(0)} | H_1 \mathcal{Q} | \Theta^{(2)} \rangle \\ &= +\langle \Theta^{(0)} | H_1 \mathcal{Q} X^{-1} \mathcal{Q} \bar{H}_1 \mathcal{Q} X^{-1} \mathcal{Q} H_1 | \Theta^{(0)} \rangle \\ &= \langle \Theta^{(1)} | \mathcal{Q} \bar{H}_1 \mathcal{Q} | \Theta^{(1)} \rangle, \\ &\vdots \end{aligned} \quad (2.12c)$$

where $\bar{H}_1 \equiv H_1 - E^{(1)}$. The total energy of the unperturbed state is defined as

$$E_{\text{ref}} \equiv \langle \Theta^{(0)} | H | \Theta^{(0)} \rangle = E^{(0)} + E^{(1)}. \quad (2.13)$$

2.2.3. Computable expression

Working algebraic expressions of $|\Theta^{(k)}\rangle$ and $E^{(k)}$ are easily obtained in case X is invertible, i.e. if the eigenstates of H_0 in \mathcal{Q} space are known, which is not the case in the present work. Under closer inspection, one actually needs matrix elements of

$$A \equiv -X^{-1}\mathcal{Q}\bar{H}_1, \quad (2.14)$$

noting in passing that $\mathcal{Q}\bar{H}_1|\Theta^{(0)}\rangle = \mathcal{Q}H_1|\Theta^{(0)}\rangle$. Since by definition

$$\mathcal{Q}(H_0 - E^{(0)})\mathcal{Q}A = -\mathcal{Q}\bar{H}_1, \quad (2.15)$$

the matrix \mathbf{A} of A is the solution of the system of linear equations

$$\mathbf{M}\mathbf{A} = -\bar{\mathbf{H}}_1, \quad (2.16)$$

where $\mathbf{M} \equiv \mathbf{H}_0 - E^{(0)}\mathbf{1}$ and where the left matrix index necessarily belongs to \mathcal{Q} space whereas the right index is either in \mathcal{Q} or \mathcal{P} space. In expanded form, the linear system thus reads, with $i \neq 0$,

$$\sum_{k \neq 0} M_{ik} A_{kj} = -(\bar{H}_1)_{ij}, \quad (2.17)$$

where the sum is restricted to \mathcal{Q} -space states. In case one is only interested in $X^{-1}\mathcal{Q}\bar{H}_1|\Theta^{(0)}\rangle$, a simpler linear system involving the vectors \mathbf{a} and \mathbf{h}_1 made out of the first column A_{k0} and $(H_1)_{k0}$ of \mathbf{A} and \mathbf{H}_1 , respectively, needs to be solved, i.e.

$$\mathbf{M}\mathbf{a} = -\mathbf{h}_1. \quad (2.18)$$

⁶Some of the projectors \mathcal{Q} are redundant but are kept to make the systematic structure of the equations more apparent.

As discussed in Chapter 5, a sparse matrix representation of M makes the iterative solution of the linear equation system accessible under certain hypothesis for realistic ab initio nuclear structure calculations.

Given \mathbf{A} , the energy corrections can eventually be computed as

$$E^{(2)} = \langle \Theta^{(0)} | H_1 A | \Theta^{(0)} \rangle = \mathbf{h}_1^\dagger \mathbf{a}, \quad (2.19a)$$

$$E^{(3)} = \langle \Theta^{(0)} | H_1 A^2 | \Theta^{(0)} \rangle = \mathbf{h}_1^\dagger \mathbf{A} \mathbf{a} = \mathbf{a}^\dagger \bar{\mathbf{H}}_1 \mathbf{a}, \quad (2.19b)$$

$$\vdots$$

knowing that $E^{(1)} = (H_1)_{00}$.

2.2.4. Hylleraas functional

Formal perturbation theory can be alternatively derived through a variational method due to Hylleraas [25]. Let us consider a variational ansatz

$$|\Xi\rangle \equiv |\Theta^{(0)}\rangle + \sum_{k=1}^{\infty} |\Xi^{(k)}\rangle, \quad (2.20)$$

where $\langle \Theta^{(0)} | \Xi^{(k)} \rangle = 0 \forall k \geq 1$ and where the variational component $|\Xi^{(k)}\rangle$ is proportional to H_1^k . Computing the expectation of H in $|\Xi\rangle$ and sorting the various orders in H_1 , Ritz' variational principle leads to

$$\begin{aligned} E &\leq E^{(0)} + E^{(1)} \\ &+ \left[\langle \Xi^{(1)} | \mathcal{Q} H_1 | \Theta^{(0)} \rangle + \langle \Theta^{(0)} | H_1 \mathcal{Q} | \Xi^{(1)} \rangle \right. \\ &\left. + \langle \Xi^{(1)} | \mathcal{Q} (H_0 - E^{(0)}) \mathcal{Q} | \Xi^{(1)} \rangle \right] + O(H_1^3), \end{aligned} \quad (2.21)$$

For E to be a minimum of the right-hand side expression for an arbitrary H_1 , each term associated with a given power of H_1 must be either minimal or constant in order to indeed reach E . The sum of the corresponding terms delivers the individual perturbative components $E^{(k)}$ in Eq. (2.6b) given the uniqueness of the series in powers of H_1 .

Noting that $E^{(0)}$ and $E^{(1)}$ are free from any variational components, the variational approach starts with the second-order energy correction $E^{(2)}$ that is the minimum of the so-called Hylleraas functional

$$\begin{aligned} L[\Xi^{(1)}] &\equiv \langle \Xi^{(1)} | \mathcal{Q} H_1 | \Theta^{(0)} \rangle \\ &+ \langle \Theta^{(0)} | H_1 \mathcal{Q} | \Xi^{(1)} \rangle \\ &+ \langle \Xi^{(1)} | \mathcal{Q} (H_0 - E^{(0)}) \mathcal{Q} | \Xi^{(1)} \rangle. \end{aligned} \quad (2.22)$$

It is straightforward to realize that the saddle-point of Eq. (2.22) is obtained for $|\Xi^{(1)}\rangle = |\Theta^{(1)}\rangle$ the solution of Eq. (2.11a).

This alternative derivation is of interest because it underlines the fact that the use of an approximate ansatz to the exact solution of Eq. (2.11a) delivers a variational estimate⁷ of $E^{(2)}$.

⁷One however obtains a variational upper bound of the exact eigen energy if and only if $E^{(0)}$ is the lowest eigenvalue of H_0 [25].

2.3. PGCM-PT

The above formal perturbation theory is now specified to the case where the unperturbed state is generated through the projected generator coordinate method (PGCM). The unperturbed state is thus of multi reference character given that a PGCM state is nothing but a linear combination of non-orthogonal product states whose coefficients result from solving Hill-Wheeler-Griffin's (HWG) secular problem [43], i.e. a generalized many-body eigenvalue problem. The PGCM Perturbation Theory (PGCM-PT) of present interest adapts to the nuclear many-body problem the multi-reference perturbation theory recently formulated in the context of quantum chemistry [65] where the reference state arises from a non-orthogonal configuration interaction (NOCI) calculation involving Slater determinants. In order to do so, the method is presently generalized to the mixing of Bogoliubov vacua.

In the present context, PGCM must thus be viewed as the unperturbed, i.e. zeroth-order, limit of the PGCM-PT formalism that is universally applicable, i.e. independently of the closed or open-shell nature of the system and of the ground or excited character of the PGCM state generated through the initial HWG problem. Because PGCM states efficiently capture strong static correlations associated with the spontaneous breaking of symmetries and their restoration as well as with large amplitude collective fluctuations, one is only left with incorporating the remaining weak dynamical correlations, which PGCM-PT offers to do consistently. Because of the incorporation of static correlations into the zeroth-order state, the hope is that nuclear observables associated with a large set of nuclei and quantum states can be sufficiently converged at low orders in PGCM-PT.

2.3.1. PGCM unperturbed state

Ansatz

A multi-reference PGCM state reads as

$$\begin{aligned} |\Theta_{\mu}^{\tilde{\sigma}M}\rangle &\equiv \int dq f_{\mu}^{\tilde{\sigma}}(q) P_{M0}^{\tilde{\sigma}} |\Phi(q)\rangle \\ &= \frac{d_{\tilde{\sigma}}}{v_G} \sum_q f_{\mu}^{\tilde{\sigma}}(q) \sum_{\theta} D_{M0}^{\tilde{\sigma}*}(\theta) |\Phi(q; \theta)\rangle, \end{aligned} \quad (2.23)$$

where integrals over the collective coordinate q and the rotation angle θ have been discretized as actually done in a practical calculation.

In Eq. (2.23), $B_q \equiv \{|\Phi(q)\rangle; q \in \text{set}\}$ denotes a set of non-orthogonal Bogoliubov states differing by the value of the collective deformation parameter q . Such an ansatz is characterized by its capacity to efficiently capture static correlations from a low-dimensional, i.e. from several tens to a few hundreds, configuration mixing at the price of dealing with non-orthogonal vectors. This constitutes a very advantageous feature, especially as the mass A of the system, and thus the dimensionality of \mathcal{H}_A , grows.

The product states belonging to B_q are typically obtained in a first step by solving repeatedly Hartree-Fock-Bogoliubov (HFB) mean-field equations with a Lagrange term associated with a constraining operator⁸ Q such that the solution satisfies

$$\langle \Phi(q) | Q | \Phi(q) \rangle = q. \quad (2.24)$$

⁸The generic operator Q can embody several constraining operators such that the collective coordinate q may in fact be multi dimensional.

The constrained HFB total energy $\mathbf{H}^{00}(q)$ (see Eq. (1.38)) delivers as a function of q the so-called HFB potential energy curve (PEC). Details about Bogoliubov states and the associated algebra, as well as constrained HFB equations, can be found in Sec. 1.2. The constraining operator Q is such that the product states belonging to B_q break a corresponding symmetry of the Hamiltonian as soon as $q \neq 0$. Because physical states must carry good symmetry quantum numbers one acts on $|\Phi(q)\rangle$ with the operator⁹

$$P_{M0}^{\tilde{\sigma}} = \frac{d_{\tilde{\sigma}}}{v_G} \int_{D_G} d\theta D_{M0}^{\tilde{\sigma}*}(\theta) R(\theta) \quad (2.25)$$

in Eq. (2.23) to project the HFB state onto eigenstates of the symmetry operators with eigenvalues $(\tilde{\sigma}, M)$ and incorporate additional static correlations. The operator $P_{M0}^{\tilde{\sigma}}$ is expressed in terms of the symmetry rotation operator $R(\theta)$ and the IRREP $D_{MK}^{\tilde{\sigma}}(\theta)$ of the symmetry group G_H . See App. A for a discussion of the actual symmetry group, symmetry quantum numbers and symmetry projector of present interest.

Due to the symmetry projection, the PGCM state eventually is constructed from the extended set¹⁰ of Bogoliubov states $B_{q;\theta} \equiv \{|\Phi(q;\theta)\rangle; q \in \text{set and } \theta \in D_G\}$ obtained from B_q by further acting with the symmetry rotation operator, i.e.

$$|\Phi(q;\theta)\rangle \equiv R(\theta)|\Phi(q)\rangle. \quad (2.26)$$

Because $R(\theta) \in G_H$, the HFB potential energy surface (PES) $\mathbf{H}^{00}(q;\theta)$ (Eq. (1.45)) in the two-dimensional plane associated with the order parameter $\varrho = qe^{i\theta}$ of the (intermediately broken) symmetry is independent of the rotation angle θ . This is qualitatively illustrated in Fig. 2.2.

Mixing states belonging to $B_{q;\theta}$, PGCM states account for large amplitude fluctuations of both the norm q and the angle θ of the order parameter ϱ . Doing so constitutes an efficient way to incorporate strong static correlations and extract at the same time collective excitations associated with both of these fluctuations, i.e. vibrational and rotational excitations along with their coupling. In this context, the coefficients $D_{M0}^{\tilde{\sigma}}(\theta)$ associated with the symmetry restoration are entirely determined by the group structure¹¹. Consequently, the sole unknowns to be determined are the coefficients $f_{\mu}^{\tilde{\sigma}}(q)$ associated with the mixing over q .

Hill-Wheeler-Griffin's equation

The unknown coefficients $\{f_{\mu}^{\tilde{\sigma}}(q); q \in \text{set}\}$ are determined via the application of Ritz' variational principle

$$\frac{\delta}{\delta f_{\mu}^{\tilde{\sigma}*}(q)} \frac{\langle \Theta_{\mu}^{\tilde{\sigma}M} | H | \Theta_{\mu}^{\tilde{\sigma}M} \rangle}{\langle \Theta_{\mu}^{\tilde{\sigma}M} | \Theta_{\mu}^{\tilde{\sigma}M} \rangle} = 0, \quad (2.27)$$

⁹The present work is effectively concerned with HFB states that are invariant under spatial rotation around a given symmetry axis. Extending the formulation to the case where $|\Phi(q)\rangle$ does not display such a symmetry poses no formal difficulty but requires a more general projection operator P^{σ} ; see App. A for details.

¹⁰Seeing the PGCM state as a configuration mixing of states belonging to $B_{q;\theta}$ rather than as resulting from the projection of the states belonging B_q allows one to define the SR limit of PGCM-PT via the truncation of the double sum in Eq. (2.23) to a single term such that the PGCM unperturbed state reduces to one symmetry-breaking state $|\Phi(q;0)\rangle$.

¹¹This is true because the present work is only concerned with HFB states that are invariant under spatial rotation around a given symmetry axis. If not, the configuration mixing with respect to the rotation (i.e. Euler) angles is not entirely fixed by the structure of the group; see App. A for details.

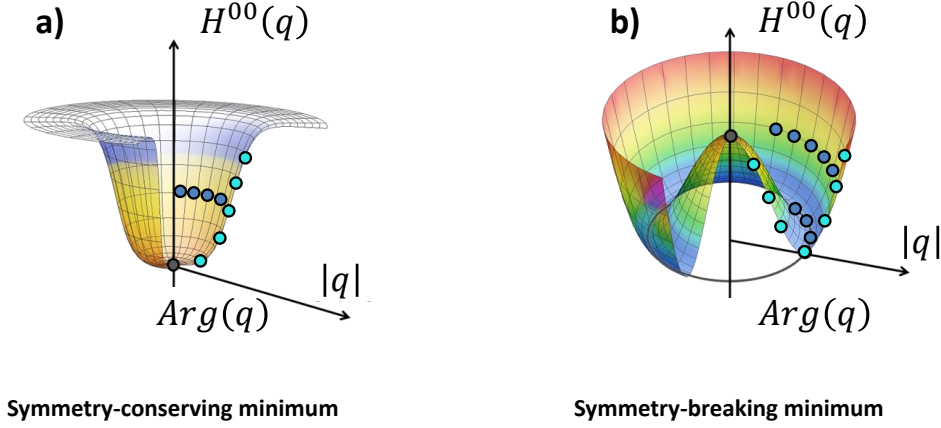


Figure 2.2. (color online) Schematic representation of the HFB PES $\mathbf{H}^{00}(q; \theta)$ in the two-dimensional plane associated with the order parameter $\varrho = qe^{i\theta}$ of the (intermediately broken) symmetry. Light (dark) blue circles represent configurations along the q (θ) direction. Left (right) panel: system characterized by a symmetry-conserving (-breaking) minimum.

that eventually leads to solving Hill-Wheeler-Griffin's equation¹²

$$\sum_q H_{p0q0}^{\tilde{\sigma}} f_{\mu}^{\tilde{\sigma}}(q) = \mathcal{E}_{\mu}^{\tilde{\sigma}} \sum_q N_{p0q0}^{\tilde{\sigma}} f_{\mu}^{\tilde{\sigma}}(q). \quad (2.28)$$

The HWG equation is nothing but a NOCI eigenvalue problem expressed in the set of non-orthogonal projected HFB states $\text{PB}_{q\tilde{\sigma}} \equiv \{P_{00}^{\tilde{\sigma}}|\Phi(q)\rangle; q \in \text{set}\}$. The coefficients $f_{\mu}^{\tilde{\sigma}}(q)$ are presently defined such that the set of PGCM states $\text{PGCM}_{\sigma} \equiv \{|\Theta_{\mu}^{\sigma}\rangle; \mu = 1, 2, \dots\}$ emerging from Eq. (2.28) are (ortho-)normalized.

Equation (2.28) involves so-called *operator kernels*¹³

$$O_{p0q0}^{\tilde{\sigma}} \equiv \langle \Phi(p) | O P_{00}^{\tilde{\sigma}} | \Phi(q) \rangle, \quad (2.29)$$

whose explicit expressions in terms of input quantities are worked out in App. D. The kernel associated with the identity operator $N \equiv 1$ is the norm kernel denoted as $N_{p0q0}^{\tilde{\sigma}}$.

The more the vectors in $\text{PB}_{q\tilde{\sigma}}$ are linearly dependent, the more the generalized eigenvalue problem of Eq. (2.28) tends to be singular. In order to avoid numerical instabilities, singular eigenvalues must be removed. The standard method to deal with the problem, which is feasible for the manageable number of states in $\text{PB}_{q\tilde{\sigma}}$, is recalled in App. J.

¹²The diagonalization is performed separately for each value of $\tilde{\sigma}$, i.e. within each IRREP of G_H .

¹³The two 0 indices in $O_{p0q0}^{\tilde{\sigma}}$ relate to the fact that the ket and the bra denote HFB vacua belonging to B_q . This notation is necessary to make those kernels consistent with the more general ones $O_{pIqJ}^{\tilde{\sigma}}$ introduced later on in Sec. 2.3.3, which also involve Bogoliubov states obtained via elementary, i.e. quasi-particle, excitations of those belonging to B_q .

2.3.2. Partitioning

Now that the nature of the multi-reference unperturbed state $|\Theta_\mu^\sigma\rangle$ has been detailed, the formal perturbation theory developed in Sec. 2.2 can be explicitly applied. The formulation starts with the choice of an appropriate partitioning of the Hamiltonian (Eq. 2.1), i.e. by defining an unperturbed Hamiltonian H_0 of which $|\Theta_\mu^\sigma\rangle$ is an eigenstate.

Definition

The goal is to design H_0 such that PGCM-PT reduces to standard Møller-Plesset MBPT whenever the PGCM unperturbed state reduces to a single (unconstrained) Hartree-Fock Slater determinant¹⁴. To achieve this goal, one introduces the state-specific partitioning

$$H_0 \equiv \mathcal{P}_\mu^{\tilde{\sigma}} F_{[|\Theta\rangle]} \mathcal{P}_\mu^{\tilde{\sigma}} + \mathcal{Q}_\mu^{\tilde{\sigma}} F_{[|\Theta\rangle]} \mathcal{Q}_\mu^{\tilde{\sigma}}, \quad (2.30)$$

where the one-body operator

$$F_{[|\Theta\rangle]} \equiv \sum_{a_1 b_1} f_{b_1}^{a_1} [|\Theta\rangle] C_{b_1}^{a_1}, \quad (2.31a)$$

$$f_{b_1}^{a_1} [|\Theta\rangle] \equiv t_{b_1}^{a_1} + \sum_{a_2 b_2} v_{b_1 b_2}^{a_1 a_2} [\rho^\Theta]_{a_2}^{b_2}, \quad (2.31b)$$

involves the convolution of the two-body interaction with a *symmetry-invariant* one-body density matrix¹⁵

$$[\rho^\Theta]_{a_1}^{b_1} \equiv \frac{\langle \Theta | C_{b_1}^{a_1} | \Theta \rangle}{\langle \Theta | \Theta \rangle}, \quad (2.32)$$

i.e. a one-body density matrix computed from a symmetry-conserving state $|\Theta\rangle$ ¹⁶.

As soon as the PGCM unperturbed state $|\Theta_\mu^{\tilde{\sigma}M}\rangle$ is not symmetry-conserving, e.g., it corresponds to an excited state $|\Theta_\mu^{\tilde{\sigma}M}\rangle$ of an even-even nucleus with $J \neq 0$, the one-body operator $F_{[|\Theta\rangle]}$ must necessarily be built from a different state $|\Theta\rangle$. In this situation, it is natural to employ the corresponding symmetry-conserving ground state¹⁷. Contrarily, whenever the PGCM unperturbed state $|\Theta_\mu^{\tilde{\sigma}M}\rangle$ is symmetry-conserving, e.g. for the ground state of an even-even system, it is natural to choose it¹⁸, i.e. to take $|\Theta\rangle \equiv |\Theta_\mu^{\tilde{\sigma}M}\rangle$, to build $F_{[|\Theta\rangle]}$.

¹⁴This limit is discussed in some details in Sec. 2.3.2. The more subtle case where the PGCM unperturbed state reduces to a single Bogoliubov state is also discussed.

¹⁵In case $|\Theta\rangle$ were to denote the exact ground-state of the system, $F_{[|\Theta\rangle]}$ would be nothing else but the so-called Baranger one-body Hamiltonian [81], which is itself the energy-independent part of the one-nucleon self-energy in self-consistent Green's function theory [82].

¹⁶In the present work, a symmetry-conserving state represents a state whose associated one-body density matrix is symmetry-invariant, i.e. belongs to the *trivial* IRREP of G_H . While for the SU(2) group this requires the many-body state itself to be symmetry invariant, i.e. to be a $J = 0$ state, for the U(1) group this condition is automatically satisfied for the *normal* one-body density matrix (cf. Sec. 1.2.2).

¹⁷For odd-even or odd-odd nuclei eigenstates, the symmetry-invariant density matrix associated with a *fake* odd system described in terms of, e.g., a statistical mixture [83, 84] can typically be envisioned.

¹⁸The explicit expression of the one-body density matrix of a PGCM state can be found in App. G.

Eigenstates of H_0

Introducing¹⁹ the M -independent unperturbed energy

$$E_\mu^{\tilde{\sigma}(0)} \equiv \langle \Theta_\mu^{\tilde{\sigma}M} | F_{[|\Theta\rangle]} | \Theta_\mu^{\tilde{\sigma}M} \rangle = \sum_{a_1 b_1} f_{b_1}^{a_1} [|\Theta\rangle] \left[\rho^{\Theta_\mu^{\tilde{\sigma}0}} \right]_{a_1}^{b_1}, \quad (2.33)$$

one can write

$$H_0 \equiv E_\mu^{\tilde{\sigma}(0)} \mathcal{P}_\mu^{\tilde{\sigma}} + \mathcal{Q}_\mu^{\tilde{\sigma}} F_{[|\Theta\rangle]} \mathcal{Q}_\mu^{\tilde{\sigma}}, \quad (2.34)$$

such that the PGCM state is by construction, and independently of the nature of $F_{[|\Theta\rangle]}$, an eigenstate of H_0 with eigenvalue $E_\mu^{\tilde{\sigma}(0)}$.

Because the PGCM unperturbed state is a linear combination of non-orthogonal product states, there is no preferred one-body basis of \mathcal{H}_1 that can be used to represent this state or the other eigenstates of H_0 conveniently. This feature reflects in the fact that, while $F_{[|\Theta\rangle]}$ is a one-body operator with an explicit second-quantized representation, H_0 is a genuine *many-body* operator with no simple second-quantized form. This further results into the fact that the other eigenstates of H_0 are not accessible via excitations of the unperturbed state that are simply built from a given set of one-body creation and annihilation operators. As a matter of fact, $|\Theta_\mu^\sigma\rangle$ constitutes the only explicitly known eigenstate of H_0 given that no explicit eigen representation of H_0 in the complementary $\mathcal{Q}_\mu^{\tilde{\sigma}}$ space is trivially accessible. This difficulty was anticipated in Sec. 2.2 where formal perturbation theory was presented *without* assuming that such an eigen-representation was available. The practical consequences for the second-order implementation, i.e. PGCM-PT(2), are discussed in detail below in Sec. 2.3.3.

Symmetries

Being built from a symmetry-invariant one-body density matrix, $F_{[|\Theta\rangle]}$ is symmetry invariant, i.e. it belongs to the trivial IRREP of G_H such that

$$[F, R(\theta)] = 0, \quad \forall \theta, \quad (2.35)$$

which is notably responsible for the M -independence of $E_\mu^{\tilde{\sigma}(0)}$ in Eq. (2.33). Using Eqs. (A.11) and (A.12), one can further prove that

$$[\mathcal{P}_\mu^{\tilde{\sigma}}, R(\theta)] = 0, \quad \forall \theta, \quad (2.36)$$

and thus similarly for $\mathcal{Q}_\mu^{\tilde{\sigma}}$. This results in the fact that H_0 itself, and thus H_1 , are scalars with respect to G_H , i.e.

$$[H_0, R(\theta)] = [H_1, R(\theta)] = 0, \quad \forall \theta, \quad (2.37)$$

such that the partitioning is indeed symmetry conserving. Consequently, the eigenstates of H_0 , most of which are not known explicitly as discussed in the previous section, carry the symmetry quantum numbers $\sigma = (\tilde{\sigma}, M)$.

The unperturbed PGCM state $|\Theta_\mu^{\tilde{\sigma}M}\rangle$ introduced in Eq. (2.23) can be rewritten as

$$|\Theta^{(0)}\rangle \equiv P_{M0}^{\tilde{\sigma}} |\bar{\Theta}^{(0)}\rangle = P_{M0}^{\tilde{\sigma}} (P_{00}^{\tilde{\sigma}} |\bar{\Theta}^{(0)}\rangle), \quad (2.38)$$

¹⁹The dependence of $E_\mu^{\tilde{\sigma}(0)}$ on $|\Theta\rangle$ is dropped for simplicity.

where $|\bar{\Theta}^{(0)}\rangle$ is an eigenstate of J_z with eigenvalue $M = 0$. Exploiting the scalar character of H_0 , H_1 and $\mathcal{Q}_\mu^{\tilde{\sigma}}$, the k^{th} -order perturbed state (Eq. (2.11)) can similarly be shown to read

$$|\Theta^{(k)}\rangle \equiv P_{M0}^{\tilde{\sigma}}|\bar{\Theta}^{(k)}\rangle = P_{M0}^{\tilde{\sigma}}(P_{00}^{\tilde{\sigma}}|\bar{\Theta}^{(k)}\rangle). \quad (2.39)$$

Thus, one can choose to solve for $|\Theta^{(0)}\rangle = |\Theta_\mu^{\tilde{\sigma}0}\rangle$ and thus for $|\Theta^{(k)}\rangle = P_{00}^{\tilde{\sigma}}|\bar{\Theta}^{(k)}\rangle$, while further acting a posteriori on the obtained solution with the operator $P_{M0}^{\tilde{\sigma}}$ to generate all the associated states of the IRREP.

Furthermore, the intermediate states entering $|\bar{\Theta}^{(k)}\rangle$ as a result of the repeated action of H_1 and X^{-1} (see Eq. (2.11)) on $|\bar{\Theta}^{(0)}\rangle$ also carry $M = 0$; i.e. PGCM-PT can effectively be implemented without any loss of generality within the restricted $\sigma = (\tilde{\sigma}, M = 0)$ sub-block, i.e. without ever connecting to states with $M \neq 0$.

$U(1)$ -conserving single-reference limit

The presently developed PGCM-PT can be investigated in the limit where the unperturbed state becomes of single-reference nature. It corresponds to reducing the set $B_{q\theta}$ in Eq. (2.23) to a single HF(B) state such that PGCM-PT must exhibit some connection with single-reference (B)MBPT [60] (see also App. E for a summary of BMBPT main formulas) in this limit. In fact, the characteristics of the single-reference limit depends on the symmetry properties of the unperturbed product state, which requires us to distinguish two cases.

Let us first consider the case where $q_{U(1)} = 0$, either because the HFB PES $\mathbf{H}^{00}(q; \theta)$ minimizes for $q_{U(1)} = 0$ or because the solution is constrained to it. In this situation, $B_{q\theta}$ is reduced to the particle-number conserving Slater determinant $|\Phi(q; 0)\rangle = |\Phi(q)\rangle$ obtained from the constrained HF equations for which q associated with other symmetries than $U(1)$ can still be non zero as briefly described in App. E.1.2. The projectors on \mathcal{P} and \mathcal{Q} spaces reduce in that case to

$$\mathcal{P}(q) \equiv |\Phi(q)\rangle\langle\Phi(q)|, \quad (2.40a)$$

$$\mathcal{Q}(q) \equiv 1 - \mathcal{P}(q), \quad (2.40b)$$

such that Eq. (2.36) is not fulfilled anymore. Furthermore, the one-body operator $F_{[\Theta]}$ is naturally constructed from the SR unperturbed state $|\Theta\rangle = |\Phi(q)\rangle$ such that Eq. (2.35) is also lost along the way. Eventually, either of these two features implies that Eq. (2.37) is violated as well, i.e. the partitioning becomes symmetry breaking in the SR limit.

With these elements at hand, the unperturbed Hamiltonian in PGCM-PT becomes

$$H_0(q) \equiv E^{(0)}(q)\mathcal{P}(q) + \mathcal{Q}(q)F_{[\Phi(q)]}\mathcal{Q}(q), \quad (2.41a)$$

with

$$\begin{aligned} E^{(0)}(q) &\equiv \langle\Phi(q)|F_{[\Phi(q)]}|\Phi(q)\rangle \\ &= \sum_{a_1 b_1} f_{b_1}^{a_1} \left[\rho^{\Phi(q)} \right]_{a_1}^{b_1}. \end{aligned} \quad (2.41b)$$

Generally, the above definition of H_0 does not match the one of MBPT (see App. E.1.2).

Only in the unconstrained case, i.e. whenever $\lambda_q = 0$, does the SR reduction of PGCM-PT directly relate to Møller-Plesset MBPT. In particular, the unperturbed state $|\Phi(q)\rangle$ is

built from the eigenstates of $F_{[|\Phi(q)\rangle]}$ in that special case whereas it is not true otherwise. Furthermore, Eq. (2.41a) becomes

$$\begin{aligned} H_0(q) &= F_{[|\Phi(q)\rangle]} \\ &= E^{(0)}(q) + \sum_k e_k(q) : A_k^k : , \end{aligned} \quad (2.42)$$

where the latter equality makes use of the one-body eigenbasis of F and where

$$E^{(0)}(q) \equiv \sum_{i=1}^A e_i(q) . \quad (2.43)$$

While the definition of $E^{(0)}(q)$ above is still at variance with the choice made in App. E.1.2 for Møller-Plesset MBPT, it only shifts $H_0(q)$ by a constant such that both expansions match from the first order on. Details of the corresponding expansion are discussed in App. E.1.2.

$U(1)$ -breaking single-reference limit

In the more general case, the set $B_{q\theta}$ reduces to a particle-number breaking Bogoliubov state $|\Phi(q)\rangle$ in the single-reference limit. Formally, Eqs. (2.40)-(2.41) still hold such that H_0 does not match the one in BMBPT (see App. E.1.1).

However, and contrary to Sec. 2.3.2, $|\Phi(q)\rangle$ cannot be an eigenstate of the $U(1)$ -conserving one-body operator F such that even in the unconstrained case, i.e. whenever $\lambda_q = 0$, the SR reduction of PGCM-PT does not match Møller-Plesset BMBPT. Correspondingly, and even though $|\Phi(q)\rangle$ is an eigenstate of H_0 by construction, the eigenstates in \mathcal{Q} space differ from the elementary quasi-particle excitations of $|\Phi(q)\rangle$ (Eq. (1.40)) and cannot be directly accessed. As a result, the perturbative expansion is less straightforward to implement than in standard BMBPT where H_0 is a generalized, i.e. particle-number-non-conserving, one-body operator whose eigenstates are nothing but $|\Phi(q)\rangle$ and its elementary quasi-particle excitations (see App. E.1.1).

It will be of interest to see to what extent the partitionings at play in (B)MBPT on the one hand and in the SR reduction of PGCM-PT on the other do influence numerical results. This comparison will be performed in Chapter 5.

2.3.3. Application to second order (PGCM-PT(2))

Now that the unperturbed reference state and the associated partitioning have been introduced, the perturbative expansion built according to the formal perturbation theory recalled in Sec. 2.2 is specified up to second order, thus defining PGCM-PT(2).

Zeroth and first-order energies

Given the unperturbed state $|\Theta^{(0)}\rangle \equiv |\Theta_\mu^{\tilde{\sigma}0}\rangle$ delivered by Eqs. (2.23) and (2.28), the zeroth-order energy is given by Eq. (2.33) whereas the first-order energy is obtained through

$$\begin{aligned} E_{\text{ref}} &= E^{(0)} + E^{(1)} \\ &= \langle \Theta^{(0)} | H | \Theta^{(0)} \rangle \\ &= \sum_{pq} f^*(p) H_{p0q0}^{\tilde{\sigma}} f(q) , \end{aligned} \quad (2.44)$$

First-order interacting space

According to Eq. (2.12b), the second-order energy $E^{(2)}$ requires the knowledge of the first-order wave-function. Accessing $|\Theta^{(1)}\rangle$ is rendered non-trivial by the fact that \mathcal{Q} -space eigenstates of H_0 are not known a priori. This difficulty leads to the necessity to solve Eq. (2.18)²⁰.

However, solving Eq. (2.18) requires the identification of a suitable basis of \mathcal{Q} space, i.e. the appropriate *first-order interacting space* over which $|\Theta^{(1)}\rangle$ can be exactly expanded. In standard single-reference²¹ perturbation theories, the first-order wave function is a linear combination of single and double excitations of the unperturbed state, i.e. the first-order interacting space is well partitioned. In the present case, the PGCM unperturbed state prevents a straightforward identification of the first-order interacting space in terms of elementary excitations of a preferred reference vacuum. Indeed, each excitation of a Bogoliubov product state entering $|\Theta^{(0)}\rangle$ can have a non-zero overlap with any of the other HFB vacua making up $|\Theta^{(0)}\rangle$, and thus with $|\Theta^{(0)}\rangle$ itself. Eventually, this means that (i) \mathcal{Q} cannot be built explicitly and that (ii) Eq. (2.18) cannot be solved exactly. While the first difficulty can be bypassed by using Eq. (2.5b) repeatedly, the second one requires a procedure to optimally approximate the first-order interacting space.

Rather than referring to the orthonormal representation of \mathcal{H}_A associated with a preferred reference vacuum and its elementary excitations, one can appropriately consider the multiple representations built out of each product state entering $|\Theta^{(0)}\rangle$, i.e. each Bogoliubov state belonging to $B_{q\theta}$. This leads to writing the ansatz

$$\begin{aligned} |\Theta^{(1)}\rangle &\equiv \frac{d_{\tilde{\sigma}}}{v_G} \sum_q \sum_{\theta} \sum_I a^I(q; \theta) |\Phi^I(q; \theta)\rangle \\ &= \frac{d_{\tilde{\sigma}}}{v_G} \sum_q \sum_{\theta} \sum_I a^I(q; \theta) R(\theta) |\Phi^I(q)\rangle, \end{aligned} \quad (2.45)$$

where the index I runs over all single (S), double (D), triple (T)... excitations of the Bogoliubov vacua $|\Phi^I(q; \theta)\rangle$ defined in Eq. (1.46). The second line of Eq. (2.45) has been obtained thanks to Eq. (1.48) whereas the coefficients

$$\{a^I(q; \theta); q \in \text{set}, \theta \in D_G \text{ and } I \in \text{S,D,T}, \dots\}$$

denote the unknowns to be determined.

The fact that, as pointed out in Sec. 2.3.2, the first-order wave function is given by

$$|\Theta^{(1)}\rangle \equiv P_{00}^{\tilde{\sigma}} |\bar{\Theta}^{(1)}\rangle \quad (2.46)$$

fully fixes the dependence of the coefficients on the angle θ of the order parameter that are constrained to take the separable form

$$a^I(q; \theta) \equiv a^I(q) D_{00}^{\tilde{\sigma}*}(\theta), \quad (2.47)$$

²⁰The more elaborate Eq. (2.17) needs to be solved to access $|\Theta^{(k)}\rangle$ with $k > 1$.

²¹Standard multi-reference perturbation theories rely on an unperturbed state mixing orthogonal elementary excitations of a common vacuum state restricted to a certain valence/active space. In such a situation, the first-order interacting space is also well partitioned [28] as it is built out of single and double²² excitations outside the valence/active space from each orthogonal product state entering the unperturbed state wave function.

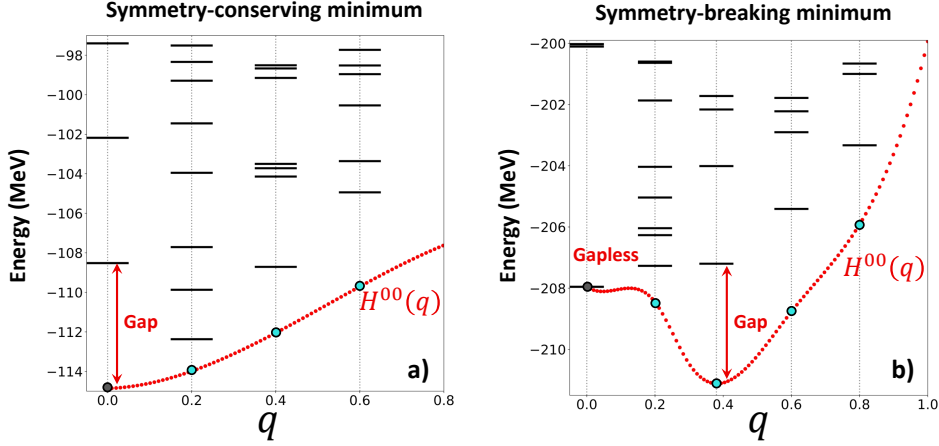


Figure 2.3. (color online) Schematic energetic representation as a function of the norm q of the order parameter of the considered symmetry of excited Bogoliubov states $\{|\Phi^I(q)\rangle; q \in \text{set and } I \in \text{S,D,T}, \dots\}$ employed to expand $|\Theta^{(1)}\rangle$. The (red) dotted curve represents the constrained HFB energy $\mathbf{H}^{00}(q; 0)$ associated with the vacua $B_q = \{|\Phi(q)\rangle; q \in \text{set}\}$ entering the unperturbed PGCM state $|\Theta^{(0)}\rangle$. Left (right) panel: system characterized by a symmetry-conserving (-breaking) minimum of $\mathbf{H}^{00}(q; 0)$. In single-reference methods, the problematic gapless symmetry-conserving solution encountered in open-shell nuclei is replaced by a gentle gap-full one by allowing the unperturbed state to spontaneously break the symmetry.

which drastically reduces the cardinal of the unknown coefficients to

$$\{a^I(q); q \in \text{set and } I \in \text{S,D,T}, \dots\}.$$

Explicitly projecting over \mathcal{Q} space to only retain the orthogonal component to $|\Theta^{(0)}\rangle$, Eq. (2.47) is used to rewrite Eq. (2.45) under the compact form

$$|\Theta^{(1)}\rangle = \sum_q \sum_I a^I(q) |\Omega^I(q)\rangle, \quad (2.48)$$

where the expansion now runs over the reduced set of non-orthogonal states

$$|\Omega^I(q)\rangle \equiv \mathcal{Q}P_{00}^{\tilde{\sigma}} |\Phi^I(q)\rangle. \quad (2.49)$$

As schematically illustrated in Fig. 2.3, the first-order wave-function is thus expanded over (projected) excitations of the HFB vacua carrying different values of the norm q of the order parameter.

In principle, all excitation ranks are involved in Eq. (2.49), which is unmanageable. The idea is to truncate the expansion based on the fact that (i) the Hylleraas functional justifies that an approximation to $|\Theta^{(1)}\rangle$ delivers a variational upper bound to $E^{(2)}$ that can be systematically improved and on the fact that (ii) doing so on the basis of Eq. (2.48) can provide an optimal approximation. In order to motivate the latter point, let us further investigate the expression of $E^{(2)}$. After noticing that²³

$$\langle \Theta^{(0)} | H_1 \mathcal{Q} = \langle \Theta^{(0)} | (H - H_0) (1 - |\Theta^{(0)}\rangle \langle \Theta^{(0)}|)$$

²³Because symmetry blocks associated with different values of M are explicitly separated throughout the whole formalism as explained in Sec. 2.3.2, one effectively has $\mathcal{P} = |\Theta^{(0)}\rangle \langle \Theta^{(0)}|$ everywhere in the following.

$$= \langle \Theta^{(0)} | (H - E_{\text{ref}}), \quad (2.50)$$

let us insert the definition of $\langle \Theta^{(0)} |$ along with multiple completeness relations in \mathcal{H}_A to write the second-order energy (Eq. (2.12b)) as

$$\begin{aligned} E^{(2)} &= \langle \Theta^{(0)} | (H - E_{\text{ref}}) | \Theta^{(1)} \rangle \\ &= \frac{d_{\tilde{\sigma}}}{v_G} \sum_{p\theta} f_{\mu}^*(p) D_{M0}^{\tilde{\sigma}}(\theta) \\ &\quad \times \sum_{I \in S, D} \langle \Phi(p; \theta) | (H - E_{\text{ref}}) | \Phi^I(p; \theta) \rangle \langle \Phi^I(p; \theta) | \Theta^{(1)} \rangle \end{aligned} \quad (2.51)$$

where the excitation rank is naturally truncated given that the two-body Hamiltonian can at most couple each vacuum $\langle \Phi(p; \theta) |$ to its double excitations. Equation (2.51) demonstrates that any excited component of $|\Theta^{(1)}\rangle$ in a given representation of \mathcal{H}_A can only contribute to $E^{(2)}$ if it corresponds to a linear combination of single and double excitations associated with another representation. Looking for the first-order interacting space spanned by product states uniquely contributing to $E^{(2)}$, it is sufficient to include single and double excitations from each Bogoliubov state entering $|\Theta^{(0)}\rangle$. The approximation presently employed consists thus in replacing Eq. (2.48) by

$$|\Theta^{(1)}\rangle = \sum_q \sum_{I \in S, D} a^I(q) |\Omega^I(q)\rangle. \quad (2.52)$$

Equation of motion

The last step of the process consists in determining the unknown coefficients $\{a^I(q); q \in \text{set and } I \in S, D\}$. This is done by solving Eq. (2.18) according to

$$\sum_q \sum_{J \in S, D} M_{IpJq} a^J(q) = -h_1^I(p), \quad (2.53)$$

with $I \in S, D$. The ansatz in Eq. (2.52) does constitute an approximation given that, even if only single and double excitations contribute to the energy, the coefficients are influenced by the presence of higher-rank excitations in the wave function²⁴. Thus truncating the linear system to $J \in S, D$ defines the working approximation that can be variationally and systematically improved if needed.

The elements entering Eq. (2.53) are given by

$$\begin{aligned} M_{pIqJ} &\equiv \langle \Omega^I(p) | H_0 - E^{(0)} | \Omega^J(q) \rangle \\ &= \langle \Phi^I(p) | \mathcal{Q} H_0 \mathcal{Q} P_{00}^{\tilde{\sigma}} | \Phi^J(q) \rangle - E^{(0)} \langle \Phi^I(p) | \mathcal{Q} P_{00}^{\tilde{\sigma}} | \Phi^J(q) \rangle \\ &= F_{pIqJ}^{\tilde{\sigma}} - E^{(0)} N_{pIqJ}^{\tilde{\sigma}} \\ &\quad + \sum_{p'q'} f^*(q') f(p') (2E^{(0)} N_{pIp'0}^{\tilde{\sigma}} N_{q'0qJ}^{\tilde{\sigma}} - F_{pIp'0}^{\tilde{\sigma}} N_{q'0qJ}^{\tilde{\sigma}} - N_{pIp'0}^{\tilde{\sigma}} F_{q'0qJ}^{\tilde{\sigma}}), \quad (2.54a) \\ h_1^I(p) &\equiv \langle \Omega^I(p) | H_1 | \Theta^{(0)} \rangle \\ &= \langle \Phi^I(p) | (H - E_{\text{ref}}) | \Theta^{(0)} \rangle \end{aligned}$$

²⁴This is similar to the situation encountered in coupled cluster theory where the energy is a functional of the sole single and double amplitudes that are themselves influenced by the presence of higher-rank amplitudes in the wave-function.

$$= \sum_{p'} f(p') (H_{pIp'0}^{\tilde{\sigma}} - E_{\text{ref}} N_{pIp'0}^{\tilde{\sigma}}), \quad (2.54b)$$

knowing that the expressions of the *operator kernels*

$$O_{pIqJ}^{\tilde{\sigma}} \equiv \langle \Phi^I(p) | O P_{00}^{\tilde{\sigma}} | \Phi^J(q) \rangle, \quad (2.55)$$

generalizing those introduced in Sec. 2.3.1, in terms of input quantities are worked out in App. D²⁵. The kernel associated with the identity operator $N \equiv 1$ is the generalized norm kernel denoted as $N_{pIqJ}^{\tilde{\sigma}}$. In Eq. (2.54), the sole matrix elements involving excitations in both the ket and the bra are those of a zero or a one-body operator, which limits the complexity of the calculation. On the other hand, matrix elements of the two-body Hamiltonian only involve single or double excitations of the bra.

Second-order energy

Once the coefficients $\{a^I(q); q \in \text{set and } I \in \text{S,D}\}$ have been obtained by solving Eq. (2.53), the second-order energy can be computed via Eq. (2.19a). In expanded form, it reads as

$$\begin{aligned} E^{(2)} &= \sum_q \sum_{I \in \text{S,D}} h_1^{I*}(q) a^I(q) \\ &\equiv \sum_q \sum_{I \in \text{S,D}} e^{(2)I}(q) \\ &\equiv \sum_q e_S^{(2)}(q) + e_D^{(2)}(q), \end{aligned} \quad (2.56)$$

such that the contributions of each configuration I at deformation q could be isolated, along with their partial sums over the categories of single and double excitations.

One can further compute $E^{(3)}$ from the same information, i.e. from the knowledge of $|\Theta^{(1)}\rangle$. According to Eq. (2.19b), this however requires to access matrix elements of the two-body Hamiltonian with excited configurations on both sides, which is significantly more costly than for $E^{(2)}$. These matrix elements are not provided in the present work but can be worked out to access $E^{(3)}$ in a future work.

Linear redundancies

Linear redundancies pose significant difficulties to the solving of the PGCM-PT(2) linear system (Eq. (2.53)). While of similar nature as for the PGCM itself, these difficulties are much more acute due to the incomparable dimensionality at play in Eq. (2.53) compared to the HWG equation (Eq. (2.28)) and to the significant linear dependencies of the excitations of the different non-orthogonal HFB vacua. The numerical method implemented to overcome the problem is detailed at length in Chapter 5 and App. M.

Intruder states

Multi-reference approaches are susceptible to troublesome intruder states that induce singularities in the perturbative corrections. These singularities originate from the possibility that the unperturbed state becomes accidentally degenerate with another eigenstate of H_0 . This causes the first-order wave-function coefficients to blow-up.

²⁵A generalization of the computation of such matrix elements to the case where vacua are orthogonal Slater determinants is found in [85].

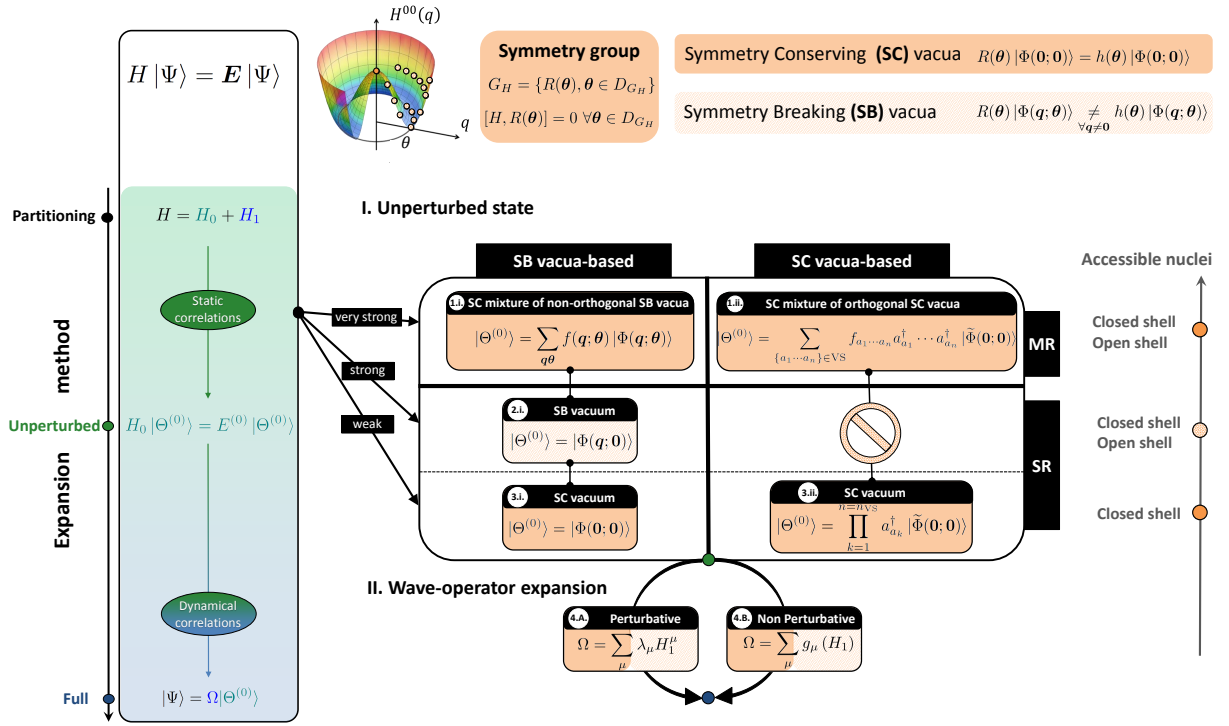


Figure 2.4. (color online) Schematic representation of the existing options to define the partitioning and unperturbed state at the heart of expansion many-body methods. Standard single-reference symmetry-conserving schemes appear as particular limits of more general choices, i.e. single-reference symmetry-breaking schemes that are themselves limits of the multi-reference symmetry-conserving scheme introduced in the present work. Moving up in generality allows one to tackle stronger static correlations, which effectively enlarge the classes of nuclei that can be accessed in a controlled fashion.

Being related to the definition of the partitioning, the nuisance of intruder states can be mitigated by changing the definition of H_0 . Rather than using an explicitly different H_0 , the difficulties can be bypassed by adding a constant shift to the chosen H_0 . While real energy shifts can only move the problematic poles along the real axis [86], often causing the divergences to reappear in a slightly different situation, imaginary shifts move the poles into the complex plane and provide a more robust way to remove intruder-state divergences [87]. The corresponding method is detailed in Chapter 5 and App. N.

2.4. Discussion

In the past ten years, perturbative and non-perturbative expansion methods have been instrumental to extend the reach of ab initio calculations over the nuclear chart. Figure 2.4 provides a sketched panorama of such many-body methods, detailing in particular their character and their applicability depending on the nature of the unperturbed state and the associated partitioning. While the current limitation to mass numbers $A \lesssim 100$ is chiefly computational, there does not exist a symmetry-conserving approach universally applicable to doubly closed-shell, singly open-shell and doubly open-shell nuclei and scaling gently, i.e. polynomially, with the number of nucleons.

The present work addresses such a challenge by formulating a perturbative expansion on top of a multi-reference unperturbed state mixing *deformed non-orthogonal Bogoliubov vacua*, i.e. an unperturbed state obtained via the projected generator coordinate method. As a result, (strong) static correlations can be captured in a versatile and efficient fashion at the level of the unperturbed state such that only (weak) dynamical correlations are left to be accounted for via perturbative corrections. Interestingly, the novel method, coined as PGCM-PT, recovers more standard symmetry-conserving and symmetry-breaking single-reference many-body perturbation theories as particular cases.

In addition to being adapted to all types of nuclei, a key feature of PGCM-PT is to apply to both ground and excited states, i.e. each state coming out of a PGCM calculation can be consistently corrected perturbatively. Another crucial aspect of PGCM-PT relates to the scaling of its cost with nuclear mass. The only other MR perturbation theory applied so far to nuclear systems, MCPT [28], is based on an unperturbed state mixing (a large number of) orthogonal excitations built within a limited configuration space out of a symmetry-conserving vacuum²⁶. Contrarily, the PGCM unperturbed state considered here is built from a low-dimensional linear combination of non-orthogonal vacua. While this is accessed via a diagonalization procedure, the associated low dimensionality is expected to scale much more gently with both mass number and the degree of collective correlations than for more traditional multi-reference methods like MCPT.

The novel PGCM-PT formalism has been laid out in detail in the present chapter. While the generic features of the multi-reference perturbation theory have been described in the bulk of the chapter, many technical appendices are provided to fully characterize the approach, in particular the explicit algebraic expressions of the many-body matrix elements constituting the key ingredients to the approach and entering the main equations that need to be solved in practice. For the future, it is of interest to envision the possibility to develop non-perturbative versions of PGCM-PT, i.e. a method in which PGCM states are corrected via a non-perturbative expansion.

²⁶The vacuum can be the particle vacuum whenever the unperturbed state is obtained from a small-scale no-core shell model [28].

Before applying the novel method in practical applications, Chapter 3 describes a rank-reduction method of the Hamiltonian operator to circumvent the difficulty of treating three-body forces explicitly in *ab initio* calculations.

Chapter 3.

Interlude: In-medium interactions

Contents

3.1. Introduction	41
3.2. Formalism	44
3.2.1. Definitions	44
3.2.2. Standard NOkB approximation	45
3.2.3. Generalized k -body approximation	46
3.3. Many-body methods and one-body density matrices	49
3.3.1. Many-body methods	49
3.3.2. Trial one-body density matrices	50
3.4. Results	51
3.4.1. Studied nuclei	51
3.4.2. Numerical setting	52
3.4.3. Measure of the systematic deviations	52
3.4.4. Ground-state binding energy	53
3.4.5. PHFB absolute energies and radii	59
3.4.6. Spectroscopy	64
3.4.7. Optimal one-body density matrix	70
3.5. Discussion	73

The implementation of the novel expansion method formulated in Chapter 2 is hampered, as any other method, by the presence of three-nucleon operators in the Hamiltonian. In order to circumvent this difficulty, a versatile rank-reduction method for the Hamiltonian is formulated and tested in the present chapter.

3.1. Introduction

Dealing explicitly with three- or even four-nucleon interactions is non-trivial but tractable in a self-consistent mean-field HF or Hartree-Fock-Bogoliubov (HFB) calculation. However, it becomes extremely cumbersome, if not impossible, beyond a certain nuclear mass when we want to solve the A -body Schrödinger equation to sufficient accuracy beyond the mean field. Consequently, ab initio calculations of mid-mass nuclei are typically performed on the basis of the so-called Normal-Ordered 2-Body approximation (NO2B) that captures dominant effects of three-nucleon interactions while effectively working with two-nucleon

operators [88, 89]. In large-scale no-core shell-model calculations, the error induced by the NO2B approximation of the Hamiltonian was estimated to be of the order of 1-3% up to the oxygen region¹.

The NO2B approximation was originally designed by normal ordering the Hamiltonian with respect to a Slater determinant through the standard Wick's theorem [91]. The procedure involves the contraction of the three-body operator with the *one-body* density matrix of that product-state Slater determinant. The approximate Hamiltonian resulting from the NO2B approximation can be consistently employed in many-body methods applicable to closed-shell nuclei that expand the exact solution with respect to a *symmetry-conserving*², e.g. $J^\Pi = 0^+$, Slater determinant. In this context, the approximate NO2B Hamiltonian naturally displays the same symmetries as the original one. However, the naive extension of the NO2B approximation to methods applicable to open-shell systems via the use of symmetry-breaking reference states poses a difficulty. Indeed, ignoring the normal-ordered three-body term delivers in such a situation an approximate operator that itself *explicitly* breaks the corresponding symmetry(ies) of the full Hamiltonian. This feature is unwelcome as it lacks the transparency of restricting the symmetry breaking to approximations of the many-body state, especially in view of the eventual restoration of the symmetry or symmetries.

For many-body methods that break the U(1) symmetry associated with particle-number conservation [46, 48, 51, 60, 67] via the use of Bogoliubov reference states, a *particle-number-conserving* normal-ordered k -body (PNOkB) approximation of an arbitrary n -body operator was recently formulated and validated numerically [61]. Using the PNOkB approximation, ab initio calculations on singly open-shell nuclei based on U(1)-breaking and restored formalisms can thus be safely performed. As the focus is now shifting to methods that (also) break the SU(2) symmetry associated with angular-momentum conservation [92] to describe doubly open-shell nuclei, the symmetry-conserving NOKB approximation should be extended to this symmetry group, which happens to be neither easy nor transparent.

The difficulty is bypassed from the outset when open-shell systems are described through a multi-reference method based on an explicitly correlated and symmetry-conserving reference state, e.g. in the multi-reference in-medium similarity renormalization group method [37, 93]. In this context, it is natural to approximate the three-body interaction through its truncated normal-ordering with respect to the correlated reference state on the basis of Mukherjee-Kutzelnigg Wick theorem [94]. The benefit however comes with the prize of having to contract the three-body operator not only with the one-body, but also with the two-body and three-body density matrices of the correlated state. A somewhat similar situation occurs within self-consistent Green's function (SCGF) theory that can be formulated in terms of effective k -body vertices obtained by contracting initial n -body operators ($n \geq k$) with fully correlated $(n - k)$ -body density matrices [40].

In conclusion, several approaches exist to produce so-called *effective*, i.e. nucleus-

¹For low-resolution Hamiltonians obtained via, e.g., the application of similarity renormalization group (SRG) transformations [22], the efficiency of the NO2B approximation can be understood on the basis of phase-space arguments in the calculation of homogeneous infinite nuclear matter [90]. In particular, the analysis of Ref. [90] makes clear that the quality of the approximation can only improve as the density (mass) of matter (nuclei) increases.

²In the present work, a symmetry-conserving state represents a state whose associated one-body density matrix is symmetry-invariant, i.e. belongs to the *trivial* irreducible representation of the symmetry group of the Hamiltonian. While for the SU(2) group it is necessary that the many-body state itself is symmetry invariant, i.e. a $J = 0$ state, for the U(1) group this condition is automatically satisfied for the *normal* one-body density matrix.

dependent, interactions. The aim is to eventually discard the effective operator(s) of highest n -body character(s) whose contribution to, e.g., ground-state energies is (are) expected³ to be much smaller than for the original operator(s) carrying the same n -body character(s). Such a procedure always involves a contraction of the original operator(s) with a (set of) density matrix (matrices) reflecting (i) the symmetries and (ii) the correlations of the many-body state it (they) originate from and that is typically the reference state or the fully correlated state at play in the many-body method of interest.

Consequently a novel method is introduced to build a set of effective k -body interactions in view of approximating the initial Hamiltonian. While the Hamiltonian is indeed our primary target, the procedure can in principle be applied to any observable. Our goal is thus to formally justify and test numerically a novel approximation method that

1. only invokes contractions with a one-body density matrix,
2. uses a symmetry-invariant one-body density matrix,
3. is flexible regarding the many-body state used to compute that one-body density matrix,
4. re-expresses the approximate Hamiltonian in normal-ordered form with respect to the particle vacuum.

The benefits are that

1. the method does not involve l -body density matrices with $l > 1$,
2. the approximate Hamiltonian resulting from omitting certain effective k -body terms always possesses the same symmetry group as the original one,
3. the method does not necessarily have to employ the one-body density matrix associated with the many-body (reference) state at play in the method used to solve Schrödinger's equation,
4. the resulting Hamiltonian is explicitly expressed in the original single-particle basis such that it can naturally be employed as the starting point of any many-body method.

Points (3) and (4) underline the fact that the approximation of the Hamiltonian and the solution of the Schrödinger equation, although not unrelated, constitute two different problems and do not necessarily have to be dealt with on the basis of the same many-body scheme.

Per se, the method is applicable independently of the closed- or (doubly) open-shell character of the system as well as of the ground or excited nature of the targeted state. Still, point (2) implies that only one-body densities deriving from a $J^\Pi = 0^+$ state can be employed in the approximation procedure, which obviously implies that the employed one-body density matrix does not necessarily derive from the targeted state/nucleus. With excited states of even-even nuclei in mind, one can most naturally approximate the Hamiltonian through the use of a one-body density matrix associated with the ground state. With odd-even or odd-odd systems in mind, one can employ the symmetry-invariant

³Once again, this property can be justified for low-resolution Hamiltonians on the basis of phase-space arguments [90].

density matrix associated with a *fake* odd system described in terms of, e.g., a statistical mixture [83, 84] in close spirit with the ensemble-normal ordering technique used in valence-space IMSRG calculations of odd nuclei [95]. Here, the focus is on even-even systems.

The chapter is organized as follows. Sec. 3.2 is dedicated to the formulation of the method and its relation to existing ones. After explaining in Sec. 3.3 the hierarchy of one-body density matrices and many-body methods presently employed to test the approximation method, the corresponding numerical results are presented in Sec. 3.4. Finally, a discussion is provided in Sec. 3.5.

3.2. Formalism

3.2.1. Definitions

An arbitrary particle-number conserving operator O as defined in Eq. (1.4) is considered in this section.

Distance

In the following, the extent to which two one-body density matrices ρ and ρ' deviate from one another will need to be characterized. The distance

$$d(\rho, \rho') \equiv \|\rho - \rho'\|, \quad (3.1)$$

provides such a diagnostic, where the *Frobenius norm* $\|\cdot\|$ for an arbitrary mode- n tensor T is defined as

$$\|T\| \equiv \sqrt{\sum_{i_1 \dots i_n} T_{i_1 \dots i_n} T_{i_1 \dots i_n}^*}. \quad (3.2)$$

The superscript denotes elementwise complex conjugation.

Convolution

The convolution of the mode- $2n$ tensor $o^{(n)}$ associated with an n -body operator O^{nn} with the mode- $2m$ tensor ($m \leq n$) defining an m -body density matrix $\rho^{(m)}$ generates the mode- $2(n-m)$ tensor $o^{(n)} \cdot \rho^{(m)}$ with elements

$$\left[o^{(n)} \cdot \rho^{(m)} \right]_{b_1 \dots b_{n-m}}^{a_1 \dots a_{n-m}} \equiv \sum_{\substack{a_{n-m+1}, \dots, a_n \\ b_{n-m+1}, \dots, b_n}} o_{b_1 \dots b_n}^{a_1 \dots a_n} \left[\rho^{(m)} \right]_{a_{n-m+1} \dots a_n}^{b_{n-m+1} \dots b_n}. \quad (3.3)$$

The tensor $o^{(n)} \cdot \rho^{(m)}$ is obviously a pure number whenever $m = n$ and nothing but the initial tensor $o^{(n)}$ whenever $m = 0$.

Given two density matrices $\rho^{(l)\Theta}$ and $\rho^{(k)\Psi}$, it is straightforward to check that the convolution is such that the following identity holds

$$\begin{aligned} \left(o^{(n)} \cdot \rho^{(m)\Theta} \right) \cdot \rho^{(l)\Psi} &= \left(o^{(n)} \cdot \rho^{(l)\Psi} \right) \cdot \rho^{(m)\Theta} \\ &= o^{(n)} \cdot \left(\rho^{(m)\Theta} \otimes \rho^{(l)\Psi} \right). \end{aligned} \quad (3.4)$$

3.2.2. Standard NOkB approximation

Wick's theorem

Let us consider a symmetry-conserving product state $|\Phi\rangle$, i.e. a $J^\Pi = 0^+$ Slater determinant. The standard Wick's theorem [91] for a state $|\Phi\rangle$ entails four elementary contractions

$$c_a^\dagger c_b^\dagger - : c_a^\dagger c_b^\dagger : = 0, \quad (3.5a)$$

$$c_a^\dagger c_b - : c_a^\dagger c_b : = \rho_a^{\Phi b}, \quad (3.5b)$$

$$c_a c_b^\dagger - : c_a c_b^\dagger : = \delta_{ab} - \rho_b^{\Phi a}, \quad (3.5c)$$

$$c_a c_b - : c_a c_b : = 0, \quad (3.5d)$$

where $: \dots :$ denotes the normal ordering with respect to $|\Phi\rangle$.

Applying Wick's theorem, the operator O defined in Eq. (1.4) is rewritten as

$$O = \sum_{k=0}^N \mathbf{O}^{kk}[\rho^\Phi], \quad (3.6)$$

where $\mathbf{O}^{kk}[\rho^\Phi]$ is a k -body operator in normal-ordered form⁴ with respect to $|\Phi\rangle$

$$\mathbf{O}^{kk}[\rho^\Phi] \equiv \frac{1}{k!} \frac{1}{k!} \sum_{\substack{a_1 \dots a_k \\ b_1 \dots b_k}} \mathbf{o}_{b_1 \dots b_k}^{a_1 \dots a_k}[\rho^\Phi] : C_{b_1 \dots b_k}^{a_1 \dots a_k} : . \quad (3.7)$$

Considering O^{nn} ($n \leq N$) and $k \leq n$, there are

$$(n-k)! \binom{n}{n-k} \binom{n}{n-k} \quad (3.8)$$

ways to perform $(n-k)$ non-zero contractions. Consequently, the matrix elements of $\mathbf{O}^{kk}[\rho^\Phi]$ are related to those defining the original contributions to O through

$$\mathbf{o}_{b_1 \dots b_k}^{a_1 \dots a_k}[\rho^\Phi] = \sum_{n=k}^N \frac{1}{(n-k)!} \left[O^{(n)} \cdot \rho^{\Phi \otimes (n-k)} \right]_{b_1 \dots b_k}^{a_1 \dots a_k}. \quad (3.9)$$

Approximation

The normal-ordered k -body (NOkB) approximation $O^{\text{NOkB}}[\rho^\Phi]$ to the operator O proceeds by truncating the sum in Eq. (3.6) to the desired maximum value k . While the original operator is obviously independent of ρ^Φ , $O^{\text{NOkB}}[\rho^\Phi]$ does acquire such a dependence as soon as $k < N$.

For example, the standard NO2B approximation consists of ignoring beyond normal-ordered 2-body terms to define the approximate Hamiltonian as [88, 89]

$$H^{\text{NO2B}}[\rho^\Phi] \equiv \mathbf{H}^{00}[\rho^\Phi] + \mathbf{H}^{11}[\rho^\Phi] + \mathbf{H}^{22}[\rho^\Phi]. \quad (3.10)$$

Generalizing the approach to a U(1)-breaking product state, i.e. a Bogoliubov reference state, Wick's theorem gives rise to non-zero *anomalous* contractions (Eqs. (3.5a) and (3.5d))

⁴In the present work, a k -body operator and the tensor representing it are written with a standard font (bold font), e.g. O^{kk} (\mathbf{O}^{kk}), if the operator is in normal order with respect to the particle vacuum $|0\rangle$ (a many-body state $|\Phi\rangle$).

such that the truncation procedure generates a particle-number-breaking operator. A different truncation scheme was thus formulated to design a particle-number conserving normal-ordered k -body (PNOkB) approximation in Ref. [61]. A similar problem arises when using a SU(2) non-invariant Slater determinant, i.e. whenever $|\Phi\rangle$ is not a $J^\Pi = 0^+$ state. Indeed, the standard NOkB approximation yields an operator that is not rotationally invariant in such a case. Rather than extending the tedious approach designed in Ref. [61] for the U(1) case, a novel method is proposed in Sec. 3.2.3 that avoids such complications from the outset by involving the one-body density matrix stemming from a symmetry-conserving many-body state.

Approximate operator in standard form

Starting from Eq. (3.6), it is interesting to re-express the operator in a normal-ordered form with respect to the particle vacuum (Eq. (1.5)). Doing so requires a backward application of Wick's theorem, i.e. with respect to $|0\rangle$. The only required non-zero contraction is given by

$$: c_a^\dagger c_b : - N(: c_a^\dagger c_b :) = : c_a^\dagger c_b : - c_a^\dagger c_b = -\rho_a^{\Phi^b}, \quad (3.11)$$

which is nothing but the opposite of the elementary contraction at play in the first step. The original n -body part of O is obtained in terms of the various contributions entering Eq. (3.6) such that the connection between their matrix elements is given by

$$o_{b_1 \dots b_n}^{a_1 \dots a_n} = \sum_{l=n}^N \frac{(-1)^{l-n}}{(l-n)!} \left[\mathbf{o}^{(l)}[\rho^\Phi] \cdot \rho^{\Phi \otimes (l-n)} \right]_{b_1 \dots b_n}^{a_1 \dots a_n}. \quad (3.12)$$

Truncating Eq. (3.6) according to the NOkB approximation and inserting the result into Eq. (3.12) yields the matrix elements of the approximate n -body part of O in normal order with respect to the particle vacuum.

3.2.3. Generalized k -body approximation

The standard NOkB approximation relies on the standard Wick's theorem and is therefore strictly defined with respect to a symmetry-conserving many-body *product* state. Because this restriction is too severe in open-shell systems, a generalization of the procedure is now envisioned such that the involved one-body density matrix can originate from a more general many-body state.

Two-step procedure

Given the operator O and the one-body density matrix ρ associated with an *arbitrary* $J^\Pi = 0^+$ state, one first *defines* the set of anti-symmetrized matrix elements

$$\mathbf{o}_{b_1 \dots b_k}^{a_1 \dots a_k}[\rho] \equiv \sum_{n=k}^N \frac{1}{(n-k)!} \left[\mathbf{o}^{(n)} \cdot \rho^{\otimes (n-k)} \right]_{b_1 \dots b_k}^{a_1 \dots a_k}, \quad (3.13)$$

in strict *analogy* with Eq. (3.9) but relaxing the necessity for the density matrix to originate from a Slater determinant⁵.

⁵The matrix elements introduced in Eq. (3.13) are not obtained through a set of algebraic operations on the original operator but via a straight convolution of tensors. Still, the present procedure could be

The key point of the present development relates to the fact that, independently of the nature of ρ , the inverse operation embodied by Eq. (3.12) remains valid in the present context and recovers the original operator's matrix elements, i.e.

$$o_{b_1 \dots b_n}^{a_1 \dots a_n} = \sum_{l=n}^N \frac{(-1)^{l-n}}{(l-n)!} \left[\mathbf{o}^{(l)}[\rho] \cdot \rho^{\otimes(l-n)} \right]_{b_1 \dots b_n}^{a_1 \dots a_n}. \quad (3.14)$$

This identity is proven in App. F. One can thus conclude that the *combined* operations embodied by Eqs. (3.9) and (3.12) are actually valid outside the reach of standard Wick's theorem. Indeed, the two steps are utterly general operations, i.e. tensor products that are mutually inverse one another, independently of the nature of ρ (i.e. whether it stems from a Slater determinant or not). The standard Wick's theorem is recovered as a particular case of the general tensor identities (3.13)-(3.14), namely when the one-body density matrix does originate from a Slater determinant.

Thus, the purpose of Eqs. (3.13) and (3.14) is to start from the set of tensors defining each n -body contribution to the original operator O in Eqs. (1.4)-(1.5) and to recover it after having gone through an intermediate set defined in strict analogy with the tensors generated via the single-reference normal ordering. While there is no benefit in applying the two-step procedure *per se*, it ensures that the original operator is exactly recovered when doing so. Based on this property, the method provides a useful way to produce nucleus-dependent approximations to the operator through the truncation of the intermediate set of tensors.

Approximation

In close analogy with the NOKB approximation, the k -body approximation of O is now introduced. First, the set of tensors defined through Eq. (3.13) is truncated according to

$$\bar{\mathbf{o}}^{(l)}[\rho] \equiv \mathbf{o}^{(l)}[\rho] \text{ for } l \leq k, \quad (3.15a)$$

$$\bar{\mathbf{o}}^{(l)}[\rho] \equiv 0 \text{ for } l > k. \quad (3.15b)$$

Second, inserting Eq. (3.15) into Eq. (3.14) generates the set of tensors $\bar{o}^{(n)}[\rho]$ defining the k -body approximation of O in normal order with respect to the particle vacuum according to

$$O^{kB}[\rho] \equiv \sum_{n=0}^k \bar{O}^{nn}[\rho], \quad (3.16)$$

where the truncation of the sum naturally derives from Eq. (3.15). While the original operator O is independent of ρ , $O^{kB}[\rho]$ does acquire such a dependence as a result of the truncation characterized by Eq. (3.15).

While O^{kB} can be built on the basis of an arbitrarily correlated (symmetry-conserving) state, it does not require the use of $\rho^{(l)}$ with $l > 1$. As a result, the procedure is significantly simpler than the one associated with the application of Kutzelnigg-Mukherjee's Wick theorem or the one at play in SCGF theory. The practicality of the approach also relates to the fact that the effective Hamiltonian is expressed in normal-ordered form with respect

formulated within the frame of the *quasi*-normal ordering of Ref. [96], which is itself an extension of Kutzelnigg and Mukherjee's universal normal-ordering involving the sole one-body density matrix. In this context, it becomes possible to associate an actual quasi-normal-ordered operator to the tensor $\mathbf{o}^{(k)}[\rho]$. However, given that such a quasi-normal-ordered operator is of no use in the present context, there is no need to invoke it.

to the particle vacuum in the working single-particle basis. As a result, $H^{kB}[\rho]$ can be straightforwardly used in place of H as the input to any many-body method of interest.

Example

One is typically interested in the 2-body approximation $H^{2B}[\rho]$ of an initial Hamiltonian containing a 3-body interaction

$$\begin{aligned} H &\equiv T + V + W \\ &\equiv \frac{1}{(1!)^2} \sum_{\substack{a_1 \\ b_1}} t_{b_1}^{a_1} C_{b_1}^{a_1} + \frac{1}{(2!)^2} \sum_{\substack{a_1 a_2 \\ b_1 b_2}} v_{b_1 b_2}^{a_1 a_2} C_{b_1 b_2}^{a_1 a_2} + \frac{1}{(3!)^2} \sum_{\substack{a_1 a_2 a_3 \\ b_1 b_2 b_3}} w_{b_1 b_2 b_3}^{a_1 a_2 a_3} C_{b_1 b_2 b_3}^{a_1 a_2 a_3}, \end{aligned} \quad (3.17)$$

where $t_{b_1}^{a_1}$ denotes matrix elements of the kinetic energy whereas $v_{b_1 b_2}^{a_1 a_2}$ and $w_{b_1 b_2 b_3}^{a_1 a_2 a_3}$ denote anti-symmetric matrix elements of two- and three-body interactions, respectively.

Setting

$$\begin{aligned} O^{00} &\longrightarrow 0, \\ O^{11} &\longrightarrow T, \\ O^{22} &\longrightarrow V, \\ O^{33} &\longrightarrow W, \end{aligned}$$

Eq. (3.15) gives for $k = 2$

$$\bar{\mathbf{h}}^{(0)}[\rho] \equiv t^{(1)} \cdot \rho + \frac{1}{2!} v^{(2)} \cdot \rho^{\otimes(2)} + \frac{1}{3!} w^{(3)} \cdot \rho^{\otimes(3)}, \quad (3.18a)$$

$$\bar{\mathbf{h}}^{(1)}[\rho] \equiv t^{(1)} + v^{(2)} \cdot \rho + \frac{1}{2!} w^{(3)} \cdot \rho^{\otimes(2)}, \quad (3.18b)$$

$$\bar{\mathbf{h}}^{(2)}[\rho] \equiv v^{(2)} + w^{(3)} \cdot \rho, \quad (3.18c)$$

$$\bar{\mathbf{h}}^{(3)}[\rho] \equiv 0. \quad (3.18d)$$

Except for the key fact that ρ does not necessarily relate to a Slater determinant, Eq. (3.18) is formally identical to Eq. (3.10) defining $H^{\text{NO}2B}$. Inserting Eq. (3.18) into Eq. (3.14), one eventually obtains the three tensors

$$\bar{h}^{(0)}[\rho] \equiv \frac{1}{3!} w^{(3)} \cdot \rho^{\otimes(3)}, \quad (3.19a)$$

$$\bar{h}^{(1)}[\rho] \equiv t^{(1)} - \frac{1}{2!} w^{(3)} \cdot \rho^{\otimes(2)}, \quad (3.19b)$$

$$\bar{h}^{(2)}[\rho] \equiv v^{(2)} + w^{(3)} \cdot \rho, \quad (3.19c)$$

defining the normal-ordered contributions to $H^{2B}[\rho]$ with respect to the particle vacuum, i.e.

$$H^{2B}[\rho] = \bar{h}^{(0)}[\rho] + \frac{1}{(1!)^2} \sum_{\substack{a_1 \\ b_1}} \bar{h}_{b_1}^{a_1}[\rho] C_{b_1}^{a_1} + \frac{1}{(2!)^2} \sum_{\substack{a_1 a_2 \\ b_1 b_2}} \bar{h}_{b_1 b_2}^{a_1 a_2}[\rho] C_{b_1 b_2}^{a_1 a_2}. \quad (3.20)$$

In addition to the fact that, by construction, $H^{2B}[\rho]$ does not contain a three-body operator, its structure differs from the original operator expressed in normal order with respect to the particle vacuum (Eq. (3.17)) by the fact that it incorporates the pure number $\bar{h}^{(0)}[\rho]$.

3.3. Many-body methods and one-body density matrices

Equations (3.19) define a set of nucleus-dependent 0-, 1- and 2-body operators entering $H^{2B}[\rho]$. As in the NO2B approximation, the inclusion of a large part of W into these effective operators, while treating T and V exactly, gives a clear argument that omitting $\mathbf{h}^{(3)}[\rho]$ leads to small, hopefully small enough, errors. Still, one is left with the question of the optimal character of the one-body density matrix to be employed for a given system and many-body approximation.

In the hypothesis that exact eigenstates of H in the A -body Hilbert space \mathcal{H}_A are known, one may expect that employing the one-body density matrix of the exact ground-state⁶ is optimal to reproduce the ground-state energy⁷. In fact, this intuition is not correct.

From a formal viewpoint, it would be interesting to find the optimal one-body density matrix to be used in $H^{2B}[\rho]$ to best reproduce, e.g., the energy associated with the (approximate) ground state $|\Psi\rangle$ of the full Hamiltonian H . This would however not be of practical use. Consequently, the numerical results displayed in Sec. 3.4 rely on testing a set of trial one-body density matrices while obtaining the solution to the A -body problem via various approximation methods. As will be concluded, the results are very robust with respect to the employed one-body density matrix as long as the latter respects a minimal set of properties.

3.3.1. Many-body methods

The many-body methods presently used to solve the A -body Schrödinger equation for a collection of doubly closed, singly open-shell and doubly open-shell even-even nuclei (to be specified later on) are

1. axially deformed Hartree-Fock-Bogoliubov (dHFB) theory [43] as defined in Sec. 1.2.4,
2. the particle-number- and angular-momentum-Projected Hartree-Fock-Bogoliubov (PHFB) method [43, 97] based on dHFB states,
3. the PGCM [43] mixing PHFB states along the axial quadrupole moment of the underlying dHFB states (see Chaps. 2 and 4),
4. quasi-particle random phase approximation for axially deformed and superfluid nuclei (dQRPA) in the finite amplitude method (FAM) formulation [98, 99],
5. deformed Bogoliubov many-body perturbation theory⁸ at third order (dBMBPT(3)) [45, 47, 53]. See App. E for a brief summary of the formalism.

A schematic representation of the structure of the implementation of many-body methods (developed in the context of this thesis) is found in App. P⁹. Deformed HFB theory

⁶This reasoning has of course a chance to be correct only if the target state $|\Psi\rangle$ is a $J^\Pi = 0^+$ state. If not, the optimal density matrix cannot be equal to ρ^Ψ for symmetry reasons as already briefly discussed in the introduction.

⁷One may further think that the density matrix associated with a statistical symmetry-conserving average of a set of exact low-lying states is optimal to best reproduce the low-lying spectroscopy.

⁸Whereas BMBPT has already been applied quite systematically to semi-magic spherical nuclei [46, 60], it is the first time it is performed on top of a deformed Bogoliubov state in order to describe doubly open-shell nuclei.

⁹dQRPA results were provided by Y. Beaujeault-Taudière [100].

constitutes the mean-field baseline that can capture the bulk of static correlations in open-shell nuclei through the spontaneous breaking of U(1) and SU(2) symmetries. Based on it, PHFB, PGCM and dQRPA on the one hand and dBMBPT on the other hand, provide systematic beyond-mean-field extensions whose aim is to capture many-body correlations. While PHFB, PGCM and dQRPA¹⁰ do so via the addition of static correlations associated with the restoration of broken symmetries and the fluctuation of shapes, dBMBPT targets dynamical correlations through the resummation of elementary, i.e. quasi-particle, excitations. The former approaches access collective excited states whereas the latter naturally addresses absolute binding energies and associated ground-state observables.

The string of dHFB, PHFB, PGCM and dQRPA calculations can presently be performed with the full inclusion of three-body forces, i.e. employing a realistic nuclear Hamiltonian H without any form of approximation. Such ab initio calculations are the first of their kind [99] and allow us to benchmark the approximation of H by $H^{2B}[\rho]$ on the basis of non-trivial many-body methods¹¹. While it can be envisioned to do so in the future [45], BMBPT is not yet implemented with full three-body interactions. Deformed BMBPT calculations are therefore presently performed with $H^{2B}[\rho]$ for various approximations to ρ and compared to those done earlier [46, 60] on the basis of the PNO2B approximation [61].

3.3.2. Trial one-body density matrices

Employing the many-body schemes introduced above, the goal is to approximate H by $H^{2B}[\rho]$ with ρ computed from various $J^\Pi = 0^+$ trial states¹², i.e.

1. a spherical harmonic oscillator Slater determinant¹³ (ρ^{sHOSD}),
2. a spherical HF(B) state ($\rho^{\text{sHF(B)}}$),
3. a PHFB state (ρ^{PHFB}),
4. a PGCM ground-state (ρ^{PGCM}),

¹⁰While helpful to discuss the performance of a many-body method, the distinction between dynamical and static correlation effects involve a fuzzy boundary, prominently displayed in the dQRPA case. Namely, the dQRPA equations can be derived within different schemes, e.g. as a harmonic limit of the GCM equations [101] or via the linearization of time-dependent HFB equations [102, 103]. Depending on these viewpoints, dQRPA either falls in the category of post-HFB extensions grasping static correlations (associated with fluctuation of shapes), or in the category of beyond-mean-field approaches aiming at capturing dynamical correlations (in terms of 2-quasi-particle excitations). In the present work, we make the arbitrary choice to categorize dQRPA among the former class of approaches.

¹¹PHFB and PGCM calculations based on realistic chiral Hamiltonians have been performed recently for the first time but at the price of approximating three-body operators [93, 104]. The exact treatment of W in realistic PGCM calculations typically increases the CPU time by three orders of magnitude compared to using $H^{2B}[\rho]$.

¹²Because correlations captured by QRPA do not feed back into the ground-state, there is no non-trivial one-body density matrix ρ^{sQRPA} associated with the spherical QRPA solution to be used in the construction of $H^{2B}[\rho]$.

¹³In open-shell nuclei, the invariant density matrix is obtained via the use of the equal filling approximation. This approach can be justified on the basis of a specific *statistical mixture* of sHO Slater determinants carrying the appropriate number of particles [84] or on the basis of a specific *linear combination* of sHO Slater determinants carrying different number of particles such that the linear combination has the correct number of particles on average [105].

5. a standard spherical MBPT¹⁴ ground-state (ρ^{sMBPT}).

In the numerical results discussed in Sec. 3.4, $\rho^{\text{sHF(B)}}$, ρ^{PHFB} and ρ^{PGCM} are extracted from the corresponding calculations performed with the *full* H . Contrarily, ρ^{sMBPT} is obtained from a calculation performed with the PNO2B approximation whereas ρ^{sHOSD} does not require any a priori calculation.

The two options $\rho^{\text{sHF(B)}}$ and ρ^{sMBPT} originate from *symmetry-restricted* HFB and BMBPT calculations, i.e. *spherical* HF(B) ensures the $J^\Pi = 0^+$ character of the state whereas *standard spherical* MBPT ensures particle-number conservation¹⁵. In the latter case, the restriction implies that the use of ρ^{sMBPT} is limited to doubly closed-shell nuclei.

While the expression of $\rho^{\text{sHF(B)}}$ is textbook material [43], it is not the case for ρ^{PHFB} and ρ^{PGCM} . Consequently, the derivation of the corresponding expressions are provided in App. G. For the sake of generality and future use, the derivation is actually performed for a more general quantity than presently needed, i.e. App. G provides the expressions for the *transition* one-body density matrix between two arbitrary initial ($J_i^{\Pi_i}$) and final ($J_f^{\Pi_f}$) PGCM states. The result of present interest is then obtained by setting $J_i^{\Pi_i} = J_f^{\Pi_f} = 0^+$. While the expression for ρ^{sMBPT} is known material [106, 107], the expression of ρ^{BMBPT} it presently derives from is not. Consequently, the derivation of ρ^{BMBPT} is provided in App. E.3 for the sake of completeness and future use.

3.4. Results

3.4.1. Studied nuclei

A set of properties (i.e. binding energies, matter radii, low-lying spectra as well as electromagnetic properties) are computed for a set of representative nuclei using the many-body methods and the one-body density matrices introduced in Sec. 3.3. The set ranges from light to medium-mass nuclei and contains

1. doubly closed-shell (^{16}O , ^{40}Ca),
2. singly open-shell (^{18}O),
3. and doubly open-shell (^{20}Ne , ^{30}Ne , $^{24,40}\text{Mg}$, $^{42,48}\text{Ar}$),

systems. The goal is to cover oblate, spherical and prolate representatives among which some nuclei are *soft* and others are *rigid* with respect to axial deformation¹⁶.

¹⁴Standard spherical MBPT denotes many-body perturbation theory based on a spherical Slater determinant reference state rather than on a particle-number-breaking Bogoliubov reference state. The former is automatically obtained from the latter in closed-shell nuclei where the dHFB reference state reduces to the spherical HF Slater determinant.

¹⁵While it is not a problem to compute ρ from a particle-number-breaking state carrying the correct particle number on average as in spherical Hartree-Fock-Bogoliubov (sHFB), it happens that ensuring the correct average particle-number requires a non-trivial procedure in BMBPT beyond HFB [47]. For simplicity, we thus presently limit ourselves to nuclei for which dBMBPT automatically reduces to standard spherical MBPT.

¹⁶Some of these nuclei, e.g. ^{24}Mg , display a triaxial minimum if allowed to. Still, present calculations are restricted to axial symmetry.

3.4.2. Numerical setting

The numerical solver allowing us to perform dHFB, PHFB, PGCM, dQRPA [99] and dBMBPT calculations based on full two- and three-nucleon interactions is briefly introduced in App. P. For the present purpose, it is sufficient to specify that the one-body spherical harmonic oscillator basis is employed. The finite number of oscillator shells is set by the parameter e_{\max} such that $2n + l \leq e_{\max}$, where n and l denote the principal quantum number and the orbital angular momentum of a given shell, respectively. The value of the harmonic oscillator frequency $\hbar\omega$ is further needed to fully characterize the working basis. Except if specified otherwise, all calculations are presently performed with $e_{\max} = 8$ and $\hbar\omega = 20$ MeV. While these values do not permit to generate fully converged calculations of all the nuclei listed above, the conclusions drawn at the end of the chapter are independent of them.

When representing an n -body operator, the natural truncation of the tensor-product basis of the n -body Hilbert space is set by $e_{n\max} \equiv ne_{\max}$. One and two-body operators are thus represented using $e_{1\max} = e_{\max}$ and $e_{2\max} = 2e_{\max}$, respectively. However, $e_{3\max} = 8, 10, 12$ ($\ll 3e_{\max}$) is used to represent the three-nucleon interaction given that employing $3e_{\max}$ is largely beyond today's capacities¹⁷. This truncation will play a key role regarding the quality of the approximation associated with $H^{2B}[\rho]$ in medium-mass and/or neutron-rich nuclei.

The chiral effective field theory Hamiltonian H presently employed combines a two-nucleon interaction at next-to-next-to-next-to-leading order (N3LO) [108, 109] with an N²LO three-nucleon interaction [110]. It is then evolved to a lower momentum scale $\lambda_{\text{sallows rg}}$ via particle-vacuum SRG transformations [22, 111, 112]. While by default results obtained for $\lambda_{\text{srg}} = 1.88 \text{ fm}^{-1}$ are discussed, $\lambda_{\text{srg}} = 2.23 \text{ fm}^{-1}$ will also be used for comparison.

3.4.3. Measure of the systematic deviations

In order to assess quantitatively the errors induced by the approximation and compare the different effective interactions, measures of the average deviation between the results obtained with $H^{2B}[\rho]$ and H are introduced for each method, i.e.

$$r_{\text{HFB}} \equiv \frac{1}{n_{\text{data}} n_{\text{nuclei}}} \sum \left| \frac{E_{\text{HFB}}[\rho] - E_{\text{HFB}}}{E_{\text{HFB}}} \right|, \quad (3.21a)$$

$$r_{\text{PHFB}} \equiv \frac{1}{n_{\text{data}} n_{\text{nuclei}}} \sum \sum_J \left| \frac{E_{\text{PHFB}}^{J^\Pi}[\rho] - E_{\text{PHFB}}^{J^\Pi}}{E_{\text{PHFB}}^{J^\Pi}} \right|, \quad (3.21b)$$

$$r_{\text{BMBPT}} \equiv \frac{1}{n_{\text{data}} n_{\text{nuclei}}} \sum \left| \frac{E_{\text{BMBPT}}[\rho] - E_{\text{BMBPT}}^{\text{PNO2B}}}{E_{\text{BMBPT}}^{\text{PNO2B}}} \right|, \quad (3.21c)$$

$$r_{\text{PGCM}} \equiv \frac{1}{n_{\text{data}} n_{\text{nuclei}}} \sum \sum_J \sum_O \left| \frac{O_{\text{PGCM}}^{J^\Pi}[\rho] - O_{\text{PGCM}}^{J^\Pi}}{O_{\text{PGCM}}^{J^\Pi}} \right|, \quad (3.21d)$$

where in practice states up to $J = 6$ are taken into account when applicable and where O denotes any observable computed within the PGCM formalism (energy, electric and

¹⁷A novel framework capable of handling values up to $e_{3\max} = 28$ in the normal-ordered two-body approximation was proposed very recently [42]. However, as discussed later, the present truncation of $e_{3\max} = 14$ allows us to reach converged results for the light nuclei considered here.

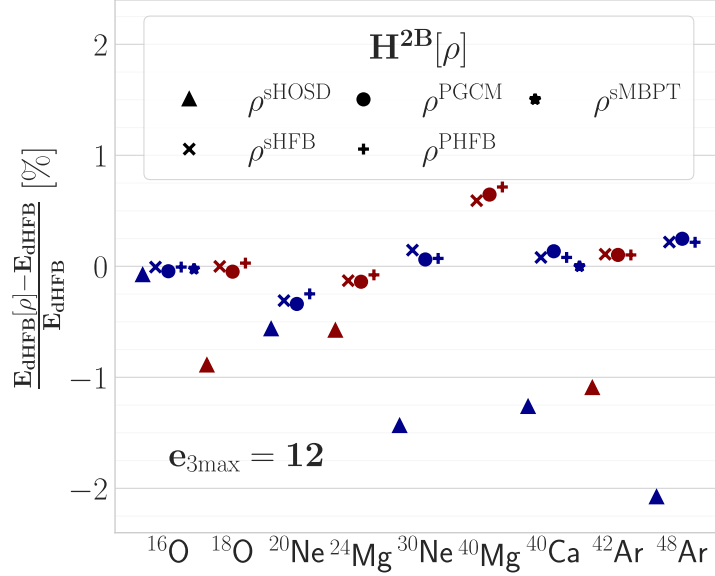


Figure 3.1. Error (in %) of dHFB ground-state energies obtained with $H^{2B}[\rho]$ for the various test one-body density matrices. The error corresponding to the use of ρ^{sHOSD} for ^{40}Mg amounts to 2.6% and lies outside the figure. Calculations were performed with $e_{\text{max}} = 8$, $e_{3\text{max}} = 12$ and $\lambda_{\text{srg}} = 1.88 \text{ fm}^{-1}$.

magnetic moments, transitions and radii). In each case, n_{data} denotes the number of terms in the sum(s).

The deviation on PHFB excitation energies is given by the formula

$$r_{\text{PHFB-S}} \equiv \frac{1}{n_{\text{data}}} \sum_{n_{\text{nuclei}}} \sum_J \left| \frac{\delta E_{\text{PHFB}}^{J^\pi}[\rho] - \delta E_{\text{PHFB}}^{J^\pi}}{\delta E_{\text{PHFB}}^{J^\pi}} \right|. \quad (3.22)$$

3.4.4. Ground-state binding energy

Deformed HFB

Let us first discuss the use of $H^{2B}[\rho]$ at the mean-field, i.e. dHFB, level. Fig. 3.1 displays the error (in %) of the corresponding dHFB ground-state energies compared to the reference values obtained from the full H . Results are provided for $\rho = \rho^{\text{sHOSD}}$ (\blacktriangle), $\rho^{\text{sHF(B)}}$ ($+$), ρ^{PHFB} (\times) and ρ^{PGCM} (\bullet), as well as for $\rho = \rho^{\text{sMBPT}}$ (\star) whenever applicable, i.e. in doubly closed-shell nuclei.

One first observes that $H^{2B}[\rho]$ perform well for the five test one-body density matrices although a notable degradation is visible for $\rho = \rho^{\text{sHOSD}}$. As can be inferred from Tab. 3.1, the weaker performance of $\rho = \rho^{\text{sHOSD}}$ is systematic but especially pronounced as the mass and/or the isospin-asymmetry of the system increases. While the same trend is at play for $\rho^{\text{sHF(B)}}$, ρ^{PHFB} and ρ^{PGCM} , the error systematically remains below 0.2% for these three density matrices, with the exception of ^{40}Mg whose error lies around 0.7%. For ρ^{sHOSD} , the average error over the set is significantly larger (1.2%) throughout the panel and peaks at about 2.6% in ^{40}Mg (not shown in the figure).

From a general standpoint, it is not surprising that the error due to the use of $H^{2B}[\rho]$ is small at the mean-field level. To best appreciate this feature, let us focus on doubly closed-shell ^{16}O and ^{40}Ca for which dHFB reduces to sHF. As shown in Tab. 3.1, the

	Closed shell	Open shell	Mass ≤ 30	Mass > 30	Neutron-rich	All
ρ^{sHOSD}	0.67	1.32	0.71	1.76	2.04	1.18
$\rho^{\text{sHF(B)}}$	0.04	0.20	0.10	0.25	0.29	0.17
ρ^{PHFB}	0.04	0.21	0.09	0.28	0.33	0.17
ρ^{PGCM}	0.05	0.23	0.09	0.30	0.37	0.18
ρ^{sMBPT}	0.04					

Table 3.1. Average difference (in %) between ground-state dHFB energies computed with $H^{2B}[\rho]$ and H for different sub-categories in the test panel and the various test one-body density matrices. The neutron-rich subcategory encompasses ^{30}Ne , ^{40}Mg and ^{48}Ar . See Eq. (3.21a) for the definition of the cost function. Calculations are performed with $e_{\text{max}} = 8$, $e_{3\text{max}} = 12$ and $\lambda_{\text{srg}} = 1.88 \text{ fm}^{-1}$.

error is below 0.05% in these two nuclei for all test one-body density matrices except for ρ^{sHOSD} . As explained in App. H.3, the error would even be strictly zero in such a situation if ρ were equated to the *variational* sHF one-body density matrix throughout the sHF iterations based on $H^{2B}[\rho]$. This procedure would be equivalent to working within the NO2B approximation, which is indeed exact at the sHF level, i.e. the NO2B approximation of the Hamiltonian only impacts post-sHF methods by construction. The fact that one rather takes ρ to be a fixed, e.g. ρ^{sHF} obtained from the full H , a priori determined one-body density matrix to build $H^{2B}[\rho]$ induces a marginal error in sHF calculations.

While the error remains below 0.05% in ^{16}O and ^{40}Ca for appropriate density matrices, the distinctly worse result obtained in ^{40}Ca for $\rho = \rho^{\text{sHOSD}}$ underlines the fact that obtaining a very accurate description is not automatic even in this optimal situation, i.e. it is crucial that the test density matrix contains relevant physical information¹⁸. Having said that, the results obtained with the other four test density matrices are so similar¹⁹ that no clear characteristic can be easily identified as far as the optimal choice is concerned. Neither the consistency with the employed many-body method nor the degree of correlations encoded in the one-body density matrix seem to constitute a decisive feature. For example, ρ^{sHFB} performs as well as the more advanced ρ^{sMBPT} that incorporates dynamical correlations beyond the mean field, as can be seen in Tab. 3.1. We will come back repeatedly to this question throughout the following sections.

While spherical doubly closed-shell nuclei are particularly amenable to a very accurate description, it is pertinent to investigate the dependence of the approximation on the axial quadrupole deformation of the HFB state. All nuclei in the set but $^{16,18}\text{O}$ and ^{40}Ca are doubly open-shell systems and thus spontaneously break rotational symmetry at the dHFB level, ^{20}Ne and ^{24}Mg displaying the largest deformation of all.

The upper panel of Fig. 3.2 displays the dHFB total energy curve (TEC) calculated in ^{20}Ne from the full H as a function of the axial quadrupole deformation²⁰. This nucleus is significantly deformed, as is evident from the minimum of the TEC located at

¹⁸The poorer performance of ρ^{sHOSD} is (at least in part) due to the fact that it misses effects from the Coulomb interaction. This is consistent with the fact that the quality seems to degrade with increasing mass and isospin asymmetry.

¹⁹Because sHFB reduces to sHF in doubly closed-shell nuclei, notice that $\rho^{\text{sHFB}} = \rho^{\text{PHFB}}$ in this case such that both test density matrices give identical results by construction.

²⁰The dimensionless axial quadrupole moment β_{20} used in the figures is defined Eq. (4.3).

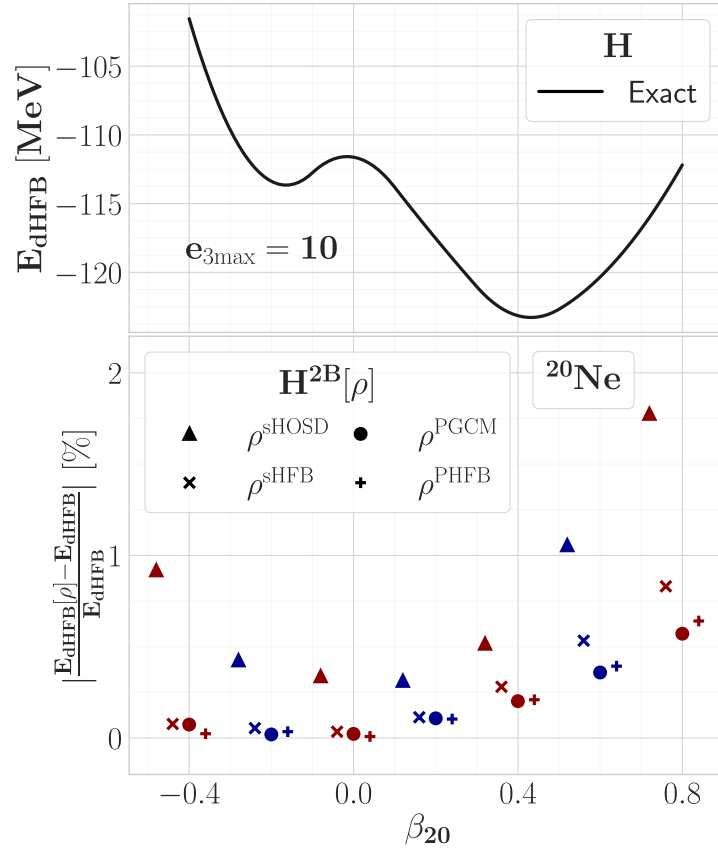


Figure 3.2. Upper panel: dHFB total energy curve of ^{20}Ne as a function of the axial quadrupole deformation computed with the full H . Lower panel: Error (in %) in the total energy curve when using $H^{2B}[\rho]$ with the various test one-body density matrices. Calculations are performed with $e_{\text{max}} = 8$, $e_{3\text{max}} = 10$ and $\lambda_{\text{srg}} = 1.88 \text{ fm}^{-1}$.

$\beta_{20} = 0.45$. As visible from the lower panel, the error induced by $H^{2B}[\rho]$ is essentially zero at sphericity²¹, except for $\rho = \rho^{\text{sHOSD}}$ where it is equal to 0.3%, and grows only mildly with the deformation. The error remains below 1% up to a large deformation of $\beta_{20} = 0.8$ ($\beta_{20} = -0.4$) on the prolate (oblate) side²² for $\rho = \rho^{\text{sHFB}}$, ρ^{PHFB} or ρ^{PGCM} . For $\rho = \rho^{\text{sHOSD}}$, the error is about twice as large along the TEC.

There exists a trend along the TEC, the results obtained with ρ^{sHFB} degrading slightly faster with the deformation than those obtained with ρ^{PGCM} and ρ^{PHFB} . The trend is however not quantitatively significant as can be inferred from the systematic error over open-shell nuclei provided in Tab. 3.1. Eventually, it is remarkable that all three one-body density matrices give excellent and essentially equivalent results up to large deformations, especially given the fact that ρ^{sHFB} does not encode any information about deformation properties of ^{20}Ne . This is a first indication of the robustness of the in-medium 2-body reduction method of 3-body interaction operators.

For orientation, it is interesting to analyze how the various components of $H^{2B}[\rho]$ (Eqs. (3.19)-(3.20)) and H (Eq. (3.17)) contribute to the dHFB energy. Figure 3.3 decomposes the dHFB total energy accordingly in ^{16}O and ^{20}Ne . Results are provided for a schematic model space and $\rho = \rho^{\text{sHFB}}$. Focusing first on ^{16}O and making the hypothesis that the sHF density matrix is the same in both calculations²³, the inspection of Eq. (3.19) makes clear that (a) the 0-body part of $H^{2B}[\rho]$ is strictly equal to the sHF contribution originating from the three-body interaction in H and that (b) the energy contribution associated with the 1- and 2-body parts of $H^{2B}[\rho]$ originating from the three-body interaction exactly cancel out. These features are indeed observed in the upper panel of Fig. 3.3 such that the total sHF energies are identical in both calculations. While this formal analysis does not hold for dHFB in general, the results displayed in the lower panel demonstrate that it remains valid in practice in a well-deformed nucleus such as ^{20}Ne , which eventually elucidates the high-quality results obtained above over a large set of nuclei.

Deformed BMBPT

While it is satisfying that the error induced by $H^{2B}[\rho]$ is negligible at the mean-field, i.e. dHFB, level, it is to some extent expected and surely not sufficient to claim victory. The performance of $H^{2B}[\rho]$ must thus be tested in beyond mean-field methods where the accurate compensation observed above between the terms of H and those of $H^{2B}[\rho]$ is not guaranteed to hold.

While such a test must eventually be carried out for various ab initio methods in the future, the present section focuses on ground-state energies obtained from dBMBPT, which resums dynamical correlations in a perturbative fashion on top of a (possibly deformed and superfluid) HFB state. Present calculations are performed at the BMBPT(3) level that is known to reproduce essentially exact results based on SRG-evolved interactions to better than 2% in oxygen isotopes and those computed from non-perturbative expansion methods to better than 2% in semi-magic nuclei up to the nickel region [46, 60].

²¹Contrarily to ^{16}O and ^{40}Ca , sHFB does not reduce to sHF at sphericity in ^{20}Ne because neutrons and protons remain superfluid. Consequently, the error due to the use of $H^{2B}[\rho]$ cannot be made strictly equal to zero by any optimization of the test one-body density matrix.

²²Note that the edge of the displayed TEC lies 10 MeV (27 MeV) above the minimum on the prolate (oblate) side.

²³This hypothesis is very well validated in practice, even more so in a small model space such as the one employed in the present calculation.

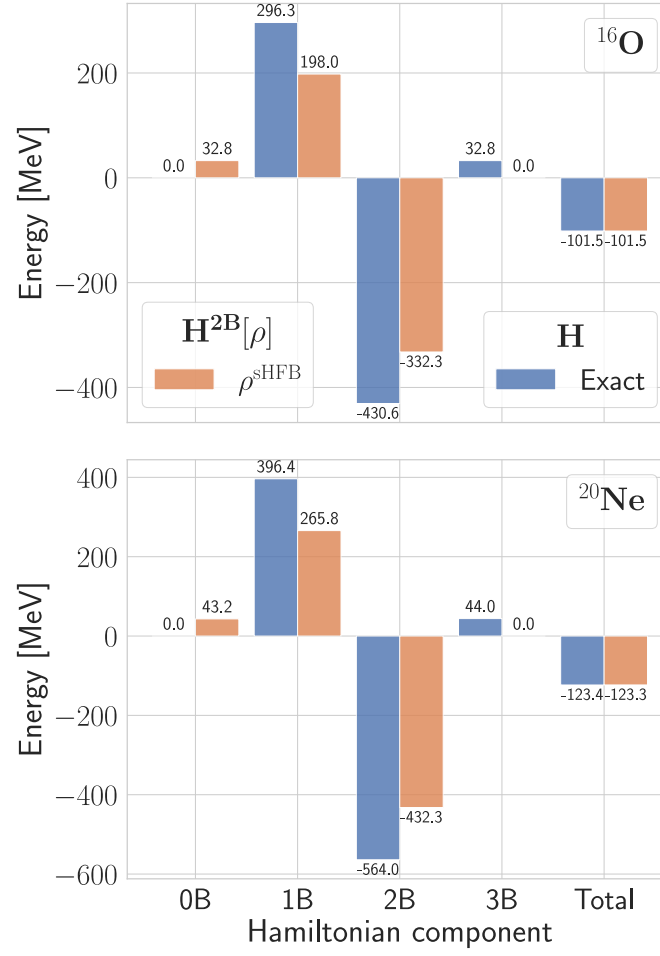


Figure 3.3. Contributions of the various components of $H^{2B}[\rho]$ and H to the dHFB energy. Upper panel: ^{16}O . Lower panel: ^{20}Ne . Calculations are performed with $e_{\text{max}} = 6$ and $e_{3\text{max}} = 6$.

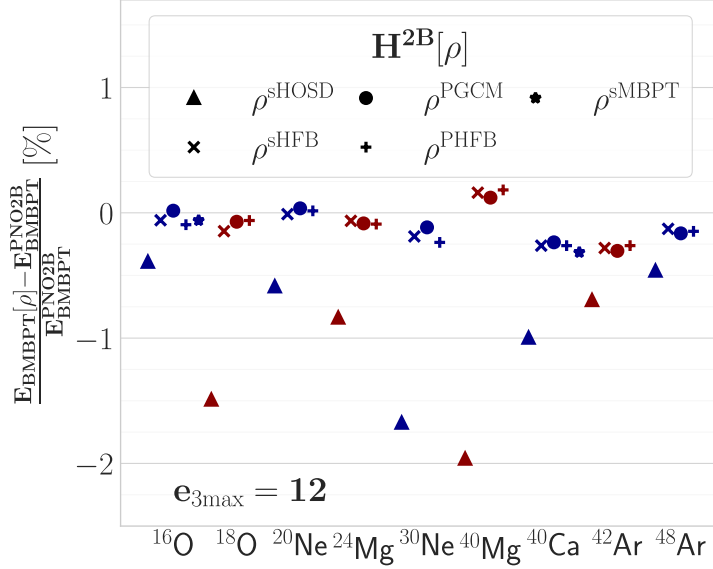


Figure 3.4. Difference of dBMBPT(3) ground-state energies (in %) obtained with $H^{2B}[\rho]$ and within the PNO2B approximation of H for the various test one-body density matrices. Calculations are performed with $e_{\text{max}} = 8$, $e_{3\text{max}} = 12$ and $\lambda_{\text{srg}} = 1.88 \text{ fm}^{-1}$.

Although envisioned in the future, BMBPT calculations with explicit three-nucleon forces are not available yet. Consequently, calculations with $H^{2B}[\rho]$ are presently benchmarked against those obtained using the PNO2B approximation [61], which is the approximation employed so far in all published BMBPT calculations of semi-magic nuclei [46, 60]. In doubly closed-shell nuclei, the PNO2B approximation reduces to NO2B, which has itself been benchmarked against the use of full three-body interactions and shown to offer a typical 1 – 2% accuracy up to ^{16}O [88].

Deformed BMBPT(3) binding energy differences (in %) are displayed in Fig. 3.4. Results produced within both approximations agree to better than 0.3% over the whole set of considered nuclei, except for $\rho = \rho^{\text{sHOSD}}$ where the difference increases up to 2%. Just as for the dHFB results discussed above, the use of a one-body density matrix encoding either static or dynamical correlations beyond the mean-field does not have a significant impact

	Closed shell	Open shell	Mass ≤ 30	Mass > 30	Neutron-rich	All
ρ^{sHOSD}	0.69	1.1	1.00	1.03	1.37	1.01
$\rho^{\text{sHF(B)}}$	0.16	0.14	0.09	0.21	0.16	0.14
ρ^{PHFB}	0.18	0.14	0.10	0.21	0.19	0.15
ρ^{PGCM}	0.13	0.13	0.06	0.21	0.13	0.13
ρ^{sMBPT}	0.19					

Table 3.2. Average difference (in %) of ground-state dBMBPT(3) energies obtained with $H^{2B}[\rho]$ and within the PNO2B approximation of H for different sub-categories in the test panel and the various test one-body density matrices. The neutron-rich subcategory encompasses ^{30}Ne , ^{40}Mg and ^{48}Ar . See Eq. (3.21c) for details on the cost function. Calculations are performed with $e_{\text{max}} = 8$, $e_{3\text{max}} = 12$ and $\lambda_{\text{srg}} = 1.88 \text{ fm}^{-1}$.

on the quality of $H^{2B}[\rho]$ such that the results are essentially equivalent to those obtained with $\rho = \rho^{\text{sHF(B)}}$. This can be confirmed quantitatively by inspecting the numbers reported in Tab. 3.2. Interestingly, the results also show that the average deviation is independent of the closed- or open-shell character of the nuclei under consideration whereas it slightly increases with the mass even though the deviation remains tiny in all cases.

These remarkable results indicate that the in-medium interaction and PNO2B approximation methods are equivalent as far as quantitative ab initio dBMBPT calculations of mid-mass nuclei are concerned. Given the earlier benchmarking of the NO2B approximation in doubly-closed shell nuclei, the presently developed in-medium approximation method is well validated in fully-correlated binding energy calculations.

3.4.5. PHFB absolute energies and radii

In the following, we wish to go beyond ground-state energies and test the in-medium approximation method on spectroscopic properties. In order to do so, PHFB, PGCM and dQRPA calculations will be employed. While these techniques resum static correlations associated with the restoration of broken symmetries and the fluctuation of shapes, they do not account for dynamical correlations. As a result, whereas *relative* energies and spectroscopic quantities can be well converged and meaningful, *absolute* energies are not realistic, i.e. they are far from converged ab initio values. Still, it is useful to first investigate how these absolute energies differ when computed from H and $H^{2B}[\rho]$.

In this section we thus analyse total (ground- and excited-state) energies obtained at the PHFB level. In addition, corresponding ground-state matter radii are presented. In doing so, the dependence of the results on numerical parameters such as $e_{3\text{max}}$, e_{max} and λ_{srg} is also investigated.

Systematic analysis

The upper panels of Fig. 3.5 display binding energies of the lowest-lying $J^\Pi = 0^+, 2^+, 4^+$ states obtained via PHFB calculations with $e_{3\text{max}} = 8$ and 12 (at fixed $e_{\text{max}} = 8$). The energy of each state obtained from H (—) is compared to those generated from $H^{2B}[\rho]$ with $\rho = \rho^{\text{sHOSD}}$ (\blacktriangle), $\rho^{\text{sHF(B)}}$ (\blackplus), ρ^{PHFB} (\blacktimes) and ρ^{PGCM} (\bullet), as well as with $\rho = \rho^{\text{sMBPT}}$ (\star) whenever applicable. Energies are shifted by the dHFB value obtained from the full H for the corresponding system such that all nuclei can be displayed on the same figure.

Reference energies are well reproduced in light nuclei for all test one-body density matrices and both values of $e_{3\text{max}}$, i.e. absolute deviations remain below 1 MeV until ^{24}Mg . Increasing the mass and/or isospin asymmetry renders the approximation more and more sensitive to the value of $e_{3\text{max}}$. Given that ab initio calculations are known to be increasingly more sensitive to $e_{3\text{max}}$ with the mass and isospin-asymmetry of the system [113], it is not surprising that any approximation of the three-nucleon displays the same feature. Going from $e_{3\text{max}} = 8$, through $e_{3\text{max}} = 10$ (not shown) and to $e_{3\text{max}} = 12$, a clear convergence of the results is observed, although full convergence is not quite reached for the heaviest and most neutron-rich nuclei. Eventually, converged results display a similar error in medium-mass nuclei to the one obtained in lighter systems, except for $\rho = \rho^{\text{sHOSD}}$. Below, only results obtained for the largest reachable value of $e_{3\text{max}}$ (typically 12 but not always) are shown.

The lowest panels of Fig. 3.5 display ground-state root-mean-square matter radii (results are similar for excited-states radii). The conclusions are the same as for the energies. Eventually, radii are extremely well reproduced for all nuclei, states and test density

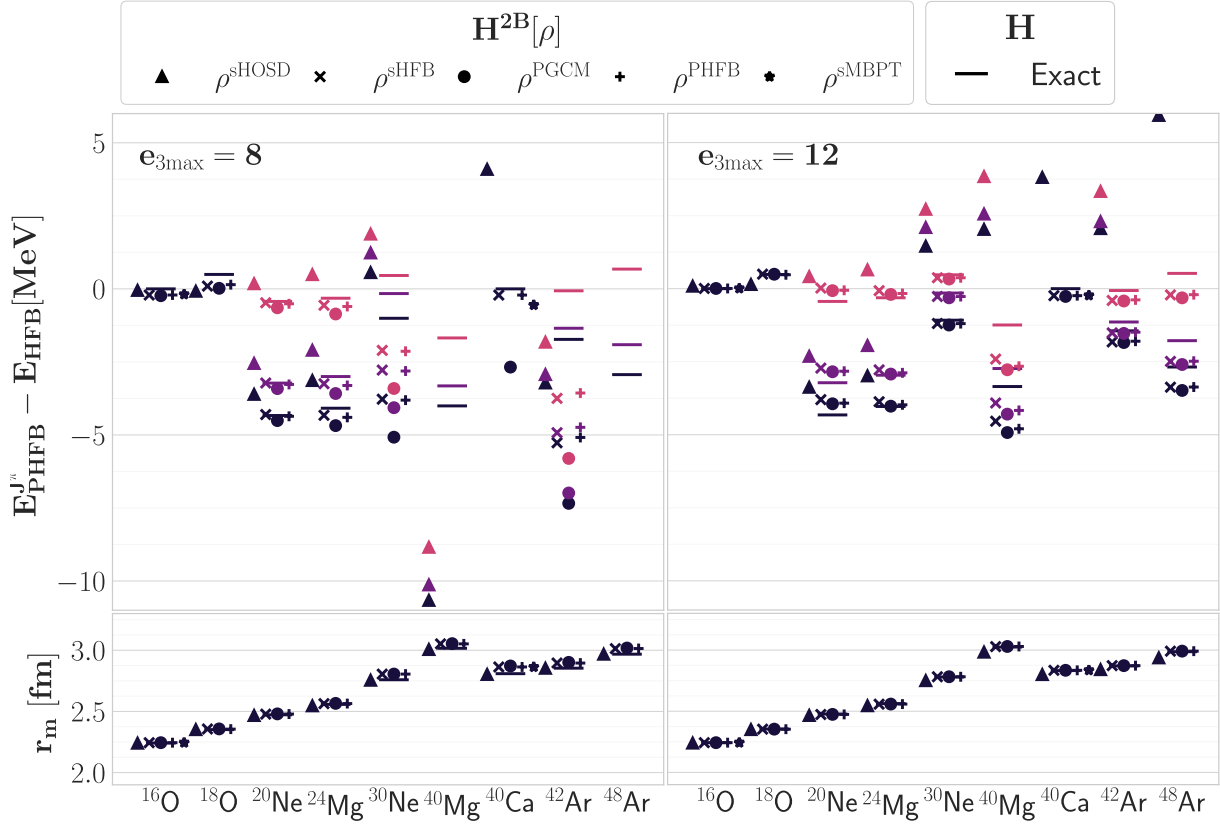


Figure 3.5. Results of PHFB calculations with H and $H^2B[\rho]$ for several test one-body density matrices ρ . Left and right panels display results obtained for $e_{3\text{max}} = 8$ and 12, respectively, at fixed $e_{\text{max}} = 8$. Upper panel: absolute energies of lowest $J^{\text{II}} = 0^+, 2^+, 4^+$ states to which the dHFB energy obtained from H in each nucleus is subtracted. Lower panel: ground-state root-mean-square matter radii. Calculations are performed with $\lambda_{\text{srg}} = 1.88 \text{ fm}^{-1}$.

	Closed-shell	Open shell	Mass ≤ 30	Mass > 30	Neutron-rich	All
ρ^{sHOSD}	0.67	1.36	0.62	1.68	2.34	1.09
$\rho^{\text{sHF(B)}}$	0.04	0.22	0.13	0.24	0.30	0.17
ρ^{PHFB}	0.04	0.22	0.10	0.27	0.34	0.17
ρ^{PGCM}	0.05	0.24	0.11	0.29	0.38	0.19
ρ^{sMBPT}	0.04					

Table 3.3. Average error (in %) on absolute PHFB energies of low-lying $J^\Pi = 0^+, 2^+, 4^+$ and 6^+ states for different sub-categories in the test panel and the various test one-body density matrices. Calculations are performed with $e_{3\text{max}} = 8$, $e_{3\text{max}} = 12$ and $\lambda_{\text{srg}} = 1.88 \text{ fm}^{-1}$. See Eq. (3.21b) for details on the cost function.

matrices, with the exception of $\rho = \rho^{\text{sHOSD}}$ for which a slight underestimation is visible in the heaviest systems.

Focusing on the right panels of Fig. 3.5, one does notice that the situation regarding the performance of the test one-body density matrices is qualitatively and quantitatively similar to the one encountered in dHFB and dBMBPT(3) calculations. As soon as the results are converged with respect to $e_{3\text{max}}$, PHFB energies and radii obtained with $H^{2B}[\rho]$ reproduce the reference results equally well with all employed one-body density matrices but ρ^{sHOSD} , i.e. it seems necessary (compared to ρ^{sHOSD}) and sufficient (compared to ρ^{PHFB} , ρ^{PGCM} and ρ^{sMBPT}) to employ a test one-body density matrix encoding the information of the spherical mean-field, i.e. $\rho^{\text{sHF(B)}}$.

The above analysis is put in more quantitative terms via the computation of systematic errors. The corresponding results are shown in Tab. 3.3. By construction, PHFB results are identical to sHF ones in doubly closed-shell nuclei given that the sole 0^+ ground-state has been considered for these nuclei and given that the projections on particular number and angular momentum are superfluous for a sHF state. In the other nuclei where the projections typically add few MeV of correlations energy to the ground state, the average error over $J^\Pi = 0^+, 2^+, 4^+, 6^+$ PHFB states is essentially the same as for dHFB ground-state energies, independently of the test one-body density matrix.

Dependence on e_{max}

Figure 3.6 probes the dependence of the results on the value of e_{max} at fixed $e_{3\text{max}}$. First, one notices that radii are insensitive to e_{max} and are perfectly reproduced. Second, no change is visible in the PHFB energies of ^{20}Ne when going from $e_{\text{max}} = 8$ to $e_{\text{max}} = 10$. In the more neutron-rich ^{30}Ne isotope, there exists a slight change of approximate PHFB energies. While the agreement with the reference results are still quantitatively good, the energies degrade slightly when going from $e_{\text{max}} = 8$ to $e_{\text{max}} = 10$. The slight evolution away from the reference results relates in fact to the lack of convergence of the results with respect to $e_{3\text{max}}$ discussed earlier. In the present case, $e_{3\text{max}}$ had to be set to 10 in order to be able to perform PHFB calculations with the explicit 3-body interaction at $e_{\text{max}} = 10$.

While pushing the calculations to large values of $e_{3\text{max}}$ would probably improve the agreement further, the overall conclusion is that the high quality of $H^{2B}[\rho]$ depends only mildly on e_{max} as long as the reference calculations themselves are converged enough. Although not shown, the same convergence behavior as a function of e_{max} is at play in the

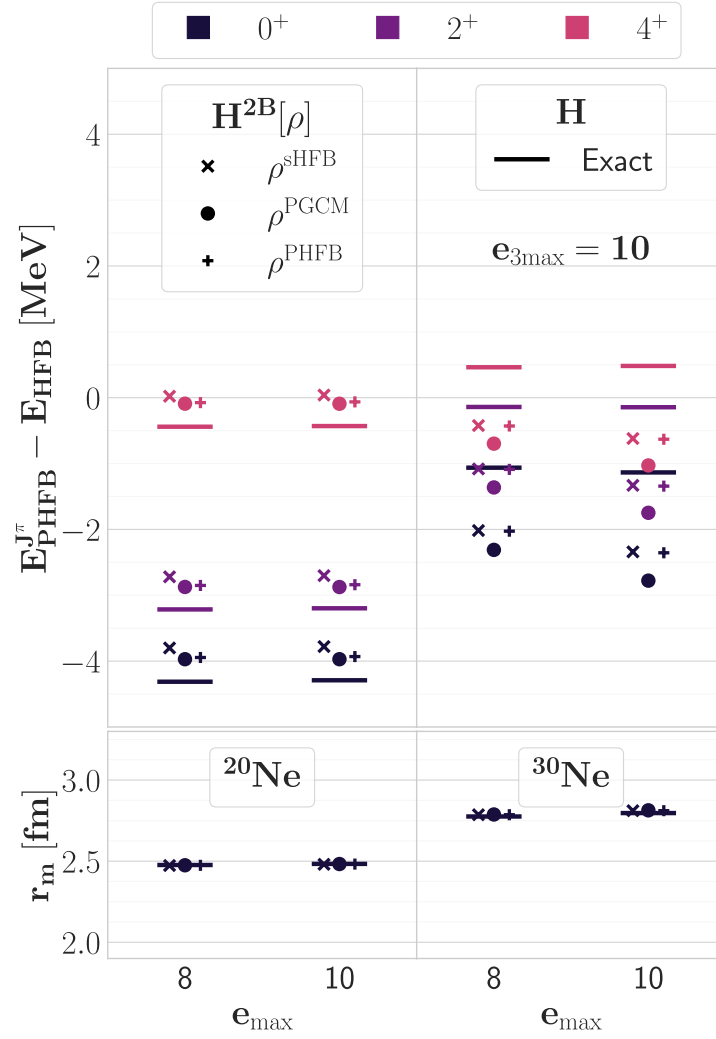


Figure 3.6. Same as Fig. 3.5 for ^{20}Ne (left) and ^{30}Ne (right) for $e_{\text{max}} = 8$ and 10 at fixed $e_{3\text{max}} = 10$.

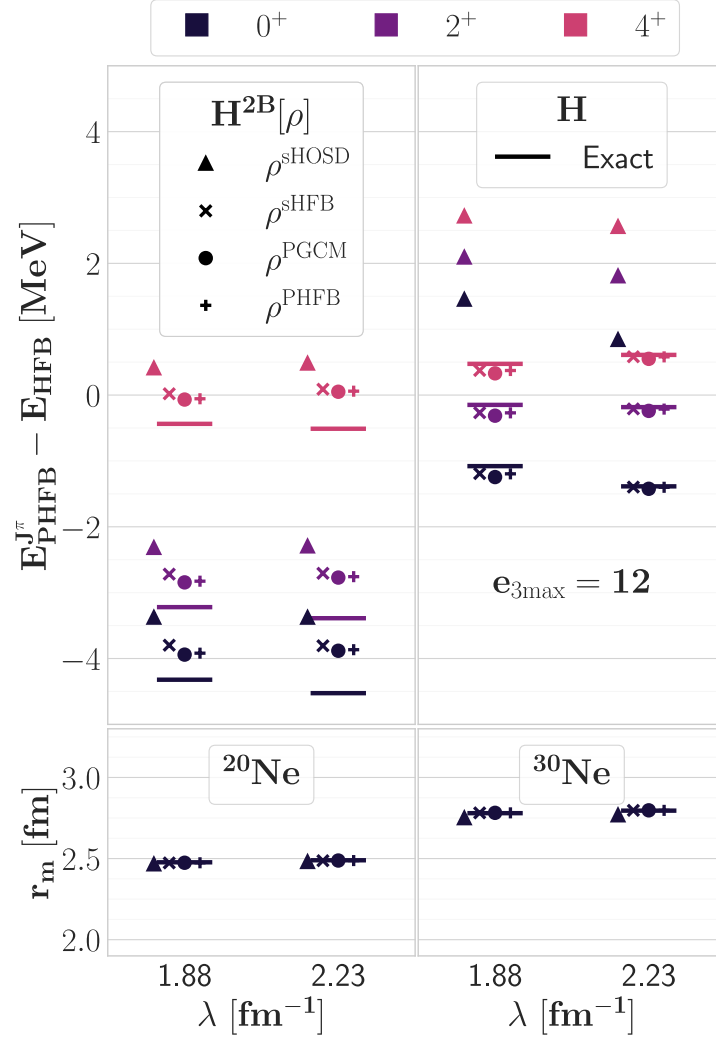


Figure 3.7. Same as Fig. 3.6 but for two values of the SRG parameter λ_{SRG} . Calculations are performed with $e_{\text{max}} = 8$ and $e_{3\text{max}} = 12$.

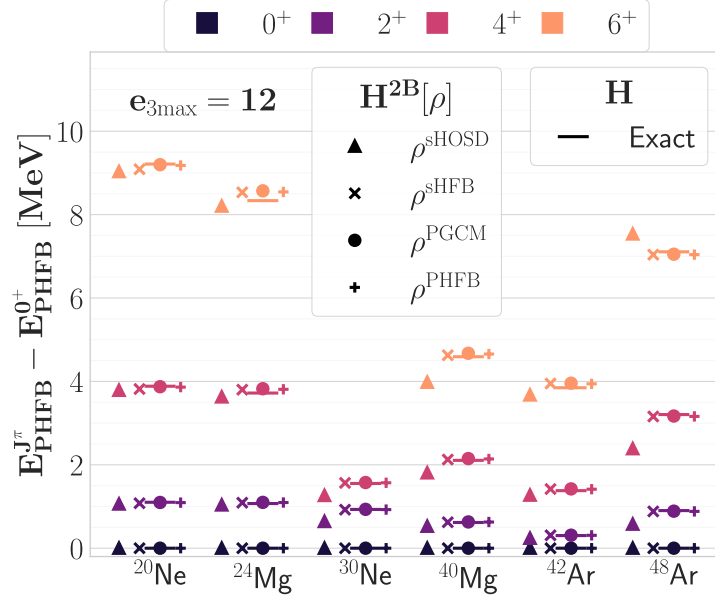


Figure 3.8. Low-lying PHFB excitation spectra of doubly open-shell nuclei. Reference results calculated from H are compared to those computed from $H^{2B}[\rho]$ using the various one-body test density matrices. Calculations are performed with $e_{\max} = 8$, $e_{3\max} = 12$ and $\lambda_{\text{srg}} = 1.88 \text{ fm}^{-1}$.

BMBPT(3) ground-state energies reported on in Sec. 3.4.4.

Dependence on λ_{srg}

Figure 3.7 probes the dependence of the results on the resolution scale of the Hamiltonian. The SRG Hamiltonian at $\lambda_{\text{srg}} = 2.23 \text{ fm}^{-1}$ is less evolved than the one at $\lambda_{\text{srg}} = 1.88 \text{ fm}^{-1}$ and produces spectra that are slightly less compressed. Still, no significant dependence on λ_{SRG} is observed as far as the quality of the results obtained with $H^{2B}[\rho]$ is concerned.

Although not shown, the same convergence behavior as a function of λ_{srg} is obtained in the BMBPT(3) ground-state energies reported in Sec. 3.4.4.

3.4.6. Spectroscopy

Having analyzed absolute PHFB energies and radii, we are now in the position to investigate spectroscopic observables.

PHFB

Low-lying PHFB excitation spectra of doubly open-shell nuclei computed from H and $H^{2B}[\rho]$ are compared in Fig. 3.8. Being based on the minimum of the dHFB TEC, these spectra describe the low-lying part of the ground-state rotational band.

Reference results are well reproduced for all one-body test densities except ρ^{sHOSD} for which a degrading arises with increasing mass. Even in nuclei for which absolute PHFB energies were not converged yet with respect to $e_{3\max}$ (e.g. ^{40}Mg and ^{20}Ne), energy differences are fully consistent with the reference values.

As for quantitative measures, systematic results are reported on in Tab. 3.4. Reference excitation energies are reproduced to better than 2% throughout the whole panel for

	Mass ≤ 30	Mass > 30	Neutron-rich	Total
ρ^{sHOSD}	5.86	15.38	16.79	10.62
$\rho^{\text{sHF(B)}}$	1.47	1.56	0.91	1.51
ρ^{PHFB}	1.17	1.68	1.11	1.43
ρ^{PGCM}	1.27	1.90	1.22	1.51

Table 3.4. Average error (in %) on PHFB low-lying excitation energies computed from $H^{2B}[\rho]$ for various sub-categories of nuclei and test one-body density matrices. See Eq. (3.22) for details on the cost function. Calculations are performed with $e_{\text{max}} = 8$, $e_{3\text{max}} = 12$ and $\lambda_{\text{srg}} = 1.88 \text{ fm}^{-1}$.

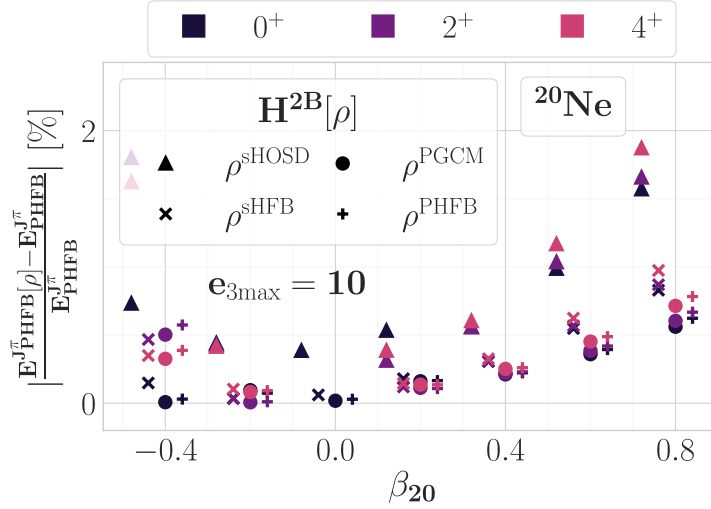


Figure 3.9. Same as the bottom panel of Fig. 3.2 for $J^\Pi = 0^+, 2^+, 4^+$ PHFB states.

$\rho^{\text{sHF(B)}}$, ρ^{PHFB} and ρ^{PGCM} , which amounts to making errors of the order of a few tens of keVs. This is obviously negligible compared to other sources of uncertainties in state-of-the-art ab initio calculations. While this outcome further demonstrates the robustness of the approximation method, the 10% average error obtained for ρ^{sHOSD} underlines the fact that the employed one-body density matrix must be realistic enough to deliver high accuracy results. Given that the purpose of ab initio PHFB (and PGCM below) calculations is to access excitation energies and not absolute ones, one can be fully satisfied with the performances of $H^{2B}[\rho]$ in the present context.

PGCM

While PHFB calculations already provide a good test whenever the system is *rigid* with respect to collective variables, the PGCM opens the way to the wider class of so-called *soft* nuclei. More generally, it allows us to include static correlations induced by shape fluctuations and to access associated vibrational excitations.

Here, PGCM calculations of ^{20}Ne and ^{30}Ne along the axial quadrupole coordinate are performed. In order to obtain a first indication of the performance of $H^{2B}[\rho]$, Fig. 3.9 extends the study performed at the dHFB level in Sec. 3.4.4 by displaying the error obtained for the TEC of $J^\Pi = 0^+, 2^+, 4^+$ PHFB energies for the various test one-body density matrices. The J^Π projected TEC constitutes the diagonal part of the Hamiltonian

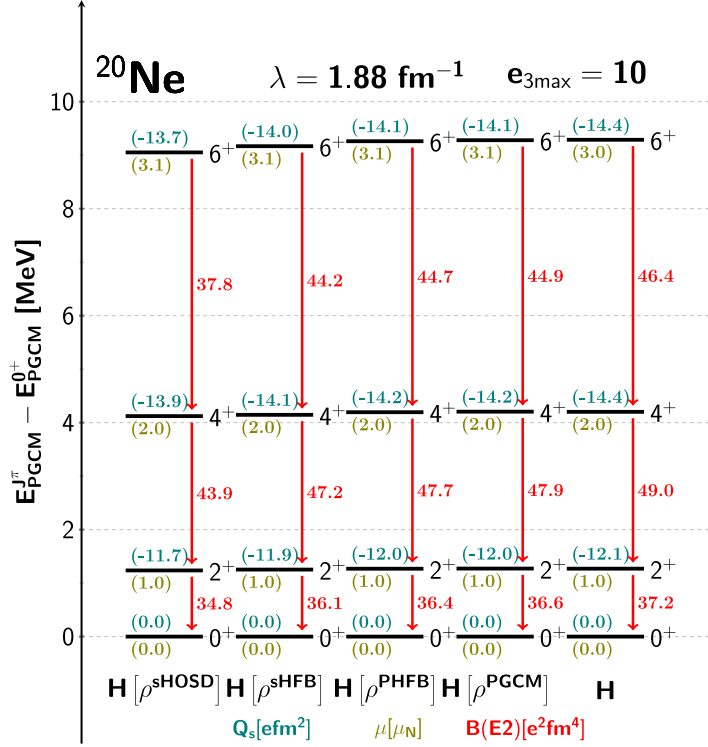


Figure 3.10. Low-lying part of the PGCM ground-state rotational band of ^{20}Ne . Reference results calculated from H are compared to those computed from $H^{2B}[\rho]$ using various test one-body density matrices. Each energy level is displayed along with the magnetic dipole (below) and electric quadrupole (above) moments of the associated state. $B(E2)$ transitions strengths are displayed using red arrows. Calculations are performed with $e_{\text{max}} = 8$, $e_{3\text{max}} = 10$ and $\lambda_{\text{srg}} = 1.88 \text{ fm}^{-1}$.

matrix in the Hill-Wheeler-Griffin secular equation of the PGCM calculation. The errors obtained along the projected TECs are strictly similar to those displayed in Fig. 3.2 at the dHFB level. This result gives confidence regarding the quality of the results that can be expected at the PGCM level.

Reference and approximate low-lying PGCM excitation energies of the ground-state rotational band and associated electromagnetic observables are compared for ^{20}Ne and ^{30}Ne in Figs. 3.10 and 3.11, respectively. Due to numerical limitations, only three-body matrix elements up to $e_{3\text{max}} = 10$ could be included in the full calculation, hence hindering the convergence in ^{30}Ne . Still, building on the results reported in Fig. 3.9 an excellent agreement emerges in both nuclei for PGCM energies and electromagnetic observables, even more so in ^{20}Ne where sub-percent accuracy (see Tab. 3.5) is achieved. As before, a decent but less optimal reproduction of the reference results is obtained for $\rho = \rho^{\text{sHOSD}}$. The excellent results obtained for electromagnetic observables testify to the stability of the PGCM wave-functions themselves with respect to the in-medium approximation of the three-nucleon interaction.

dQRPA

QRPA is a method of choice to study excited states of both single- or few-particle and collective characters, with energies ranging from a few MeV to tens of MeV. In this context, the performance of $H^{2B}[\rho]$ can be assessed by looking at, e.g., electromagnetic

Nucleus	^{20}Ne		^{30}Ne	
Quantity	Spectrum	Observables	Spectrum	Observables
ρ^{sHOSD}	2.95	1.43	4.53	2.85
$\rho^{\text{sHF(B)}}$	1.46	0.71	2.60	2.57
ρ^{PHFB}	0.36	0.55	2.59	
ρ^{PGCM}	0.26	0.48	2.98	2.85

Table 3.5. Average error (in %) on PGCM excitation energies and spectroscopic observables computed from $H^{2B}[\rho]$ in ^{20}Ne and ^{30}Ne for various test one-body density matrices. See Eq. (3.21d) for details on the cost function. Calculations are performed with $e_{\text{max}} = 8$, $e_{3\text{max}} = 10$ and $\lambda_{\text{srg}} = 1.88 \text{ fm}^{-1}$.

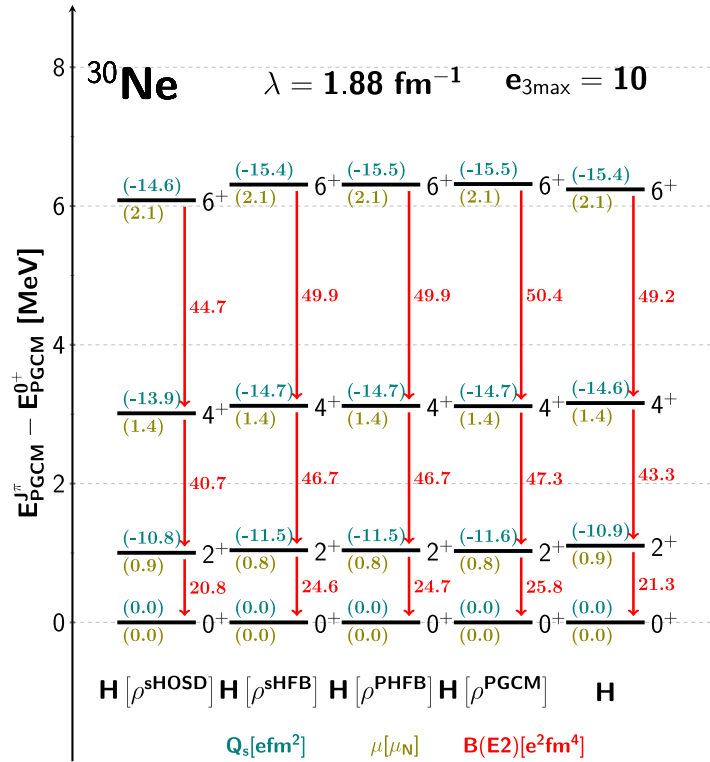


Figure 3.11. Same as Fig. 3.10 for ^{30}Ne .

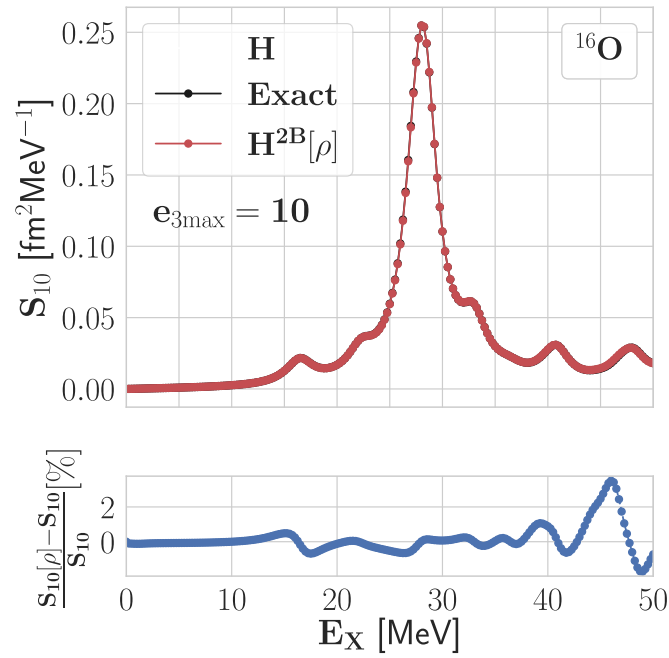


Figure 3.12. Electric isovector dipole strength of ^{16}O as a function of the excitation energy (upper panel). Reference results calculated from H are compared to those computed from $H^{2B}[\rho]$ using ρ^{sHFB} . The relative deviation from the strength computed with the exact Hamiltonian is displayed as a function of the excitation energy in the lower panel. Calculations are performed with $e_{\text{max}} = 8$, $e_{3\text{max}} = 10$ and $\lambda_{\text{srg}} = 1.88 \text{ fm}^{-1}$.

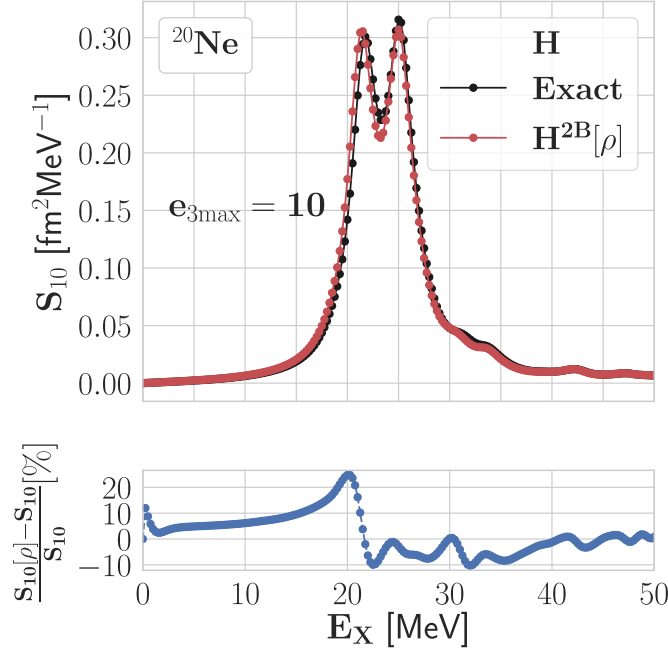


Figure 3.13. Same as Fig. 3.12 for ^{20}Ne .

strength functions. Figures 3.12 and 3.13 display the electric isovector dipole ($E1$) strength computed with both H and $H^{2B}[\rho^{\text{sHFB}}]$, for ^{16}O and ^{20}Ne respectively. Similar results are obtained for the other test one-body density matrices and are reported in Table 3.6.

In ^{16}O , where dQRPA reduces to sRPA built on top of a sHF Slater determinant, the difference between the strength functions are hardly noticeable. As in sHF calculations discussed earlier on, this relates to the fact that the sRPA error would actually be strictly zero if the ρ entering $H^{2B}[\rho]$ were taken as the *variational* sHF density matrix obtained from that approximate Hamiltonian. Because the ρ^{sHF} coming from the calculation performed with H slightly differs from the variational one obtained from $H^{2B}[\rho^{\text{sHF}}]$, the error is not strictly zero but remains tiny. As seen from the bottom panel of Fig. 3.12 the relative error of the $E1$ strength at each excitation energy does not exceed 4% over the interval $[0, 50]$ MeV. This error essentially relates to the horizontal position of the individual dQRPA modes that, as seen in Tab. 3.6, are shifted by a tiny amount, i.e. 0.05% on average. This relates to the fact that approximating H by $H^{2B}[\rho]$ slightly affects dHFB quasi-particle energies, inducing in turn a small shift (1% on average) in the position of the dQRPA eigenmodes. Computing the observable total photo-emission cross section by integrating the differential photo-emission cross section deduced from the $E1$ strength, the error on the latter generates a tiny 0.02% error. While the error remains very small for the other test one-body density matrices, the choice $\rho = \rho^{\text{sHFB}}$ is optimal in the present case.

Moving to Fig. 3.13, the dQRPA dipole strength of ^{20}Ne obtained from $H^{2B}[\rho^{\text{sHFB}}]$ at the minimum of the dHFB TEC is also visually very close to the reference one, although slightly deteriorated compared to the ^{16}O case. Looking at the bottom panel, the situation suddenly appears less favorable with a relative error at fixed excitation energies that can reach nearly 30% on the left side of the giant resonance. This error results from a more substantial shift in quasi-particle energies. The steep slope of the $E1$ strength function before and after the giant resonance exacerbates the relative error made at fixed excitation

Nucleus	¹⁶ O		²⁰ Ne	
Quantity	Excitation energy	Total photo-emission cross section	Excitation energy	Total photo-e
ρ^{sHOSD}	0.39	0.04	0.46	
$\rho^{\text{sHF(B)}}$	0.05	0.02	1.09	
ρ^{PHFB}	0.14	0.23	1.13	
ρ^{PGCM}	0.15	0.24	1.19	

Table 3.6. Average relative error (in %) on dQRPA excitation energies and on the total photo-emission cross section computed from $H^{2B}[\rho]$ in ¹⁶O and ²⁰Ne for various test one-body density matrices. Calculations are performed with $e_{\text{max}} = 8$, $e_{3\text{max}} = 10$ and $\lambda_{\text{srg}} = 1.88 \text{ fm}^{-1}$.

energies. However, propagated to the total photo-emission cross section, this only results in a negligible error of 0.63% (see Tab. 3.6). In this case, the optimal character of $\rho = \rho^{\text{sHF(B)}}$ is not apparent as all test one-body density matrices deliver similar results.

The above results validates the quality and robustness of $H^{2B}[\rho]$ in the dQRPA context. Although not shown for brevity, essentially identical results hold for one-body transition operators with other multipolarities. Furthermore, the dependence of the results on $e_{3\text{max}}$ is along the same line as the one discussed in Sec. 3.4.5.

3.4.7. Optimal one-body density matrix

The in-medium approximation of three-body interactions proposed in the present work appears to be very robust with respect to the employed symmetry-invariant one-body density matrix. All dHFB, dBMBPT, PHFB PGCM and dQRPA results presented above are of equally excellent quality for $\rho = \rho^{\text{sHF(B)}}$, ρ^{PHFB} and ρ^{PGCM} but systematically deteriorate for the more simplistic choice $\rho = \rho^{\text{sHOSD}}$.

In this context, it is of interest to better assess this robustness and possibly characterize the optimal one-body density matrix to be used in the design of $H^{2B}[\rho]$. For this purpose, trial (symmetry-invariant) one-body density matrices $\{\rho^{\text{sRd}}\}$ are generated by means of the random sampling described in App. H. To evaluate the corresponding approximation $H^{2B}[\rho^{\text{sRd}}]$, the ground-state energy error

$$\Delta E_{\Psi}^{2B}[\rho] \equiv \frac{\langle \Psi | H^{2B}[\rho] | \Psi \rangle}{\langle \Psi | \Psi \rangle} - \frac{\langle \Psi | H | \Psi \rangle}{\langle \Psi | \Psi \rangle} \quad (3.23)$$

is considered; see App. H.1 for the working expression and a related discussion. The error function $\Delta E_{\Psi}^{2B}[\rho^{\text{sRd}}]$ computed for a large set of randomly generated matrices is shown in Fig. 3.14 as a function of the distance $\|\rho^{\text{sRd}} - \rho^{\Psi}\|$ between the trial one-body density matrix and the ground-state one ρ^{Ψ} in the many-body calculation of interest. The data points corresponding to the physical one-body density matrices (ρ^{sHOSD} , $\rho^{\text{sHF(B)}}$, ρ^{PHFB} and ρ^{PGCM}) are also displayed to better make sense of the results obtained so far. In addition to the distance to ρ^{Ψ} , each trial one-body density matrix is characterized by its von Neumann entropy

$$S[\rho] \equiv -\text{Tr}(\rho \ln \rho) , \quad (3.24)$$

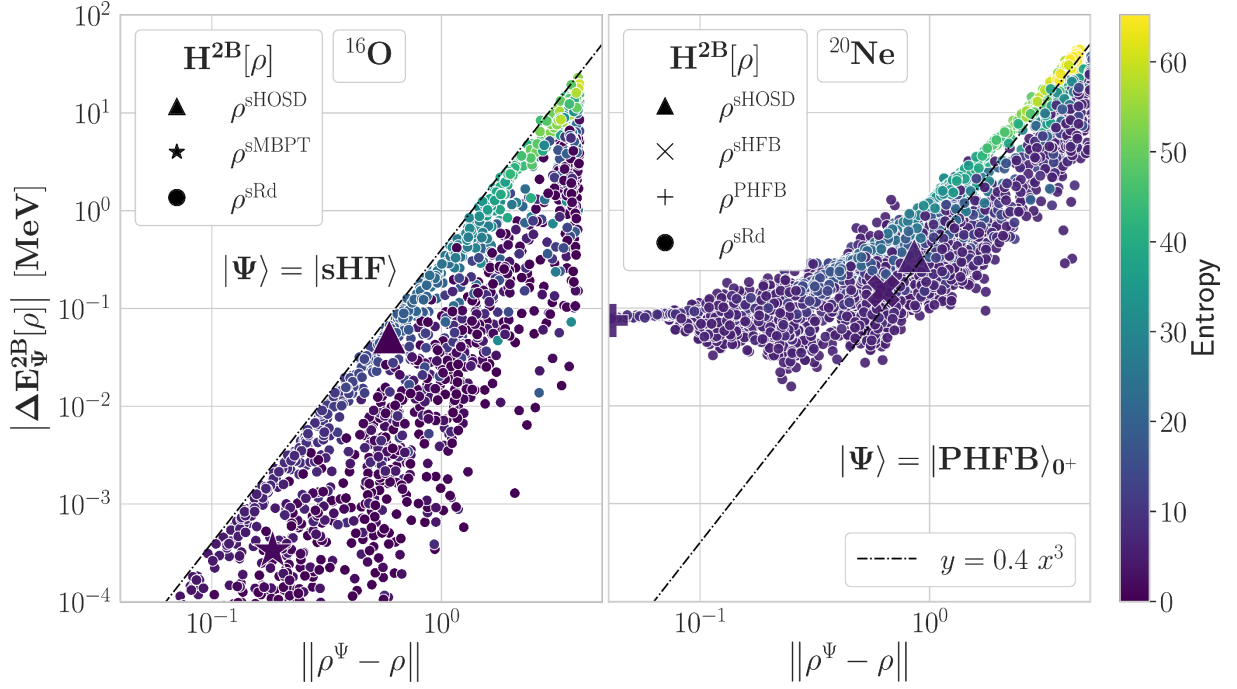


Figure 3.14. Ground-state energy error $\Delta E_{\Psi}^{2B}[\rho]$ associated with the use of $H^{2B}[\rho]$ as a function of the distance $\|\rho - \rho^{\Psi}\|$ between the test one-body density matrix ρ and the actual ground-state one ρ^{Ψ} in log-log scale. Left panel: sHF ($J^{\Pi} = 0^{+}$) solution for ^{16}O . Right panel: PHFB ($J^{\Pi} = 0^{+}$) solution for ^{20}Ne . Data points are for physical and randomly-sampled test one-body density matrices. For the latter, the color scale characterizes their von Neumann entropy. The dashed-dotted lines denote the cubic envelop extracted from the left panel and reported on the right panel. Calculations are performed for $e_{\text{max}} = 6$ and $e_{3\text{max}} = 6$.

which, in the eigenbasis of ρ with eigenvalues $\{r_a\}$ reads as Shannon's entropy of information theory

$$S[\rho] \equiv - \sum_a r_a \ln r_a. \quad (3.25)$$

In the present context, the size of the entropy essentially characterizes how much the many-body state ρ differs from a Slater determinant for which $S[\rho] = 0$, i.e. it is a measure of many-body correlations.

Results for ^{16}O computed in a small model space at the sHF level are shown in the left panel of Fig. 3.14 while the right panel displays results for ^{20}Ne computed at the PHFB level. The sHF calculation of ^{16}O illustrates the situation encountered for an uncorrelated state, i.e. the many-body solution $|\Psi\rangle$ is nothing but a symmetry-conserving Slater determinant. In this particular case, the ground-state energy error (see Eq. (H.2)) takes the simple form

$$\Delta E_{\text{sHF}}^{2B}[\rho] = \frac{1}{3!} w^{(3)} \cdot (\rho - \rho^{\text{sHF}})^{\otimes(3)} \quad (3.26)$$

and is thus minimal, actually zero, for $\rho = \rho^{\text{sHF}}$. The fact that the optimal one-body density matrix is nothing but the one of the many-body state under scrutiny is confirmed numerically in the left panel of Fig. 3.14. In absence of genuine correlations, one expects from Eq. (3.26) that the sampled errors are bounded by a cubic envelope in the variable $\|\rho - \rho^{\text{sHF}}\|$, which indeed appears clearly in the numerical results. The coefficient (0.4) of that cubic envelope extracted from the data is a measure of the employed three-body interaction strength in the utilized model space.

Besides the null error delivered by $\rho = \rho^{\text{sHF}}$, the errors associated with the physical one-body density matrices ρ^{sHOSD} and ρ^{sMBPT} are provided on the figure. Compared to the full range of sampled one-body density matrices²⁴ ρ^{sHOSD} and ρ^{sMBPT} are rather close to ρ^{sHF} . This is particularly true of ρ^{sMBPT} , which is a sign of the weakly-correlated character of ^{16}O when eventually going beyond the mean-field on the basis of an SRG-evolved Hamiltonian. Given the cubic upper-bound, such a proximity between the two density matrices implies a tiny error on the energy obtained for $\rho = \rho^{\text{sMBPT}}$. Despite originating from a Slater determinant and thus sharing the same null entropy as ρ^{sHF} , ρ^{sHOSD} is about 3 times more distant from it than ρ^{sMBPT} . In agreement with the cubic law governing the error, plus being located closer to the envelope, the associated error is about 170 times larger. Given the softness of the employed three-body interaction, ρ^{sHOSD} still provides a small absolute error in the end. Eventually, the sampling provides a fair understanding that, as long as the test one-body density is not too distant from ρ^{sHF} , its detailed properties do not matter much and the error is bound to be small.

Compared to the previous case, the right panel of Fig. 3.14 allows one to appreciate the qualitatively different situation encountered for a genuinely-correlated state. Indeed, the error $\Delta E_{\text{PHFB}}^{2B}[\rho]$ behaves now differently as a function of the distance²⁵ $\|\rho - \rho^{\text{PHFB}}\|$. As visible from Eq. (H.2), $\Delta E_{\text{PHFB}}^{2B}[\rho]$ contains non-zero constant and linear terms in addition to the cubic term encountered in Eq. (3.26).

²⁴Given that ρ^{sHF} relates to a Slater determinant with 16 particles, the maximum distance is reached for densities associated with Slater determinants obtained by promoting the 16 particles from hole states into particle states, i.e. $\text{Max}_\rho \|\rho - \rho^{\text{sHF}}\| = \sqrt{32} \approx 5.7$, which is indeed the maximum value visible on the left panel of Fig. 3.14.

²⁵Because of the log-log scale employed, the point at zero distance associated with ρ^{PHFB} is artificially placed on the left border of the figure.

The constant term yields the error $\Delta E_{\text{PHFB}}^{2B}[\rho^{\text{PHFB}}]$ associated with the actual ground-state density, i.e. when setting $\rho = \rho^{\text{PHFB}}$. The fact that this error is nonzero is a fingerprint of the fact the PHFB ground-state wave-function carries (at least) genuine three-body correlations. The value of the corresponding error additionally depends on the size of the three-body interaction convolved with the irreducible three-body density matrix (see Eq. (H.2)). As analyzed in Ref. [90] in connection with the NO2B approximation, a low-resolution Hamiltonian makes the energy contribution from the residual three-body interaction small. For $(e_{\text{max}} = 6; e_{3\text{max}} = 6)$ this error is $\Delta E_{\text{PHFB}}^{2B}[\rho^{\text{PHFB}}] \approx 0.1 \text{ MeV}$ whereas the better converged value obtained earlier on for $(e_{\text{max}} = 8; e_{3\text{max}} = 12)$ is 0.5 MeV (0.4%); i.e. the error is small.

Increasing the distance from $\rho = \rho^{\text{PHFB}}$, one can lower the error such that a minimum $\text{Min}_{\rho} \Delta E_{\text{PHFB}}^{2B}[\rho]$ is found for $\|\rho - \rho^{\text{PHFB}}\| = \text{few } 10^{-1}$ with a value several times smaller than $\Delta E_{\text{PHFB}}^{2B}[\rho^{\text{PHFB}}]$. Past the minimum the error typically increases and is eventually dominated by the cubic terms at large distances such that the cubic envelope extracted from the left panel becomes visible.

The physical density matrices ρ^{sHOSD} and ρ^{sHFB} are found right past the minimum such that their error is small and in fact similar to the one found at the origin. The profile of the error as a function of the distance $\|\rho - \rho^{\text{PHFB}}\|$ rationalizes the fact that small errors can be found over a substantial range of density matrices to which the various physical one-body density matrices one may typically access all belong. This feature provides practitioners with a significant flexibility as far as the choice of the employed one-body density matrix is concerned. Beyond that appropriate interval the error rapidly increases with the distance, as testified by the use of ρ^{sHOSD} sitting on the edge of it, such that one may not be too cavalier either regarding the choice of ρ .

3.5. Discussion

Main lessons

The above results demonstrate the usefulness of the proposed in-medium reduction method for three-body interaction operators in nuclear ab initio calculations. The fact that the method relies on the sole use of a one-body density matrix gives much credit to the *simplicity* of the method. Furthermore, the high-quality approximation was shown to be robust with respect to the employed one-body density matrix, which gives much credit to the *flexibility* of the method.

These conclusions have been validated for nuclei with closed and open-shell characters, i.e. displaying weak and strong correlations, for a large class of observables in light and mid-mass systems as well as for stable and exotic isotopes. While convincingly substantiated via the use of both perturbative and non-perturbative many-body methods, a further validation of the quality of the approximation on the basis of (non-perturbative) ab initio methods built on different paradigms is desirable in the future.

Algorithm

The independence of the results with respect to a large class of one-body density matrices is of key importance for practical applications in the future, especially given that ab initio calculations aspire to move up the nuclear chart towards heavy, doubly open-shell nuclei. Specifically, the high-quality results obtained for $\rho = \rho^{\text{sHFB}}$ allow one to build $H^{2B}[\rho]$ at

the sole cost of running first a spherical HFB calculation with full three-body forces, thus bypassing the need to run any deformed HFB code followed by projections, which would already be too costly with explicit three-body forces in heavy nuclei requiring large values of $e_{3\max}$. Eventually, the envisioned working algorithm is

1. run a spherical HFB calculation with three-nucleon forces to extract ρ^{sHFB} ,
2. build $H^{2B}[\rho^{\text{sHFB}}]$,
3. run the many-body method of interest with the two-body Hamiltonian $H^{2B}[\rho^{\text{sHFB}}]$,

such that even in (heavy) open-shell nuclei

- no two-body density matrix has to be extracted,
- no genuine open-shell calculation with an explicit three-nucleon operator has to be performed.

Odd-even and odd-odd nuclei

While the method presented in this article relies on the use of symmetry-invariant one-body densities, which can be generated only starting from $J^\Pi = 0^+$ states (or a superposition of such states), it can also be easily used to construct effective k -body interactions for odd-even and odd-odd nuclei. For this purpose, one can employ the one-body density generated in a mean-field calculation of a spherical Bogoliubov vacuum constrained to have odd-even or odd-odd numbers of particles on average. In the case of odd-even systems, it was demonstrated in Ref. [83] that such a vacuum represents a good approximation to the true mean-field solution obtained with an odd number parity wave function.

Of course, the accuracy of the k -body interactions constructed in this way will have to be properly checked but there is no reason to believe that they would perform particularly worse than those generated to describe even-even nuclei.

Conclusion

The present chapter introduced a novel method to approximate n -body operators in terms of k -body ones with $k < n$. This is highly pertinent to overcome the steep increase of the computational cost of many-body calculations due to the presence of three-nucleon interactions, especially as ab initio calculations aspire to move to heavier nuclei than presently possible.

The main advantages are that the method is accurate, universal, simple and flexible. The universality of the method not only relates to its applicability to all nuclei, independently of their closed or open-shell character, but also to its independence with respect to the many-body method eventually used to solve Schrödinger's equation. The simplicity of the method relates to the fact that it requires the convolution of the, e.g., three-body operator with a sole symmetry-invariant one-body density matrix, even in open-shell nuclei. This is at variance with existing methods that either convolve the three-body operator with one-, two- and three-body density matrices in open-shell systems or with a symmetry-breaking one-body density matrix, thus leading to an approximate operator that explicitly breaks symmetries of the initial Hamiltonian. Eventually, the flexibility of the method relates to the possibility to use various one-body density matrices as an entry. As a matter of fact, the functional form of the error due to the use of the approximate Hamiltonian could

be exploited to explain why accurate results can be obtained for a rather large class of one-body density matrices. Such a flexibility can be exploited to use a (not too) simple density matrix in practical calculations, e.g. the density matrix extracted from a spherical Hartree-Fock-Bogoliubov calculation.

Further perspectives

Extensive numerical results have demonstrated the high accuracy of the approach over a wide range of nuclei and observables. The approximation method is thus ready to be employed in routine ab initio calculations in the future. Furthermore, the in-medium reduction procedure is ready to be tested on four-nucleon interactions [114, 115, 116] and/or three-body nuclear currents [117] in order to deal with them at a reduced computational cost.

Chapter 4.

Results: PGCM

Contents

4.1. Introduction	77
4.2. Many-body calculations	78
4.2.1. Nuclear Hamiltonian	78
4.2.2. PGCM	79
4.2.3. IM-NCSM	82
4.3. Results	83
4.3.1. Model-space convergence	83
4.3.2. ^{20}Ne	86
4.3.3. Isotopic chain	93
4.4. Discussion	104

Using the novel PGCM-PT many-body formalism developed in Chapter 2 and the rank-reduction method of the Hamiltonian formulated and tested in Chapter 3, the present chapter discusses a systematic study of neon isotopes at leading order in PGCM-PT, i.e. at the PGCM level.

4.1. Introduction

The projected generator coordinate method (PGCM) based on the mixing of Bogoliubov vacua generated by solving constrained Hartree-Fock-Bogoliubov (HFB) mean-field equations has been traditionally employed with empirical effective interactions [6, 118, 119]. In spite of being ill-defined and affected by potentially dangerous spurious contaminations [120, 121, 122, 123] in this particular context, such PGCM calculations have been successfully applied to describe numerous nuclear phenomena over the last few decades.

The PGCM has also been employed in the context of so-called valence-space calculations based on appropriate effective interactions [124, 125, 126] (although less often). Employing sophisticated realizations of the PGCM ansatz, solutions obtained from an exact diagonalization for pf-shell Ca isotopes [127] or the complete set of sd-shell nuclei [128] have recently been shown to be accurately reproduced. These works demonstrate the capacity of the PGCM to efficiently capture strong *static* correlations emerging within a small energy window around the Fermi energy.

In the present chapter, the objective is to employ the PGCM for *ab initio* calculations. PGCM calculations have already been performed on the basis of realistic Hamiltonians

that were pre-processed via unitary similarity renormalization group (SRG) transformations [100] (see Chapter 3) and possibly further pre-processed via unitary IMSRG transformations [93, 104]. However, and independently of the pre-processing of the Hamiltonian¹, the PGCM is not amenable to an exact solution of A -body Schrödinger's equation. Indeed, while very efficient at grasping strong static (collective) correlations, the PGCM is not suited to capture weak, so-called dynamical, correlations². Through the novel formulation of a multi-reference perturbation theory (PGCM-PT) formalism in Chapter 2, the PGCM is embedded, for the first time, into a genuine *ab initio* expansion method capable of grasping dynamical correlations in a systematic fashion.

While the PGCM-PT formalism was explained in detail in Chapter 2, the present chapter discusses numerical results obtained through its leading order, i.e. PGCM, reduction. Specifically focusing on even-even neon isotopes, the objectives are to

1. benchmark PGCM calculations against quasi-exact results obtained via the so-called in-medium no core shell model (IM-NCSM),
2. deliver *ab initio* predictions of spectroscopic properties of even-even Ne isotopes,
3. gauge uncertainties and convergence of the many-body results associated with the order-by-order chiral effective field theory (χ EFT) expansion of the Hamiltonian.

Based on the above results, the following chapter, i.e. Chapter 5, will present the first PGCM-PT calculations beyond zeroth order and characterize the way absolute and relative PGCM energies are amended by the inclusion of dynamical correlations.

This chapter is organized as follows. All the ingredients of the calculations (Hamiltonians, many-body formalisms, numerical settings, uncertainty evaluations) are detailed in Sec. 4.2 whereas a large body of results is presented in Sec. 4.3. A discussion is then provided in Sec. 4.4.

4.2. Many-body calculations

4.2.1. Nuclear Hamiltonian

The present calculations employ the family of χ EFT Hamiltonians H introduced in Ref. [130] and constructed at next-to-leading (NLO), next-to-next-to-leading (N²LO) and next-to-next-to-next-to-leading (N³LO) orders according to Weinberg's power counting [8, 131, 132]. Consistent non-local regulators and cut-off values ($\Lambda = 500$ MeV) are employed

¹IMSRG transformations pre-process the Hamiltonian in order to decouple as much as possible a given many-body state from the rest of the Hilbert space [129]. The decoupling can in principle, i.e. in absence of any approximation, be exact whenever the many-body state is a single *product* state, which thus becomes an exact eigenstate of the transformed Hamiltonian at the end of the process. Contrarily, the decoupling is typically not exact, even in the absence of any approximation, whenever the many-body state is more general, e.g. when it is a PGCM state. Consequently, while the IMSRG constitutes per se a method to solve Schrödinger's equation when the so-called single-reference (SR-IMSRG) [57] implementation can be applied, it is not the case for the more versatile multi-reference (MR-IMSRG) [34] approach that can only be seen as a pre-processing of the Hamiltonian on top of which an appropriate many-body method must be applied. This point is further discussed and illustrated in Chapter 5.

²Dynamical correlations are essentially accounted for, at least in principle, through the effective Hamiltonian in valence space calculations. This is the reason why PGCM can well reproduce exact solutions in this particular context. See Sec. 4.3.3 for an illustration of this feature.

in the two-nucleon and three-nucleon sectors; see Ref. [130] for the details of the fitting protocol. This family of interactions was shown to robustly reproduce selected experimental energies and radii from p-shell nuclei to nickel isotopes and to resolve several deficiencies of the previous generations of χ EFT Hamiltonians.

The values of the SRG scale λ_{srg} employed in the many-body calculations presented below are specified later on.

4.2.2. PGCM

The PGCM formalism presently employed has been described in Chapter 2 and the reader is referred to it for technical details.

Choice of collective coordinates

The PGCM state $|\Theta_\mu^{\tilde{\sigma}M}\rangle$ mixes a set of Bogoliubov states $B_q \equiv \{|\Phi(q)\rangle; q \in \text{set}\}$ differing by the value of the (typically multi-dimensional) collective deformation parameter q that are obtained by solving constrained Hartree-Fock-Bogoliubov equations. As an intermediate step, the calculation thus delivers a HFB total energy surface (TES) as a function of q .

Typically, q presently collects quadrupole ($q_{2\mu}$) and axial octupole (q_{30}) moments, i.e.

$$Q_{\lambda\mu} \equiv r^\lambda Y_\mu^\lambda(\theta, \varphi), \quad (4.1a)$$

$$q_{\lambda\mu} \equiv \frac{1}{2} \langle \Phi(q) | Q_{\lambda\mu} + (-1)^\mu Q_{\lambda-\mu} | \Phi(q) \rangle, \quad (4.1b)$$

where $Y_\mu^\lambda(\theta, \varphi)$ is a spherical harmonic of degree λ and order μ , such that

$$q_{20} \equiv \langle \Phi(q) | Q_{20} | \Phi(q) \rangle, \quad (4.2a)$$

$$q_{21} \equiv \frac{1}{2} \langle \Phi(q) | Q_{21} - Q_{2-1} | \Phi(q) \rangle, \quad (4.2b)$$

$$q_{22} \equiv \frac{1}{2} \langle \Phi(q) | Q_{22} + Q_{2-2} | \Phi(q) \rangle, \quad (4.2c)$$

$$q_{30} \equiv \langle \Phi(q) | Q_{30} | \Phi(q) \rangle. \quad (4.2d)$$

In the present calculations, q_{10} and q_{11} are set to zero to avoid the spurious motion of the nucleus' center of mass. Similarly, q_{21} is set to zero to fix the orientation of the nucleus. From the moments, one introduces deformation parameters according to

$$\beta_2 \equiv \frac{4\pi}{(3R^2A)} \sqrt{q_{20}^2 + 2q_{22}^2}, \quad (4.3a)$$

$$\gamma_2 \equiv \arctan \left(\frac{\sqrt{2}q_{22}}{q_{20}} \right), \quad (4.3b)$$

$$\beta_3 \equiv \frac{4\pi}{(3R^3A)} q_{30}, \quad (4.3c)$$

with $R \equiv 1.2A^{1/3}$ and $A \equiv N + Z$ the mass number. Whenever the deformation is purely axial, β_2 reduces to the traditional axial quadrupole deformation parameter.

Each state $|\Phi(q)\rangle$ is further projected, whenever necessary, onto good symmetry quantum numbers $\sigma \equiv (\text{JMIINZ}) \equiv (\tilde{\sigma}M)$ [97], i.e. onto total angular momentum J and projection M , parity $\Pi = \pm 1$ as well as neutron N and proton Z numbers. This procedure generates

a set of projected Bogoliubov states $PB_{q\tilde{\sigma}}$ for each realization $\tilde{\sigma}$ of the symmetry quantum numbers and an associated projected HFB (PHFB) TES.

Eventually, the unknown coefficients $\{f_{\mu}^{\tilde{\sigma}}(q); q \in \text{set}\}$ of the PGCM mixing are determined via the application of Ritz' variational principle. This leads to solving Hill-Wheeler-Griffin's (HWG) equation³ [133, 134] that is nothing but a generalized eigenvalue problem represented in the set of non-orthogonal PHFB states $PB_{q\tilde{\sigma}}$. The practical aspect of dealing with the linear redundancies associated with the non-orthogonality of the PHFB states when solving HWG's equation are briefly discussed in App. J.

Numerical setting

In the present chapter, two sets of HFB and HWG solvers are used. While the first set [135, 136] offers more flexibility regarding the enforced/relaxed symmetries in the computation of the HFB states and operator kernels entering HWG's equation⁴, the second set, implemented in the context of this thesis and discussed in App. P, can exactly handle three-nucleon interactions as mentioned in Chapter 3.

Based on these solvers, the calculations performed in the present study involve

1. the potential breaking of
 - a) global neutron and proton gauge symmetries,
 - b) rotational symmetry,
 - c) parity,
2. the associated restoration of
 - a) N and Z ,
 - b) J and M ,
 - c) Π ,
3. The use of constraints for
 - a) axial quadrupole (q_{20}),
 - b) non-axial quadrupole ($q_{2\pm 2}$),
 - c) axial octupole (q_{30}),
 operators.

For details on the employed many-body basis, see Chapter 3.

Uncertainties

The uncertainties of PGCM calculations are of several origins and nature⁵:

- Numerical representation:

³The diagonalization is performed separately for each value of $\tilde{\sigma}$.

⁴Full space triaxial results were provided by B. Bally [137].

⁵When adding two uncertainties σ_1 and σ_2 , presently supposed to be uncorrelated, the total one is computed as $\sigma_{\text{tot}} \equiv \sqrt{\sigma_1^2 + \sigma_2^2}$. When considering an observable $O = O_1 - O_2$, e.g. an excitation energy, its uncertainty is computed under the hypothesis that the uncertainties associated with O_1 and O_2 are fully correlated, i.e. using $\sigma_O \equiv |\sigma_{O_1} - \sigma_{O_2}|$.

- *Model-space truncation.* Results depend on the choice of the one-body basis parameters $(\hbar\omega, e_{\max})$ and the truncation of three-body operators $e_{3\max}$ as defined in Chapter 3. While the nominal results discussed in the following are obtained for $(\hbar\omega, e_{\max}, e_{3\max}) = (12, 8, 14)$, the associated uncertainty is evaluated in each nucleus according to a procedure described in Sec. 4.3.1 and typically included in the error bars shown of several of the figures below.
- *Approximate three-body interaction.* While three-body interactions terms can be handled exactly, it typically increases the runtime of PGCM calculations by three orders of magnitude compared to using a two-nucleon interaction only. In order to avoid this significant cost, the operator rank-reduction method [100] discussed in Chapter 3 is employed. The approximation was shown to induce errors below 2 – 3% across a large range of nuclei, observables and many-body methods when employing low-resolution Hamiltonians as done in the present work. Specifically, the PGCM errors on the ground-state charge radius and the low-lying excitation energies of ^{20}Ne (^{30}Ne) were shown to be of 0.7% (2.5%) and 1.5% (2.6%), respectively. While not included in the error bars appearing in some of the figures below, a conservative 2 – 3% error is to be appropriately attributed.
- *Discretization errors.* PGCM results depend on the discretization of the employed generator coordinate(s) and on the procedure described in App. J to handle linear redundancies when solving the HWG equation. The dependence of our PGCM results on these two numerical parameters have been checked and found to be negligible compared to the other sources of uncertainty.
- Many-body expansion:
 - *Generator coordinates.* PGCM results depend on the choice of generator coordinates employed in the calculation. While it is hard to envision a systematic way to evaluate an associated uncertainty, the dependence of the results on the generator coordinates that are expected to be dominant is gauged by generating results (a) with or without the octupole degree of freedom and (b) with or without the triaxial degree of freedom.
 - *Many-body truncation.* Given a PGCM ansatz, the PGCM-PT formalism developed in Chapter 2 allows one to embed it into a systematic many-body expansion. Constituting the leading-order contribution to the expansion, PGCM results carry an uncertainty associated with the corresponding truncation. Because it is the goal of Chapter 5 to present the first computation of the next correction, i.e. PGCM-PT(2), the associated uncertainty is not evaluated in the present chapter but simply commented on at various points below.
- Hamiltonian:
 - *χEFT truncation.* The hierarchy of terms in the chiral expansion allows us to increase the precision at each order and coherently assess truncation errors. These errors are consistently propagated to many-body calculations and are to be added to the errors coming from the many-body method itself. The uncertainty of a many-body observable X at $N^2\text{LO}$ and $N^3\text{LO}$ reads [130]

$$\delta X_{N^2\text{LO}} \equiv Q|X_{N^2\text{LO}} - X_{N\text{LO}}|, \quad (4.4a)$$

$$\delta X_{N^3LO} \equiv \max \left[Q |X_{N^3LO} - X_{N^2LO}|, \right. \\ \left. Q^2 |X_{N^2LO} - X_{NLO}| \right], \quad (4.4b)$$

where the expansion parameter Q denotes the ratio of a typical momentum scale characterizing medium-mass nuclei over the χ EFT breakdown scale. The value $Q = 1/3$ is presently employed; see Ref. [130] for details.

- *SRG dependence.* The particle-vacuum SRG transformation induces an intrinsic error associated with the violation of unitarity due to neglected induced operators beyond three-body terms. Furthermore, the uncertainty associated with the truncation of the many-body expansion itself depends on the transformation, which is typically minimized by working with low-resolution Hamiltonians as done in the present work. Overall, this induces a dependence of the results on the SRG parameter λ_{srg} . While the nominal results are systematically provided for $\lambda_{\text{srg}} = 1.88 \text{ fm}^{-1}$, the variation of the results obtained for $\lambda_{\text{srg}} = 2.23 \text{ fm}^{-1}$ will be quoted to provide an idea of the sensitivity of selected observables.

4.2.3. IM-NCSM

As a complement and a benchmark of the PGCM calculations, the IM-NCSM⁶ approach [139] is used to describe even-even neon isotopes.

Methodology

The IM-NCSM starts by pre-processing (already SRG-evolved) operators O through a nucleus-dependent unitary MR-IMSRG transformation $U(s)$ parameterized by the real variable s . The lowest eigenstate with appropriate symmetry quantum numbers obtained from a prior NCSM calculation in a small reference space including all basis Slater determinants with up to $N_{\text{max}}^{\text{ref}}$ HO excitation quanta above the lowest-energy basis states serves as a multi-configurational reference state. The transformed operator $O(s)$ expressed in normal-ordered form [94, 96] with respect to the NCSM reference state is truncated beyond two-body operators, i.e. at the MR-IMSRG(2) level, which induces a breaking of unitarity that needs to be monitored.

The transformation $U(s)$ is tailored to suppress the terms of the pre-processed Hamiltonian $H(s)$ that couple the NCSM reference space to the rest of the Hilbert space. This decoupling corresponds to the incorporation of dynamical correlations into the transformed Hamiltonian. While the decoupling is not complete in principle, even in the $s \rightarrow \infty$ limit, it leads in practice to an extremely fast convergence of a subsequent NCSM calculation as a function of the truncation parameter N_{max} for appropriate values of the flow parameter s . This subsequent NCSM calculation performed on the basis of $H(s)$ constitutes the last step of the IM-NCSM calculation.

Numerical setting

The oscillator frequency is set to $\hbar\omega = 20 \text{ MeV}$ in the IM-NCSM calculations. While the initial NCSM calculation is performed for $N_{\text{max}}^{\text{ref}} = 0$ or 2, the final NCSM calculation goes up to $N_{\text{max}} = 4$, which is fully converged⁷.

⁶IM-NCSM calculations were provided by R. Roth [138].

⁷While the $N_{\text{max}} = 0$ is essentially sufficient in practice, the configuration mixing within that $N_{\text{max}} = 0$ subspace is however non negligible, i.e. the initial NCSM state used for the MR-IMSRG is *not*

In the MR-IMSRG part of the calculation, $e_{\max} = 12$ and $e_{3\max} = 14$ are employed. The flow equations rely on a modified version of the so-called White generator [129] adapted to the N_{\max} -truncated reference space and the value of the flow-parameter is chosen large enough to warrant convergence of the evolved Hamiltonian, i.e. typically around $s = 80$.

A HO Hamiltonian for the center of mass is added to initial Hamiltonian and consistently evolved through MR-IMSRG to remove spurious center-of-mass excitations from the spectrum. This operator comes with a small numerical pre-factor $\lambda_{H_{\text{cm}}} = 0.2$ that is sufficient to shift the spurious states out of the way without modifying other states in any significant fashion.

Uncertainties

Nominal IM-NCSM results quoted below are obtained for $\lambda_{\text{srg}} = 2.23 \text{ fm}^{-1}$, $N_{\max}^{\text{ref}} = 2$, $N_{\max} = 4$ and $s \sim 80$. These results are accompanied with the following uncertainties

- *Many-body.* Many-body uncertainties are estimated from the maximum of the differences to the three calculations based on $N_{\max}^{\text{ref}} = 0$, $N_{\max} = 2$ and $s \sim 40$, varying only one parameter at a time. These errors are typically dominated by the effect of reducing N_{\max}^{ref} although the dependence on the flow parameter is often not negligible⁸.
- *Hamiltonian.* The chiral order-by-order uncertainties are extracted as for the PGCM calculations but using a more advanced Bayesian model. On the other hand, no uncertainty associated with the original value of λ_{srg} is presently provided.

4.3. Results

4.3.1. Model-space convergence

The convergence of PHFB results with respect to the employed HO model space has been checked for all Ne isotopes. In this test, the HFB minimum in the (q_{20}, q_{30}) plane, systematically obtained at $\beta_3 = 0$ (see Sec. 4.3.2 below), is projected on good neutron and proton numbers as well as on the desired angular momentum J . Results for two representative examples, ^{20}Ne and ^{28}Ne , are displayed in Fig. 4.1 for the ground-state energy and root-mean-square (rms) charge radius, as well as for the absolute energy of the first 2^+ state.

The three observables show a typical convergence pattern consisting of curves that gradually become independent of $\hbar\omega$ and closer to each others as the basis size increases. At each step of the way, the HO frequency delivering the least sensitive results to e_{\max} , i.e. the results that are closest to the converged value, is given by $\hbar\omega = 12 \text{ MeV}$. Taking the least favorable case, i.e. ^{28}Ne , the energy of the first 0^+ (2^+) changes by 70 keV (72 keV) when going from $e_{\max} = 10$ to $e_{\max} = 12$ whereas the ground-state charge radius increases by 10^{-4} fm . Taking the results displayed in Fig. 4.1 for $\hbar\omega \geq 12 \text{ MeV}$, their infra-red extrapolation towards the infinite basis limit is performed according to the procedure

decoupled from the rest of the $N_{\max} = 0$ space such that the subsequent NCSM diagonalization of $H(s)$ is necessary.

⁸For large enough N_{\max} , the dependence of the end results on s probes the effects of truncating the transformed Hamiltonian to the normal-ordered two-body level throughout the MR-IMSRG evolution based on the reference NCSM state.

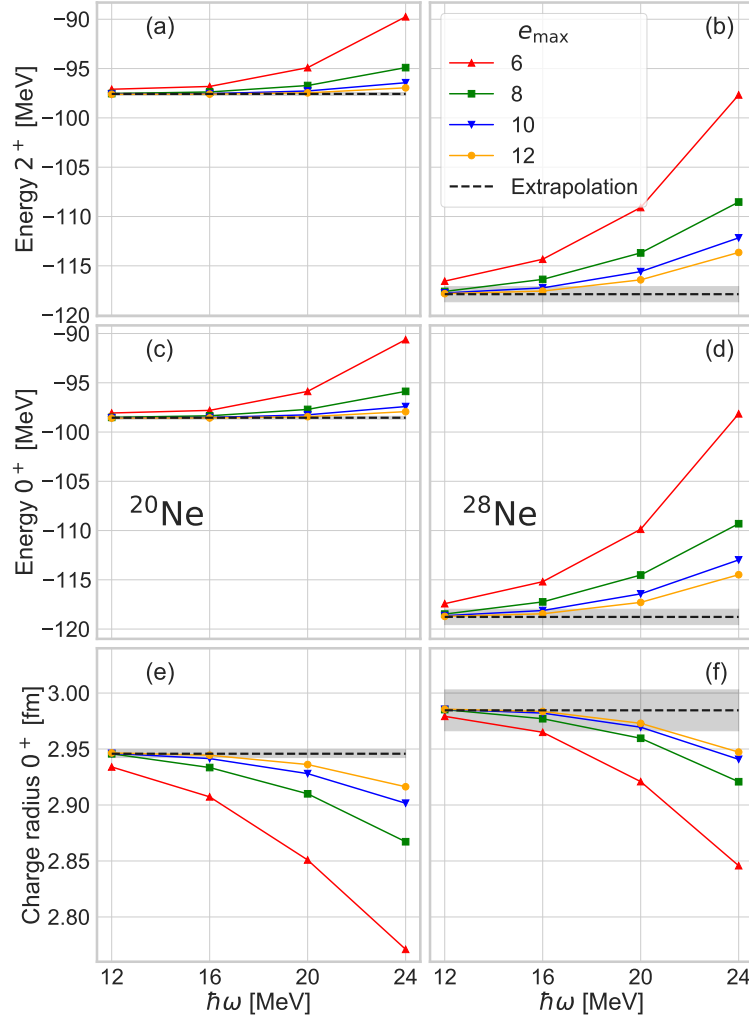


Figure 4.1. Dependence of PHFB results in ^{20}Ne (left column) and ^{28}Ne (right column) on the employed HO model space. Results are plotted as a function of $\hbar\omega$ for various values of e_{max} . The dashed lines denote extrapolated values whereas the grey band provides the associated uncertainty. The first row (panels (a) and (b)) focuses on the first 2^+ absolute energy whereas the second (panels (c) and (d)) and third (panels (e) and (f)) rows provide the ground-state energy and associated rms charge radius. Calculations employ the N^3LO χEFT Hamiltonian with $\lambda_{\text{srg}} = 1.88 \text{ fm}^{-1}$.

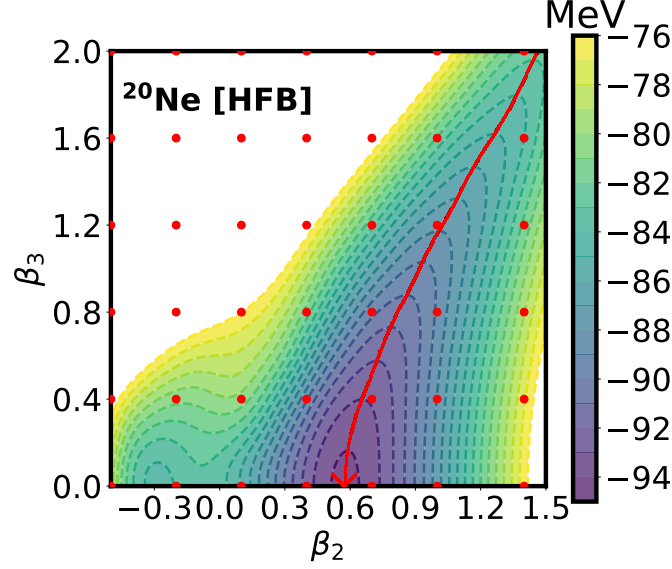


Figure 4.2. (Color online) Constrained HFB TES of ^{20}Ne in the axial (β_2, β_3) plane. The (red) full line indicates the lowest-energy path, with the arrow positioned at the minimum of the TES. The (red) dots characterize the set of HFB states used in the subsequent PGCM calculation. Calculations employ the N^3LO χEFT Hamiltonian with $\lambda_{\text{srg}} = 1.88 \text{ fm}^{-1}$.

described in Ref. [140] for both energies and radii. The result of the extrapolation is also displayed, along with its uncertainty, in Fig. 4.1.

All PGCM results presented in the following have been obtained for $(\hbar\omega, e_{\text{max}}, e_{3\text{max}}) = (12, 8, 14)$. In most of the figures shown below, these nominal values are displayed with an error bar associated with the model space convergence obtained by adding, in the sense explained above, the distance to the extrapolated result and the uncertainty on the latter. Focusing again on the least favorable case, i.e. ^{28}Ne , model-space uncertainties on the nominal energy of the first 0^+ and 2^+ states are 830 keV (0.7%) and 810 keV (0.7%), respectively, whereas the uncertainty on the ground-state charge radius is 0.02 fm (0.7%).

Furthermore, the impact of $e_{3\text{max}}$ has been studied by varying the truncation parameter in the range $e_{3\text{max}} = 8 - 14$ for selected observables. Overall, both energies and radii are found to be well converged with respect to $e_{3\text{max}}$, with changes between $e_{3\text{max}} = 12$ and 14 amounting in the least favorable cases to 2-300 keV for total binding energies and 10^{-3} fm for charge radii. These uncertainties can be thus effectively incorporated in the larger ones resulting from the infinite-basis extrapolation discussed above.

Given that model-space uncertainties tend to cancel out in excitation spectra, the errors on the latter are typically smaller than for absolute energies. One must note that model-space uncertainties of the nominal calculations are sub-leading compared to the error associated with the rank-reduction of the three-nucleon interaction whose maximal value along the Ne chain has been evaluated in Chapter 3 to be respectively 2.5% and 2.6% for the ground-state charge radius and low-lying excitation energies of ^{30}Ne [100].

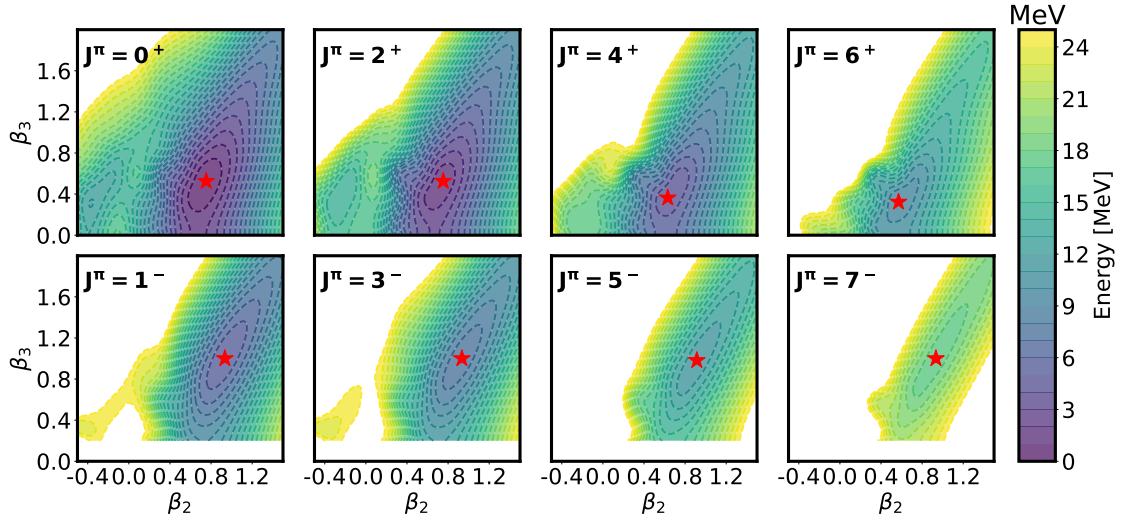


Figure 4.3. (Color online) Projected HFB TES of ^{20}Ne in the axial (β_2, β_3) plane for spin-parity values $J^\pi = 0^+, 1^-, 2^+, \dots, 7^-$. In each case, the minimum of the TES is indicated by a (red) star. Calculations employ the N^3LO χEFT Hamiltonian with $\lambda_{\text{srg}} = 1.88 \text{ fm}^{-1}$.

4.3.2. ^{20}Ne

The present study focuses first on the stable ^{20}Ne isotope. This nucleus has been extensively studied experimentally and theoretically in the past [141, 142, 143], in part because it is one of the few nuclei displaying a strong admixture of cluster configurations in the ground state. The ab initio description of this doubly open-shell nucleus is thus a challenge given that it is necessary to appropriately capture both dynamical and strong static correlations.

Total energy surfaces

Figure 4.2 displays the HFB TES of ^{20}Ne in the axial (β_2, β_3) plane. The energy minimum is found for the reflection-symmetric prolate shape characterized by deformation parameters $(\beta_2 = 0.57, \beta_3 = 0)$. Still, the TES is more shallow in the octupole direction than in the quadrupole direction such that one may anticipate octupole shape fluctuations in the ground-state and an octupole vibration at an energy lower than the quadrupole one.

Figure 4.3 shows the PHFB TES in the axial (β_2, β_3) plane for spin-parity $J^\pi = 0^+, 1^-, 2^+, \dots, 7^-$. Each HFB state is projected onto neutron and proton numbers $(N, Z) = (10, 10)$ using $N_{\varphi_n} = N_{\varphi_p} = 7$ mesh points in the interval $\varphi_{n,p} \in [0, \pi]$. The projection on good angular momentum involves $N_\beta = 20$ Euler angles in the interval $\varphi_\beta \in [0, \pi]$. Static correlations associated with symmetry restorations favor deformed configurations in both β_2 and β_3 directions for both positive- and negative-parity states. The minimum of the 0^+ TES is thus located at $(\beta_2 = 0.75, \beta_3 = 0.53)$ and the TES is softer along both β_2 and β_3 directions than at the HFB level. With increasing J , the energy minimum of positive-parity states becomes more stable but drifts to configurations with smaller multipole moments. The minimum of the 1^- TES is located at larger deformations $(\beta_2 = 0.93, \beta_3 = 1.0)$ than for 0^+ TES. While the minimum also becomes more stable with increasing J , it however remains at the same deformations.

The above results are qualitatively very similar to those obtained through relativistic

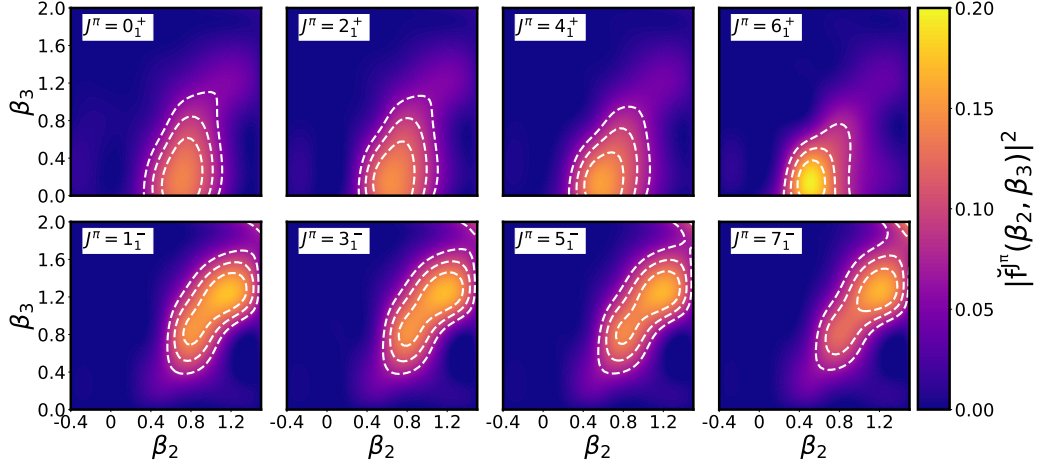


Figure 4.4. (Color online) Collective PGCM wave-functions in the axial (β_2, β_3) plane of low-lying positive- and negative-parity states. Calculations employ the $N^3\text{LO } \chi\text{EFT}$ Hamiltonian with $\lambda_{\text{srg}} = 1.88 \text{ fm}^{-1}$.

multi-reference energy density functional (MR-EDF) calculations [141, 142]. While being also quantitatively close, the present ab initio calculation produces more rigid TES than the EDF ones, especially on the oblate side.

Low-lying spectroscopy

Based on the PHFB states associated with the grid displayed in Fig. 4.2, a PGCM calculation of ^{20}Ne is performed.

Figure 4.4 displays the collective wave functions $\{\tilde{f}_\mu^{\check{q}}(p); q \in \text{set}\}$ (see App. J) of the low-lying yrast states with positive and negative parities. Along the positive-parity band, collective wave-functions are peaked around a reflection-symmetric prolate configuration located at $(\beta_2 = 0.55, \beta_3 = 0)$. While displaying significant shape fluctuations, in particular along the octupole degree of freedom as expected from the TES, the collective wave functions become increasingly concentrated with increasing angular momentum, thus indicating a stabilization of the nuclear shape under rotation. The behavior is different along the negative-parity band. Indeed, the wave-functions extend over a larger range of deformations that does not decrease with J . Overall, one observes a significant contribution of reflection-asymmetric shapes along the positive-parity and the presence of a negative-parity band at low energy built on an octupole vibration as was already anticipated from the HFB TES.

The low-lying spectrum corresponding to the collective wave-functions displayed in Fig. 4.4, labelled PGCM-2D, is compared in Fig. 4.5 (panel (c)) to experimental data (panel (e)) and to IM-NCSM results (panel (d)). Experimental excitation energies are well reproduced by PGCM and IM-NCSM results. IM-NCSM results, which act as quasi-exact solutions for the employed Hamiltonian, are thus reproduced by the 2D axial GCM within their respective uncertainties. As explained earlier, the rank-reduction of the three-nucleon force (see Sec. 4.2.2) and missing dynamical correlations (see Chapter 5) would add several percents of uncertainties to the PGCM results, making both sets of results fully compatible. One notices that the χEFT uncertainty at $N^3\text{LO}$ is estimated to be sub-leading compared to many-body uncertainties in both sets of calculations. The agreement between both theoretical spectra is remarkable given that individual PGCM energies are about 60 MeV

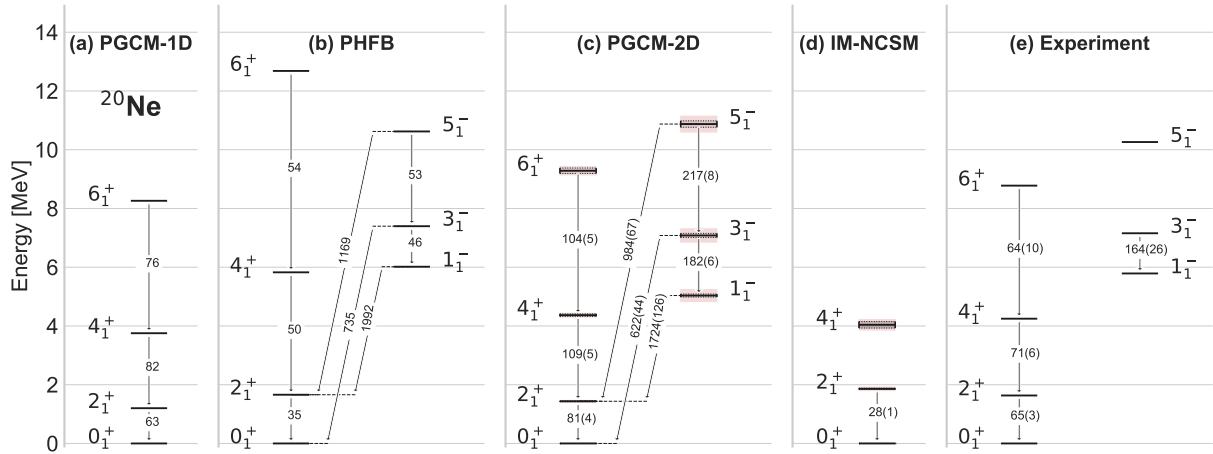


Figure 4.5. (Color online) Low-lying positive- and negative-parity bands in ^{20}Ne . The intra-band $E2$ transition strengths (in e^2fm^4) are indicated along vertical arrows whereas a selection of $E3$ transition strengths (in e^3fm^6) are indicated along oblique lines. Panel (a): PGCM results obtained by restricting the mixing to the quadrupole axial degree of freedom. Panel (b): PHFB results based on the HFB configuration corresponding to the minimum of the 0^+ TES located at $(\beta_2 = 0.75, \beta_3 = 0.53)$ (see Fig. 4.3). Panel (c): PGCM results obtained using the set of points in the axial (β_2, β_3) plane displayed in Fig. 4.2. Panel (d): IM-NCSM results. Panel (e): experimental data. PGCM results in panel (c) display model-space (black box) plus χEFT (pink band) uncertainties. IM-NCSM results in panel (d) display total many-body (black box) plus χEFT (pink band) uncertainties. The N^3LO χEFT Hamiltonian with $\lambda_{\text{srg}} = 1.88 \text{ fm}^{-1}$ ($\lambda_{\text{srg}} = 2.23 \text{ fm}^{-1}$) is employed in PGCM (IM-NCSM) calculations.

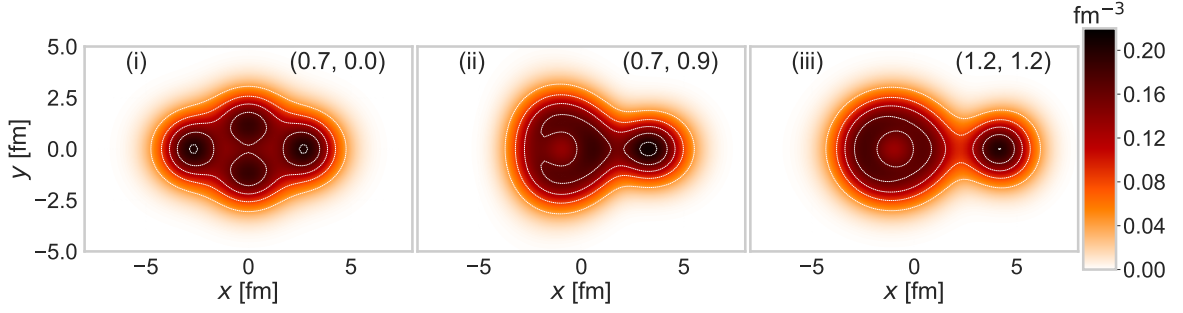


Figure 4.6. (Color online) Point matter distribution of ^{20}Ne in the x-y plane corresponding to three constrained HFB configurations located at (i) $(\beta_2 = 0.7, \beta_3 = 0)$, (ii) $(\beta_2 = 0.7, \beta_3 = 0.9)$ and (iii) $(\beta_2 = 1.2, \beta_3 = 1.2)$ in the axial (β_2, β_3) plane. Calculations employ the N³LO χ EFT Hamiltonian with $\lambda_{\text{srg}} = 1.88 \text{ fm}^{-1}$.

away from the converged values due to missing dynamical correlations (see Sec. 4.3.3 along with 5 for a detailed discussion). This proves that dynamical correlations contribute (essentially) identically to the energy of all low-lying states whereas static correlations are essential to describe their (mostly) collective nature. While constituting the mere leading order of the PGCM-PT expansion, the PGCM is thus, at least in the present example, well suited in itself to describe the low-lying spectrum. Still, one expects dynamical correlations to provide sub-leading corrections.

Electric quadrupole transition strengths within each band are decently accounted for by the PGCM calculation, although being too large by a factor 1.1-1.6 compared to experimental data and by a factor 2.9 compared to the reference IM-NCSM value for the $B(E2 : 2_1^+ \rightarrow 0_1^+)$ ⁹. One expects missing dynamical correlations to reduce the collective character of the states and thus to decrease the $B(E2)$ transitions. One also notes that relativistic MR-EDF calculations [141] produced smaller $B(E2)$ transitions by spreading the collective wave-functions onto the oblate side¹⁰, which does not happen here due to the stiffer TES.

Interestingly, limiting the PGCM mixing to reflection-symmetric HFB states (panel (a)) compresses too much the positive-parity band in addition to forbidding the access to the negative-parity one. Contrarily, reducing the approach to a PHFB calculation based on the sole reflection-asymmetric HFB state located at the minimum of the 0^+ PHFB TES ($\beta_2 = 0.75, \beta_3 = 0.53$) spreads out the positive-parity band too much and reduces too significantly the collectivity in the negative-parity band compared to experiment (panel (b)). The full 2D PGCM calculation of reference is optimal and situated in between these two limiting cases, which indicates not only the need for octupole configurations but also for their fluctuations.

Density distributions

Point matter densities of ^{20}Ne associated with three different HFB configurations are displayed in the x-y plane in Fig. 4.6. The three chosen configurations correspond to (i) the maximum of the 0^+ ground-state collective wave-function ($\beta_2 = 0.7, \beta_3 = 0$),

⁹While IM-NCSM energies and radii are very robust, it is less clear for $B(E2)$ values at this point in time such that the reference should be taken with a grain of salt.

¹⁰Excitation energies of the positive parity band were however slightly worse than in the present calculation.

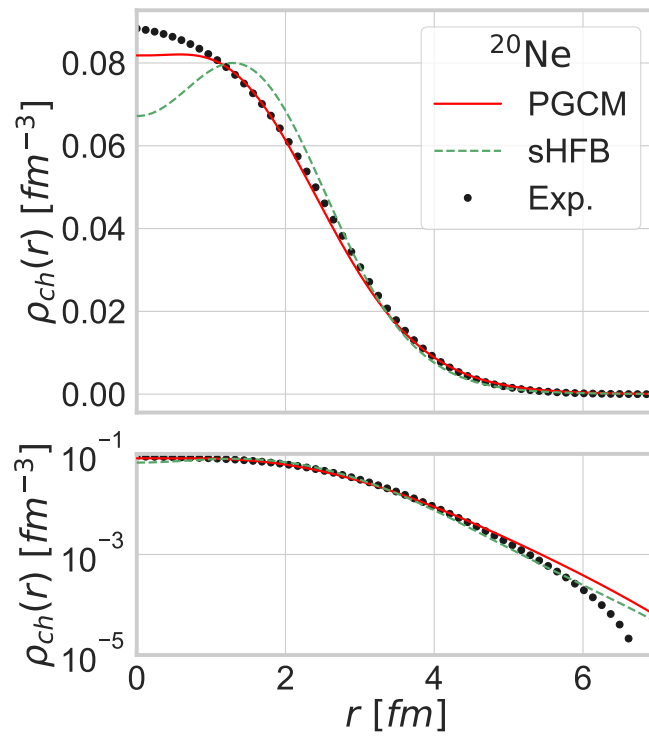


Figure 4.7. (Color online) Spherical HFB, PGCM and experimental ^{20}Ne ground-state charge density distributions in linear (upper panel) and logarithmic (lower panel) scales. Calculations employ the N^3LO χEFT Hamiltonian with $\lambda_{\text{srg}} = 1.88 \text{ fm}^{-1}$.

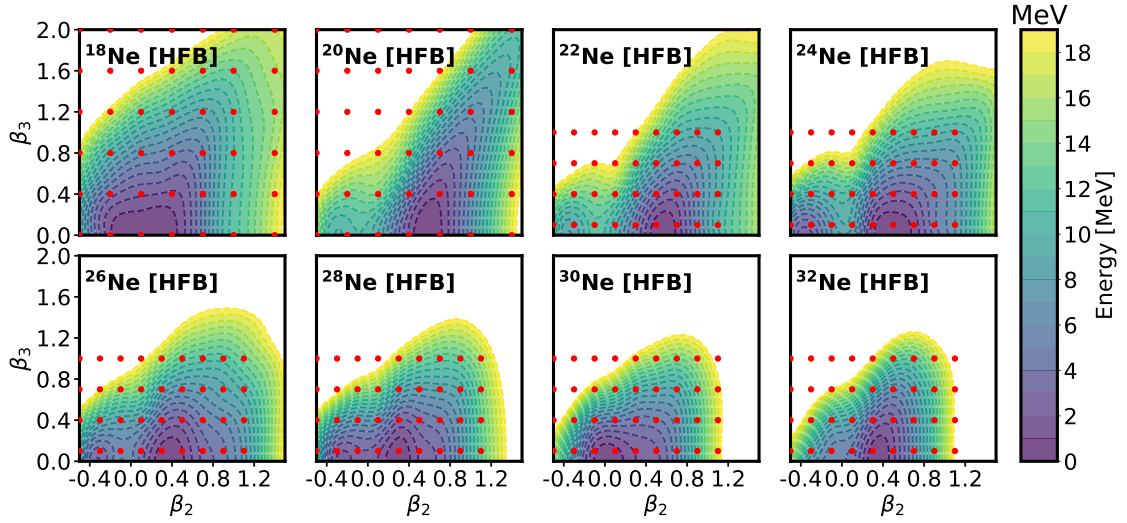


Figure 4.8. (Color online) HFB TES of $^{18-32}\text{Ne}$ in the axial (β_2, β_3) plane. The (red) dots characterize in each case the set of HFB states used in the subsequent PGCM calculations. Calculations employ the N^3LO χEFT Hamiltonian with $\lambda_{\text{srg}} = 1.88 \text{ fm}^{-1}$.

(ii) the half-maximum of the 0^+ ground-state collective wave-function with the largest octupole deformation ($\beta_2 = 0.7$, $\beta_3 = 0.9$) and (iii) the maximum of the 1^- state collective wave-function ($\beta_2 = 1.2$, $\beta_3 = 1.2$). Panels (i) and (ii) demonstrate that the ground-state not only displays clustering but actually mixes configurations ranging from a dominant compact $\alpha + ^{12}\text{C} + \alpha$ structure to a sub-leading quasi- $^{16}\text{C} + \alpha$ structure. Panel (iii) proves that the low-lying negative parity band is built out of a proper $^{16}\text{C} + \alpha$ cluster structure.

Of course, intrinsic cluster structures are not observable per se and can only be probed indirectly. Still, the observable charge density distribution displays fingerprints of many-body correlations among which are the strong static correlations associated with intrinsic shape deformation and fluctuation. In order to illustrate this feature, the radial PGCM charge density distribution of the 0^+ ground-state is compared to experimental data and to the charge density computed from the spherical HFB (sHFB) configuration in Fig. 4.7. Charge density distributions with respect to the center of mass are obtained from point-proton and point-neutron density distributions according to the procedure described in App. I. As visible from the upper panel of Fig. 4.7, the PGCM charge density reproduces very satisfactorily the experimental data. While it is too low in the center of the nucleus, many-body correlations partly fill up the artificial depletion displayed at the nuclear center by the sHFB density and suppress the latter accordingly in the interval $r \in [1, 2] \text{ fm}$. Furthermore, static correlations associated with shape deformation and fluctuation increase the charge density distribution in the interval $r \in [4, 5] \text{ fm}$ to improve the agreement with experimental data. However, and as visible in the lower panel of Fig. 4.7, the long tail part of the PGCM density overshoots the experimental density. This is consistent with both the too low two-neutron separation energy and the too high rms charge radius r_{ch} discussed later on.

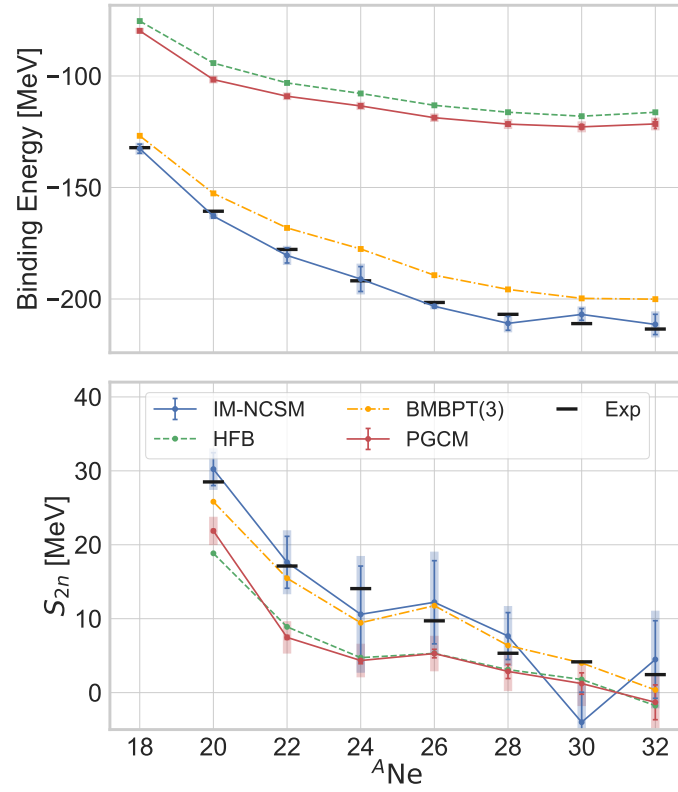


Figure 4.9. (Color online) Absolute ground-state energies (upper panel) and two-neutron separation energies (lower panel) along the Ne isotopic chain. Results from HFB, PGCM, BMBPT and IM-NCSM calculations are compared to experimental data. The $N^3\text{LO}$ χEFT Hamiltonian with $\lambda_{\text{srg}} = 1.88 \text{ fm}^{-1}$ ($\lambda_{\text{srg}} = 2.23 \text{ fm}^{-1}$) is employed in IM-NCSM calculations. BMBPT calculations are performed with $e_{\text{max}} = 10$.

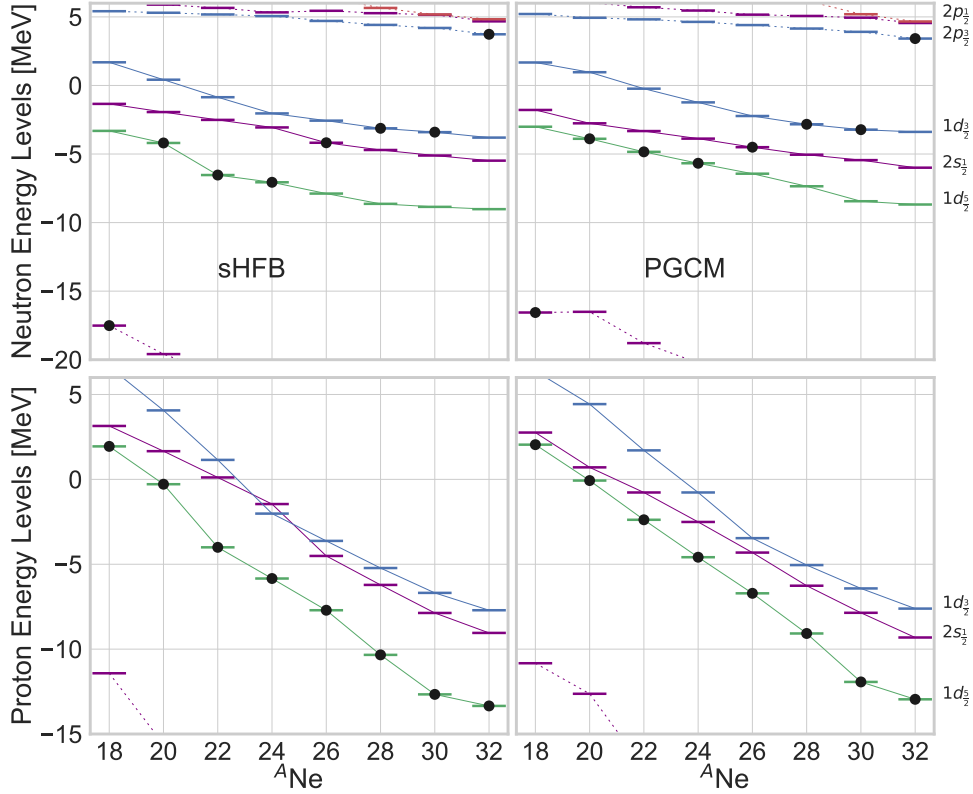


Figure 4.10. (Color online) Evolution of neutron (upper panels) and proton (lower panels) Baranger’s single-particle spectra of the 0^+ ground-state in $^{18-32}\text{Ne}$. Results from spherical HFB (left column) and PGCM (right column) calculations in the axial (β_2, β_3) plane are shown. Black dots denote the last occupied orbital associated with a naive filling of the shells. Calculations employ the N^3LO χEFT Hamiltonian with $\lambda_{\text{srg}} = 1.88 \text{ fm}^{-1}$.

4.3.3. Isotopic chain

The PGCM spectroscopic results obtained in the non-trivial ^{20}Ne isotope are very encouraging. In order to deepen the analysis, the study is now extended to other Ne isotopes and to additional observables.

Total energy surfaces

Figure 4.8 shows the evolution of the HFB TES in the axial (β_2, β_3) plane along the Neon chain. The already studied ^{20}Ne nucleus (Fig. 4.2) appears to be transitional between ^{18}Ne , whose TES is very soft in both β_2 and β_3 directions, and heavier Ne isotopes that become increasingly rigid against octupole deformation¹¹. The quadrupole deformation

¹¹Octupole collectivity typically builds from strong correlations between nucleons near the Fermi surface sitting on orbitals of opposite parity and differing by three units of angular momentum $\Delta l = 3$. While such conditions are fulfilled for proton and neutron numbers $Z, N \approx 34, 56, 88, 134$ [144], one also expects a large softness against octupole deformation in light self-conjugate nuclei featuring an asymmetric di-nucleus clustering, such as the $^{16}\text{O} + \alpha$ configuration of ^{20}Ne [145, 146]. The fragmenta-

of the prolate minimum decreases gradually to reach the spherical ^{30}Ne isotope before increasing again in ^{32}Ne . At the same time, the softness against quadrupole deformation fluctuates as the absolute prolate minimum becomes connected to a local oblate minimum in $^{24-28}\text{Ne}$ before spreading again on the prolate side in ^{30}Ne to generate a non-zero prolate deformation in ^{32}Ne .

Ground-state energies

The upper panel of Fig. 4.9 displays the absolute ground-state energy along the Ne isotopic chain. Experimental data are well reproduced by IM-NCSM calculations within uncertainties, with the exception of ^{30}Ne that wrongly appears less bound than ^{28}Ne . Overall, the results are similar, and even better, than coupled cluster calculations in the SDT-1 approximation (CCSDT-1) performed with the $\Delta\text{NNLO}_{\text{GO}}(394)$ Hamiltonian [92]. Strikingly, PGCM binding energies miss between 60 and 90 MeVs, the difference increasing with neutron number. The gain compared to HFB energies is small on that scale (i.e. $\sim 5 - 7$ MeV) and could never compensate, even with a more elaborate PGCM ansatz, for the difference that is obviously due to missing dynamical correlations. While the goal is to bring in these correlations within a symmetry-conserving scheme, i.e. on top of the PGCM unperturbed state via PGCM-PT introduced Chapter 2, their effect can already be appreciated through the results of single-reference Bogoliubov many-body perturbation theory (BMBPT) [45, 46, 47, 53, 60] calculations performed on top of a deformed HFB reference state¹² that are displayed in Fig. 4.9. The bulk of correlations is indeed recovered at the BMBPT(3) level, and we note that the gain in energy increases with neutron number and therefore corrects for the overall trend at the same time. BMBPT(3) energies are still about 7 – 15 MeV away from IM-NCSM and experimental values, which is similar in magnitude to the static correlations gained via symmetry restorations and shape fluctuations within the PGCM¹³. Thus the *consistent* “sum” of static and dynamical correlations accessible via PGCM-PT can be expected to bring the absolute values very close to IM-NCSM results; see Chapter 5 for a related discussion.

The lower panel of Fig. 4.9 displays two-neutron separation energies S_{2n} to appreciate the stability of Ne isotopes against two-neutron emission. Except for ^{30}Ne whose S_{2n} is wrongly predicted to be negative, IM-NCSM results reproduce experimental data within uncertainties, similarly to CCSDT-1 calculations with the $\Delta\text{NNLO}_{\text{GO}}(394)$ Hamiltonian [92]. Consistently with the too flat curve in the upper panel, PGCM S_{2n} are too low across the chain such that the drip-line is wrongly predicted to be located at ^{30}Ne instead of

tion of the nucleus in two symmetric or asymmetric clusters can be understood from the dynamical symmetries of the anisotropic harmonic oscillator potential with frequencies in rational ratios [147]. Super-deformed systems are susceptible to cluster into two asymmetric (symmetric) spherical fragments for proton and neutron numbers $Z, N \approx 2, 10, 28, 60, 110, 182$ ($Z, N \approx 4, 16, 40, 80, 140$). Consequently, Ne isotopes with neutron numbers close to 8 are expected to be soft against octupole deformation, while a competition between the development of octupole collectivity (due to protons) and the restoring force towards a reflection-symmetric configuration (due to neutrons) makes neutron-rich Ne isotopes stiffer against octupole deformations. The interpretation of these features in terms of molecular covalent bonds is developed in Ref. [142].

¹²First results of this kind were presented in Ref. [100].

¹³In ^{20}Ne , one has $E_{\text{BMBPT}} = 152.6$ MeV, $E_{\text{IM-NCSM}} = 162.6$ MeV and $E_{\text{PGCM}} - E_{\text{HFB}} = 7.4$ MeV, knowing that $E_{\text{EXP}} = 160.6$ MeV. It must be noted that, just as BMBPT, CCSDT-1 calculations relying on a purely “vertical” expansion on top of a deformed mean-field state also provides slightly underbound Ne isotopes with the $\Delta\text{NNLO}_{\text{GO}}(394)$ Hamiltonian [92] and thus require the addition of 3-5 MeVs of static correlations associated with symmetry restoration and shape fluctuations.

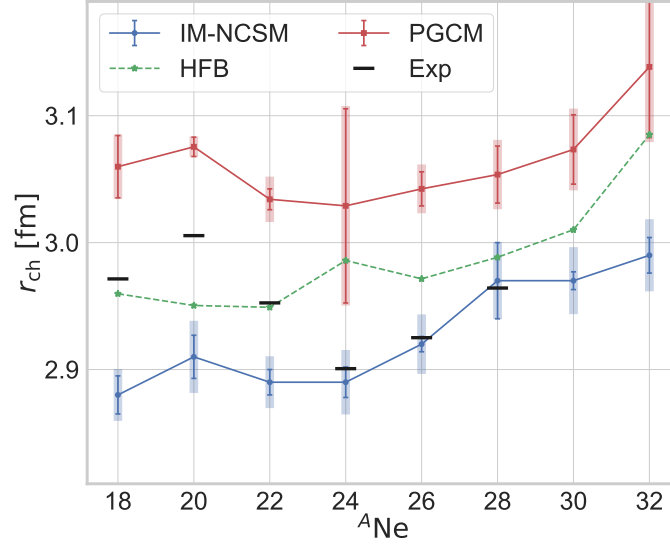


Figure 4.11. (Color online) Theoretical (HFB, PGCM, BMBPT, IM-NCSM) and experimental ground-state rms charge radius along the Neon isotopic chain. HFB and BMBPT results correspond to the HFB minimum in the axial (β_2, β_3) plane. PGCM calculations are performed over the axial (β_2, β_3) plane. The $N^3\text{LO } \chi\text{EFT}$ Hamiltonian with $\lambda_{\text{srg}} = 1.88 \text{ fm}^{-1}$ ($\lambda_{\text{srg}} = 2.23 \text{ fm}^{-1}$) is employed in IM-NCSM calculations. BMBPT calculations are performed with $e_{\text{max}} = 10$.

^{34}Ne [148]. While static collective correlations captured through PGCM have no impact on the S_{2n} , the comparison with IM-NCSM (or CCSDT-1) results underlines the importance of dynamical correlations to reproduce the evolution of binding energies with neutron number. As a matter of fact, dynamical correlations brought in at the BMBPT(3) level correct for the wrong trend of HFB binding energies such that the S_{2n} s become perfectly consistent with IM-NCSM results and experimental data. Once again, there is no obvious reason to believe that consistently correcting PGCM results for dynamical correlations will not bring the same benefit.

To further put the binding energy evolution in perspective within our theoretical scheme, Fig. 4.10 displays the evolution of neutron and proton (non-observable) Baranger’s spherical shell structure [82, 149] along the Neon chain for both spherical HFB and PGCM 0^+ ground states¹⁴. The last occupied orbit associated with a naive filling of the shells is indicated with a black dot for each isotope. One first observes that static correlations do tend to compress the spectrum around the Fermi energy but without changing it qualitatively here. The most important feature for the present discussion relates to the very large gap between neutron sd and pf shells. The fact that this gap is barely compressed going from sHFB to PGCM such that the neutron $2p_{3/2}$ remains unbound demonstrates that cross-shell correlations in the PGCM state are insufficient to bind $^{32,34}\text{Ne}$ and probably too weak already in $^{28,30}\text{Ne}$ to properly describe the physics of the island of inversion.

¹⁴Baranger’s single-particle energies embody the genuine one-body shell structure that can be extracted from any many-body calculation [82, 149], i.e. their definition is not associated with a mean-field approximation as the HF single-particle energies are for example.

Ground-state rms charge radii

Figure 4.11 displays the ground-state charge rms radius in $^{18-32}\text{Ne}$. One first observes that IM-NCSM values are similar to the ones obtained in CCSDT-1 calculations performed with the $\Delta\text{NNLO}_{\text{GO}}(394)$ Hamiltonian [92], i.e. they are too small below ^{24}Ne but accurate above it up to ^{28}Ne , which is the last isotope in which r_{ch} is known. The overall trend is qualitatively reproduced and the known sub-shell closure at $N = 14$ is nicely captured. However, the trend predicted by the two methods differ beyond ^{28}Ne , which would make the measurement of r_{ch} in $^{30,32}\text{Ne}$ of prime interest.

Except for $^{18-22}\text{Ne}$ where octupole fluctuations are important and ^{24}Ne , radii associated with the HFB minimum in the axial (β_2, β_3) plane roughly follow the trend of IM-NCSM (and CCSDT-1) predictions but are about 0.05 fm larger.

Compared to HFB results, PGCM systematically increases the rms charge radius by mixing in more deformed configurations than the HFB minimum (see Figs. 4.2 and 4.4). PGCM results overestimate experiment by ~ 0.1 fm and IM-NCSM results by ~ 0.2 fm all throughout the isotopic chain even though the isotopic dependence is closer to IM-NCSM than HFB, in particular in $^{18-22}\text{Ne}$ where the inclusion of octupole shape fluctuations improves it. Static collective correlations make PGCM largely exaggerate rms charge radii and must be compensated for by missing dynamical correlations. Given that dynamical correlations brought on top of the deformed mean-field increase charge radii [150], it will be interesting to see how and why they decrease charge radii when brought on top of the PGCM state via PGCM-PT.

Low-lying spectroscopy

Figure 4.12 displays the systematic of the first 2^+ and 4^+ excitation energies in $^{18-32}\text{Ne}$. Except for the rotational character of the ground-state band in ^{30}Ne , experimental data are well reproduced by IM-NCSM calculations all along the isotopic chain. As for PGCM calculations, the excellent results obtained in ^{20}Ne do extend to ^{22}Ne . Starting with ^{24}Ne , the trend of PGCM results is however at odds with IM-NCSM and experimental values. In particular, the steep decrease of the first 2^+ (4^+) energy beyond ^{26}Ne (^{24}Ne), well captured by IM-NCSM calculations, is absent from the PGCM results. Furthermore, the experimental $\Delta E_1^{4^+}/\Delta E_1^{2^+}$ ratio displayed in the lower panel of Fig. 4.12 demonstrates that the nature of the ground-state band changes brutally beyond ^{26}Ne as one enters the island of inversion to approach the rotational value in ^{30}Ne . As could have been anticipated from the evolution of the HFB TES in Fig. 4.8, this qualitative change is not captured by PGCM calculations that predict ^{30}Ne ground-state to be spherical.

The above discussion underlines that the ability of the PGCM to nicely reproduce the low-lying spectroscopy of $^{20-22}\text{Ne}$ cannot be naively and automatically generalized to all nuclei. It is however unclear whether what is observed along the Ne isotopic chain constitutes an intrinsic limitation of the PGCM ansatz, in which case all defects must be corrected by the addition of dynamical correlations, or whether a richer PGCM ansatz could already change the situation at play.

To investigate this question, the results of sd valence-space calculations¹⁵ performed with the USDB interaction [152] are reported on in Fig. 4.13. The restriction to a valence space is meant to effectively remove, or largely suppress, the explicit role of dynamical correlations and see if enriching the PGCM ansatz is sufficient to reach full configuration

¹⁵Valence space calculations were provided by T. R. Rodriguez [151].

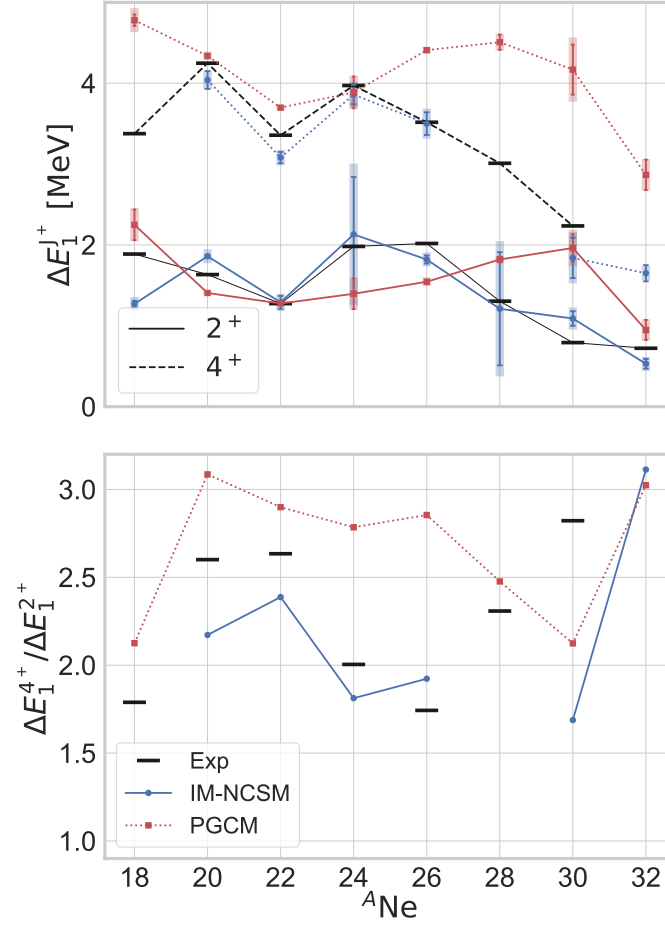


Figure 4.12. (Color online) Low-lying spectroscopy in $^{18-32}\text{Ne}$. First ΔE_1^{2+} and ΔE_1^{4+} excitation energies (upper panel) and their ratio $\Delta E_1^{4+}/\Delta E_1^{2+}$ (lower panel). PGCM results with model-space (black box) plus χEFT (pink band) uncertainties and IM-NCSM results with total many-body (black box) plus χEFT (pink band) uncertainties are compared to experimental data. The N^3LO χEFT Hamiltonian with $\lambda_{\text{srg}} = 1.88 \text{ fm}^{-1}$ ($\lambda_{\text{srg}} = 2.23 \text{ fm}^{-1}$) is employed in PGCM (IM-NCSM) calculations.

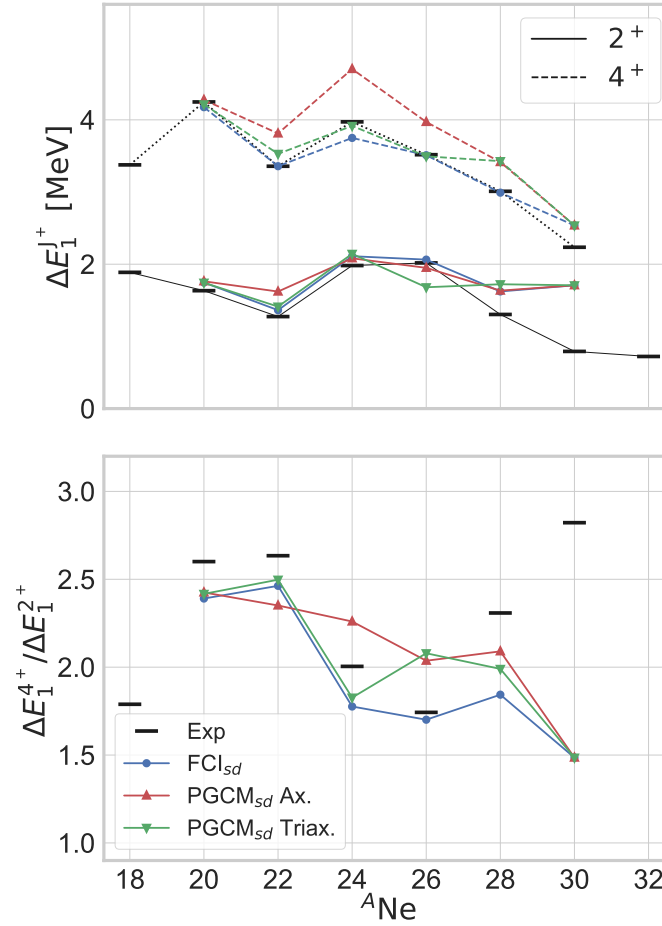


Figure 4.13. (Color online) Low-lying spectroscopy in $^{18-32}\text{Ne}$ from sd valence-space calculations. First ΔE_1^{2+} and ΔE_1^{4+} excitation energies (upper panel) and their ratio $\Delta E_1^{4+} / \Delta E_1^{2+}$ (lower panel). PGCM results obtained by mixing states along the axial quadrupole coordinate are compared to experimental data and to full configuration interaction (FCI) results as well as to PGCM results obtained by adding the triaxial quadrupole coordinate.

interaction (FCI) results [128]. To do so, the PGCM on purely axial states discussed above is enriched via the explicit addition of triaxially-deformed HFB states. When restricted to a small valence space around the Fermi level, the PGCM based on axial states is able to track the exact 2_1^+ excitation energy very closely all the way to the border of the sd shell, i.e. up to ^{30}Ne . However, the reproduction of the 4_1^+ excitation energy is already quite off in the middle of the shell such that the $\Delta E_1^{4^+}/\Delta E_1^{2^+}$ ratio does not track the steep decrease visible in both the data and the FCI results. Enlarging the PGCM ansatz to include triaxial states significantly improves the situation up to ^{24}Ne , in particular by capturing the drop of the ratio that is not described correctly in the PGCM ab initio calculations (see Fig. 4.12). Thus, enriching the PGCM ansatz itself can help significantly prior to resorting to an explicit account of dynamical correlations. Beyond ^{26}Ne both sets of PGCM calculations reproduce FCI results very well, which is somewhat anecdotal given the smallness of the configuration space as one reaches the end the sd shell and given that sd-shell valence space calculations based on traditional empirical interactions do not reproduce the physics of the island of inversion anyway.

Having learnt that adding triaxiality can improve the low-lying spectroscopy of certain isotopes, PGCM calculations of $^{20,24,30}\text{Ne}$ have been extended to include this degree of freedom into the PGCM ansatz. Corresponding results are shown in Fig. 4.14.

Starting with ^{20}Ne , one observes that the already well reproduced spectroscopy is not spoiled by the addition of triaxial configurations. More specifically, excitation energies are barely modified whereas $B(E2)$ transition strengths within both bands are decreased, in a way that is more consistent with experimental data for the ground-state band.

In the valence-space results presented in Fig. 4.13, the addition of triaxial configurations were mostly useful to improve the behavior of the $\Delta E_1^{4^+}/\Delta E_1^{2^+}$ ratio around mid shell. In the ab initio calculation, the ground-state band is marginally compressed in ^{24}Ne , moving it slightly away from IM-NCSM results and experimental data. Correspondingly, the $\Delta E_1^{4^+}/\Delta E_1^{2^+}$ ratio is only marginally lowered from 2.78 in the axial calculation to 2.67 in the triaxial one, i.e the inclusion of the triaxial degree of freedom does not bring the improvement that could be expected from valence-space calculations.

Let us now come to the most challenging ^{30}Ne isotope located in the island of inversion. As for the axial PGCM calculation, one first notices that the rotational behavior of the experimental ground-state band is not reproduced by the IM-NCSM calculation. Thus, one cannot exclude that the computed band is not the correct one, especially given that the trend of IM-NCSM ground-state binding energies precisely presents a glitch in ^{30}Ne as observed earlier in Fig. 4.9. As a matter of fact, the problem of the PGCM calculation relates to the fact that the excited intruder positive-parity band is probably the right candidate for the ground-state band, only that it is wrongly positioned above the spherical one. Indeed, both excitation energies with respect to the band-head and intra-band $B(E2)$ transitions are consistent with experimental data. This failure is consistent with the large gap between the sd and pf shells observed in the PGCM Baranger neutron spectrum (Fig. 4.10) that is a fingerprint of the lack of cross-shell correlations in the computed ground-state. While incorporating full dynamical correlations must correct for this defect, a more efficient strategy could consist in enriching the PGCM ansatz. As seen from the lower panel of Fig. 4.14, the triaxial PGCM does compress the intruder band and lower it slightly, but not nearly enough. At this point in time, one is thus left with two scenarios (i) the account of missing dynamical correlations inverses the order of the two bands or (ii)

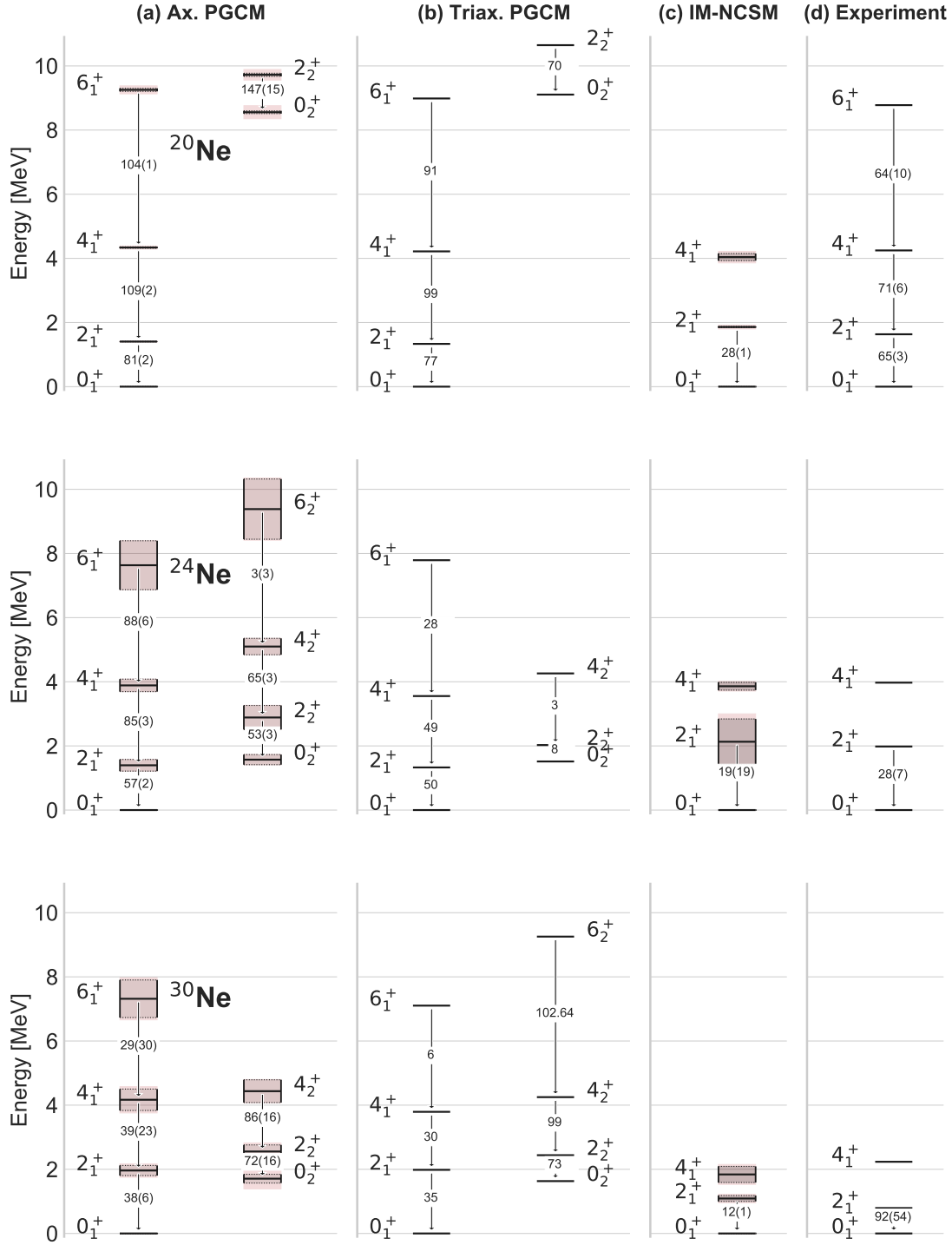


Figure 4.14. (Color online) First two positive-parity bands in $^{20,24,30}\text{Ne}$. The $E2$ transition strengths (in $\text{e}^2 \text{fm}^4$) are indicated along vertical arrows. Panel (a): PGCM results obtained using HFB configurations in the axial (β_2, β_3) plane. Panel (b): PGCM results obtained adding triaxially deformed HFB configurations. Panel (c): IM-NCSM results. Panel (d): experimental data. PGCM results in panel (a) display model-space (black box) plus χEFT (pink band) uncertainties. IM-NCSM results in panel (c) display total many-body (black box) plus χEFT (pink band) uncertainties. The N^3LO χEFT Hamiltonian with $\lambda_{\text{srg}} = 1.88 \text{ fm}^{-1}$ ($\lambda_{\text{srg}} = 2.23 \text{ fm}^{-1}$) is employed in PGCM (IM-NCSM) calculations.

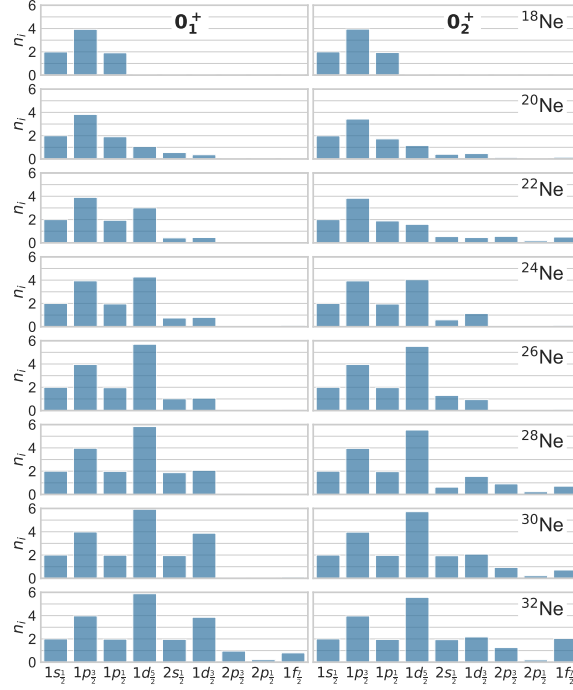


Figure 4.15. (Color online) Average neutron natural orbital occupations (including the $2j + 1$ degeneracy factor) for the first two PGCM 0^+ states of $^{18-32}\text{Ne}$. Calculations employ the N^3LO χEFT Hamiltonian with $\lambda_{\text{srg}} = 1.88 \text{ fm}^{-1}$.

further enriching the PGCM ansatz brings it down¹⁶, decreasing or even cancelling the need for dynamical correlations to operate the inversion. Still, given that the IM-NCSM ground-state band is not rotational (even within estimated uncertainties) and that the $\Delta E_1^{4+}/\Delta E_1^{2+}$ ratio is in fact close to the PGCM value, one must contemplate the fact that the Hamiltonian is to be blamed, i.e. that the associated uncertainties are underestimated.

Natural orbitals average occupation

To further analyze the results displayed above, the (non-observable) average occupation of neutron natural orbitals, i.e. the eigenvalues of the PGCM one-body density matrix, are displayed in Fig. 4.15 for the first two 0^+ states in $^{18-32}\text{Ne}$. The $^{28-30}\text{Ne}$ data confirm that, within the present theoretical calculation, the band built on the excited 0_2^+ state is the intruder band benefiting, although not enough at the strict PGCM level, from correlations built out of particle-hole excitations into the pf shell. Contrarily, the pf natural orbitals display zero occupation in the 0_1^+ ground-state in these two isotopes belonging to the island of inversion. Again, while enriching the PGCM ansatz can improve the situation, adding dynamical correlations associated with explicit particle-hole excitations into the pf shell is likely to be necessary to make the intruder band become the ground-state one.

¹⁶A preliminary study indicates that generating the Bogoliubov states via a variation after projection on particle number (VAPPN) calculation [135] does go in the right direction but it is not sufficient to invert the two bands per se.

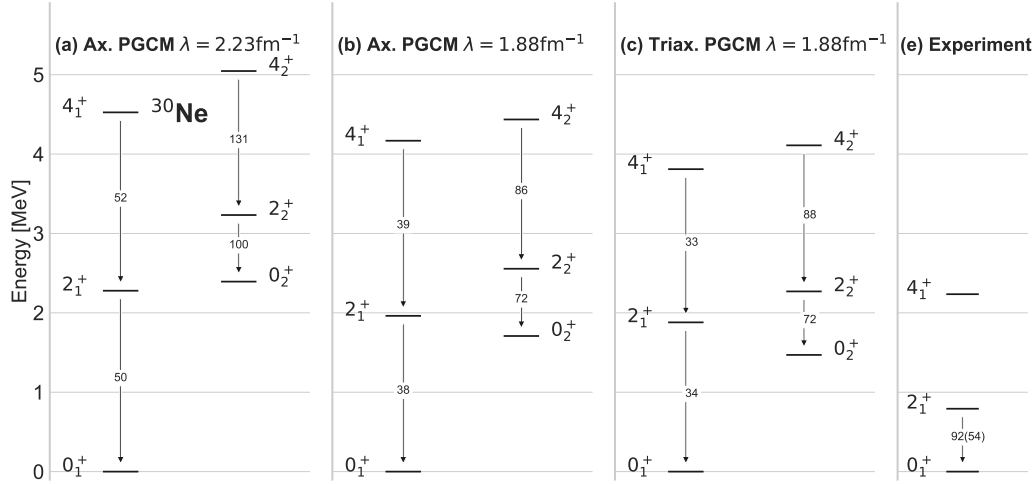


Figure 4.16. (Color online) Adaptation of the lower panel of Fig. 4.14 via the addition of the axial PGCM results obtained from the $N^3\text{LO } \chi\text{EFT}$ Hamiltonian $\lambda_{\text{srg}} = 2.23 \text{ fm}^{-1}$.

		^{18}Ne	^{20}Ne	^{22}Ne	^{24}Ne	^{26}Ne	^{28}Ne	^{30}Ne	^{32}Ne
$\Delta E_1^{J^+}$	2+	21.6	0.5	1.4	6.1	5.6	12.0	16.1	5.6
	4+	23.5	1.5	0.6	5.3	1.6	3.2	8.6	0.4
$M1$	2+	13.6	0.1	5.9	1.2	4.2	0.5	7.2	1.6
	4+	11.3	0.0	4.5	4.5	3.2	5.0	3.7	0.3
$Q2$	2+	32.6	20.2	16.6	21.5	17.8	19.0	26.8	16.4
	4+	32.9	22.9	17.5	21.2	18.3	21.1	10.0	16.6
r_{ch}	0+	7.1	6.1	5.6	5.9	5.7	5.6	5.4	5.3

Table 4.1. Percentage of variation of selected PGCM results along the Neon isotopic chain for $\lambda_{\text{srg}} \in [1.88, 2.23] \text{ fm}^{-1}$.

SRG dependence

The above PGCM results have been obtained from the Hamiltonian characterized by $\lambda_{\text{srg}} = 1.88 \text{ fm}^{-1}$. Figure 4.16 illustrates the variation of the PGCM low-lying spectroscopy in ^{30}Ne when using $\lambda_{\text{srg}} = 2.23 \text{ fm}^{-1}$. Softening the Hamiltonian from $\lambda_{\text{srg}} = 2.23 \text{ fm}^{-1}$ to $\lambda_{\text{srg}} = 1.88 \text{ fm}^{-1}$, the PGCM spectrum is compressed, and the intruder band lowered, by as much as what was produced by the addition of triaxial configurations.

As visible from Tab. 4.1, ^{30}Ne is one of the two isotopes in which the sensitivity of the spectrum is the largest, i.e. of the order of 10 – 20%. Contrarily, the first 2^+ and 4^+ states in ^{20}Ne only vary by about 1% under the same modification of λ_{srg} . Among the selected quantities, the spectroscopic quadrupole moment appears to be the most sensitive one, with variations of the order of 20% throughout the isotopic chain. It will be of interest to investigate how much these variations are tamed down by the inclusion of dynamical correlations on top of PGCM.

Spectroscopic observables

A last set of spectroscopic quantities are displayed in Fig. 4.17. As visible from the upper panel, the situation for the $B(E2 : 2_1^+ \rightarrow 0_1^+)$ is similar to the one encountered for

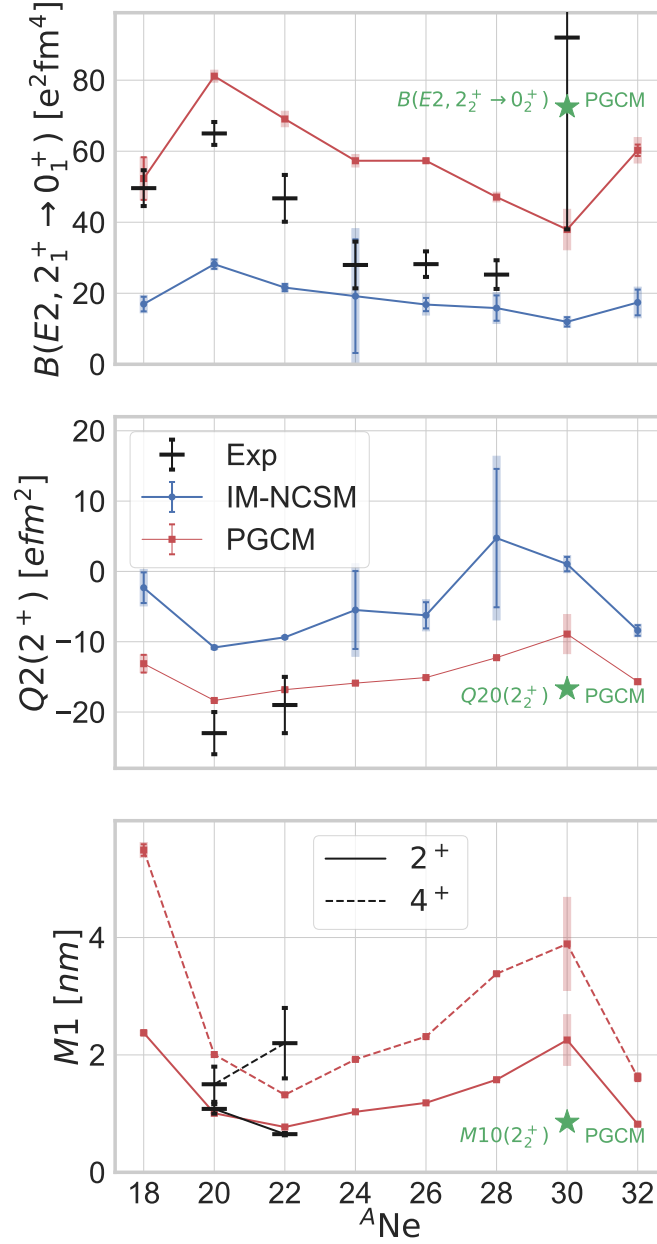


Figure 4.17. (Color online) Theoretical (PGCM, IM-NCSM) and experimental electromagnetic moments along the Neon isotopic chain. Upper panel: reduced electric quadrupole transition $B(E2 : 2_1^+ \rightarrow 0_1^+)$ to which is added the PGCM $B(E2 : 2_2^+ \rightarrow 0_2^+)$ value in ^{30}Ne . Middle panel: spectroscopic electric quadrupole moment of the first 2^+ state. Lower panel: spectroscopic magnetic dipole moment of the first 2^+ and 4^+ states. PGCM calculations are performed in the axial (β_2, β_3) plane. The N^3LO χEFT Hamiltonian with $\lambda_{\text{srg}} = 1.88 \text{ fm}^{-1}$ ($\lambda_{\text{srg}} = 2.23 \text{ fm}^{-1}$) is employed in PGCM (IM-NCSM) calculations.

rms charge radii earlier on. IM-NCSM transition probabilities are too small below ^{24}Ne , accurate between ^{24}Ne and ^{28}Ne and quite far off in ^{30}Ne even though the experimental error bar are large. Contrarily, the collective character of the PGCM makes the $B(E2 : 2_1^+ \rightarrow 0_1^+)$ to be well reproduced below ^{24}Ne and overestimated between ^{24}Ne and ^{28}Ne . In ^{30}Ne , the E2 transition is again too small because the first band does not correspond to the experimental one. As visible from the added point on the figure, the $B(E2 : 2_2^+ \rightarrow 0_2^+)$ of the intruder band is in better agreement with the experimental value.

In the middle panel, the PGCM spectroscopic quadrupole moment of the first 2^+ state reproduces well experimental data in $^{20,22}\text{Ne}$, confirming once more the adequacy of the PGCM description of these two nuclei. PGCM results differ from IM-NCSM values that are too small, probably due to a lack of collective character. Last but not least, the PGCM spectroscopic dipole moment of the first 2^+ and 4^+ nicely account for the available experimental data in $^{20,22}\text{Ne}$.

Accessing experimental electromagnetic moments in more neutron-rich isotopes would allow one to better investigate the consistency of the picture that emerges from our theoretical study and would thus be welcome in the future.

4.4. Discussion

This chapter proposed an extensive ab initio study of neon isotopes based on projected generator coordinate method calculations, in comparison with IM-NCSM. The main conclusion is that, in spite of missing so-called dynamical correlations, PGCM is shown to be a suitable ab initio method to address the low-lying spectroscopy of complex nuclei within theoretical uncertainties. For instance, the energy spectrum and electric multipole transition strengths of the low-lying parity-doublet bands in ^{20}Ne are reproduced by taking into account the effect of dynamical octupole fluctuations.

Still, describing absolute binding energies, accounting consistently for a wide range of spectroscopic observables, tackling many nuclei displaying different characteristics and achieving high accuracy, eventually requires the inclusion of dynamical correlations on top of the PGCM. In fact, certain salient features, such as the physics of the island of inversion around ^{30}Ne , require this inclusion from the outset to achieve a qualitatively correct description. This incorporation is now possible thanks to the novel multi-reference perturbation theory (PGCM-PT) formulated in Chapter 2. The first PGCM-PT results are presented in the following chapter. The key question behind the present work and the associated many-body developments regards the optimal way to consistently incorporate static and dynamical correlations in view of describing complex nuclei. We are only at the beginning of this journey, hence finding this optimal strategy will require time and a significant amount of trial-and-error. Chapter 5 represents a first step in this direction.

Chapter 5.

Results: PGCM-PT(2)

Contents

5.1. Introduction	105
5.2. Many-body calculations	107
5.2.1. VSRG pre-processing	107
5.2.2. VSRG+MR-IMSRG pre-processing	119
5.3. Discussion	128

5.1. Introduction

As explained in the introduction of Chapter 2 a key challenge in nuclear many-body theories regards the optimal way to consistently capture both static and dynamical correlations within expansion methods. While doubly closed-shell nuclei are dominated by (weak) dynamical correlations, efficiently captured through a coherent sum of (mostly low-rank) particle-hole excitations of a symmetry-conserving unperturbed product state, open-shell nuclei display strong static correlations that cannot be conveniently accounted for in this way. This makes it necessary to design expansion methods based on more general unperturbed states that can already capture static correlations. The corresponding rationale was schematically illustrated in Fig. 2.1.

A good candidate to provide appropriate unperturbed states is the PGCM. The main conclusion of Chapter 4 is that the PGCM is suitable to address the low-lying spectroscopy of complex nuclei within reasonable theoretical uncertainties in spite of missing dynamical correlations. For instance, the energy spectrum and electric multipole transition strengths of the low-lying parity-doublet bands in ^{20}Ne were reproduced by taking into account both quadrupole and octupole collective fluctuations.

Still, describing absolute binding energies, accounting consistently for a wide range of spectroscopic observables, tackling a large class of nuclei displaying different characteristics and achieving high accuracy eventually requires the inclusion of dynamical correlations on top of the PGCM. This coherent incorporation is now possible thanks to the novel multi-reference perturbation theory (PGCM-PT) formulated in Chapter 2 that embeds the PGCM within a systematic *symmetry-conserving* expansion method.

The objective of the present chapter is to discuss first proof-of-principle results of second-order PGCM-PT, i.e. PGCM-PT(2), calculations in three selected nuclei, i.e. the doubly closed-shell ^{16}O , the singly open-shell ^{18}O and the doubly open-shell ^{20}Ne that was studied at length at the PGCM level in Chapter 4.

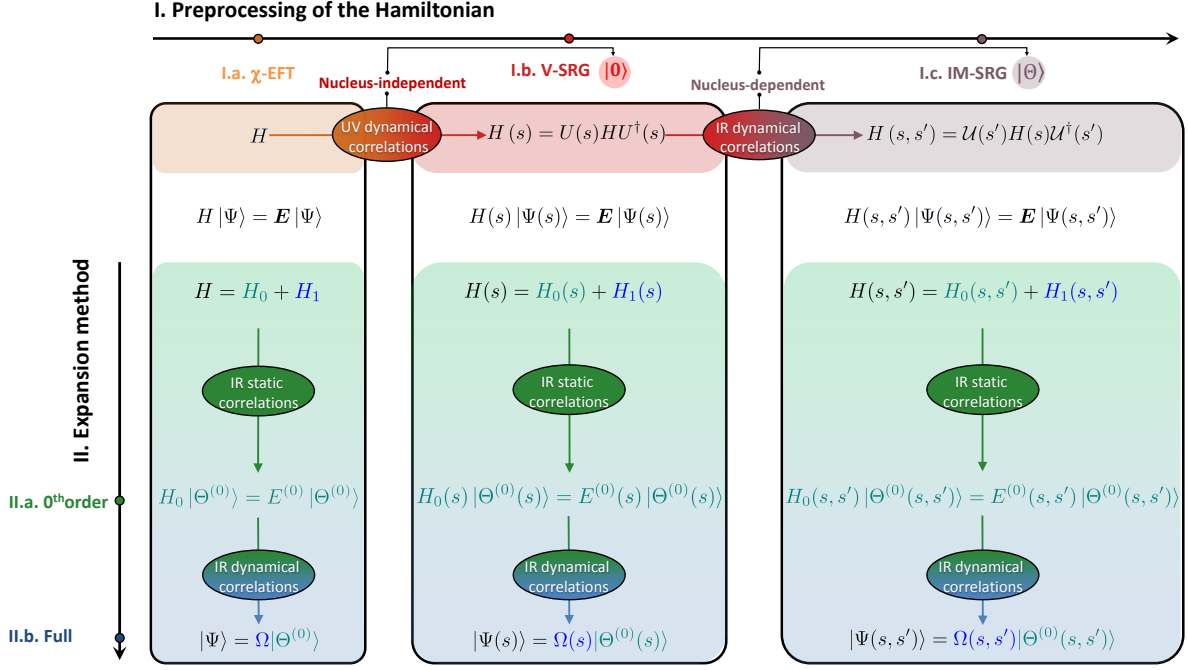


Figure 5.1. (color online) Schematic workflow of expansion many-body methods (vertical axis) versus potential pre-processings of the Hamiltonian (horizontal axis). Unitary vacuum (in-medium) similarity renormalization group transformations denote a nucleus-independent (nucleus-dependent) pre-processing of the Hamiltonian.

In addition to displaying the first set of PGCM-PT(2) results, the goal of the present work is to do so while exploiting an additional degree of freedom at our disposal in quantum many-body calculations, i.e. the possible pre-processing of the Hamiltonian via, e.g., in-medium (nucleus-dependent) unitary similarity renormalization group (IMSRG) transformations. While the nucleus-independent pre-processing of the Hamiltonian via vacuum unitary similarity renormalization group (VSRG) transformations has already become a standard tool to pre-sum UV dynamical correlations via a decoupling of a low-energy subspace from higher momentum modes, nucleus-dependent transformations can be exploited more systematically to pre-sum IR dynamical correlations.

The single-reference IMSRG (SR-IMSRG) method [34] applicable to closed-shell systems can fully decouple the unperturbed product state from the rest of the Hilbert space, i.e. from the \mathcal{Q} space, and thereby make it the actual ground-state of the pre-processed Hamiltonian at the end of the flow. In this case, the wave operator eventually becomes nothing but the identity operator and the expansion method is trivial. The more general multi-reference IMSRG (MR-IMSRG) method [57] applicable to all nuclei does not fully decouple the unperturbed state from the associated \mathcal{Q} space such that non-zero dynamical correlations remain to be included via a non-trivial, e.g. PGCM-PT, wave operator. While quite negligible on absolute energies, these remaining dynamical correlations will be shown to be mandatory to describe low-lying excitation spectra.

Eventually, a clear picture will emerge that is schematically illustrated in Fig. 5.1 (generalizing Fig. 2.1). Three complementary levers must be consistently exploited to efficiently capture correlations within expansion many-body methods in order to describe (complex) nuclei

1. the pre-processing of the Hamiltonian,
2. the possibly non-trivial nature of the unperturbed state,
3. the rationale of the expansion.

While each lever is best suited to capture a certain category of correlations, the latter are not orthogonal such that the ideal way to share the load is unclear and will require extensive trial-and-error in the future. The present work wishes to contribute to this (probably) long-term endeavor.

The present chapter is organized as follows. Section 5.2.1 details the results obtained in ^{16}O , ^{18}O and ^{20}Ne on the basis of (the two-body part of) a chiral effective field theory (χEFT) Hamiltonian pre-processed via VSRG. Section 5.2.2 then elaborates on the impact of further pre-processing the Hamiltonian via MR-IMSRG transformations on the results. The conclusion of the present chapter are provided in Sec. 5.3. Apps. L, M, N and O are directly completing this chapter with details on the numerical resolution.

5.2. Many-body calculations

The reader is referred to Chapter 2 for all necessary details about the PGCM-PT formalism as well as to Refs. [22, 111, 112] and Refs. [37, 129, 153] for vacuum and in-medium IMSRG methods, respectively. The PGCM-PT(2) solver is built on top of an axially-deformed Hartree Fock Bogoliubov (HFB) code and a consistent PGCM solver (see App. P) allowing for the projections on good particle number, angular momentum and parity.

5.2.1. VSRG pre-processing

Proof-of-principle calculations are performed using the spherical harmonic oscillator (HO) basis of the one-body Hilbert space \mathcal{H}_1 characterized by an oscillator frequency $\hbar\omega = 20$ MeV and 5 oscillator shells ($e_{\text{max}} = 4$).

The next-to-next-to-next-to-leading (N^3LO) χEFT Hamiltonian introduced in Ref. [130] and evolved via VSRG to the low-momentum resolution scale $\lambda_{\text{vsrg}} = 1.88 \text{ fm}^{-1}$ is employed. Thus, UV dynamical correlations are already processed via the VSRG decoupling of low- and high-momentum modes.

In these proof-of-principle calculations, only the two-body part of the evolved Hamiltonian is actually retained. Thus, the goal is not to reproduce experimental data but rather to benchmark PGCM-PT(2) results against those obtained from Full Configuration Interaction (FCI) calculations in the same $e_{\text{max}} = 4$ space. The FCI calculations rely on a sequence of N_{max} -truncated spaces up to $N_{\text{max}} = 8$ embedded into the $e_{\text{max}} = 4$ space¹. The results are extrapolated to the full $e_{\text{max}} = 4$ model space limit such that FCI results come with an uncertainty associated with this extrapolation².

Additional many-body methods are also included for comparisons. First, the sub-cases of PGCM and PGCM-PT obtained by only using one "seed" HFB state, i.e. omitting the GCM part of the calculation, are considered and referred to as PHFB and PHFB-PT methods. The case where the projection part is further omitted is utilized as well.

¹FCI results are provided by R. Roth [138].

²The uncertainties on excitation energies do not originate from this extrapolation but are taken from the difference between the results obtained for the largest $N_{\text{max}} = 8$ and the smallest space. Excitation energies are more accurate than absolute ones because they converge faster with N_{max} .

This single-reference limit of PGCM-PT has been formally elaborated on in Chapter 2 and denotes a symmetry-breaking scheme in case the seed state (i.e. the unperturbed state in this case), is itself symmetry breaking. This limit will be also compared to the standard single-reference symmetry-breaking Bogoliubov many-body perturbation theory (BMBPT) [45, 46, 47, 53, 60] (see App. E for details).

In the present section, three nuclei of increasing complexity are studied. In each case, a different collective coordinate q is employed at the constrained HFB (cHFB) level and for the subsequent GCM mixing. The characteristics of the associated mean-field, PGCM and PGCM-PT calculations are:

1. Doubly closed-shell ^{16}O :
 - spherically-symmetric Hartree-Fock (HF) states,
 - constraint on the root-mean-square (rms) matter radius ($q \equiv r_{\text{rms}}$),
 - no symmetry projection is needed.
2. Singly open-shell ^{18}O :
 - spherically-symmetric HFB states,
 - constraint on the pairing gap ($q \equiv \delta$ [105]),
 - projection of neutron number N is performed.
3. Doubly open-shell ^{20}Ne :
 - axially-deformed HFB states,
 - constraint on the axial quadrupole moment ($q \equiv q_{20}$),
 - projections on good angular momentum J are performed (for the deformations considered in the present chapter, ^{20}Ne does not spontaneously break particle number symmetry at mean-field level, and projection on N and Z is trivial).

^{16}O

In doubly closed-shell systems, the mean-field solution is nothing but a spherical HF state. Since the rms radius operator employed to perform constrained calculations commutes with the total angular momentum J^2 , all mean-field states involved in the ^{16}O calculation carry good symmetry quantum numbers and no symmetry projection is necessary in the subsequent PGCM and PGCM-PT calculations, hence we simply refer to them as GCM and GCM-PT, respectively.

The ground-state total energy curves (TECs) of ^{16}O are displayed in Fig. 5.2 as a function of the rms radius r_{rms} of the (underlying) HF vacua. One first observes that cHF and GCM results are underbound compared to FCI by about 20 MeV (12%), missing significant IR dynamical correlations. In the present case, the GCM³ adds essentially no energy to the HF minimum (i.e. 165 keV), which signals that static IR collective correlations are marginal in such a doubly closed-shell nucleus.

Given the negligible character of static correlations, ^{16}O acts as a good benchmark for the (P)GCM-PT formalism. First, its single-reference reduction HF-PT(2) is, as formally demonstrated in Chapter 2, identical to *canonical* MBPT(2), i.e. Møller-Plesset MBPT

³The GCM and GCM-PT(2) calculations are presently performed on the basis of the five cHF states visible on the TEC.

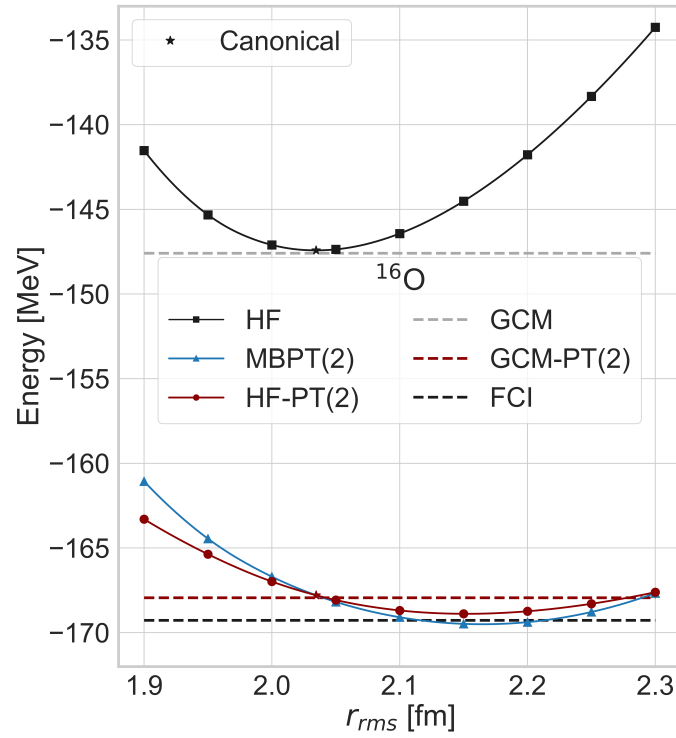


Figure 5.2. (Color online) Ground-state energy of ^{16}O as a function of r_{rms} of the (underlying) HF vacua. Calculations are performed with $\hbar\omega = 20$ MeV and $e_{\text{max}} = 4$ as well as with the two-body part of the N^3LO χEFT Hamiltonian evolved to $\lambda_{\text{vsrg}} = 1.88 \text{ fm}^{-1}$.

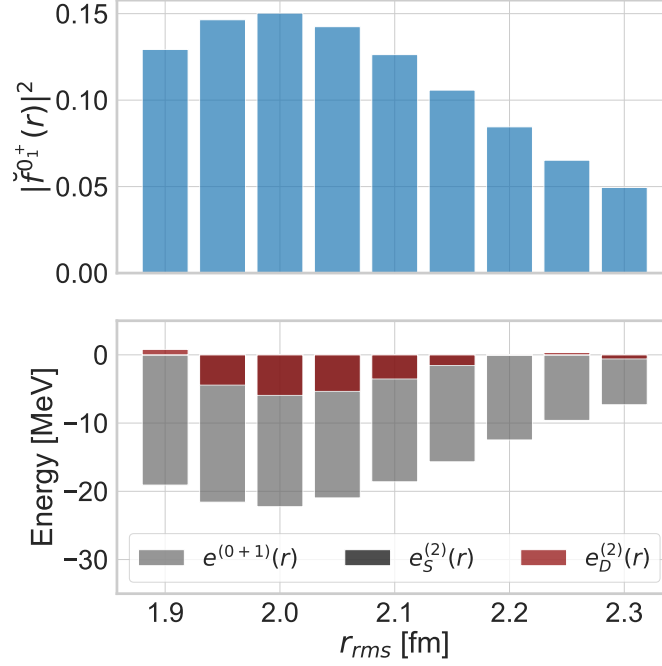


Figure 5.3. (Color online) Upper panel: collective ground-state GCM wave-function probability distribution ($|\check{f}_1^{0+}(r_{\text{rms}})|^2$) in ^{16}O as a function of the rms radius of the underlying HF vacua. Lower panel: contributions to GCM ($e_0^{(0+1)}(r_{\text{rms}})$) and GCM-PT(2) ($e_S^{(2)}(r_{\text{rms}}) + e_D^{(2)}(r_{\text{rms}})$) ground-state energies as a function of r_{rms} . GCM-PT(2) contributions are split into single (one-particle/one-hole) and double (two-particle/two-hole) excitations. Calculations are performed with $\hbar\omega = 20$ MeV and $e_{\text{max}} = 4$ as well as with the two-body part of the N^3LO χEFT Hamiltonian evolved to $\lambda_{\text{vsrg}} = 1.88 \text{ fm}^{-1}$.

based on the unconstrained HF solution at the minimum of the TEC. While the respective partitionings of the Hamiltonian provide slightly different results away from the minimum of the HF TEC, they are qualitatively and quantitatively similar. The minima of the two TECs are close to the FCI result. However, perturbation theories are not variational such that it is difficult to argue that these values are to be preferred to canonical ones. As a matter of fact MBPT(3) (not shown) does not flatten the curve in the vicinity of the lowest MBPT(2) value⁴.

Focusing on the canonical point, one observes that GCM-PT(2) is consistent with MBPT(2)/HF-PT(2), i.e. it only adds 146 keV static correlation energy. This consistency constitutes a validation of GCM-PT(2) knowing that it is formally very different from MBPT(2) and relies on a completely different numerical procedure as can be appreciated from the details given in App. M and N.

Furthermore, this consistency sheds some light on single-reference MBPT(2)/HF-PT(2) results. The upper panel of Fig. 5.3 shows that, while the GCM ground-state collective wave-function spreads over a large interval of r_{rms} values due to nuclear-size fluctuations, the Hamiltonian dictates that the contributions to the left of the HF minimum, i.e. for

⁴MBPT(2) and MBPT(3) energies are more consistent between each other in the vicinity of the canonical point than away from it, indicating some *empirical* sign of convergence (although convergence of perturbation theory cannot be inferred from lowest orders). This encourages us to prefer the canonical values at this point.

$q < r_{\text{rms}} = 2.03 \text{ fm}$, dominate it. From the energetic viewpoint, the lower panel of Fig. 5.3, which shows the decomposition⁵ of the GCM energy as a function of r_{rms} , demonstrates that the largest contributions originate from configurations centered around the HF minimum. Next⁶, the lower panel also illustrates that the physically-informed weights in the GCM unperturbed state propagate to GCM-PT(2) such that configurations around the HF minimum contribute the most to the second-order correction whereas those associated with the lowest MBPT(2)/HF-PT(2) values around $r_{\text{rms}} \in [2.1, 2.2] \text{ fm}$ are largely subleading. Eventually, the total GCM-PT(2) energy is nearly identical to canonical MBPT(2)/HF-PT(2) results. This definitely gives more credit to low-order MBPT(2)/HF-PT(2) energies obtained at the canonical point than to those obtained at smaller and larger values of r_{rms} . Interestingly, one also observes that the GCM-PT(2) energy correction is dominated by double (two-particle/two-hole) excitations given that the energy contribution of single (one-particle/one-hole) excitations is negligible at all values of r_{rms} . While this feature can be expected at the canonical point given that single excitations do not contribute to MBPT(2)/HF-PT(2)⁷, it is not obviously the case away from it.

Eventually, the GCM-PT(2) binding energy is 0.8% away from the FCI result. A common theme throughout the chapter regards the best way to go to even greater accuracy. At this point, one can either hope to enrich the PGCM unperturbed state by selecting a potentially pertinent additional collective coordinate q and/or go to PGCM-PT(3)⁸. An additional degree of freedom to achieve such a goal will be introduced in Sec. 5.2.2.

¹⁸O

The singly open-shell ¹⁸O constitutes the first nucleus in which static correlations are expected to be significant. In this particular case, static correlations relate to superfluidity and thus translate first into the spontaneous breaking of the $U(1)$ global-gauge symmetry associated with particle number conservation at the HFB level. Correspondingly, the pairing gap operator is used there as a constraint to vary the amount of pairing correlations in the HFB seeds [105]. As a next step, further static correlations are captured via the restoration of good neutron number and the inclusion of pairing fluctuations through the PGCM.

The ground-state TECs of ¹⁸O are displayed in Fig. 5.4 as a function of the pairing constraint⁹ δ of the (underlying) HFB vacua. While the PHFB TEC follows the HFB one, it is less bound, e.g. by 1.2 MeV at the canonical point. The fact that the particle-number projection after variation (PNPAV) decreases the binding reflects the fact that the distribution of particle numbers in the HFB state around the average is distorted towards heavier systems. In the next step, the GCM mixing associated with the inclusion of pairing fluctuations provide negligible correlation energy compared to the PNPAV that provides the essential IR static correlations.

Similarly to ¹⁶O, PGCM strongly underbinds the FCI result by about 25 MeV ($\sim 13\%$),

⁵The PGCM collective wave function and the contribution of each value of the collective coordinate $e_0^{(0+1)}(r_{\text{rms}})$ to the PGCM energy are introduced in App. J.

⁶The decomposition of the PGCM-PT(2) correlation energy is provided in Eq. (2.56).

⁷This is a consequence of Brillouin theorem, inducing a decoupling between the reference state and singles excitations at the canonical point.

⁸The derivation and implementation of the third order being much more intricate (see for example [154], going to the next order in perturbation is probably not the right way to improve the results at this point.

⁹By definition $\delta = 1$ corresponds to the canonical, i.e. unconstrained, HFB solution.

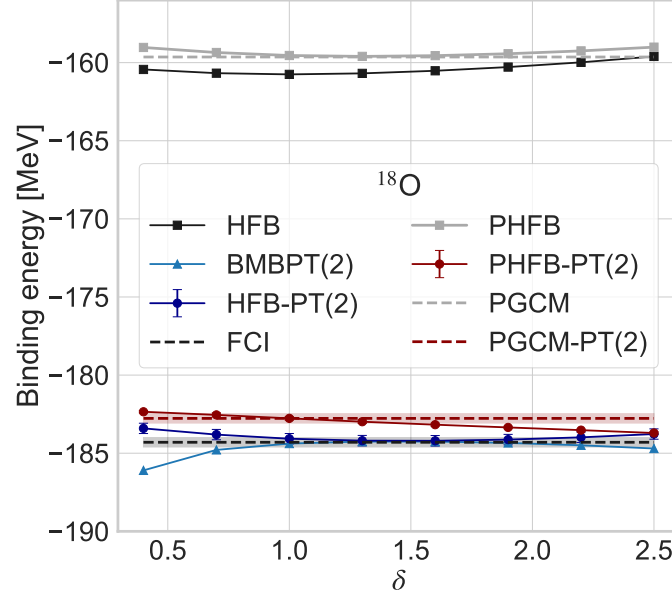


Figure 5.4. Ground-state energy of ^{18}O as a function of the pairing constraint δ calculated from various many-body methods with $\hbar\omega = 20$ MeV and $e_{\text{max}} = 4$. The two-body part of the N^3LO χEFT Hamiltonian evolved to $\lambda_{\text{vsrg}} = 1.88 \text{ fm}^{-1}$ is employed.

thus missing significant IR dynamical correlations. While formally not identical to canonical BMBPT(2), the single-reference reduction of PGCM-PT(2), here denoted by HFB-PT(2), capture dynamical correlations on top of HFB. Results of both methods are very similar and they agree with FCI within uncertainties.

While impressive, this close agreement is accidental and somewhat spurious. Indeed, PHFB-PT(2), which actually corrects for the $U(1)$ breaking of HFB-PT(2), pushes the energy up by about 1.5 MeV away from the FCI result at the canonical point. This number is close to the difference between HFB and PHFB mentioned above. This is the first example that demonstrates the impact of exactly restoring symmetries within (perturbative) expansion methods. Adding the GCM mixing into the unperturbed state, the PGCM-PT(2) result remains consistent with canonical PHFB-PT(2) within uncertainties.

Going away from the canonical point, BMBPT(2) and HFB-PT(2) differ. This behavior reflects the different nature of the partitionings used by both expansions, which is magnified when we move away from the canonical point. At the same time, PHFB-PT(2) becomes less (more) bound than PGCM-PT(2) as δ becomes smaller (greater) than 1. Once again, these behaviors do not instill trust in perturbative results away from the canonical point. Thankfully, PGCM-PT(2) is better controlled given that the configurations associated with different values of the collective coordinate δ enter the unperturbed PGCM state with weights dictated by the physical Hamiltonian. As shown in Fig. 5.5, the collective PGCM wave-function spreads significantly on both sides of the canonical point with a maximum located to the left of it ($\delta = 0.7 < 1$). While the decomposition of the PGCM energy reflects this distribution, the second-order correction is flatter with δ but also favors values smaller than 1. Eventually, the PGCM-PT(2) binding energy is very close to the canonical PHFB-PT(2) energy and lies 1.5 MeV (0.8%) above the FCI result.

Still, PGCM-PT(2) and PHFB-PT(2) results carry error bars associated with the approximate solution of the linear system at play in the formalism (see Eq. (2.53)).

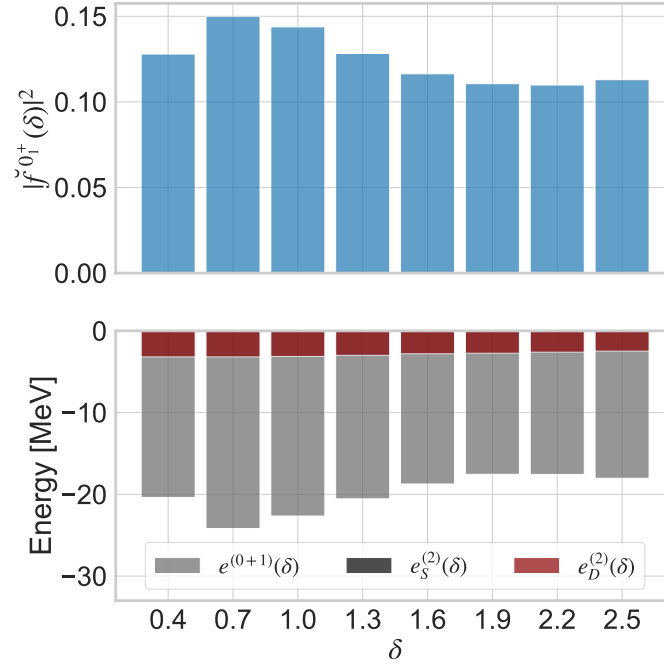


Figure 5.5. (Color online) Upper panel: collective ground-state PGCM wave-function probability distribution ($|f_0^+(\delta)|^2$) in ^{18}O as a function of the pairing constraint δ characterizing the underlying HFB vacua. Lower panel: contributions to the PGCM ($e_0^{(0+1)}(\delta)$) ground-state energy and to the PGCM-PT(2) ($e_S^{(2)}(\delta) + e_D^{(2)}(\delta)$) correlation energy. The latter is split into single (two quasi-particle) and double (four quasi-particle) contributions. Calculations are performed with $\hbar\omega = 20$ MeV and $e_{\text{max}} = 4$, using the two-body part of the N^3LO χEFT Hamiltonian evolved to $\lambda_{\text{vsrg}} = 1.88 \text{ fm}^{-1}$.

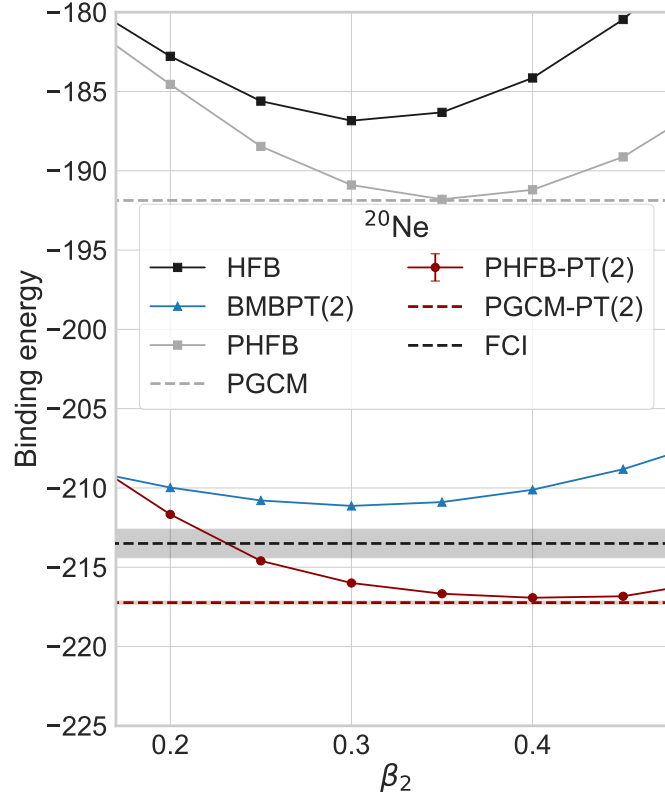


Figure 5.6. Ground-state energy of ^{20}Ne as a function of the axial quadrupole deformation β_2 of the (underlying) HFB states. Calculations are performed with $\hbar\omega = 20$ MeV and $e_{\text{max}} = 4$ using the two-body part of the N^3LO χEFT Hamiltonian evolved to $\lambda_{\text{vsrg}} = 1.88 \text{ fm}^{-1}$.

Due to its large dimension, this linear system is solved iteratively as discussed in App. M, inducing a precision uncertainty evaluated through Eq. (M.19). This resolution is potentially further impacted by linear redundancies and intruder problems that are dealt with via the simultaneous use of a norm preconditioning and a complex shift γ as detailed in Apps. M.5.3 and N, respectively. While increasing the precision, the use of an overly too large complex shift may degrade the accuracy by generating a bias in the extracted value.

In ^{18}O , which qualifies as a difficult case, the iterative procedure can be converged in a stable fashion with a complex shift $\gamma = 10$ MeV, eventually leading to a ± 0.3 MeV precision on the PGCM-PT(2) energy¹⁰ that is visualized by a band in Fig. 5.4. While the central value reported in Fig. 5.4 is obtained for $\gamma = 10$ MeV, the bias (not reported on the figure) due to this complex shift pushes the PGCM-PT(2) energy up by about 1 MeV¹¹, and therefore causes a significant fraction of the 1.5 MeV (0.8%) disagreement with the FCI result.

¹⁰The precision on the PHFB-PT(2) is better (± 0.1 MeV) thanks to the lower dimension and the near diagonal character of the linear system.

¹¹This bias is estimated by varying the shift over the interval $\gamma \in [5, 15]$ MeV.

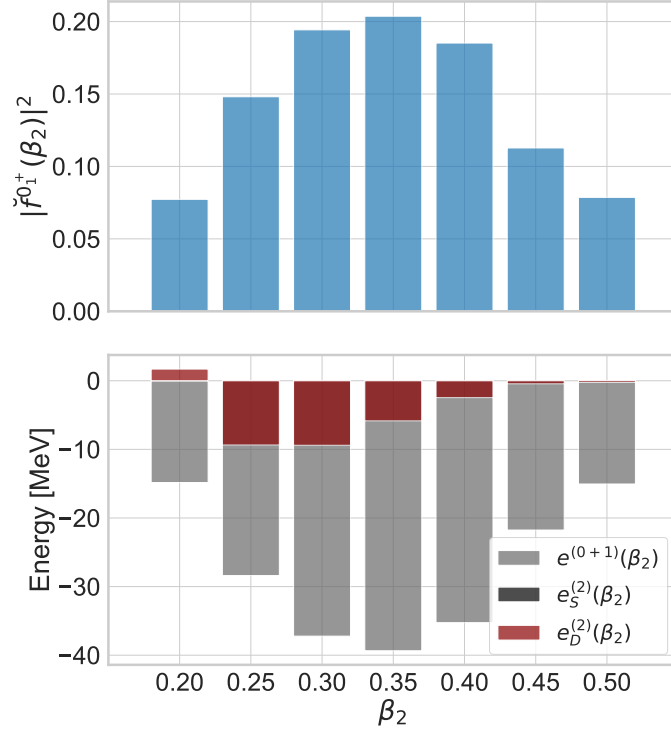


Figure 5.7. (Color online) Upper panel: collective ground-state PGCM wave-function probability distribution ($|f_0^{0+}(\beta_2)|^2$) in ^{20}Ne as a function of the axial quadrupole deformation (β_2) of the underlying HFB vacua. Lower panel: contributions to PGCM ($e_0^{(0+1)}(\beta_2)$) and PGCM-PT(2) ($e_S^{(2)}(\beta_2) + e_D^{(2)}(\beta_2)$) ground-state energies as a function of the axial quadrupole deformation (β_2) of the underlying HFB vacua. The PGCM-PT(2) contributions are split into singles (two quasi-particle) and doubles (four quasi-particle) contributions. Calculations are performed with $\hbar\omega = 20$ MeV and $e_{\text{max}} = 4$ using the two-body part of the N^3LO χEFT Hamiltonian evolved to $\lambda_{\text{vsrg}} = 1.88 \text{ fm}^{-1}$.

^{20}Ne

The doubly open-shell ^{20}Ne displays strong static correlations that manifest first through the breaking of $SU(2)$ rotational symmetry associated with angular momentum conservation at the HFB level. Accordingly, the axial quadrupole moment operator is used as a constraint to vary the deformation of the HFB seeds. As a next step, further static correlations are captured via the restoration of angular momentum and the inclusion of shape fluctuations through the PGCM. As demonstrated in Chapter 4, ^{20}Ne strongly benefits from breaking and restoring parity as well as from including octupole shape fluctuations. Still, the present calculations are restricted to axial quadrupole deformation, thus leaving some room for further improvement in the future. While $U(1)$ global gauge symmetry is also allowed to break spontaneously, it does not do so with the presently employed Hamiltonian such that all mean-field states actually reduce to (deformed) HF Slater determinants.

The ground-state TECs of ^{20}Ne are displayed in Fig. 5.6 as a function of the axial quadrupole deformation β_2 of the (underlying) HFB vacua. One first observes that the projection on J provides a significant energy gain of 5.5 MeV and moves the minimum of the PHFB TEC to larger deformation ($\beta_2 = 0.35$) than the canonical HFB minimum ($\beta_2 = 0.3$). The GCM mixing only adds 80 keV correlation energy given that the TEC

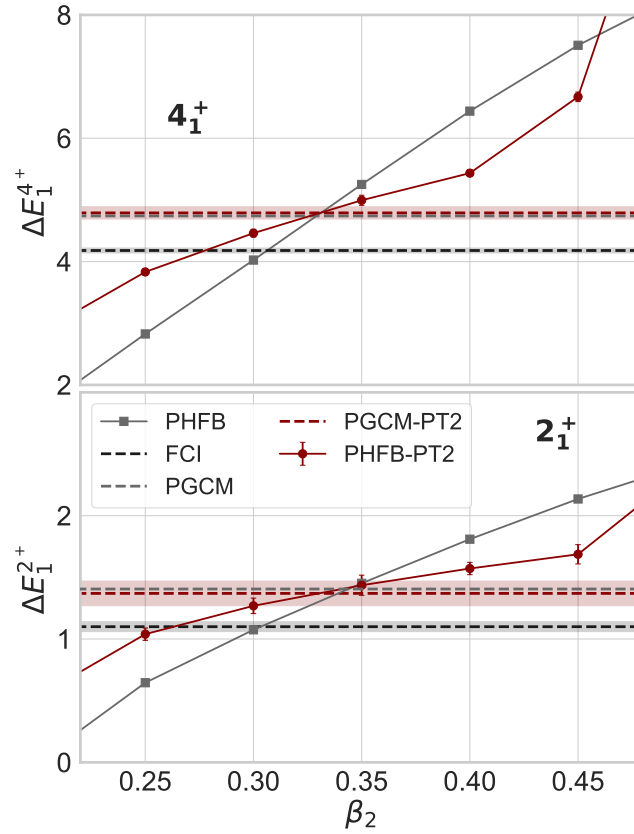


Figure 5.8. (Color online) Excitation energy in ^{20}Ne as a function of the axial quadrupole deformation (β_2) of the underlying HFB vacua. Top panel: first 4^+ state. Bottom panel: first 2^+ state. Calculations are performed with $\hbar\omega = 20$ MeV and $e_{\text{max}} = 4$ using the two-body part of the N^3LO χEFT Hamiltonian evolved to $\lambda_{\text{vsrg}} = 1.88 \text{ fm}^{-1}$.

is rather stiff along the axial quadrupole direction¹². Once again, static correlations are dominated by the symmetry restoration. Having included essential static correlations, the PGCM energy is still 21.7 MeV (10%) away from the FCI result, and misses significant dynamical correlations.

Stepping back to canonical HFB and adding dynamical correlations via BMBPT(2)¹³ lowers the energy by 24.6 MeV, yielding a result that is 2.6 MeV (1.2%) underbound compared to FCI¹⁴.

On the other hand, starting from the PHFB TEC and adding dynamical correlations via PHFB-PT(2) reduces the energy by 25.1/24.9/25.7 MeV at the HFB/PHFB/PHFB-PT(2) minimum, overshooting the FCI result by about 2.5/3.2/3.4 MeV (1.2/1.5/1.6%). While the difference between BMBPT(2) and PHFB-PT(2) TECs is similar to the difference between HFB and PHFB TECs, one observes that a consistent angular-momentum restoration favors larger deformations when adding dynamical correlations.

The mixing of quadrupole shapes in PGCM-PT(2) only adds 310 keV to the PHFB-PT(2) minimum. The PGCM-PT(2) result keeps a close memory of the PHFB-PT(2) minimum ($\beta_2 = 0.4$) rather than the PHFB-PT(2) value at the canonical HFB minimum ($\beta_2 = 0.3$). All in all, the PGCM-PT(2) energy¹⁵ overshoots FCI by 1.7%, and we keep in mind that this result is expected to improve via the inclusion of the octupole degree of freedom into the PGCM¹⁶.

In order to further analyse the theoretical content of the above results, Fig. 5.7 shows that the collective ground-state PGCM wave-function and the associated energy contributions are distributed rather symmetrically around the $J^\pi = 0^+$ PHFB minimum ($\beta_2 = 0.35$) of the TEC visible in Fig. 5.6 and spread over a large interval of β_2 values. Interestingly, dynamical correlations captured via PGCM-PT(2) favor configurations¹⁷ to the left of the HFB minimum ($\beta_2 = [0.25, 0.30]$). As a result, dynamical correlations could counterbalance the overestimated radii obtained at the PGCM level (see Fig. 4.11) due to the opposite predilection of the latter for deformations larger than the HFB minimum. This interesting and non-trivial finding will have to be confirmed by an explicit calculation of rms radii at the PGCM-PT(2) level in the future.

In addition to providing accurate absolute energies in complex systems, e.g. in doubly open-shell nuclei displaying strong collective static correlations, a key advantage of the multi-reference PGCM-PT formalism over BMBPT is that it naturally gives access to the low-lying spectroscopy within a symmetry-conserving scheme by correcting each PGCM eigenstate for dynamical correlations.

The first 2^+ and 4^+ excitation energies in ^{20}Ne are shown in Fig. 5.8 as a function of the axial quadrupole deformation. First, one observes that the PGCM 2_1^+ and 4_1^+ excitation energies are 300 keV (27%) and 560 keV (13%) away from FCI results, respectively. This is consistent with the results displayed in Chapter 4. One also sees that PHFB results at

¹²As shown in Chapter 4, the energy is softer against axial octupole deformations.

¹³Canonical BMBPT(2) is the closest point to FCI along the TEC in the present example.

¹⁴Note that canonical BMBPT(3) only provides an extra 0.3 MeV correlation energy compared to canonical BMBPT(2).

¹⁵Present PGCM-PT(2) and PHFB-PT(2) results were obtained with a complex shift $\gamma = 15$ MeV. The precision error associated with the solving of the linear system is materialized by the error band in Fig. N.3.

¹⁶The important role of octupolarity in the description of ^{20}Ne has been shown in Chapter 4. However, it is hoped for but not guaranteed that PGCM-PT(2) energy will go up with the inclusion of these correlations.

¹⁷Once again, single excitations bring negligible contributions to the correlation energy.

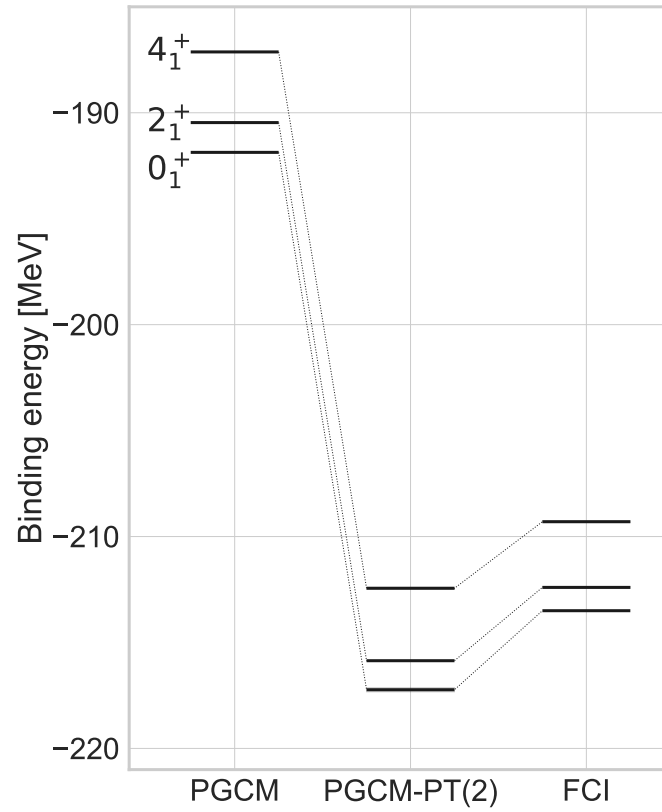


Figure 5.9. Absolute energies of the first 0^+ , 2^+ and 4^+ states in ^{20}Ne computed via PGCM, PGCM-PT(2) and FCI. Calculations are performed with $\hbar\omega = 20$ MeV and $e_{\text{max}} = 4$ as well as with the two-body part of the N^3LO χEFT Hamiltonian evolved to $\lambda_{\text{vsrg}} = 1.88 \text{ fm}^{-1}$.

the canonical deformation ($\beta_2 = 0.3$) are very close to PGCM ones but diverge away from them when going towards smaller or large deformations. Adding dynamical correlations, PHFB-PT(2) flattens the excitation energies as a function of β_2 compared to PHFB, systematically going into the direction of PGCM-PT(2) for each deformation. Given that exact results would be independent of the deformation of the underlying vacuum, this feature is an empirical sign that PHFB-PT(2) results are better converged than PGCM ones. It also implies that the PGCM-PT(2) spectrum converges with fewer states than via the PGCM. Still, at the canonical deformation ($\beta_2 = 0.3$), dynamical correlations are small, which remains true when adding shape mixing given, that PGCM-PT(2) excitation energies are essentially identical to PGCM ones.

Overall, the PGCM-PT(2) 2_1^+ and 4_1^+ excitation energies differ by 24% and 15% away from FCI results respectively, which seems to indicate that missing correlations are beyond two-particle/two-hole excitations of axially deformed HF states. While going to PGCM-PT(3) will help, it might be numerically less costly and more relevant in this case to enrich the PGCM unperturbed state via, e.g., the inclusion of octupole, triaxial and/or pairing degrees of freedom, or to start from HFB states obtained via a variation after particle-number-projection (VAPNP) calculation in order to compress the spectrum. Of course, one could also envision to design a non-perturbative extension of the multi-reference PGCM-PT formalism in the future to more efficiently capture higher-rank particle-hole excitations (see for example [155])

Eventually, previous results are summarized in Fig. 5.9 where the combined benefits of PGCM-PT is clearly apparent. Although a slight overbinding of about 3 MeV ($\sim 1.5\%$) is observed, PGCM-PT(2) brings down absolute energies to the right range of values without degrading their relative position. Since the PGCM-PT formalism is *state specific*, i.e. the calculation is performed separately on top of each PGCM eigenstate, the latter feature is far from trivial considering that each PGCM energy is corrected by about 25 MeV while their relative distance is on the MeV scale. In particular, the (non-trivial) numerical techniques used to solve the PGCM-PT(2) equations must be well controlled to maintain the consistency of the spectra. For example, it is essential to use the same complex shift γ for all states belonging to a given nucleus in order for the bias on absolute energies to be consistent and to largely cancel out in the excitation spectrum.

5.2.2. VSRG+MR-IMSRG pre-processing

In the second part, PGCM-PT(2) calculations are performed in a larger model space with $e_{\max} = 6$. The Hamiltonian introduced in Ref. [156] characterized by $\lambda_{\text{vsrg}} = 1.8 \text{ fm}^{-1}$ and containing both two- and three-nucleon interactions is employed. The Hamiltonian is further pre-processed via the MR-IMSRG¹⁸ unitary transformation based on the canonical PHFB state and the MR-IMSRG(2) truncation scheme [37, 129, 153]. The MR-IMSRG transformation is parametrized by the flow parameter $s \in [0, 20]$, where 0 means that no transformation is applied. In closed-shell nuclei (not shown here), the PHFB reference state reduces to a spherically invariant Slater determinant such that MR-IMSRG is nothing but the simpler SR-IMSRG method. In this case, pushing the transformation to $s = \infty$ (s large in practice) leads to a complete resummation of dynamical correlations into the pre-processed Hamiltonian such that the unperturbed Slater determinant becomes its exact ground state, i.e. no further correlations need to be further added. While dynamical correlations are largely resummed in open-shell nuclei via the MR-IMSRG pre-processing,

¹⁸MR-IMSRG evolved matrix elements were provided by H. Hergert [157].

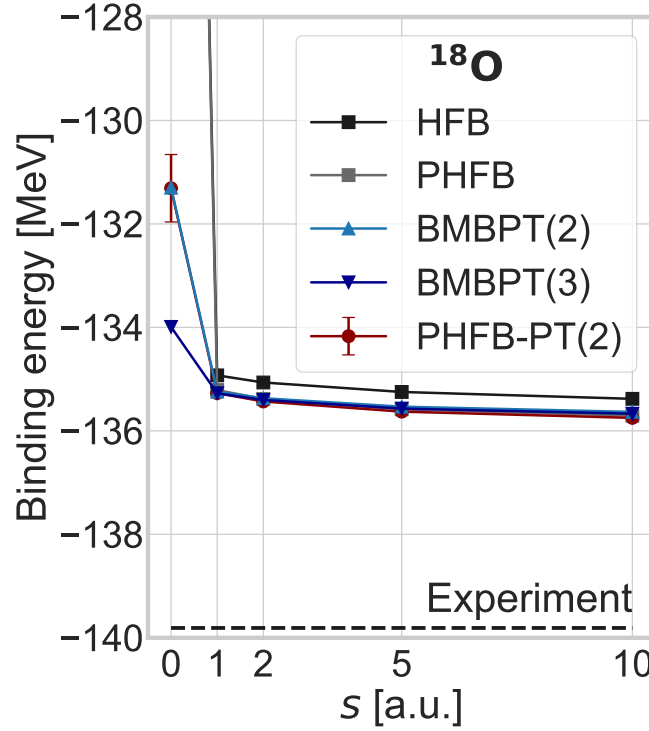


Figure 5.10. (Color online) Absolute binding energy of ^{18}O as a function of the flow parameter s associated with the MR-IMSRG pre-processing of the Hamiltonian. Calculations are performed with $\hbar\omega = 16\text{MeV}$ and $e_{\text{max}} = 6$.

the decoupling of the reference state cannot be complete such that an additional step is always needed to grasp the remaining correlations as illustrated below.

^{18}O

The absolute binding energy of ^{18}O is displayed in Fig. 5.10 as a function of s . Due to the need of PNPAV in ^{18}O , the number of single and double excitations of the HFB vacuum required to perform a PHFB-PT(2) calculation is already very large (1000000 states) for $e_{\text{max}} = 6$. The numerical implementation will be further optimized in the future, but in the meantime we speed up the calculation by discarding some configurations based on their norm, as specified in App. O. For the same reason, only PHFB-PT(2) calculations on top of the spherical ^{18}O canonical HFB vacuum have been performed, leaving a PGCM-PT(2) calculation for the future.

In spite of the change of model space and Hamiltonian, the situation encountered at $s = 0$ is qualitatively similar to the one discussed in Sec. 5.2.1. Indeed, while HFB and PHFB are largely underbound, BMBPT(2) and PHFB-PT(2) bring in the dominant fraction of dynamical correlations¹⁹, with BMBPT(3) adding an extra 2 MeV. Switching on the MR-IMSRG pre-processing, HFB and PHFB energies drop dramatically for small values of s and flatten out very quickly beyond $s = 1$. At the same time, BMBPT(2),

¹⁹Contrarily to the results obtained in Sec. 5.2.1 with a two-body interaction only and $e_{\text{max}} = 4$, PHFB-PT(2) is very close to BMBPT(2) at $s = 0$. At the same time, the contribution of BMBPT(3) is enlarged.

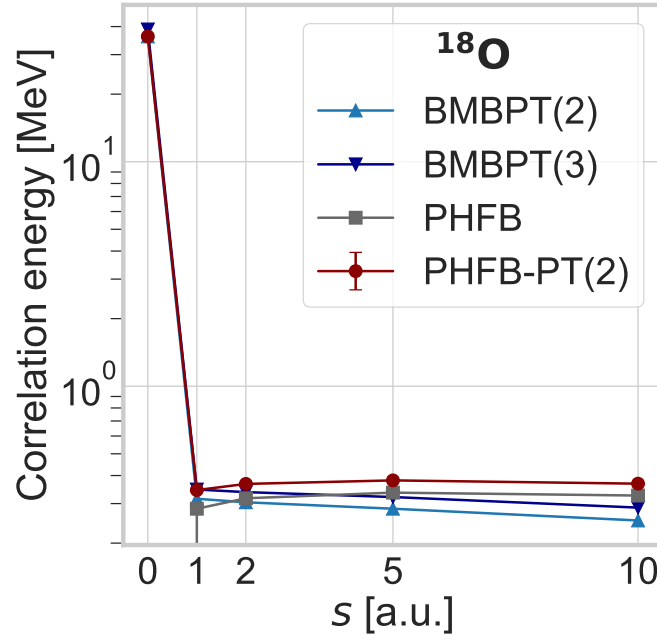


Figure 5.11. (Color online) Correlation energy, i.e. difference to the canonical HFB result, in ^{18}O as a function of the flow parameter s associated with the MR-IMSRG pre-processing of the Hamiltonian. Calculations are performed with $\hbar\omega = 16\text{MeV}$ and $e_{\text{max}} = 6$.

PHFB-PT(2) and BMBPT(3) also drop towards a similar value, about 1.5 MeV below the original BMBPT(3) result, which happens to be also similar to the PHFB value. Eventually, PHFB-PT(2) is about 4 MeV (2.9%) away from experiment. No convergence analysis as a function of the model space has been performed and reaching a converged absolute binding energy clearly requires (an extrapolation to) a larger model space.

To better appreciate the impact of the MR-IMSRG evolution, the correlation energy, i.e. the difference to the HFB result, is shown in Fig. 5.11. Having already absorbed the bulk of dynamical correlations, pre-processed Hamiltonians become more and more perturbative with increasing s such that BMBPT(2,3) and PHFB-PT(2) corrections become less important with the flow, i.e. one goes from 38.8 MeV and 36.2 MeV for BMBPT(3) and PHFB-PT(2) at $s = 0$ to 288 keV and 369 keV at $s = 10$, respectively, with an inversion of both results. At the same time, the particle number projection that is repulsive at $s = 0$ (−394 keV) brings in additional binding for $s \geq 1$ (+327 keV at $s = 10$). The above results demonstrate that correlations are reshuffled through the flow, such that the importance of dynamical correlations is strongly reduced whereas static correlations are magnified.

Dynamical correlations brought on top of PHFB via PHFB-PT(2)²⁰ becomes as small as 42 keV at $s = 10$. Thus, the PHFB state used as a reference for the MR-IMSRG pre-processing is, for all practical purposes, decoupled from the \mathcal{Q} space at the end of the transformation in the present calculation. Although the decoupling cannot be exact

²⁰The numerical solution of the PHFB-PT(2) linear system is very stable in the present example such that a small complex shift ($\gamma = 1\text{ MeV}$) can be used safely. The precision error on PHFB-PT(2) energies is essentially invisible in Fig. 5.11 whereas the bias generated for $\gamma = 1\text{ MeV}$ is negligible compared to the 42 keV difference between PHFB and PHFB-PT(2) energies at $s = 10$.

in principle, ^{18}O behaves similarly to a closed-shell nucleus such that the dynamical correlations left to be captured after PNPAV are very small.

^{20}Ne

The doubly open-shell ^{20}Ne constitutes a richer and more instructive example. Figure 5.12 shows the $J^\pi = 0^+, 2^+$ and 4^+ PHFB TECs as a function of the axial quadrupole deformation β_2 for three values ($s = 0, 10, 20$) of the MR-IMSRG flow parameter. The TECs are strongly lowered with s , e.g. the PHFB minimum gains 45.4 MeV going from $s = 0$ to $s = 20$, with most of the effect occurring for small $0 \leq s \leq 10$ [153]. At the same time, the deformation of the PHFB minimum is lowered from $\beta_2 = 0.55$ to $\beta_2 = 0.52$ while the TECs become stiffer.

In Fig. 5.13, PGCM and PGCM-PT(2) binding energies are displayed as a function of the flow parameter. Starting from $J^\pi = 0^+$ PHFB TECs, PGCM and PGCM-PT(2) calculations mix three HFB configurations with axial quadrupole deformations $\beta_2 = (0.4, 0.5, 0.6)$. Unlike in ^{18}O , the convergence of PGCM energies is not fully reached yet for $s = 20$. Still, the bulk of dynamical correlations has already been resummed into the pre-processed Hamiltonian at $s = 10$, hinting for a convergent behavior. Eventually, the PGCM energy is lowered by 45.2 MeV between $s = 0$ and $s = 20$. At the same time, PGCM-PT(2) systematically lowers the PGCM value, the added dynamical correlations reducing from 42.5 MeV at $s = 0$ to only 2.0 MeV at $s = 20$. Similarly, the difference between PHFB and PGCM-PT(2) reduces drastically with s but does not vanish, i.e. it still amounts to 2.03 MeV with the most pre-processed Hamiltonian²¹. This indicates that, while very effective, the decoupling of the PHFB state with the \mathcal{Q} space is not complete and thus less effective than in the singly open-shell ^{18}O , thus pointing to the stronger multi-reference character of ^{20}Ne associated with the breaking and restoration of $SU(2)$ symmetry.

The PGCM-PT(2) energy changes by less than 5 MeV over the interval $s \in [0, 20]$, thus strongly reducing the flow parameter dependence²². This 5 MeV residual s dependence and the reduction of the perturbative correction to 2 MeV at $s = 20$ indicate that the PGCM-PT(2) energy is better converged than the smallest of these two values, i.e. by better than 1.2%.

Turning to the low-lying spectroscopy, Fig. 5.14 displays the first 2^+ and 4^+ excitation energies as a function of β_2 for the three values of the flow parameter. Focusing first on $s = 0$, the conclusions drawn in Sec. 5.2.1 remain valid, i.e. PHFB-PT(2) flattens the excitation energies as a function of β_2 compared to PHFB whereas dynamical correlations brought in through PGCM-PT(2) do not modify the low-lying part of the PGCM ground-state rotational band. However, the picture changes drastically when pre-processing the Hamiltonian via MR-IMSRG. Indeed, the PGCM spectrum becomes more dilated with increasing s . This can be understood from the TECs in Fig. 5.12 where the decrease with s of the minimum deformation spreads out the PHFB rotational spectrum whereas the increased stiffness further pushes up the excitation energies via the coupling to shape fluctuations within the GCM. Based on this trend, one observes that PHFB-PT(2), while always flattening the dependence on β_2 , systematically corrects for this dilatation of the

²¹PHFB and PGCM energies differ by less than 200 keV all throughout the interval $s \in [0, 20]$.

²²The residual dependence of the ground-state energy on the flow parameter results both from the breaking of unitarity associated with the truncation of the flow equations at the MR-IMSRG(2) level and from the approximations to the solution to the A-body Schrödinger equation at the PGCM-PT(2) level.

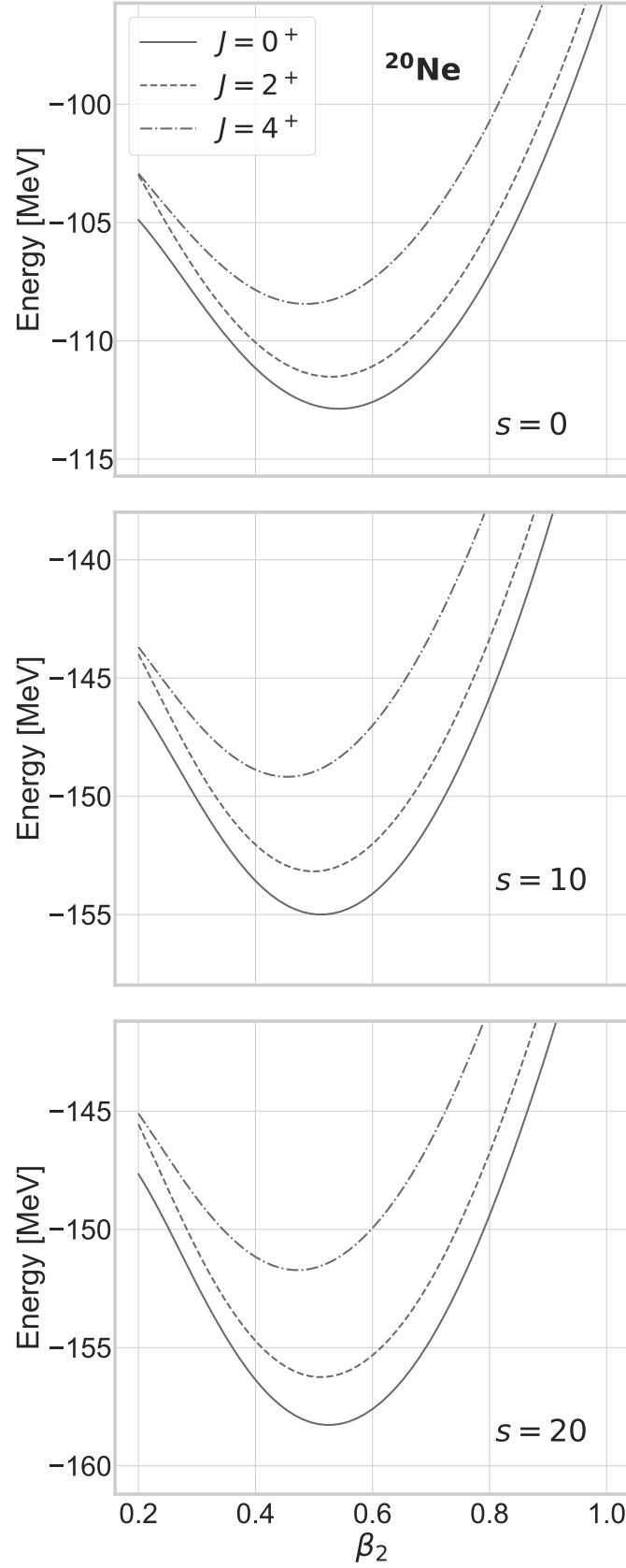


Figure 5.12. (Color online) $J^\pi = 0^+, 2^+, 4^+$ PHFB TECs in ^{20}Ne as a function of the axial quadrupole deformation β_2 for $s = 0$ (upper panel), $s = 10$ (middle panel) and $s = 20$ (lower panel). Calculations are performed with $\hbar\omega = 20\text{MeV}$ and $e_{\text{max}} = 6$.

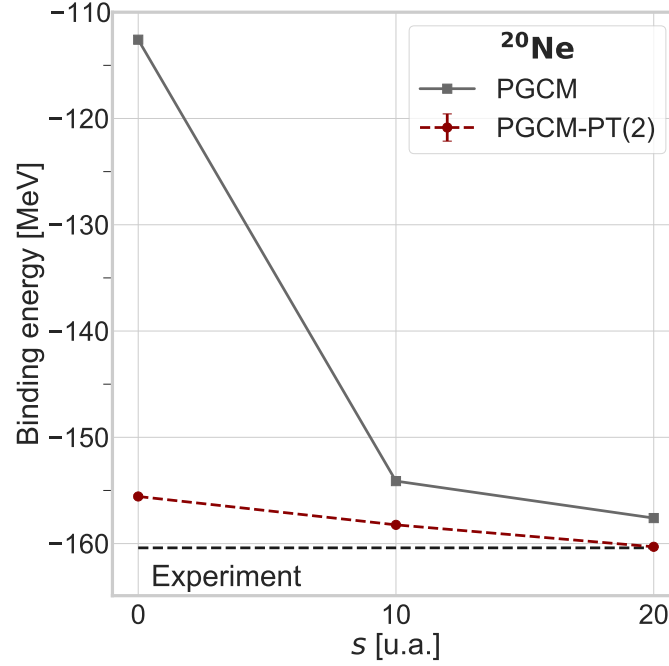


Figure 5.13. (Color online) Absolute PGCM and PGCM-PT(2) binding energies of ^{20}Ne as a function of the MR-IMSRG flow parameter s . Calculations are performed with $\hbar\omega = 20\text{MeV}$ and $e_{\text{max}} = 6$.

rotational spectrum. This non-trivial feature is confirmed at the PGCM-PT(2) level.

This key result can be better appreciated in Fig. 5.15 where PGCM and PGCM-PT(2) spectra are compared to experiment and to the spectrum obtained from a richer PGCM calculation including additional axial states along with triaxially deformed ones²³. Although the PGCM calculation based on three axial states is rudimentary, the observed dilatation of spectra is not compensated by adding further static correlations via the richer PGCM. Correspondingly, the systematic compensation of that dilatation via PGCM-PT(2) corresponds to a genuine action of the perturbation that captures dynamical correlations lying outside the reach of the PGCM. The PGCM-PT(2) correction could probably be magnified by calculating it on top of a richer PGCM reference state allowing the perturbation to span a larger configuration space. In the end, the PGCM-PT(2) 2_1^+ excitation energy is independent of s within uncertainties. While reduced compared to PGCM, the s dependence of the PGCM-PT(2) 4_1^+ excitation energy is still significant and would probably benefit from being performed on top of a richer PGCM state and/or by going to PGCM-PT(3).

The global picture at play with the pre-processing of the Hamiltonian is illustrated for ^{20}Ne in Fig. 5.16. The MR-IMSRG evolution largely reshuffles the hierarchy of correlations at play. As s grows, one observes that

1. static correlations captured through the breaking of symmetries at the HFB level as well as by their restoration and the inclusion of collective fluctuations at the PGCM level slightly increase,
2. dynamical correlations brought either on top of HFB via BMBPT(2) or on top of

²³Triaxial PGCM calculations were provided by B. Bally [135, 136, 137].

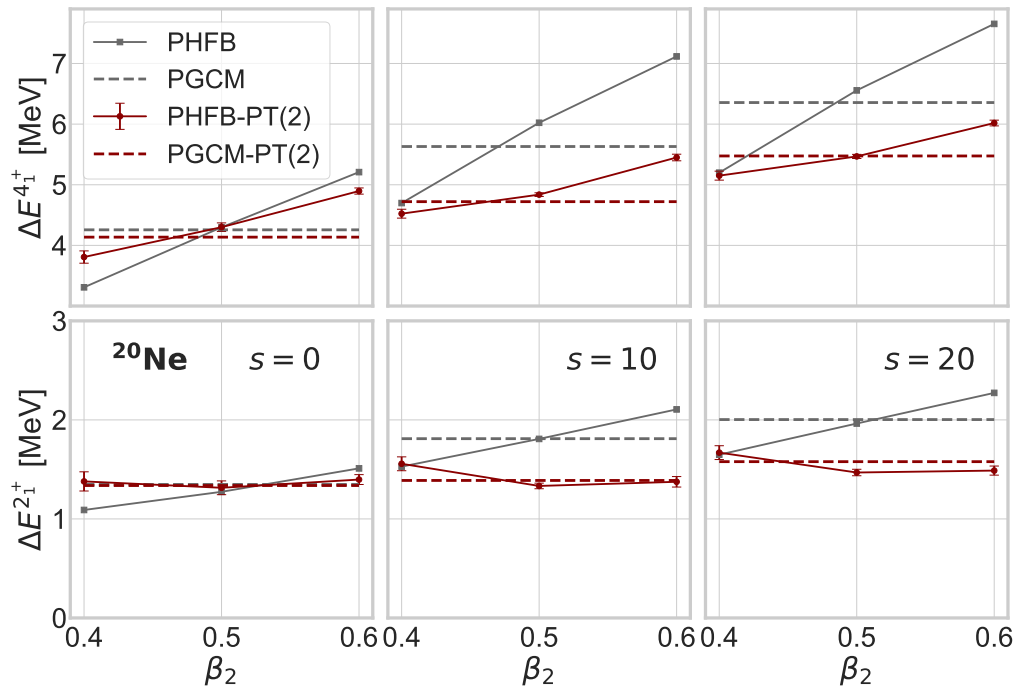


Figure 5.14. (Color online) 2_1^+ (bottom row) and 4_1^+ (top row) excitation energies as a function of β_2 for $s = 0$ (left column), $s = 10$ (middle column) and $s = 20$ (right column). Calculations are performed with $\hbar\omega = 20\text{MeV}$ and $e_{\text{max}} = 6$.

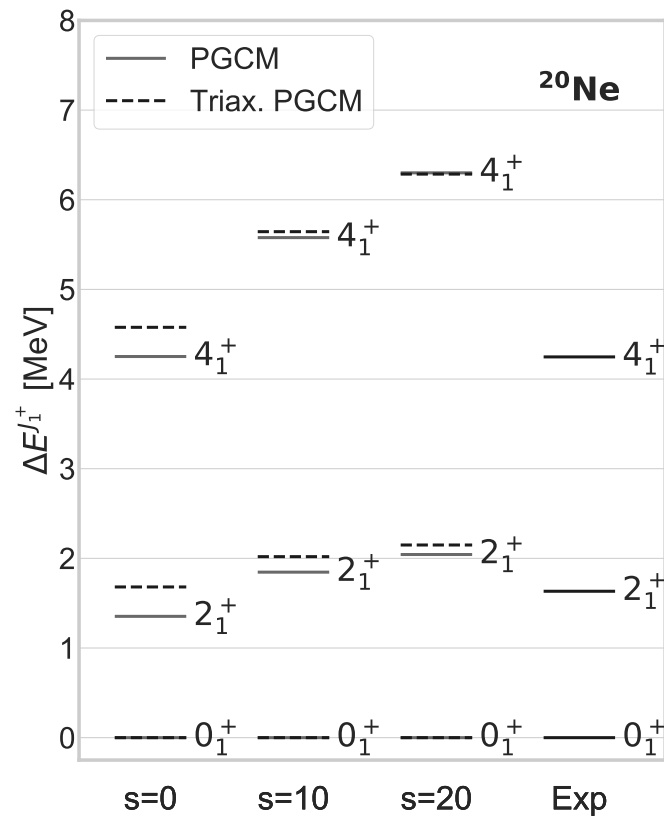


Figure 5.15. (Color online) Low lying spectrum of ^{20}Ne as a function of the MR-IMSRG flow parameter. Calculations are performed with $\hbar\omega = 20\text{MeV}$ and $e_{\text{max}} = 6$.

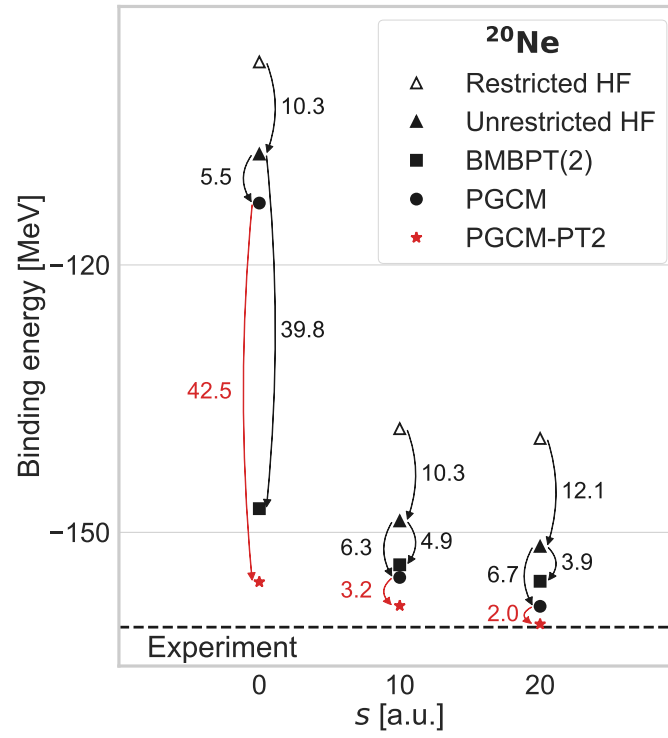


Figure 5.16. (Color online) Absolute binding energy of $^{20}\text{Ne } 0^+$ ground state for different order of the theory as a function of the MR-IMSRG flow. Calculations are performed with $\hbar\omega = 20\text{MeV}$ and $e_{\text{max}} = 6$.

PGCM via PGCM-PT(2) are drastically reduced.

Overall, dynamical correlations go from being highly dominant to being largely subleading. Still, their inclusion on top of PGCM via PGCM-PT(2) remains mandatory, in particular when dealing with low-lying excitation energies.

Eventually, the great benefit of the pre-processing relates to the fact that the many-body calculations performed with evolved Hamiltonians become numerically gentler with s , i.e. the numerical solution of the PGCM-PT(2) linear system is more precise, corrections beyond PGCM-PT(2) are minimized and the convergence with the model-space size (e_{\max}) is probably faster, although this latter point remains to be studied. Given that PGCM-PT(2) is numerically more costly than the MR-IMSRG(2) step (see App. O.1), the optimal combination of both methods is of great interest. Of course, this optimal point must be such that the error due to the breaking of unitarity through the MR-IMSRG(2) pre-processing is not larger than the error associated with PGCM-PT(2) results.

5.3. Discussion

This chapter presented the first realistic results for the novel multi-reference perturbation theory (PGCM-PT) built on top of an unperturbed state generated through the projected generator coordinate method. While the unperturbed state captures crucial static correlations via the breaking and restoration of symmetries along with collective fluctuations, the perturbative expansion brings in complementary dynamical correlations in a consistent fashion within a symmetry-conserving scheme. Furthermore, being a *state-specific* multi-reference many-body perturbation theory, PGCM-PT accesses ground and low-lying excited states on an equal footing.

First, the novel many-body formalism was shown to be both versatile and accurate by benchmarking proof-of-principle results of doubly closed-shell ^{16}O , singly open-shell ^{18}O and doubly open-shell ^{20}Ne nuclei in a small ($e_{\max} = 4$) harmonic oscillator model space against full configuration interaction (FCI). Binding energies obtained at second order, i.e. through PGCM-PT(2), were shown to be typically 0.5 – 1.5% away from FCI results.

The second focus of the present chapter was to demonstrate the benefit of combining low-order PGCM-PT with a pre-processing of the Hamiltonian via multi-reference in-medium similarity renormalization group (MR-IMSRG) transformations. The rather low cost of MR-IMSRG(2) calculations makes it possible to first capture the bulk of dynamical correlations in large model spaces. Based on such a pre-processed Hamiltonian, PGCM-PT(2) can bring in crucial static correlations *and* remaining dynamical correlations while working in a smaller model space. The present work showed that, after the MR-IMSRG(2) pre-processing, dynamical correlations brought on top of the PGCM via PGCM-PT(2) are indeed essential to describe low-lying spectra satisfactorily.

Forthcoming extensions of the formalism to other observables and vibrational states are naturally envisioned, as well as truncation techniques to reduce the computational burden of the method.

Conclusions

In the past ten years, *ab initio* methods for atomic nuclei [26, 29, 30, 31, 32, 34, 35, 37, 38, 40, 46, 52, 60, 158, 159] have proven capable of providing a predictive description of medium-mass isotopes. Their rapid progress in three directions (towards heavier systems, away from magicity and aiming at an increased precision) designate *ab initio* calculations as the working horse for next generation simulations of nuclear systems. Nuclei up to mass $A \sim 130$ [42] are now consistently described from first principles. Pioneering works [160, 161] explore the possibility to further extend the reach of *ab initio* methods via the use of systematic methods to reduce the cost of the calculations. In parallel, calculations have become more and more precise, and a new generation of simulations are now able to identify various sources of uncertainties and propagate them to many-body observables. Last, but not least, novel formalisms [26, 37, 48, 162] have opened the way towards open-shell systems and exotic physics.

Initial limitations to closed-shell nuclei have been overcome via the use of more general reference states incorporating static correlations from the outset. Three complementary strategies exploit this idea as of today. First, the MR-IMSRG procedure [57] evolves the interaction to approximately decouple a multi-determinantal reference state from the rest of the Hilbert space. By doing so, the solution of the many-body problem with the evolved interaction is made much easier, such that most (but not all!) correlations are captured at the mean-field or PGCM level. Another approach relies on an expansion performed on top of a symmetry-broken product state. Successfully implemented for perturbative [46] and non perturbative expansions [50, 52], this method provides already accurate results for absolute binding energies and radii of medium-mass open-shell nuclei. However, symmetry breaking solutions can only be an intermediate step in finite-size nuclear systems and symmetries must eventually be restored. Formulations of symmetry restorations at all order in the theory exist [7, 54] and have been successfully implemented for toy-model Hamiltonians [55, 56], but applications to nuclear systems remain (until now) inconclusive. The third route, followed e.g. by MCPT [28], consists in expanding perturbatively on top of a linear mixing of orthogonal Slater determinants. Such an approach has been employed with success, but the NCSM step providing the unperturbed state does not scale gently enough with system size to be appropriate to mid- and heavy-mass nuclei.

The present work dealt with the derivation and implementation of a perturbation theory on top of a PGCM unperturbed state, e.g. a linear mixing of non orthogonal projected Bogoliubov vacua. After the derivation of the formalism, practical calculations at first and second orders have been performed and discussed extensively.

In Chapter 1, notations and formal ingredients useful for the rest of the document have been introduced. Chapter 2 introduced the formalism of generic perturbation theory, and discussed the importance of the choice of the reference state in expansion methods. Specific derivations for PGCM reference states were given, and detailed expressions for useful quantities have been derived. PGCM-PT is not only appropriate to ground-state energies but can also be straightforwardly applied to the computation of yrast excited energies. Non-yrast states and other observables require extensions that are envisioned for

the near future.

Before applying this method to practical calculations, a symmetry-conserving rank-reduction procedure has been developed in Chapter 3 in order to circumvent the prohibitive storage and runtime requirements of handling three-body terms in the interaction. The method has been carefully tested on a wide range of many-body methods focusing both on dynamical and static correlations in closed and open-shell nuclei. The rank-reduction method is accurate, universal, simple, flexible. As such it constitutes a promising way towards heavier systems, especially taking into account the fact that it is already formalised for 4-body forces whenever they become available for practical applications. In particular, it would be interesting to explore how this techniques can be combined with the methods developed in Ref. [42], and therefore build a two-body effective interaction containing as many three-body matrix elements as possible. Similarly, it could be interesting to test the quality of the rank-reduced Hamiltonian based on one-body density matrices obtained from spherical EDF calculations in heavy nuclei as a way to avoid performing the corresponding mean-field calculation with the three-body interaction.

Chapter 4 focused on the leading order of the theory formalized in Chapter 2, and performed systematic PGCM calculations of the neon chain with state-of-the-art chiral interactions. Detailed results on ^{20}Ne showed that the method, although missing dynamical correlations, can provide a very good description of the low-lying spectroscopy, in good agreement with experiment whenever the right collective degrees of freedom are included into the PGCM ansatz. The emergence of clustered structures in ^{20}Ne associated with strong octupole shape fluctuations proved the predictive power of PGCM in particular and of *ab initio* methods in general. In a second step, systematic PGCM results along the Neon isotopic chain were compared to quasi-exact IM-NCSM results. Although the overall description is satisfactory, it is clear that correlations are missing in neutron-rich isotopes that require the use of a richer PGCM ansatz and/or the addition of dynamical correlations on top.

It was precisely the objective of Chapter 5 to complement the PGCM with dynamical correlations according to the PGCM-PT formalism developed in Chapter 2. While the PGCM reference state naturally captures long-range collective correlations, the additional state-specific perturbation theory consistently corrects it with the effect of low-rank elementary excitations. Eventually, the method was applied to Hamiltonians pre-processed via MR-IMSRG transformations. In this case, dynamical correlations were shown to adequately correct absolute energies and, most importantly, PGCM spectra that are artificially dilated by the MR-IMSRG evolution.

Overall, the present study indicates that a versatile and accurate description of complex mid- and heavy-mass nuclei will probably rely on the combination of three levers whose complementarity needs to be further investigated and optimized

1. the pre-processing of the Hamiltonian via, e.g., MR-IMSRG to efficiently capture the bulk of dynamical correlations,
2. the use of a, e.g., PGCM unperturbed state capturing collective static correlations via a low-dimensional diagonalization problem that is thus scalable to heavy nuclei,
3. the low-order truncation of a systematic expansion on top of the multi-reference unperturbed state via, e.g., PGCM-PT to bring in remaining dynamical correlations.

Each of the three steps comes with its own flexibility that must be exploited in order to

optimize their combination²⁴. First, the pre-processing is a function of a flow parameter s that must be optimized to resum the bulk of dynamical correlations without inducing a large breaking of unitarity²⁵. Second, the PGCM depends on a choice of suitable collective coordinates that must be rich enough to capture all non-perturbative static correlations at play, only leaving weak perturbative corrections to the subsequent PGCM-PT step, while maintaining a low-enough dimensionality to its advantage over large-scale diagonalization methods. Third, while PGCM-PT can in principle be implemented at various perturbative orders n , it must be limited to low orders, e.g. PGCM-PT(2), in practice to avoid a prohibitive numerical cost.

While the present work has laid the foundations of such an optimal scheme, future studies will allow us to better understand the way many-body correlations can be most efficiently captured in complex heavy nuclei within an *ab initio* setting. For example, describing nuclei displaying strong shape coexistence via *ab initio* many-body calculations constitute an interesting milestone to achieve in the years to come.

²⁴It is worth mentioning that the combination of the three steps is always consistent, i.e. there is no double counting given that each step consistently adapt to the other two.

²⁵In this context, the truncation order of the MR-IMSRG(n) procedure plays a critical role. If MR-IMSRG(3) will allow to carry the flow evolution to larger s , and thus better decouple the reference state, it is also significantly costlier numerically.

Appendix A.

Symmetry group

The symmetry group of H underlines the symmetry quantum numbers carried by its many-body eigenstates. In the present context, the group¹

$$G_H \equiv \text{SU}(2) \times \text{I} \times \text{U}(1)_N \times \text{U}(1)_Z$$

associated with the conservation of total angular momentum, parity and neutron/proton numbers is explicitly considered. The group is a compact Lie group but is non Abelian as a result of $\text{SU}(2)$.

A.1. Unitary representation

Each subgroup is represented on Fock space \mathcal{F} via the set of unitary rotation operators

$$R_{\vec{J}}(\Omega) \equiv e^{-i\alpha J_z} e^{-i\beta J_y} e^{-i\gamma J_z}, \quad (\text{A.1a})$$

$$R_N(\varphi_n) \equiv e^{-i\varphi_n N}, \quad (\text{A.1b})$$

$$R_Z(\varphi_p) \equiv e^{-i\varphi_p Z}, \quad (\text{A.1c})$$

$$\Pi(\varphi_\pi) \equiv e^{-i\varphi_\pi F}, \quad (\text{A.1d})$$

where $\Omega \equiv (\alpha, \beta, \gamma)$, φ_π and φ_n (φ_p) denote Euler, parity and neutron- (proton-) gauge angles, respectively. The one-body operators entering the unitary representations of interest denote the generators of the group made out of the three components of the total angular momentum $\vec{J} = (J_x, J_y, J_z)$, neutron-number N and proton-number Z operators as well as of the one-body operator

$$F \equiv \sum_{ab} f_{ab} c_a^\dagger c_b \quad (\text{A.2})$$

defined through its matrix elements [163]

$$f_{ab} \equiv \frac{1}{2} (1 - \pi_a) \delta_{ab}, \quad (\text{A.3})$$

where π_a denotes the parity of one-body basis states that are presently assumed to carry a good parity. The eigenstates of H are characterized by

$$J^2 |\Psi_\mu^\sigma\rangle \equiv \hbar^2 J(J+1) |\Psi_\mu^\sigma\rangle, \quad (\text{A.4a})$$

$$J_z |\Psi_\mu^\sigma\rangle \equiv \hbar M |\Psi_\mu^\sigma\rangle, \quad (\text{A.4b})$$

¹One can add translation and time-reversal symmetries to the presentation to reach the complete symmetry group of the nuclear Hamiltonian.

$$N|\Psi_\mu^\sigma\rangle \equiv N|\Psi_\mu^\sigma\rangle, \quad (\text{A.4c})$$

$$Z|\Psi_\mu^\sigma\rangle \equiv Z|\Psi_\mu^\sigma\rangle, \quad (\text{A.4d})$$

$$\Pi(\pi)|\Psi_\mu^\sigma\rangle \equiv \Pi|\Psi_\mu^\sigma\rangle, \quad (\text{A.4e})$$

where $\sigma \equiv (\text{JMIINZ})$ and where the operator $\Pi(\pi)$ is nothing but the parity operator and $J^2 \equiv \vec{J} \cdot \vec{J}$ is the Casimir of $\text{SU}(2)$.

The irreducible representations (IRREPs) of the group are given by [164]

$$\langle \Psi_\mu^\sigma | R(\theta) | \Psi_{\mu'}^{\sigma'} \rangle \equiv D_{\text{MM}'}^{\tilde{\sigma}}(\theta) \delta_{\tilde{\sigma}\tilde{\sigma}'} \delta_{\mu\mu'}, \quad (\text{A.5})$$

with $\tilde{\sigma} \equiv (\text{JIINZ})$ and

$$D_{\text{MM}'}^{\tilde{\sigma}}(\theta) \equiv D_{\text{MM}'}^{\text{J}}(\Omega) e^{-i\varphi_n N} e^{-i\varphi_p Z} e^{-\frac{i}{2}(1-\Pi)\varphi_\pi}, \quad (\text{A.6})$$

and where the rotation operators have been gathered into

$$R(\theta) \equiv R_{\vec{J}}(\Omega) R_N(\varphi_n) R_Z(\varphi_p) \Pi(\varphi_\pi), \quad (\text{A.7})$$

with

$$\theta \equiv (\Omega, \varphi_n, \varphi_p, \varphi_\pi) \quad (\text{A.8})$$

encompassing all rotation angles. The domain of definition of the group is thus

$$\begin{aligned} D_{G_H} &\equiv D_\alpha \times D_\beta \times D_\gamma \times D_{\varphi_n} \times D_{\varphi_p} \times D_{\varphi_\pi} \\ &= [0, 4\pi] \times [0, \pi] \times [0, 2\pi] \times [0, 2\pi] \times [0, 2\pi] \times \{0, \pi\}. \end{aligned}$$

In Eq. (A.5), $D_{\text{MK}}^{\text{J}}(\Omega)$ denotes Wigner D-matrices that can be expressed in terms of the (real) reduced Wigner d -functions through $D_{\text{MK}}^{\text{J}}(\Omega) \equiv e^{-iM\alpha} d_{\text{MK}}^{\text{J}}(\beta) e^{-iK\gamma}$.

Given that the degeneracy of the IRREPs is $d_{\tilde{\sigma}} = 2J + 1$ and the volume of the group is

$$\begin{aligned} v_{G_H} &\equiv \int_{D_G} d\theta \\ &\equiv \sum_{\varphi_\pi=0,\pi} \int_{[0,4\pi] \times [0,\pi] \times [0,2\pi]} d\alpha \sin \beta d\beta d\gamma \int_0^{2\pi} d\varphi_n \int_0^{2\pi} d\varphi_p \\ &= 2(16\pi^2)(2\pi)^2 \end{aligned} \quad (\text{A.9})$$

the orthogonality of the IRREPs read as

$$\int_{D_G} d\theta D_{\text{MK}}^{\tilde{\sigma}*}(\theta) D_{\text{M}'\text{K}'}^{\tilde{\sigma}'}(\theta) = \frac{v_G}{d_{\tilde{\sigma}}} \delta_{\tilde{\sigma}\tilde{\sigma}'} \delta_{\text{MM}'} \delta_{\text{KK}'}. \quad (\text{A.10})$$

Furthermore, the unitarity of the symmetry transformations, i.e. $R^\dagger(\theta)R(\theta) = R(\theta)R^\dagger(\theta) = 1$, induces

$$\sum_M D_{\text{MK}}^{\tilde{\sigma}*}(\theta) D_{\text{MK}'}^{\tilde{\sigma}}(\theta) = \delta_{\text{KK}'}, \quad (\text{A.11a})$$

$$\sum_K D_{\text{MK}}^{\tilde{\sigma}}(\theta) D_{\text{M}'\text{K}}^{\tilde{\sigma}*}(\theta) = \delta_{\text{MM}'}. \quad (\text{A.11b})$$

An irreducible tensor operator $T_K^{\tilde{\sigma}}$ of rank J and a state $|\Psi_\mu^{\tilde{\sigma}K}\rangle$ transform under rotation according to

$$R(\theta) T_K^{\tilde{\sigma}} R(\theta)^{-1} = \sum_M T_M^{\tilde{\sigma}} D_{MK}^{\tilde{\sigma}}(\theta) , \quad (\text{A.12a})$$

$$R(\theta) |\Psi_\mu^{\tilde{\sigma}K}\rangle = \sum_M |\Psi_\mu^{\tilde{\sigma}M}\rangle D_{MK}^{\tilde{\sigma}}(\theta) . \quad (\text{A.12b})$$

Peter-Weyl's theorem ensures that any function $f(\theta) \in L^2(G_H)$ can be expanded according to

$$f(\theta) \equiv \sum_{\tilde{\sigma}} \sum_{MK} f_{MK}^{\tilde{\sigma}} D_{MK}^{\tilde{\sigma}*}(\theta) , \quad (\text{A.13})$$

such that the set of complex expansion coefficients $\{f_{MK}^{\tilde{\sigma}}\}$ can be extracted thanks to the orthogonality of the IRREPs through

$$f_{MK}^{\tilde{\sigma}} = \frac{d_{\tilde{\sigma}}}{v_{G_H}} \int_{D_{G_H}} d\theta D_{MK}^{\tilde{\sigma}}(\theta) f(\theta) . \quad (\text{A.14})$$

A.2. Projection operators

The operator

$$P^\sigma \equiv P_M^J P^N P^Z P^\Pi \quad (\text{A.15})$$

collects the projection operators on good symmetry quantum numbers

$$\begin{aligned} P_M^J &\equiv \sum_K g_K P_{MK}^J \\ &\equiv \sum_K g_K \frac{2J+1}{16\pi^2} \int_{[0,4\pi] \times [0,\pi] \times [0,2\pi]} d\Omega D_{MK}^{J*}(\Omega) R_J(\Omega) , \end{aligned} \quad (\text{A.16a})$$

$$P^N \equiv \frac{1}{2\pi} \int_0^{2\pi} d\varphi_n e^{i\varphi_n N} R_N(\varphi_n) , \quad (\text{A.16b})$$

$$P^Z \equiv \frac{1}{2\pi} \int_0^{2\pi} d\varphi_p e^{i\varphi_p Z} R_Z(\varphi_p) , \quad (\text{A.16c})$$

$$P^\Pi \equiv \frac{1}{2} \sum_{\varphi_\pi=0,\pi} e^{\frac{i}{2}(1-\Pi)\varphi_\pi} \Pi(\varphi_\pi) , \quad (\text{A.16d})$$

such that one can write in a compact way

$$\begin{aligned} P^\sigma &= \frac{d_{\tilde{\sigma}}}{v_G} \sum_K g_K \int_{D_G} d\theta D_{MK}^{\tilde{\sigma}*}(\theta) R(\theta) \\ &\equiv \sum_K g_K P_{MK}^{\tilde{\sigma}} . \end{aligned} \quad (\text{A.17})$$

The so-called transfer operator $P_{MK}^{\tilde{\sigma}}$ fulfills

$$P_{MK}^{\tilde{\sigma}} = \sum_\mu |\Psi_\mu^{\tilde{\sigma}M}\rangle \langle \Psi_\mu^{\tilde{\sigma}K}| , \quad (\text{A.18a})$$

$$P_{MK}^{\tilde{\sigma}\dagger} = P_{KM}^{\tilde{\sigma}} , \quad (\text{A.18b})$$

$$P_{MK}^{\tilde{\sigma}} P_{M'K'}^{\tilde{\sigma}'} = \delta_{\tilde{\sigma}\tilde{\sigma}'} \delta_{KM'} P_{MK'}^{\tilde{\sigma}} , \quad (\text{A.18c})$$

along with the identity

$$P^\sigma R(\theta) = \sum_K g_K \sum_{M'} D_{KM'}^{\tilde{\sigma}}(\theta) P_{MM'}^{\tilde{\sigma}} . \quad (\text{A.19})$$

The present work is eventually interested in the particular case where $g_K = \delta_{K0}$.

Appendix B.

Permutation operators

Many of the algebraic expressions derived in the present document can be economically written via the use of so-called *permutation operators* that perform appropriate anti-symmetrizations of the matrix element they act on. A permutation operator $P(s_1/s_2/\dots/s_n)$, where s_i ($i = 1, \dots, n$) denotes a given set of indices, permutes the indices belonging to the various sets in all possible ways, *without* permuting the indices *within* each set. Furthermore, the sign given by the signature of each permutation multiplies the corresponding term. In the present work, the needed permutation operators read as

$$P(k_1/k_2) \equiv 1 - P_{k_1 k_2}, \quad (\text{B.1a})$$

$$P(k_1/k_2 k_3) \equiv 1 - P_{k_1 k_2} - P_{k_1 k_3}, \quad (\text{B.1b})$$

$$P(k_1/k_2 k_3 k_4) \equiv 1 - P_{k_1 k_2} - P_{k_1 k_3} - P_{k_1 k_4}, \quad (\text{B.1c})$$

$$P(k_1 k_2/k_3 k_4) \equiv 1 - P_{k_1 k_3} - P_{k_1 k_4} - P_{k_2 k_3} - P_{k_2 k_4} + P_{k_1 k_3} P_{k_2 k_4}, \quad (\text{B.1d})$$

$$\begin{aligned} P(k_1/k_2/k_3 k_4) &\equiv P(k_1 k_2/k_3 k_4) P(k_1/k_2) \\ &= 1 - P_{k_1 k_3} - P_{k_1 k_4} - P_{k_2 k_3} - P_{k_2 k_4} + P_{k_1 k_3} P_{k_2 k_4} + P_{k_3 k_4} + P_{k_1 k_3} P_{k_3 k_4} \\ &\quad + P_{k_1 k_4} P_{k_3 k_4} + P_{k_2 k_3} P_{k_3 k_4} + P_{k_2 k_4} P_{k_3 k_4} - P_{k_1 k_4} P_{k_2 k_3}, \end{aligned} \quad (\text{B.1e})$$

$$P(k_1/k_2/k_3/k_4) \equiv P(k_1 k_2/k_3 k_4) P(k_1/k_2) P(k_3/k_4), \quad (\text{B.1f})$$

where the *exchange operator* $P_{k_i k_j}$ commutes indices k_i and k_j .

Appendix C.

Similarity-transformed matrix elements

Let us consider a two-body operator O (see Eqs. (1.25)-(1.27) with $r = 2$), in normal-ordered form with respect to $|\Phi(p)\rangle$

$$\begin{aligned}
O &\equiv \mathbf{O}^{00}(p) \\
&+ \left[\mathbf{O}^{11}(p) + \{ \mathbf{O}^{20}(p) + \mathbf{O}^{02}(p) \} \right] \\
&+ \left[\mathbf{O}^{22}(p) + \{ \mathbf{O}^{31}(p) + \mathbf{O}^{13}(p) \} + \{ \mathbf{O}^{40}(p) + \mathbf{O}^{04}(p) \} \right] \\
&= \mathbf{O}^{00}(p) \\
&+ \frac{1}{(1!)^2} \sum_{k_1 k_2} \mathbf{o}_{k_1 k_2}^{k_1}(p) B_{k_2}^{k_1}(p) + \frac{1}{2!} \sum_{k_1 k_2} \mathbf{o}_{k_1 k_2}^{k_1 k_2}(p) B_{k_1 k_2}^{k_1 k_2}(p) \\
&+ \frac{1}{(2!)^2} \sum_{k_1 k_2 k_3 k_4} \mathbf{o}_{k_3 k_4}^{k_1 k_2}(p) B_{k_3 k_4}^{k_1 k_2}(p) \\
&+ \frac{1}{3!1!} \sum_{k_1 k_2 k_3 k_4} \mathbf{o}_{k_4}^{k_1 k_2 k_3}(p) B_{k_4}^{k_1 k_2 k_3}(p) + \frac{1}{1!3!} \sum_{k_1 k_2 k_3 k_4} \mathbf{o}_{k_2 k_3 k_4}^{k_1}(p) B_{k_2 k_3 k_4}^{k_1}(p) \\
&+ \frac{1}{4!} \sum_{k_1 k_2 k_3 k_4} \mathbf{o}^{k_1 k_2 k_3 k_4}(p) B_{k_1 k_2 k_3 k_4}^{k_1 k_2 k_3 k_4}(p) + \frac{1}{4!} \sum_{k_1 k_2 k_3 k_4} \mathbf{o}_{k_1 k_2 k_3 k_4}(p) B_{k_1 k_2 k_3 k_4}^{k_1 k_2 k_3 k_4}(p). \quad (\text{C.1})
\end{aligned}$$

Expressing the similarity-transformed partner ${}^Z O$ (Eq. (1.56)) under the same form, its $(p, q; \theta)$ -dependent¹ matrix elements read as

$${}^Z \mathbf{O}^{00} \equiv {}^Z \mathbf{S}^{00}, \quad (\text{C.2a})$$

$${}^Z \mathbf{o}_{k_1 k_2} \equiv {}^Z s_{k_1 k_2}, \quad (\text{C.2b})$$

$${}^Z \mathbf{o}_{k_2}^{k_1} \equiv {}^Z s_{k_2}^{k_1} + \sum_{l_1} {}^Z s_{l_1 k_2} \mathbf{z}^{l_1 k_1}, \quad (\text{C.2c})$$

$${}^Z \mathbf{o}^{k_1 k_2} \equiv {}^Z s^{k_1 k_2} + P(k_1/k_2) \sum_{l_1} {}^Z s_{l_1}^{k_1} \mathbf{z}^{l_1 k_2} - \sum_{l_1 l_2} {}^Z s_{l_1 l_2} \mathbf{z}^{l_1 k_1} \mathbf{z}^{l_2 k_2}, \quad (\text{C.2d})$$

$${}^Z \mathbf{o}_{k_1 k_2 k_3 k_4} \equiv {}^Z s_{k_1 k_2 k_3 k_4}, \quad (\text{C.2e})$$

$${}^Z \mathbf{o}_{k_2 k_3 k_4}^{k_1} \equiv {}^Z s_{k_2 k_3 k_4}^{k_1} + \sum_{l_1} {}^Z s_{l_1 k_2 k_3 k_4} \mathbf{z}^{l_1 k_1}, \quad (\text{C.2f})$$

$${}^Z \mathbf{o}_{k_3 k_4}^{k_1 k_2} \equiv {}^Z s_{k_3 k_4}^{k_1 k_2} + P(k_1/k_2) \sum_{l_2} {}^Z s_{l_2 k_3 k_4}^{k_1} \mathbf{z}^{l_2 k_2} - \sum_{l_1 l_2} {}^Z s_{l_1 l_2 k_3 k_4} \mathbf{z}^{l_1 k_1} \mathbf{z}^{l_2 k_2}, \quad (\text{C.2g})$$

¹The transformed matrix elements depend on $(p, q; \theta)$ through their dependence on Z and further depend on p through the matrix elements defining the original normal-ordered operator in Eq. (C.1). All these dependencies are dropped in Eqs. (C.2)-(C.3) for the sake of readability.

$$\begin{aligned}
 {}^Z\mathbf{o}_{k_4}^{k_1k_2k_3} &\equiv {}^Z\mathbf{s}_{k_4}^{k_1k_2k_3} + P(k_3/k_1k_2) \sum_{l_3} {}^Z\mathbf{s}_{l_3k_4}^{k_1k_2} \mathbf{z}^{l_3k_3} \\
 &\quad - P(k_1/k_2k_3) \sum_{l_2l_3} {}^Z\mathbf{s}_{l_2l_3k_4}^{k_1} \mathbf{z}^{l_2k_2} \mathbf{z}^{l_3k_3} - \sum_{l_1l_2l_3} {}^Z\mathbf{s}_{l_1l_2l_3k_4} \mathbf{z}^{l_1k_1} \mathbf{z}^{l_2k_2} \mathbf{z}^{l_3k_3}, \quad (\text{C.2h})
 \end{aligned}$$

$$\begin{aligned}
 {}^Z\mathbf{o}^{k_1k_2k_3k_4} &\equiv {}^Z\mathbf{s}^{k_1k_2k_3k_4} + P(k_4/k_1k_2k_3) \sum_{l_4} {}^Z\mathbf{s}_{l_4}^{k_1k_2k_3} \mathbf{z}^{l_4k_4} - P(k_1k_2/k_3k_4) \sum_{l_3l_4} {}^Z\mathbf{s}_{l_3l_4}^{k_1k_2} \mathbf{z}^{l_3k_3} \mathbf{z}^{l_4k_4} \\
 &\quad + P(k_1/k_2k_3k_4) \sum_{l_2l_3l_4} {}^Z\mathbf{s}_{l_2l_3l_4}^{k_1} \mathbf{z}^{l_2k_2} \mathbf{z}^{l_3k_3} \mathbf{z}^{l_4k_4} + \sum_{l_1l_2l_3l_4} {}^Z\mathbf{s}_{l_1l_2l_3l_4} \mathbf{z}^{l_1k_1} \mathbf{z}^{l_2k_2} \mathbf{z}^{l_3k_3} \mathbf{z}^{l_4k_4}, \quad (\text{C.2i})
 \end{aligned}$$

where the intermediate matrix elements are defined through²

$${}^Z\mathbf{s}^{00} \equiv \mathbf{o}^{00} + \frac{1}{2} \sum_{l_1l_2} \mathbf{o}_{l_1l_2} \mathbf{z}^{l_1l_2} + \frac{1}{8} \sum_{l_1l_2l_3l_4} \mathbf{o}_{l_1l_2l_3l_4} \mathbf{z}^{l_1l_2} \mathbf{z}^{l_3l_4}, \quad (\text{C.3a})$$

$${}^Z\mathbf{s}_{l_1l_2} \equiv \mathbf{o}_{l_1l_2} + \frac{1}{2} \sum_{l_3l_4} \mathbf{o}_{l_1l_2l_3l_4} \mathbf{z}^{l_3l_4}, \quad (\text{C.3b})$$

$${}^Z\mathbf{s}_{l_2}^{l_1} \equiv \mathbf{o}_{l_2}^{l_1} + \frac{1}{2} \sum_{l_3l_4} \mathbf{o}_{l_2l_3l_4}^{l_1} \mathbf{z}^{l_3l_4}, \quad (\text{C.3c})$$

$${}^Z\mathbf{s}^{l_1l_2} \equiv \mathbf{o}^{l_1l_2} + \frac{1}{2} \sum_{l_3l_4} \mathbf{o}_{l_3l_4}^{l_1l_2} \mathbf{z}^{l_3l_4}, \quad (\text{C.3d})$$

$${}^Z\mathbf{s}_{l_1l_2l_3l_4} \equiv \mathbf{o}_{l_1l_2l_3l_4}, \quad (\text{C.3e})$$

$${}^Z\mathbf{s}_{l_2l_3l_4}^{l_1} \equiv \mathbf{o}_{l_2l_3l_4}^{l_1}, \quad (\text{C.3f})$$

$${}^Z\mathbf{s}_{l_3l_4}^{l_1l_2} \equiv \mathbf{o}_{l_3l_4}^{l_1l_2}, \quad (\text{C.3g})$$

$${}^Z\mathbf{s}_{l_4}^{l_1l_2l_3} \equiv \mathbf{o}_{l_4}^{l_1l_2l_3}, \quad (\text{C.3h})$$

$${}^Z\mathbf{s}^{l_1l_2l_3l_4} \equiv \mathbf{o}^{l_1l_2l_3l_4}. \quad (\text{C.3i})$$

²The intermediate matrix elements incorporate all terms where both indices of a given matrix \mathbf{z} are contracted with indices of a matrix element of \mathcal{O} .

Appendix D.

PGCM-PT(2) matrix elements

From a technical viewpoint, the building blocks of the PGCM-PT formalism presented in Sec. 2.3 are many-body matrix elements of the following kind

$$\begin{aligned}
 O_{pIqJ}^{\tilde{\sigma}} &\equiv \langle \Phi^I(p) | O P_{00}^{\tilde{\sigma}} | \Phi^J(q) \rangle \\
 &= \frac{d_{\tilde{\sigma}}}{v_G} \sum_{\theta} D_{00}^{\tilde{\sigma}*}(\theta) \langle \Phi(p) | B_{l_1 \dots l_i}(p) O R(\theta) B^{k_1 \dots k_j}(q) | \Phi(q) \rangle \\
 &= \frac{d_{\tilde{\sigma}}}{v_G} \sum_{\theta} D_{00}^{\tilde{\sigma}*}(\theta) \langle \Phi(p) | {}^Z B_{l_1 \dots l_i}(p) {}^Z O {}^Z B^{k_1 \dots k_j}(q; \theta) | \Phi(p) \rangle \langle \Phi(p) | \Phi(q; \theta) \rangle \\
 &\equiv \frac{d_{\tilde{\sigma}}}{v_G} \sum_{\theta} D_{00}^{\tilde{\sigma}*}(\theta) O_{pIqJ}(\theta) \langle \Phi(p) | \Phi(q; \theta) \rangle,
 \end{aligned} \tag{D.1}$$

where I and J denote arbitrary i -tuple and j -tuple excitations¹ of the corresponding vacua and where all involved quantities have been introduced and/or worked out in the previous appendices.

While the matrix elements introduced in Eq. (D.1) are defined (and could be evaluated) for an operator and excitations of arbitrary ranks, the implementation of PGCM-PT(2) on the basis of a two-body Hamiltonian only requires a subset of them that are now worked out explicitly.

D.1. Type-1 matrix elements

The first category of matrix elements is obtained from $O_{pIqJ}^{\tilde{\sigma}}$ whenever

1. O is a two-body operator²,
2. $I = 0, S, D$, where $0 = \{\}$, $S = \{k_1 k_2\}$, $D = \{k_1 k_2 k_3 k_4\}$ stands for no/single/double excitation,
3. $J = 0$, i.e. the ket state is fixed to be the vacuum.

Starting thus from a two-body operator O in the form given by Eq. (C.1), the many-body matrix elements of interest are worked out by exploiting Eqs. (1.59), (1.60), (C.2) and (C.3) and by applying Wick's theorem with respect to $|\Phi(p)\rangle$ such that

$$O_{p0q0}(\theta) = {}^Z \mathbf{O}^{00}, \tag{D.2a}$$

¹Whenever there is no excitation, i.e. whenever the associated excitation operator is the identity, the index is conventionally put to 0.

²If working with explicit three-body interactions, O would be of three-body character.

$$O_{pSq0}(\theta) = \mathbf{z}^{k_1 k_2} Z \mathbf{O}^{00} + Z \mathbf{o}^{k_1 k_2}, \quad (\text{D.2b})$$

$$O_{pDq0}(\theta) = P(k_1/k_3 k_4) \mathbf{z}^{k_1 k_2} \mathbf{z}^{k_3 k_4} Z \mathbf{O}^{00} \\ + P(k_1 k_2/k_3 k_4) \mathbf{z}^{k_3 k_4} Z \mathbf{o}^{k_1 k_2} + Z \mathbf{o}^{k_1 k_2 k_3 k_4}, \quad (\text{D.2c})$$

where the $(p, q; \theta)$ dependencies of the various quantities appearing on the right-hand side have been omitted.

D.2. Type-2 matrix elements

The second category of matrix elements is obtained from $O_{pIqJ}^{\tilde{}}$ whenever

1. O is a one-body operator,
2. $I = 0, S, D$,
3. $J = 0, S, D$.

Starting from a one-body operator O , i.e. a sub-part of the operator given by Eq. (C.1), the evaluation of this second category of many-body matrix elements further requires the use of Eqs. (1.66)-(1.67) given that excitations of the ket are now in order.

Vacuum-to-vacuum and $(I = 0, J = 0)$ and excitation-to-vacuum $(I \neq 0, J = 0)$ matrix elements can be deduced from Eq. (D.2) and are thus not repeated here. Vacuum-to-excitation $(I \neq 0, J = 0)$ matrix elements are given by

$$O_{p0qS}(\theta) = Z \mathbf{O}^{00} \sum_{j_1} E_{j_1}^{k_1} D^{-1 \dagger j_1 k_2} \\ + \sum_{j_1 j_2} Z \mathbf{o}_{j_1 j_2} D^{-1 \dagger j_1 k_1} D^{-1 \dagger j_2 k_2} \quad (\text{D.3a})$$

$$O_{p0qD}(\theta) = P(k_1/k_3 k_4) Z \mathbf{O}^{00} \sum_{j_2 j_4} E_{j_2}^{k_1} D^{-1 \dagger j_2 k_2} E_{j_4}^{k_3} D^{-1 \dagger j_4 k_4} \\ + P(k_1 k_2/k_3 k_4) \sum_{j_1 j_2 j_4} Z \mathbf{o}_{j_1 j_2} D^{-1 \dagger j_1 k_1} D^{-1 \dagger j_2 k_2} E_{j_4}^{k_3} D^{-1 \dagger j_4 k_4}. \quad (\text{D.3b})$$

Excitation-to-excitation $(I \neq 0, J \neq 0)$ matrix elements are of course the most involved ones. Single-to-single $(I = S' = \{i_1 i_2\}, J = S = \{k_1 k_2\})$ ones read as

$$O_{pS'qS}(\theta) = P(i_1/i_2) Z \mathbf{O}^{00} D^{-1 \dagger i_1 k_1} D^{-1 \dagger i_2 k_2} \\ + P(i_1/i_2) P(k_1/k_2) \sum_{j_1} Z \mathbf{o}_{j_1}^{i_1} D^{-1 \dagger j_1 k_1} D^{-1 \dagger i_2 k_2} \\ + P(k_1/k_2) \mathbf{z}^{i_1 i_2} \sum_{j_1 j_2} D^{-1 \dagger j_1 k_1} Z \mathbf{o}_{j_1 j_2} D^{-1 \dagger j_2 k_2} \\ + P(i_1/i_2) Z \mathbf{o}^{i_1 i_2} \sum_{j_2} E_{j_2}^{k_1} D^{-1 \dagger j_2 k_2} \\ + Z \mathbf{O}^{00} \mathbf{z}^{i_1 i_2} \sum_{j_2} E_{j_2}^{k_1} D^{-1 \dagger j_2 k_2}. \quad (\text{D.3c})$$

Double-to-single $(I = D = \{i_1 i_2 i_3 i_4\}, J = S = \{k_1 k_2\})$ matrix elements read as

$$O_{pDqS}(\theta) = P(i_1 i_2/i_3 i_4) P(k_1/k_2) D^{-1 \dagger i_1 k_1} D^{-1 \dagger i_2 k_2} Z \mathbf{o}^{i_3 i_4}$$

$$\begin{aligned}
 & + P(i_1 i_2 / i_3 i_4) P(k_1 / k_2) \mathbf{z}^{i_3 i_4} D^{-1 \dagger i_1 k_1} D^{-1 \dagger i_2 k_2} \mathbf{O}^{00} \\
 & + P(i_1 / i_2 / i_3 i_4) P(k_1 / k_2) \mathbf{z}^{i_3 i_4} D^{-1 \dagger i_1 k_1} \sum_{j_2} Z_{\mathbf{O}_{i_2 j_2}} D^{-1 \dagger j_2 k_2} \\
 & + P(i_1 i_2 / i_3 i_4) \mathbf{z}^{i_1 i_2} Z_{\mathbf{O}^{i_3 i_4}} \sum_{j_2} E_{j_2}^{k_2} D^{-1 \dagger j_2 k_1} \\
 & + P(i_1 i_2 / i_3 i_4) \mathbf{z}^{i_1 i_2} \mathbf{z}^{i_3 i_4} \sum_{j_1 j_2} Z_{\mathbf{O}_{j_1 j_2}} D^{-1 \dagger j_1 k_1} D^{-1 \dagger j_2 k_2} \\
 & + P(i_1 / i_3 i_4) \mathbf{z}^{i_1 i_2} \mathbf{z}^{i_3 i_4} \mathbf{O}^{00} \sum_{j_2} E_{j_2}^{k_2} D^{-1 \dagger j_2 k_1} .
 \end{aligned} \tag{D.3d}$$

Single-to-double ($I = S = \{i_1 i_2\}, J = D = \{k_1 k_2 k_3 k_4\}$) matrix elements read as

$$\begin{aligned}
 O_{pSqD}(\theta) & = P(k_1 k_2 / k_3 k_4) P(i_1 / i_2) Z_{\mathbf{O}_{j_3 j_4}} D^{-1 \dagger j_3 k_3} D^{-1 \dagger j_4 k_4} D^{-1 \dagger i_1 k_1} D^{-1 \dagger i_2 k_2} \\
 & + P(k_1 k_2 / k_3 k_4) P(i_1 / i_2) \mathbf{O}^{00} D^{-1 \dagger i_1 k_1} D^{-1 \dagger i_2 k_2} \sum_{j_3} E_{j_3}^{k_4} D^{-1 \dagger j_3 k_3} \\
 & + P(k_1 / k_2 / k_3 k_4) P(i_1 / i_2) D^{-1 \dagger i_1 k_1} \left(\sum_{j_3} E_{j_3}^{k_3} D^{-1 \dagger j_3 k_4} \right) \left(\sum_{j_2} D^{-1 \dagger j_2 k_2} Z_{\mathbf{O}_{j_2}^{i_2}} \right) \\
 & + P(k_1 k_2 / k_3 k_4) \mathbf{z}^{i_2 i_1} \left(\sum_{j_3} E_{j_3}^{k_4} D^{-1 \dagger j_3 k_3} \right) \left(\sum_{j_1 j_2} Z_{\mathbf{O}_{j_1 j_2}} D^{-1 \dagger j_1 k_1} D^{-1 \dagger j_2 k_2} \right) \\
 & + P(k_1 / k_3 k_4) Z_{\mathbf{O}^{i_1 i_2}} \left(\sum_{j_1} E_{j_1}^{k_1} D^{-1 \dagger j_1 k_2} \right) \left(\sum_{j_3} E_{j_3}^{k_4} D^{-1 \dagger j_3 k_3} \right) \\
 & + P(k_1 / k_3 k_4) Z_{\mathbf{O}^{00}} \mathbf{z}^{i_2 i_1} \left(\sum_{j_3} E_{j_3}^{k_4} D^{-1 \dagger j_3 k_3} \right) \left(\sum_{j_1} E_{j_1}^{k_2} D^{-1 \dagger j_1 k_1} \right) .
 \end{aligned} \tag{D.3e}$$

Double-to-double ($I = D = \{i_1 i_2 i_3 i_4\}, J = D' = \{k_1 k_2 k_3 k_4\}$) matrix elements read as

$$\begin{aligned}
 O_{pDqD'}(\theta) & = P(i_4 / i_3 / i_2 / i_1) Z_{\mathbf{O}^{00}} D^{-1 \dagger k_4 i_4} D^{-1 \dagger i_3 k_3} D^{-1 \dagger i_2 k_2} D^{-1 \dagger i_1 k_1} \\
 & + P(k_4 / k_3 k_2 k_1) P(i_4 / i_3 / i_2 / i_1) \left(\sum_{j_4} Z_{\mathbf{O}_{j_4}^{i_4}} D^{-1 \dagger j_4 k_4} \right) D^{-1 \dagger i_3 k_3} D^{-1 \dagger i_2 k_2} D^{-1 \dagger i_1 k_1} \\
 & + P(i_1 i_2 / i_3 i_4) \mathbf{z}^{i_1 i_2} P(k_1 k_2 / k_3 / k_4) D^{-1 \dagger i_4 k_4} D^{-1 \dagger i_3 k_3} \sum_{j_2 j_1} D^{-1 \dagger j_1 k_1} Z_{\mathbf{O}_{j_1 j_2}} D^{-1 \dagger j_2 k_2} \\
 & + P(k_1 k_2 / k_3 k_4) P(i_1 i_2 / i_3 / i_4) Z_{\mathbf{O}^{i_1 i_2}} D^{-1 \dagger i_4 k_4} D^{-1 \dagger i_3 k_3} \left(\sum_{j_1} E_{j_1}^{k_2} D^{-1 \dagger j_1 k_1} \right) \\
 & + P(i_1 i_2 / i_3 / i_4) P(k_1 k_2 / k_3 k_4) \mathbf{z}^{i_1 i_2} \mathbf{O}^{00} D^{-1 \dagger i_4 k_4} D^{-1 \dagger i_3 k_3} \left(\sum_{j_1} E_{j_1}^{k_2} D^{-1 \dagger j_1 k_1} \right) \\
 & + P(i_1 i_2 / i_3 / i_4) P(k_1 k_2 / k_3 / k_4) \mathbf{z}^{i_1 i_2} \left(\sum_{j_1} E_{j_1}^{k_2} D^{-1 \dagger j_1 k_1} \right) \left(\sum_{j_4} Z_{\mathbf{O}_{j_4}^{i_4}} D^{-1 \dagger j_4 k_4} D^{-1 \dagger i_3 k_3} \right) \\
 & + P(i_1 / i_3 i_4) P(k_1 k_2 / k_3 k_4) \mathbf{z}^{i_1 i_2} \mathbf{z}^{i_3 i_4} \left(\sum_{j_1} E_{j_1}^{k_2} D^{-1 \dagger j_1 k_1} \right) \left(\sum_{j_4 j_3} D^{-1 \dagger j_3 k_3} Z_{\mathbf{O}_{j_3 j_4}} D^{-1 \dagger j_4 k_4} \right) \\
 & + P(i_1 i_2 / i_3 i_4) P(k_1 / k_3 k_4) \mathbf{z}^{i_1 i_2} Z_{\mathbf{O}^{i_3 i_4}} \left(\sum_{j_3} E_{j_3}^{k_4} D^{-1 \dagger j_3 k_3} \right) \left(\sum_{j_1} E_{j_1}^{k_2} D^{-1 \dagger j_1 k_1} \right)
 \end{aligned}$$

$$+ P(i_1/i_3 i_4) P(k_1/k_3 k_4) \mathbf{Z}^{i_1 i_2} \mathbf{Z}^{i_3 i_4} \mathbf{O}^{00} \left(\sum_{j_3} E_{j_3}^{k_4} D^{-1 \dagger j_3 k_3} \right) \left(\sum_{j_1} E_{j_1}^{k_2} D^{-1 \dagger j_1 k_1} \right). \quad (\text{D.3f})$$

D.3. Type-3 matrix elements

The third category of matrix elements is obtained from $O_{pIqJ}^{\tilde{\sigma}}$ whenever

1. O is a zero-body operator, i.e. the identity operator multiplied by the number O^{00} ,
2. $I = 0, S, D$,
3. $J = 0, S, D$.

All these matrix elements can be deduced from the previous cases by solely keeping the terms proportional to ${}^Z\mathbf{O}^{00} = O^{00}$ in the appropriate expressions.

Appendix E.

Single-reference (Bogoliubov) Many-Body Perturbation Theory

The presently developed perturbation theory is of multi-reference character due to the fact that the PGCM unperturbed state (Eq. (2.23)) is a linear combination of several Bogoliubov vacua. However, in the limit where the PGCM state reduces to a single Bogoliubov state, which itself reduces to a Slater determinant whenever $U(1)$ symmetry is conserved, PGCM-PT becomes of single-reference character and must thus entertain some connection with single-reference (B)MBPT [45, 54, 60]. To clarify this connection, the partitioning at play in the latter approaches and the second and third order energy corrections of the theory are now briefly discussed. BMBPT density matrices expressions are also given in this appendix.

E.1. Single-reference partitioning

E.1.1. BMBPT

Because of the inherent necessity to control the average particle number, the operator driving the perturbation in BMBPT is the grand potential Ω [46]. Whenever $|\Phi(q)\rangle$ results from a *constrained* HFB calculation (see Sec. 1.2.4), a natural partitioning is given by

$$\Omega = \Omega_0(q) + \Omega_1(q) , \quad (\text{E.1})$$

such that

$$\Omega_0(q) \equiv \mathbf{\Omega}^{00}(q) + \bar{\mathbf{\Omega}}^{11}(q) , \quad (\text{E.2a})$$

$$\begin{aligned} \Omega_1(q) \equiv & \mathbf{\Omega}^{20}(q) + \check{\mathbf{\Omega}}^{11}(q) + \mathbf{\Omega}^{02}(q) \\ & + \mathbf{\Omega}^{40}(q) + \mathbf{\Omega}^{31}(q) + \mathbf{\Omega}^{22}(q) + \mathbf{\Omega}^{13}(q) + \mathbf{\Omega}^{04}(q) , \end{aligned} \quad (\text{E.2b})$$

with $\check{\mathbf{\Omega}}^{11}(q) \equiv \mathbf{\Omega}^{11}(q) - \bar{\mathbf{\Omega}}^{11}(q)$ and where the diagonal one-body part of $\Omega_0(q)$

$$\bar{\mathbf{\Omega}}^{11}(q) \equiv \sum_k E_k(q) \beta_k^\dagger(q) \beta_k(q) , \quad (\text{E.3})$$

is built out of the positive eigenvalues generated through Eq. (1.35). In general, the partitioning defined in Eqs. (E.1)-(E.3) is *not* canonical given that, while Eq. (1.39) is fulfilled for the Routhian R , it is not for Ω except for $\lambda_q = 0$, i.e. whenever $|\Phi(q)\rangle$ is the solution of an *unconstrained* HFB calculation. The eigenstates of $\Omega_0(q)$ are nothing but

$$\Omega_0(q) |\Phi(q)\rangle = \mathbf{\Omega}^{00}(q) |\Phi(q)\rangle , \quad (\text{E.4a})$$

$$\Omega_0(q) |\Phi^{k_1 \dots}(q)\rangle = [\mathbf{\Omega}^{00}(q) + E_{k_1}(q) + \dots] |\Phi^{k_1 \dots}(q)\rangle . \quad (\text{E.4b})$$

E.1.2. MBPT

Whenever $q_{U(1)} = 0$, $|\Phi(q)\rangle$ is a Slater determinant and BMBPT reduces to MBPT. In this situation, the Bogoliubov field $\bar{\Delta}(q)$ is zero and the Lagrange term associated with the particle number constraint entering the Routhian becomes superfluous and can be omitted. As a result, Eq. (1.35) reduces to

$$h(q) (U(q))_k = e_k(q) (U(q))_k , \quad (\text{E.5})$$

i.e. to the constrained Hartree-Fock (HF) equation where the one-body HF field reads as

$$h_{l'}^l(q) \equiv f_{l'}^l[|\Phi(q)\rangle] - \lambda_q \frac{\partial \mathbf{Q}^{00}(q)}{\partial \rho_{l'}^{*l}(q)} . \quad (\text{E.6})$$

Solving Eq. (E.5) delivers constrained HF single-particle states $\{a_k^\dagger(q)\}$ through the unitary one-body basis transformation $U(q)$ along with the associated HF single-particle energies

$$e_k(q) = f_k^k[|\Phi(q)\rangle] - \lambda_q \frac{\partial \mathbf{Q}^{00}(q)}{\partial \rho_k^{*k}(q)} . \quad (\text{E.7})$$

The HF Slater determinant is built by occupying the A lowest HF single-particle states

$$|\Phi(q)\rangle \equiv A^{i_1 \dots i_A}(q) |0\rangle . \quad (\text{E.8})$$

Because the Lagrange term associated with the particle-number constraint is superfluous, the operator driving the perturbative expansion in MBPT is nothing but the Hamiltonian. Given the above, the unperturbed Hamiltonian deriving from Eq. (E.2) becomes

$$\begin{aligned} H_0(q) &\equiv \mathbf{H}^{00}(q) + : h(q) : \\ &= E^{(0)}(q) + \sum_k e_k(q) : A_k^k(q) : , \end{aligned} \quad (\text{E.9})$$

where the latter form is given in the eigenbasis of $h(q)$. Equation (E.7) makes clear that $h(q) = F_{[|\Phi(q)\rangle]}$ whenever $\lambda_q = 0$ such that $\{e_k(q)\}$ denotes nothing but the eigenvalues of $F_{[|\Phi(q)\rangle]}$ in that particular case.

The A -body eigenbasis of H_0 is given by

$$H_0(q) |\Phi(q)\rangle = E^{(0)}(q) |\Phi(q)\rangle , \quad (\text{E.10a})$$

$$H_0(q) |\Phi_{h_1 \dots}^{p_1 \dots}(q)\rangle = E_{p_1 \dots h_1 \dots}^{(0)}(q) |\Phi_{h_1 \dots}^{p_1 \dots}(q)\rangle , \quad (\text{E.10b})$$

with

$$\begin{aligned} E^{(0)}(q) &\equiv \mathbf{H}^{00}(q) = \langle \Phi(q) | H | \Phi(q) \rangle , \\ E_{p_1 \dots h_1 \dots}^{(0)}(q) &\equiv E^{(0)}(q) + e_{p_1}(q) + \dots - e_{h_1}(q) - \dots , \end{aligned}$$

where elementary particle-hole excitations of the unperturbed Slater determinant are defined through

$$|\Phi_{h_1 \dots}^{p_1 \dots}(q)\rangle \equiv A_{h_1 \dots}^{p_1 \dots}(q) |\Phi(q)\rangle . \quad (\text{E.11})$$

Whenever applied at the minimum of $\mathbf{H}^{00}(q)$, the spectrum of H_0 is ensured to be non-degenerate with respect to elementary excitations¹, i.e. it displays a gap-full spectrum

$$E_{p_1 \dots h_1 \dots}^{(0)}(q) - E^{(0)}(q) > 0. \quad (\text{E.12})$$

This is schematically illustrated in Fig. 2.3.

E.2. Second and third order BMBPT energy corrections

Injecting the BMBPT splitting defined Eq. (E.1) for BMBPT into the expression of the energy corrections given Eq. (2.12), the unperturbed part of the Hamiltonian can be analytically inverted and the energy corrections take a closed-form expression.

E.2.1. Second order

The second-order energy, extracted from Eq. (2.12b), reads [54]

$$E^{(2)}(q) \equiv -\frac{1}{2} \sum_{k_1 k_2} \frac{H_{k_1 k_2}(q) \Omega_{k_1 k_2}^{k_1 k_2}(q)}{E_{k_1 k_2}(q)} - \sum_{k_1 k_2 k_3 k_4} \frac{1}{24} \frac{H_{k_1 k_2 k_3 k_4}(q) \Omega_{k_1 k_2 k_3 k_4}^{k_1 k_2 k_3 k_4}(q)}{E_{k_1 k_2 k_3 k_4}(q)}. \quad (\text{E.13})$$

E.2.2. Third order

The third-order energy, extracted from Eq. (2.12c), reads [54]

$$\begin{aligned} E^{(3)}(q) \equiv & \sum_{k_i} \frac{H_{k_1 k_2}(q) \Omega_{k_3}^{k_1}(q) \Omega_{k_2 k_3}^{k_3 k_2}(q)}{E_{k_1 k_2}(q) E_{k_2 k_3}(q)} \\ & + \frac{1}{4} \sum_{k_i} \frac{H_{k_1 k_2}(q) \Omega_{k_3 k_4}^{k_1 k_2}(q) \Omega_{k_3 k_4}^{k_3 k_4}(q)}{E_{k_1 k_2}(q) E_{k_3 k_4}(q)} \\ & + \frac{1}{4} \sum_{k_i} \frac{H_{k_1 k_2}(q) \Omega_{k_3 k_4}(q) \Omega_{k_1 k_2 k_3 k_4}^{k_1 k_2 k_3 k_4}(q)}{E_{k_1 k_2}(q) E_{k_1 k_2 k_3 k_4}(q)} \\ & + \frac{1}{8} \sum_{k_i} \frac{H_{k_1 k_2 k_3 k_4}(q) \Omega_{k_1 k_2}^{k_1 k_2}(q) \Omega_{k_3 k_4}^{k_3 k_4}(q)}{E_{k_1 k_2}(q) E_{k_3 k_4}(q)} \\ & + \frac{1}{6} \sum_{k_i} \frac{H_{k_1 k_2 k_3 k_4}(q) \Omega_{k_5}^{k_1 k_2 k_3}(q) \Omega_{k_5 k_4}^{k_5 k_4}(q)}{E_{k_4 k_5}(q) E_{k_1 k_2 k_3 k_4}(q)} \\ & + \frac{1}{6} \sum_{k_i} \frac{H_{k_1 k_2 k_3 k_4}(q) \Omega_{k_5}^{k_1}(q) \Omega_{k_5 k_2 k_3 k_4}^{k_5 k_2 k_3 k_4}(q)}{E_{k_2 k_3 k_4 k_5}(q) E_{k_1 k_2 k_3 k_4}(q)} \\ & + \frac{1}{6} \sum_{k_i} \frac{H_{k_1 k_2}(q) \Omega_{k_3 k_4 k_5}^{k_1}(q) \Omega_{k_3 k_4 k_5 k_2}^{k_3 k_4 k_5 k_2}(q)}{E_{k_2 k_3 k_4 k_5}(q) E_{k_1 k_2 k_3 k_4}(q)} \\ & + \frac{1}{8} \sum_{k_i} \frac{H_{k_1 k_2 k_3 k_4}(q) \Omega_{k_5 k_6}^{k_1 k_2}(q) \Omega_{k_5 k_6 k_3 k_4}^{k_5 k_6 k_3 k_4}(q)}{E_{k_1 k_2 k_3 k_4}(q) E_{k_3 k_4 k_5 k_6}(q)}. \end{aligned} \quad (\text{E.14})$$

¹The fact that the unperturbed state is non-degenerate is a necessary (but not sufficient) condition for the perturbative series to converge or at least offers mean to be (partially) re-summed. Note that a degeneracy with states carrying different symmetry quantum numbers is not an issue since symmetry blocks are not connected by the perturbation within a symmetry-conserving scheme.

E.3. BMBPT transition density matrix

The BMBPT(2) transition one-body density matrix is presently derived within the frame of a so-called *expectation-value* many-body scheme rather than within a *projective* one, i.e. it is computed directly through Eq. (1.11) for $l = 1$ and $|\Theta\rangle \equiv |\Psi^{\text{BMBPT}(2)}\rangle$. The derivation can actually be performed within the larger frame of the Bogoliubov configuration-interaction (BCI) formalism such that BCI-like expansion coefficients are eventually obtained within the frame of BMBPT(2) [54].

The present applications are eventually limited to standard MBPT, i.e. calculations are restricted to doubly closed-shell nuclei for which BMBPT reduces to MBPT on top of a $J^\Pi = 0^+$ Slater determinant.

E.3.1. BCI state

In BCI, many-body states are written as a CI-like expansion on top of the (deformed) Bogoliubov vacuum. Presently truncated to single and double excitations, the BCISD ansatz reads as

$$\begin{aligned} |\Psi(q)\rangle \equiv & \left(1 + \sum_{k_1 k_2} C^{k_1 k_2}(q) \beta_{k_1}^\dagger(q) \beta_{k_2}^\dagger(q) \right. \\ & + \sum_{k_1 k_2 k_3 k_4} C^{k_1 k_2 k_3 k_4}(q) \beta_{k_1}^\dagger(q) \beta_{k_2}^\dagger(q) \beta_{k_3}^\dagger(q) \beta_{k_4}^\dagger(q) \Big) \\ & \times |\Phi(q)\rangle, \end{aligned} \quad (\text{E.15})$$

where the unknown coefficients, anti-symmetric with respect to the exchange of any pair of upper indices, can be obtained by diagonalization of Ω or via BMBPT.

E.3.2. Expression in quasi-particle space

Definition

Considering two different BCISD states $|\Psi^i(q)\rangle$ and $|\Psi^f(q)\rangle$, the four transition one-body density matrices defined in terms of quasi-particle operators are given by

$$\rho^{fi k_2}_{k_1}(q) \equiv \frac{\langle \Psi^f(q) | \beta_{k_1}^\dagger(q) \beta_{k_2}(q) | \Psi^i(q) \rangle}{\sqrt{\langle \Psi^f(q) | \Psi^f(q) \rangle \langle \Psi^i(q) | \Psi^i(q) \rangle}}, \quad (\text{E.16a})$$

$$\kappa^{fi k_2 k_1}(q) \equiv \frac{\langle \Psi^f(q) | \beta_{k_1}(q) \beta_{k_2}(q) | \Psi^i(q) \rangle}{\sqrt{\langle \Psi^f(q) | \Psi^f(q) \rangle \langle \Psi^i(q) | \Psi^i(q) \rangle}}, \quad (\text{E.16b})$$

$$-\kappa^{*fi}_{k_2 k_1}(q) \equiv \frac{\langle \Psi^f(q) | \beta_{k_1}^\dagger(q) \beta_{k_2}^\dagger(q) | \Psi^i(q) \rangle}{\sqrt{\langle \Psi^f(q) | \Psi^f(q) \rangle \langle \Psi^i(q) | \Psi^i(q) \rangle}}, \quad (\text{E.16c})$$

$$-\sigma^{*fi k_1}_{k_2}(q) \equiv \frac{\langle \Psi^f(q) | \beta_{k_1}(q) \beta_{k_2}^\dagger(q) | \Psi^i(q) \rangle}{\sqrt{\langle \Psi^f(q) | \Psi^f(q) \rangle \langle \Psi^i(q) | \Psi^i(q) \rangle}}, \quad (\text{E.16d})$$

among which the relations

$$\kappa^{*fi}_{k_2 k_1}(q) = \left(\kappa^{if k_2 k_1}(q) \right)^*, \quad (\text{E.17a})$$

$$\sigma^{*fi k_1}_{k_2}(q) = \left(\rho^{if k_2}_{k_1}(q) \right)^* - 1, \quad (\text{E.17b})$$

hold.

Matrix elements

Starting from Eqs. (E.15)-(E.16) and applying Wick's theorem, one obtains

$$\begin{aligned} \rho^{fi k_2}_{k_1}(q) &= \frac{1}{\sqrt{\langle \Psi^f(q) | \Psi^f(q) \rangle \langle \Psi^i(q) | \Psi^i(q) \rangle}} \\ &\times \left[\frac{1}{2} \sum_{k_3} C^{f*}_{k_1 k_3}(q) C^{i k_2 k_3}(q) \right. \\ &\quad \left. + \frac{1}{12} \sum_{k_3 k_4 k_5} C^{f*}_{k_1 k_3 k_4 k_5}(q) C^{i k_2 k_3 k_4 k_5}(q) \right], \end{aligned}$$

and

$$\begin{aligned} \kappa^{fi k_1 k_2}(q) &= \frac{1}{\sqrt{\langle \Psi^f(q) | \Psi^f(q) \rangle \langle \Psi^i(q) | \Psi^i(q) \rangle}} \\ &\times \left[\frac{1}{2} C^{i k_1 k_2}(q) \right. \\ &\quad \left. + \frac{1}{4} \sum_{k_3 k_4} C^{f*}_{k_3 k_4}(q) C^{i k_1 k_2 k_3 k_4}(q) \right]. \end{aligned}$$

The expressions of κ^{fi*} and σ^{*fi} are then deduced via Eq. (E.17) whereas the norm entering the denominators of the transition one-body density matrices reads, e.g., as

$$\begin{aligned} \langle \Psi^i(q) | \Psi^i(q) \rangle &\equiv 1 \\ &+ \sum_{k_1 k_2} C^{i*}_{k_1 k_2}(q) C^{i k_1 k_2}(q) \\ &+ \sum_{k_1 k_2 k_3 k_4} C^{i*}_{k_1 k_2 k_3 k_4}(q) C^{i k_1 k_2 k_3 k_4}(q). \end{aligned}$$

E.3.3. Expression in one-particle space

Inserting the inverse Bogoliubov transformation, the normal one-body density matrix expressed in terms of particle operators is obtained under the form

$$\begin{aligned} \rho^{fi b}_a(q) &\equiv \frac{\langle \Psi^f(q) | c_a^\dagger c_b | \Psi^i(q) \rangle}{\sqrt{\langle \Psi^f(q) | \Psi^f(q) \rangle \langle \Psi^i(q) | \Psi^i(q) \rangle}} \\ &= \sum_{k_1 k_2} \left[U^{k_2 b}(q) \rho^{fi k_2}_{k_1}(q) U_{k_1 a}^*(q) \right. \\ &\quad - V_{k_2}^{*b}(q) \sigma^{*fi k_1}_{k_2}(q) V_a^{k_1}(q) \\ &\quad - V_{k_2}^{*b}(q) \kappa^{*fi}_{k_2 k_1}(q) U_{k_1 a}^*(q) \\ &\quad \left. + U^{k_2 b}(q) \kappa^{fi k_2 k_1}(q) V_a^{k_1}(q) \right]. \quad (\text{E.18}) \end{aligned}$$

E.3.4. One-body density matrix

In the present work, one is interested in the case where $|\Psi^i(q)\rangle = |\Psi^f(q)\rangle \equiv |\Psi(q)\rangle$ such that Eq. (E.18) reduces to

$$\begin{aligned} \rho_a^{\Psi^b}(q) = & \sum_{k_1 k_2} \left[V_{k_2}^{*b}(q) V_a^{k_1}(q) \right. \\ & + U^{k_2 b}(q) \boldsymbol{\rho}^{\Psi^{k_2}}_{k_1}(q) U_{k_1 a}^*(q) \\ & - \left(V_b^{k_2}(q) \boldsymbol{\rho}^{\Psi^{k_2}}_{k_1}(q) V_{k_1}^{*a}(q) \right)^* \\ & - \left(V_b^{k_2}(q) \boldsymbol{\kappa}^{\Psi^{k_2 k_1}}(q) U^{*k_1 a}(q) \right)^* \\ & \left. + U^{k_2 b}(q) \boldsymbol{\kappa}^{\Psi^{k_2 k_1}}(q) V_a^{k_1}(q) \right]. \end{aligned} \quad (\text{E.19})$$

When time-reversal symmetry is preserved, the one-body density matrix can be chosen to be real such that the final expression reads as

$$\begin{aligned} \rho_a^{\Psi^b}(q) = & \rho_a^{\Phi^b}(q) \\ & + \sum_{k_1 k_2} \left[U^{k_2 b}(q) \boldsymbol{\rho}^{\Psi^{k_2}}_{k_1}(q) U_{k_1 a}^*(q) \right. \\ & - V_b^{k_2}(q) \boldsymbol{\rho}^{\Psi^{k_2}}_{k_1}(q) V_{k_1}^{*a}(q) \\ & - V_b^{k_2}(q) \boldsymbol{\kappa}^{\Psi^{k_2 k_1}}(q) U^{*k_1 a}(q) \\ & \left. + U^{k_2 b}(q) \boldsymbol{\kappa}^{\Psi^{k_2 k_1}}(q) V_a^{k_1}(q) \right], \end{aligned} \quad (\text{E.20})$$

where $\rho^\Phi(q)$ denotes the one-body density matrix of the reference state $|\Phi(q)\rangle$ such that the additional terms relate to BCISD corrections on top of it.

E.3.5. BMBPT coefficients

The coefficients of the BCISD state obtained at first- and second-order in BMBPT are now explicitly provided [54]. Given that the present application is limited to a $J^\Pi = 0^+$ Slater determinant reference state $|\Phi\rangle$, the resulting one-body density matrix $\rho_a^{\Psi^b}$ is actually proportional to $\delta_{j_a j_b}$ and relates to a many-body state that is an eigenvector of the particle-number operator.

First-order correction

At first order in BMBPT, singles and doubles BCI-like coefficients read as

$$C^{(1)k_1 k_2}(q) \equiv - \frac{\Omega^{k_1 k_2}(q)}{E_{k_1 k_2}(q)}, \quad (\text{E.21a})$$

$$C^{(1)k_1 k_2 k_3 k_4}(q) \equiv - \frac{\Omega^{k_1 k_2 k_3 k_4}(q)}{E_{k_1 k_2 k_3 k_4}(q)}. \quad (\text{E.21b})$$

Second-order correction

At second order in BMBPT, singles and doubles BCI-like coefficients read

$$\begin{aligned}
 C^{(2)k_1k_2}(q) \equiv & \frac{1}{6}P(k_1/k_2) \sum_{k_3k_4k_5} \frac{C^{(1)k_1k_4k_5k_3}(q)\Omega_{k_4k_5k_3}^{k_2}(q)}{E_{k_1k_2}(q)} \\
 & + \frac{1}{2} \sum_{k_3k_4} \frac{C^{(1)k_1k_2k_3k_4}(q)\Omega_{k_3k_4}(q)}{E_{k_1k_2}(q)} \\
 & + \frac{1}{2} \sum_{k_3k_4} \frac{C^{(1)k_3k_4}(q)\Omega_{k_3k_4}^{k_1k_2}(q)}{E_{k_1k_2}(q)} \\
 & + P(k_1/k_2) \sum_{k_3} \frac{C^{(1)k_1k_3}(q)\check{\Omega}_{k_3}^{k_2}(q)}{E_{k_1k_2}(q)}, \tag{E.22a}
 \end{aligned}$$

$$\begin{aligned}
 C^{(2)k_1k_2k_3k_4}(q) \equiv & \frac{1}{2}P(k_1k_2/k_3k_4) \sum_{k_5k_6} \frac{C^{(1)k_1k_2k_5k_6}(q)\Omega_{k_5k_6}^{k_3k_4}(q)}{E_{k_1k_2k_3k_4}(q)} \\
 & + P(k_4/k_1k_2k_3) \sum_{k_5} \frac{C^{(1)k_1k_2k_3k_5}(q)\check{\Omega}_{k_5}^{k_4}(q)}{E_{k_1k_2k_3k_4}(q)} \\
 & + P(k_1/k_2k_3k_4) \sum_{k_5} \frac{C^{(1)k_1k_5}(q)\Omega_{k_5}^{k_2k_3k_4}(q)}{E_{k_1k_2k_3k_4}(q)} \\
 & + P(k_1k_2/k_3k_4) \left[C^{(1)k_1k_2}(q)C^{(1)k_3k_4}(q) \right], \tag{E.22b}
 \end{aligned}$$

where anti-symmetrizing operators $P(\dots/\dots)$ were defined in App. B.

Appendix F.

Inverse tensor transformations

Given the operator O , i.e. the set of tensors $\{o^{(n)}; n = 0, \dots, N\}$, and the one-body density matrix ρ , a second set of matrices is introduced through

$$\mathbf{o}^{(k)}[\rho] \equiv \sum_{n=k}^N \frac{1}{(n-k)!} o^{(n)} \cdot \rho^{\otimes(n-k)} \quad (\text{F.1})$$

with $k = 0, \dots, N$. In a second step, the third set of tensors is defined via

$$\tilde{o}^{(n)}[\rho] \equiv \sum_{l=n}^N \frac{(-1)^{l-n}}{(l-n)!} \mathbf{o}^{(l)}[\rho] \cdot \rho^{\otimes(l-n)} \quad (\text{F.2})$$

with $n = 0, \dots, N$.

The third set of tensors is now shown to be the same as the initial one. Noting that

$$\begin{aligned} \mathbf{o}^{(l)}[\rho] \cdot \rho^{\otimes(l-n)} &= \sum_{k=l}^N \frac{1}{(k-l)!} \left(o^{(k)} \cdot \rho^{\otimes(k-l)} \right) \cdot \rho^{\otimes(l-n)} \\ &= \sum_{k=l}^N \frac{1}{(k-l)!} o^{(k)} \cdot \rho^{\otimes(k-n)}, \end{aligned} \quad (\text{F.3})$$

one obtains

$$\begin{aligned} \tilde{o}^{(n)}[\rho] &= \sum_{l=n}^N \sum_{k=l}^N \frac{(-1)^{l-n}}{(l-n)!} \frac{1}{(k-l)!} o^{(k)} \cdot \rho^{\otimes(k-n)} \\ &= \sum_{k=n}^N \left[\sum_{l=n}^k (-1)^{l-n} \frac{1}{(l-n)!(k-l)!} \right] o^{(k)} \cdot \rho^{\otimes(k-n)} \\ &= \sum_{k=n}^N \left[\sum_{l=n}^k (-1)^{l-n} \binom{k-n}{l-n} \right] \frac{1}{(k-n)!} o^{(k)} \cdot \rho^{\otimes(k-n)} \\ &= \sum_{k=n}^N \delta_{kn} \frac{1}{(k-n)!} o^{(k)} \cdot \rho^{\otimes(k-n)} \\ &= o^{(n)}, \end{aligned} \quad (\text{F.4})$$

such that each original tensor $o^{(n)}$, and thus the full original operator O , is recovered through the two-step procedure.

Appendix G.

PGCM transition density matrix

A workable expression for the transition one-body density matrix between two PGCM states is obtained and eventually reduced to the particular case of the normal one-body density matrix of a $J^pi = 0^+$ state.

G.1. Inputs

G.1.1. Off-diagonal one-body density matrix

Given a state $|\Phi(q)\rangle$ defined through the Bogoliubov transformation $(U(q), V(q))$ and the common index

$$\theta \equiv (\Omega, \varphi_n, \varphi_p, \varphi_\pi) \quad (\text{G.1})$$

encompassing all rotation angles, the state obtained through multiple rotations

$$|\Phi(q, \theta)\rangle \equiv R_J(\Omega) R_N(\varphi_n) R_Z(\varphi_p) \Pi(\varphi_\pi) |\Phi(q)\rangle, \quad (\text{G.2})$$

is also a Bogoliubov state whose Bogoliubov transformation $(U(q, \theta), V(q, \theta))$ can be obtained from $(U(q), V(q))$ and from the characteristics of the rotation operators [43, 165].

A crucial quantity in terms of which the final results will be expressed is the so-called *off-diagonal* one-body density matrix

$$\rho(q'; q, \theta)_a^b \equiv \frac{\langle \Phi(q') | c_a^\dagger c_b | \Phi(q, \theta) \rangle}{\langle \Phi(q') | \Phi(q, \theta) \rangle}, \quad (\text{G.3})$$

which involves two different Bogoliubov states and, as such, can be computed explicitly from the sole knowledge of $(U(q'), V(q'))$ and $(U(q, \theta), V(q, \theta))$ [43, 165].

G.2. Definition

Considering two PGCM states, the one-body *transition* density matrix can now be defined through^{1 2}

$$\rho_{\mu_f \mu_i a}^{\sigma_f \sigma_i b} \equiv \langle \Psi_{\mu_f}^{\sigma_f} | c_a^\dagger c_b | \Psi_{\mu_i}^{\sigma_i} \rangle$$

¹In the present derivation, the density matrix is restricted to be diagonal in the isospin quantum number, i.e. single-particle states a and b carry the same isospin projection quantum number.

²PGCM states being normalized, there is no need of an explicit denominator (contrary to the situation encountered in App. E.3).

$$\begin{aligned}
 &= \int dq_f dq_i f_{\mu_f}^{\sigma_f*}(q_f) f_{\mu_i}^{\sigma_i}(q_i) \\
 &\quad \times \langle \Phi(q_f) | P^{\sigma_f\dagger} c_a^\dagger c_b P^{\sigma_i} | \Phi(q_i) \rangle \\
 &= \int dq_f dq_i \sum_{K_f K_i} \tilde{f}_{\mu_f q_f}^{\sigma_f K_f*} \tilde{f}_{\mu_i q_i}^{\sigma_i K_i} \delta_{(\Pi_f \pi_a \pi_b) \Pi_i} \\
 &\quad \times \delta_{N_f N_i} \delta_{Z_f Z_i} \rho_{q_f q_i}^{J_f M_f K_f \sigma_i K_i^b}_a,
 \end{aligned} \tag{G.4}$$

where

$$\rho_{q_f q_i}^{J_f M_f K_f \sigma_i K_i^b}_a \equiv \langle \Phi(q_f) | P_{M_f K_f}^{J_f\dagger} c_a^\dagger c_b P_{M_i K_i}^{J_i} P^{N_i} P^{Z_i} P^{\Pi_i} | \Phi(q_i) \rangle, \tag{G.5}$$

and where the action of $P^{N_f} P^{Z_f} P^{\Pi_f}$ was easily resolved.

G.3. Simplified expressions

G.3.1. Expanding the projectors

In order to evaluate this matrix element, the left angular-momentum projector is expanded according to Eq. (A.16a) such that Eq. (G.5) is rewritten as

$$\begin{aligned}
 \rho_{q_f q_i}^{J_f M_f K_f \sigma_i K_i^b}_a &= \frac{2J_f + 1}{16\pi^2} \int d\Omega \sum_{M'} D_{M_f K_f}^{J_f}(\Omega) D_{M_i M'}^{J_i*}(\Omega) \\
 &\quad \times \langle \Phi(q_f) | c_a^\dagger[\Omega] c_b[\Omega] P_{M' K_i}^{J_i} P^{N_i} P^{Z_i} P^{\Pi_i} | \Phi(q_i) \rangle,
 \end{aligned} \tag{G.6}$$

where the rotated creation and annihilation operators are defined as

$$c_a^\dagger[\Omega] \equiv R_{\vec{J}}(\Omega)^\dagger c_a^\dagger R_{\vec{J}}(\Omega), \tag{G.7a}$$

$$c_b[\Omega] \equiv R_{\vec{J}}(\Omega)^\dagger c_b R_{\vec{J}}(\Omega), \tag{G.7b}$$

and where the identity

$$R_{\vec{J}}(\Omega)^\dagger P_{M_i K_i}^{J_i} = \sum_{M'} D_{M_i M'}^{J_i*}(\Omega) P_{M' K_i}^{J_i}, \tag{G.8}$$

has been used.

G.3.2. Spherical one-body basis

In case one-body basis states carry spherical indices ($a \equiv n_a, j_a, m_a, \pi_a, q_a \equiv \alpha_a, j_a, m_a$), the operators $c_{\alpha_a j_a m_a}^\dagger$ and $(-1)^{m_a - j_a} c_{\alpha_a j_a - m_a}$ transform like the m_a^{th} component of a rank- j_a spherical tensor under the action of $SU(2)$, which leads to

$$c_{\alpha_a j_a m_a}^\dagger[\Omega] \equiv \sum_m D_{m_a m}^{j_a*}(\Omega) c_{\alpha_a j_a m}^\dagger, \tag{G.9a}$$

$$c_{\alpha_b j_b m_b}[\Omega] \equiv \sum_m D_{m_b m}^{j_b}(\Omega) c_{\alpha_b j_b m}. \tag{G.9b}$$

Consequently, the transition density matrix can be simplified as

$$\rho_{q_f q_i}^{J_f M_f K_f \sigma_i K_i^b}_a = \frac{2J_f + 1}{16\pi^2} \sum_{mm'} \sum_{M'}$$

$$\begin{aligned}
 & \times \left(\int d\Omega D_{M_f K_f}^{J_f}(\Omega) D_{M_i M'}^{J_i^*}(\Omega) D_{m_b m}^{j_b}(\Omega) D_{m_a m'}^{j_a^*}(\Omega) \right) \\
 & \times \langle \Phi(q_f) | c_{\alpha_a j_a m'}^\dagger c_{\alpha_b j_b m} P_{M' K_i}^{J_i} P^{N_i} P^{Z_i} P^{\Pi_i} | \Phi(q_i) \rangle.
 \end{aligned} \tag{G.10}$$

The integral over Wigner-D matrices is performed analytically and generates a sum over Clebsch-Gordan coefficients and 3j-symbols according to

$$\begin{aligned}
 & \frac{1}{16\pi^2} \int d\Omega D_{M_f K_f}^{J_f}(\Omega) D_{M_i M'}^{J_i^*}(\Omega) D_{m_b m}^{j_b}(\Omega) D_{m_a m'}^{j_a^*}(\Omega) \\
 & = \sum_{\lambda=\max(|J_i-J_f|, |j_a-j_b|)}^{\min(J_i+J_f, j_a+j_b)} (-1)^{M_f-K_f+J_f-J_i+j_b-j_a} \\
 & \times \begin{pmatrix} J_f & J_i & \lambda \\ -M_f & M_i & M_f-M_i \end{pmatrix} \begin{pmatrix} j_b & j_a & \lambda \\ m_b & -m_a & M_f-M_i \end{pmatrix} \\
 & \times (-1)^{m'-m_a} C_{J_f-K_f, J_i(m-m'+K_f)}^{\lambda(m-m')} C_{j_b m, j_a-m'}^{\lambda(m-m')}.
 \end{aligned} \tag{G.11}$$

The remaining matrix element in Eq. (G.10) is easily obtained in terms of the off-diagonal one-body density matrix defined through Eq. (G.3)

$$\begin{aligned}
 & \langle \Phi(q_f) | c_{\alpha_a j_a m'}^\dagger c_{\alpha_b j_b m} P_{M' K_i}^{J_i} P^{N_i} P^{Z_i} P^{\Pi_i} | \Phi(q_i) \rangle \\
 & = \frac{2J_i+1}{16\pi^2} \frac{1}{(2\pi)^2} \frac{1}{2} \int d\theta D_{M' K_i}^{J_i^*}(\Omega) e^{i\varphi_n N_i} e^{i\varphi_p Z_i} \\
 & \times e^{\frac{i}{2}(1-\Pi)\varphi_\pi} \rho(q_f; q_i, \theta)_{\alpha_a j_a m'}^{\alpha_b j_b m} \langle \Phi(q_f) | \Phi(q_i, \theta) \rangle,
 \end{aligned} \tag{G.12}$$

knowing that the overlap $\langle \Phi(q_f) | \Phi(q_i, \theta) \rangle$ between two arbitrary non-orthogonal Bogoliubov states can be computed in several ways [64, 166] as detailed in App. K.2.

G.3.3. Special case of the one-body density matrix of a $J^\pi = 0^+$ state

The expression of the one-body density matrix of a $J^\pi = 0^+$ state can be further simplified. In the above set of equations, it corresponds to setting $J_i = J_f = 0$, $M_i = M_f = 0$ and $\Pi_i = +1$. In this case, the triangular inequalities encoded in the 3j-symbols impose that

$$\lambda = 0, \tag{G.13a}$$

$$m_a = m_b, \tag{G.13b}$$

$$j_a = j_b, \tag{G.13c}$$

$$m = m', \tag{G.13d}$$

such that Eq. (G.11) becomes

$$\frac{1}{16\pi^2} \int d\Omega D_{00}^0(\Omega) D_{00}^{0*}(\Omega) D_{m_b m}^{j_b}(\Omega) D_{m_a m'}^{j_a^*}(\Omega) \delta_{m_a m_b} \delta_{j_a j_b} \delta_{m m'} \frac{1}{2j_a + 1}. \tag{G.14}$$

The fact that the initial and final states are the same and thus carry the same parity further requires that $\pi_a = \pi_b$. Eventually, Eq. (G.10) reduces to

$$\begin{aligned}
 \rho_{q_f q_i}^{0^+ N_i Z_i^b}_a & \equiv \delta_{j_a j_b} \delta_{m_a m_b} \delta_{\pi_a \pi_b} \frac{1}{16\pi^2} \frac{1}{(2\pi)^2} \frac{1}{2} \\
 & \times \frac{1}{2j_a + 1} \int d\theta e^{i\varphi_n N_i} e^{i\varphi_p Z_i} \langle \Phi(q_f) | \Phi(q_i, \theta) \rangle \sum_{m=-j_a}^{j_a} \rho(q_f; q_i, \theta)_{\alpha_a j_a m}^{\alpha_b j_b m}.
 \end{aligned} \tag{G.15}$$

The diagonal character of the one-body density matrix in (j, m) and its independence on m is made clear in Eq. (G.15) and ends the derivation.

G.4. Anomalous transition one-body density matrix

G.4.1. PGCM anomalous density matrix

Although not used in the body of this thesis, expressions for anomalous transition density matrices between nuclei with different number of particles have been derived, and are given here for sake of completeness. The *ab initio* study of pair transitions is envisioned in a near future.

In this section only one nucleon species is considered for convenience. As densities are assumed to be diagonal in isospin, the same derivation can be achieved for protons and neutrons. As such, the proton density will be considered. Since the derivation is similar to the normal projected density matrices, only the main steps of the derivation are explicated. The PGCM proton density matrix between two states $|\Psi_{\mu_i}^{J_i^\pi M_i Z}\rangle$ and $|\Psi_{\mu_f}^{J_f^\pi M_f Z+2}\rangle$ is defined as

$$\begin{aligned} \kappa_{\mu_f \mu_i}^{J_f^\pi M_f J_i^\pi M_i Z} &\equiv \langle \Psi_{\mu_f}^{J_f^\pi M_f Z} | c_b c_a | \Psi_{\mu_i}^{J_i^\pi M_i Z+2} \rangle, \\ &= \int dq_i dq_f \sum_{K_i K_f} f_{K_f \mu_f}^{J_f^\pi i*}(q_f) f_{K_i \mu_i}^{J_i^\pi}(q_i) \kappa_{q_f q_i}^{J_f^\pi M_f K_f J_i^\pi M_i K_i Z}^{ab}, \end{aligned} \quad (\text{G.16a})$$

where

$$\kappa_{q_f q_i}^{J_f^\pi M_f K_f J_i^\pi M_i K_i Z}^{ab} \equiv \langle \Phi(q_f) | P_{M_f K_f}^{J_f^\pi} c_b c_a P_{M_i K_i}^{J_i^\pi} P^{(Z+2)} | \Phi(q_i) \rangle. \quad (\text{G.17})$$

G.4.2. Spherical one-body basis

The final expression reads

$$\begin{aligned} \kappa_{q_f q_i}^{J_f^\pi M_f K_f J_i^\pi M_i K_i Z}^{ab} &\equiv = \frac{(2J_f + 1)(2J_i + 1)}{128\pi^4} \sum_{\lambda=\max(|J_f-J_i|, |J_a-j_k|)}^{\min(J_f+J_i, j_a+j_k)} (-1)^{M_f+J_f-J_i+j_a-j_k} \\ &\times \begin{pmatrix} J_f & J_i & \lambda \\ -M_f & M_i & M_f - M_i \end{pmatrix} \begin{pmatrix} j_a & j_b & \lambda \\ m_a & m_b & M_f - M_i \end{pmatrix} \\ &\times \sum_{mm'} C_{J_f K_f J_i(m+m'-K_f)}^{\lambda(m+m')} C_{j_a m_j b m'}^{\lambda(m+m')} \int d\theta D_{(K_f+m+m')K_i}^{J_i^*}(\Omega) e^{i\varphi_p(Z+2)} \\ &\times e^{\frac{i}{2}(1-\Pi)\varphi_\pi(q_f; q_i, \theta)} \alpha_{1j_a m'} \alpha_{bj_b m} \langle \Phi(q_f) | \Phi(q_i, \theta) \rangle. \end{aligned} \quad (\text{G.18})$$

Appendix H.

Error-function sampling

H.1. Error function

The error function introduced in Eq. (3.23) can be interpreted as the first-order correction to the energy due to the perturbation $\delta H[\rho] \equiv H^{2B}[\rho] - H$. Knowing that for a generic n -body operator $O^{(nn)}$

$$\begin{aligned} \frac{\langle \Psi | O^{(nn)} | \Psi \rangle}{\langle \Psi | \Psi \rangle} &= \frac{1}{n!} \frac{1}{n!} \sum_{\substack{a_1 \dots a_n \\ b_1 \dots b_n}} o_{b_1 \dots b_n}^{a_1 \dots a_n} \frac{\langle \Psi | A_{b_1 \dots b_n}^{a_1 \dots a_n} | \Psi \rangle}{\langle \Psi | \Psi \rangle} \\ &= \left(\frac{1}{n!} \right)^2 o^{(n)} \cdot \rho^{(n)\Psi}, \end{aligned} \quad (\text{H.1})$$

Eq. (3.23) can be written as

$$\begin{aligned} \Delta E_{\Psi}^{2B}[\rho] &= - \left(\frac{1}{3!} \right)^2 w^{(3)} \cdot \rho^{(3)\Psi} \\ &\quad + \left(\frac{1}{2!} \right)^2 \left(w^{(3)} \cdot \rho^{(2)\Psi} \right) \cdot \rho \\ &\quad - \frac{1}{2!} \left(w^{(3)} \cdot \rho^{\Psi} \right) \cdot \rho^{\otimes(2)} \\ &\quad + \frac{1}{3!} w^{(3)} \cdot \rho^{\otimes(3)} \\ &= - \left(\frac{1}{3!} \right)^2 w^{(3)} \cdot \lambda^{(3)\Psi} \\ &\quad + \left(\frac{1}{2!} \right)^2 \left(w^{(3)} \cdot \lambda^{(2)\Psi} \right) \cdot (\rho - \rho^{\Psi}) \\ &\quad + \frac{1}{3!} w^{(3)} \cdot (\rho - \rho^{\Psi})^{\otimes(3)} \end{aligned} \quad (\text{H.2})$$

where $\lambda^{(n)\Psi}$ denotes the *irreducible* n -body density matrix (or cumulants) [167, 168] that, for $n \geq 2$, encodes genuine n -body correlations in $|\Psi\rangle$. Whenever $|\Psi\rangle$ reduces to a Slater determinant, one has $\lambda^{(n)\Psi} = 0$ for $n \geq 2$.

Inspecting Eq. (H.2), one observes that the error

1. only depends on the three-nucleon interaction and involves up to the 3-body (irreducible) density matrix of $|\Psi\rangle$,
2. can be written as a cubic polynomial in the variable $\rho - \rho^{\Psi}$ whenever involving irreducible density matrices of $|\Psi\rangle$,

3. is zero (and thus minimal in absolute value) for $\rho = \rho^\Psi$ whenever $|\Psi\rangle$ contains *at most* genuine 2-body correlations, which is notably the case whenever $|\Psi\rangle$ reduces to a Slater determinant,
4. is in general non-zero for $\rho = \rho^\Psi$ and measures in that case genuine 3-body correlations encoded into $\lambda^{(3)\Psi}$. While the error does not minimize for $\rho = \rho^\Psi$ in general, the fact that $\rho = \rho^\Psi$ is the optimal solution whenever $|\Psi\rangle$ contains at most genuine 2-body correlations indicates that the optimal ρ cannot be very different from ρ^Ψ whenever $|\Psi\rangle$ is a weakly correlated $J^\Pi = 0^+$ state.

H.2. Random one-body density matrices

The goal is to sample the error function $\Delta E_\Psi^{2B}[\rho]$ within the space of one-body density matrices $\{\rho\}$ associated with $J^\Pi = 0^+$ states¹. Thus, a large set of density matrices $\{\rho^{\text{sRd}}\}$ is randomly generated in the sHO basis $\{|a\rangle; a \equiv \alpha_a j_a m_a\}$ under the constraints that

$$\rho_a^b = (\rho_b^a)^*, \quad (\text{H.3a})$$

$$\rho_a^b \equiv \delta_{j_a j_b} \delta_{m_a m_b} \delta_{\pi_a \pi_b} \varrho_{\alpha_a}^{\alpha_b}, \quad (\text{H.3b})$$

$$\text{Tr} \rho = \mathbb{1}^{(1)} \cdot \rho = A, \quad (\text{H.3c})$$

$$0 \leq \text{diag}(\rho)_b^b \leq 1, \forall b, \quad (\text{H.3d})$$

where $\mathbb{1}^{(1)}$ denotes the identity operator on \mathcal{H}_1 and where $\text{diag}(\rho)$ gathers the eigenvalues. More specifically, the procedure works as follows

1. choice of a reference one-body density matrix ρ^{ref} ,
2. diagonalization of ρ^{ref}

$$\rho^{\text{ref}} \equiv L^T \text{diag}(r) L, \quad (\text{H.4})$$

where L denotes an orthogonal matrix.

3. choice of two coefficients α_d, α_o characterizing the amplitude of the random perturbation to be performed next.
4. sampling of a random perturbation δr of the diagonal matrix elements of r verifying

$$\sum_a \delta r_a = 0, \quad (\text{H.5a})$$

$$r_a + \delta r_a \in [0, 1], \forall a, \quad (\text{H.5b})$$

$$|\delta r_a| \leq \alpha_d, \forall a. \quad (\text{H.5c})$$

5. sampling of a random skew-symmetric matrix δl with all upper-diagonal coefficients chosen via a normal distribution $\mathcal{N}(0, 1)$.

¹Strictly speaking, and as the procedure detailed in Sec. 3.2.3 makes clear, the one-body density matrix employed in the construction of $H^{2B}[\rho]$ does not have to be actually related to a many-body state, i.e. it does not have to be *N-representable*. It is at least mandatory to use trial one-body density matrices carrying the fingerprints of the symmetry constraints associated with a true state in order for $H^{2B}[\rho]$ to display appropriate symmetries, which translates into Eqs. (H.3a), (H.3b) and (H.3c) as far as hermiticity, angular momentum, parity and particle number are concerned.

6. exponentiation of δl to obtain an orthogonal matrix

$$\delta L \equiv \exp [\alpha_o \delta l] . \quad (\text{H.6})$$

7. computation of the random neighbour of ρ^{ref}

$$\rho^{sRd} \equiv (L\delta L)^T \text{diag}(r + \delta r) L\delta L . \quad (\text{H.7})$$

Although the sampling is not uniform, all densities with the required properties can in principle be obtained via this method.

H.3. Spherical Hartree-Fock field

Given a test one-body density matrix ρ and considering that the many-body state of interest $|\Psi\rangle$ is a Slater determinant, the one-body Hamiltonian at play in the HF minimization problem based on $H^{2B}[\rho]$ is, given Eq. (H.2),

$$\begin{aligned} [h^{\text{HF}(2B)}[\rho^\Psi; \rho]]_b^a &\equiv \frac{\delta \langle \Psi | H^{2B}[\rho] | \Psi \rangle}{\delta [\rho^\Psi]_a^b} \\ &= \frac{\delta \langle \Psi | H | \Psi \rangle}{\delta [\rho^\Psi]_a^b} + \frac{\delta \Delta E_\Psi^{2B}[\rho]}{\delta [\rho^\Psi]_a^b} \\ &= [h^{\text{HF}}[\rho^\Psi]]_b^a - \frac{1}{2!} \left[w^{(3)} \cdot (\rho^\Psi - \rho)^{\otimes(2)} \right]_b^a . \end{aligned} \quad (\text{H.8})$$

In Eq. (H.8), $h^{\text{HF}}[\rho^\Psi]$ denotes the one-body HF Hamiltonian obtained from the full H whose associated solution is ρ^{sHF} . Equation (H.8) allows one to appreciate the implications of using $H^{2B}[\rho]$ at the sHF level, i.e. in the mean-field calculation of a doubly closed-shell nucleus such as ^{16}O and ^{40}Ca . One observes that

- in general, the use of $H^{2B}[\rho]$ generates an additional term on top of $h^{\text{HF}}[\rho^\Psi]$, eventually leading to $\rho^\Psi \neq \rho^{\text{sHF}}$ and $\Delta E_\Psi^{2B}[\rho^{\text{sHF}}] \neq 0$ at convergence,
- even when using $H^{2B}[\rho^{\text{sHF}}]$, the additional term differs from zero such that $\rho^\Psi \neq \rho^{\text{sHF}}$ and $\Delta E_\Psi^{2B}[\rho^{\text{sHF}}] \neq 0$ at convergence,
- only if one were to set $\rho = \rho^\Psi$ in $H^{2B}[\rho]$ throughout the iterative procedure, thus modifying the approximate Hamiltonian along the way, would the correction term vanish in Eq. (H.8) at convergence and the sHF solution based on $H^{2B}[\rho]$ be the same as the one obtained from H . This particular case is equivalent to constructing $H^{2B}[\rho]$ through Wick's theorem with respect to the self-consistent sHF Slater determinant itself and is thus identical to the NO2B procedure, which indeed does not lead to any approximation at the HF level.

Appendix I.

Charge density distribution

Generically speaking, the electromagnetic charge density operator is expressed as an expansion in many-body operators acting on nucleonic degrees of freedom. These operators not only account for the point distribution of protons but also for their own charge distribution, along with the one of neutrons, and for charge distributions associated with the light charged mesons they exchange. In practice, the charge density distribution¹ is usually computed as [169, 170, 171]

$$\rho_{ch}(r) = \rho_{ch}^p(r) + \rho_{ch}^n(r), \quad (\text{I.1})$$

where ρ_{ch}^p (ρ_{ch}^n) is determined by folding the point-proton (point-neutron) density with the finite charge distribution of the proton (neutron). Following Ref. [170], the latter are included by parameterizing proton and neutron charge form factors as a linear superposition of Gaussians

$$G_{p/n}(r) = \sum_i \frac{\theta_i^{p/n}}{[\pi(r_i^{p/n})^2]^{3/2}} e^{-(r/r_i^{p/n})^2}, \quad (\text{I.2})$$

whose widths $r_i^{p/n}$ and relative weights $\theta_i^{p/n}$ are adjusted to reproduce electron scattering data. Three and two Gaussians are sufficient to reproduce the proton and neutron form factors, respectively, with parameters² given in Tab. I.1. Convoluting Eq. (I.2) with point-proton and point-neutron distributions ρ_p and ρ_n yields the two contributions to the nuclear charge density [171]

$$\rho_{ch}^p(r) = \sum_{i=1}^3 \frac{\theta_i^p}{r_i^p \sqrt{\pi}} \int_0^\infty dr' \frac{r'}{r} \rho_p(r') \left[e^{-\left(\frac{r-r'}{r_i^p}\right)^2} - e^{-\left(\frac{r+r'}{r_i^p}\right)^2} \right], \quad (\text{I.3a})$$

$$\rho_{ch}^n(r) = \sum_{i=1}^2 \frac{\theta_i^n}{r_i^n \sqrt{\pi}} \int_0^\infty dr' \frac{r'}{r} \rho_n(r') \left[e^{-\left(\frac{r-r'}{r_i^n}\right)^2} - e^{-\left(\frac{r+r'}{r_i^n}\right)^2} \right]. \quad (\text{I.3b})$$

Finally, one needs to correct for spurious center-of-mass contamination and include the Darwin-Foldy relativistic correction. Assuming that the center-of-mass wave function

¹An additional relativistic correction that depends on spin-orbit terms, ρ_{ch}^{ls} , is sometimes considered. Given that proton and neutron spin-orbit contributions largely cancel out in $N = Z$ nuclei, this term is omitted in the present calculation of ^{20}Ne .

²The proton r.m.s. radius resulting from this parameterization is $\langle R_p^2 \rangle^{1/2} = 0.88$ fm. This is consistent with the values reported in the older CODATA evaluations (e.g. the 2010 evaluation [172], $\langle R_p^2 \rangle^{1/2} = 0.8775(51)$ fm), but overestimates the value found in more recent evaluations ($\langle R_p^2 \rangle^{1/2} = 0.8414(19)$ fm, adopted from the 2014 evaluation [173] on). A smaller value of the proton r.m.s. charge radius would lead to less smoothing of the point-proton distribution. Given the small difference between the possible values of $\langle R_p^2 \rangle^{1/2}$, however, this would be hardly noticeable in the final charge density curves.

	proton	neutron
$\theta_1^{\text{p/n}}$	0.506	1
$\theta_2^{\text{p/n}}$	0.328	-1
$\theta_3^{\text{p/n}}$	0.166	-
$(r_1^{\text{p/n}})^2 [\text{fm}^2]$	0.432	0.469
$(r_2^{\text{p/n}})^2 [\text{fm}^2]$	0.139	0.546
$(r_3^{\text{p/n}})^2 [\text{fm}^2]$	1.526	-
$\langle R_{\text{p/n}}^2 \rangle [\text{fm}^2]$	0.775	-0.116

Table I.1. Proton and neutron parameters entering the Gaussian expansion (I.2). Taken from Ref. [170]. The resulting mean-square charge radii are also reported.

factorizes in the ground-state of a harmonic oscillator Hamiltonian characterized by the frequency $\tilde{\omega}$, the inclusion of these two corrections can be performed at the price of proceeding to the replacement [170, 174]

$$r_i^2 \longrightarrow r_i^2 - \frac{b^2}{A} + \frac{1}{2} \left(\frac{\hbar}{m} \right)^2 \quad (\text{I.4})$$

in Eqs. (I.3), where m is the nucleon mass, hence $\hbar/m = 0.21 \text{ fm}$, and $b^2 = (m \hbar \tilde{\omega})^{-1}$. Employing Bethe's formula [174], the latter term can be approximated with $b^2 \approx A^{1/3} \text{ fm}^2$. Let us note that, for ^{16}O , such an approximation is consistent with the value of $\hbar \tilde{\omega}$ found in Ref. [175] and is thus safe to use in present calculations of ^{20}Ne .

Appendix J.

Linear redundancies in HWG

The linear redundancies due to the non-orthogonality of the HFB states mixed into the PGCM state must be dealt with when solving the HWG equation. Because of the manageable number of such HFB states, it can be done by diagonalizing the norm matrix $\mathbf{N}^{\tilde{\sigma}}$ and by removing the eigenvectors associated with eigenvalues smaller than a given threshold ϵ_{th} . The threshold must be chosen such that the end results do not depend on its particular value.

In the second step, the Hamiltonian H can be safely diagonalized in the orthonormal basis generated in the first step. Since $\mathbf{N}^{\tilde{\sigma}}$ is a Hermitian positive-definite matrix, the basis transformation can be written as

$$\mathbf{N}^{\tilde{\sigma}} = \mathbf{S}^{\tilde{\sigma}\dagger} \check{\mathbf{N}}^{\tilde{\sigma}} \mathbf{S}^{\tilde{\sigma}}, \quad (\text{J.1})$$

where $\mathbf{S}^{\tilde{\sigma}}$ is a unitary matrix and where $\check{\mathbf{N}}^{\tilde{\sigma}}$ is diagonal with strictly positive eigenvalues. Defining

$$\mathbf{G}^{\tilde{\sigma}} \equiv \mathbf{S}^{\tilde{\sigma}\dagger} (\check{\mathbf{N}}^{\tilde{\sigma}})^{-1/2} \mathbf{S}^{\tilde{\sigma}}, \quad (\text{J.2})$$

and only keeping the rows of $\mathbf{S}^{\tilde{\sigma}}$ corresponding to eigenvalues of $\check{\mathbf{N}}^{\tilde{\sigma}}$ larger than ϵ_{th} , HWG's equation is transformed into the associated orthonormal basis and becomes

$$\sum_q \check{H}_{p0q0}^{\tilde{\sigma}} \check{f}_{\mu}^{\tilde{\sigma}}(q) = \mathcal{E}_{\mu}^{\tilde{\sigma}} \check{f}_{\mu}^{\tilde{\sigma}}(p), \quad (\text{J.3})$$

with

$$\check{\mathbf{H}}^{\tilde{\sigma}} \equiv \mathbf{G}^{\tilde{\sigma}\dagger} \mathbf{H}^{\tilde{\sigma}} \mathbf{G}^{\tilde{\sigma}}, \quad (\text{J.4a})$$

$$\mathbf{f}^{\tilde{\sigma}} \equiv \mathbf{G}^{\tilde{\sigma}} \check{\mathbf{f}}^{\tilde{\sigma}}. \quad (\text{J.4b})$$

The solutions $\{\check{f}_{\mu}^{\tilde{\sigma}}(p); q \in \text{set}\}$ play the role of orthonormal collective wave functions as a function of q that can be interpreted as probability amplitudes. Left-multiplying Eq. J.3 by $\check{f}_{\mu}^{\tilde{\sigma}*}(p)$, one can thus decompose the PGCM energy in terms of contributions associated with each deformation q

$$\mathcal{E}_{\mu}^{\tilde{\sigma}} = \sum_q h_{\mu}^{\tilde{\sigma}*}(q) \check{f}_{\mu}^{\tilde{\sigma}}(q) \equiv \sum_q e_0^{(0+1)}(q), \quad (\text{J.5})$$

with

$$h_{\mu}^{\tilde{\sigma}}(q) \equiv \sum_p \check{H}_{q0p0}^{\tilde{\sigma}} \check{f}_{\mu}^{\tilde{\sigma}}(p). \quad (\text{J.6})$$

Note that the same decomposition of the PGCM energy can be achieved prior to diagonalizing the norm kernel.

Appendix K.

Memory optimization

The storage of the interaction matrix elements necessary to perform *ab initio* calculations in large computational bases is challenging. Several methods exist to reduce this memory burden. For example, one most commonly takes advantage of the rotational symmetry to store matrix elements in J -coupled form. However, this storage is not well adapted to PGCM calculations based on symmetry breaking HFB states where the contraction of the interaction with rotated density matrices need to be performed in m -scheme. In the present Appendix, the workflow to calculate a Hamiltonian kernel while optimizing memory and runtime is detailed.

K.1. J -coupling scheme

In the present calculations, the one-body Hilbert space is spanned by spherical harmonic oscillator eigenstates that are labelled by 5 quantum numbers

$$k \equiv (n_k, l_k, j_k, m_k, t_k), \quad (\text{K.1})$$

where n_k denotes the radial quantum number, l_k the orbital angular momentum, j_k the total angular momentum, m_k its projection and t_k the isospin projection.

Introducing the reduced index

$$\tilde{k} \equiv (n_k, l_k, j_k, t_k), \quad (\text{K.2})$$

and building the m -scheme, i.e. tensor-product, basis of the two-body Hilbert space according to

$$|k_1 k_2\rangle \equiv |k_1\rangle \otimes |k_2\rangle, \quad (\text{K.3})$$

the J -coupled two-body basis is obtained through

$$|\tilde{k}_1 \tilde{k}_2 JM\rangle \equiv \frac{1}{1 + \delta_{\tilde{k}_1 \tilde{k}_2}} \sum_{m_1 m_2} C_{j_{k_1} m_{k_1} j_{k_2} m_{k_2}}^{JM} |k_1 k_2\rangle, \quad (\text{K.4})$$

where Clebsch-Gordan coefficients have been introduced. Conversely, uncoupled basis states can be expanded on J -coupled ones via

$$|k_1 k_2\rangle \equiv (1 + \delta_{\tilde{k}_1 \tilde{k}_2}) \sum_{JM} C_{j_{k_1} m_{k_1} j_{k_2} m_{k_2}}^{JM} |\tilde{k}_1 \tilde{k}_2 JM\rangle. \quad (\text{K.5})$$

The two-body interaction being invariant under rotation, Wigner-Eckart theorem implies that its matrix elements are diagonal in (J, M) when expressed in the J -coupled basis. Furthermore, matrix elements can be factorized in terms of a geometrical factor and a reduced tensor independent of M . Therefore, only the reduced tensor is stored in memory.

K.1.1. Contractions with one-body density matrices

When the PGCM solely involves spherically invariant HFB states, all necessary contractions of the two-body interaction with off-diagonal one-body density matrices associated with pairs of HFB vacua can be conveniently worked out in the J -coupled two-body basis in a way that only involves the reduced tensor. When employing deformed HFB states and projecting onto good angular momentum, interaction matrix elements must however be expressed in the uncoupled basis prior to performing the contractions. Two strategies are then possible

- Uncouple J -coupled matrix elements prior to the calculation and work with the corresponding set of uncoupled matrix elements. This however induces a large memory requirement.
- Decouple interaction matrix elements on the fly, thus reducing the storage workload while substantially increasing the runtime.

In order to tackle this problem efficiently, a workflow that decouples each matrix element only once has been devised, thus reducing drastically both memory and runtime requirements in a way that is easily parallelized. The workflow is as follows

1. Pre-compute all off-diagonal one-body density matrices.
2. Split the initial one-body basis into subsets of states carrying the same quantum numbers (m, π) .
3. Select $[(m_1, \pi_1), (m_2, \pi_2), (m_3, \pi_3), (m_4, \pi_4)]$.
 - a) Decouple the sub-part of the interaction characterized by this combination of quantum numbers and store it contiguously in memory.
 - b) Perform the contraction of the interaction sub-part with the corresponding sub-blocks of the off-diagonal one-body density matrices. This part can be completely vectorized since the decoupled interaction is stored contiguously in memory.
4. Go back to 3. until all combinations of quantum numbers have been exhausted.

The loop in step 3 can be easily parallelized. Except for the overhead associated with the storage of all off-diagonal one-body density matrices, the memory consumption scales linearly with the number of cores.

K.2. Evaluation of the norm overlap

As discussed in Chap. 1, the overlap between a left Bogoliubov vacuum and a rotated right Bogoliubov vacuum can be evaluated according to [63]

$$\langle \Phi(p) | \Phi(q; \theta) \rangle = (-1)^n \frac{\det(C^*(p)) \det(C(q))}{\prod_k^n v_k(p) v_k(q)} \text{pf} \left[\begin{pmatrix} V(p)^T U(p) & V^T(p) \mathbf{r}^T(\theta) V^*(q) \\ -V(q)^\dagger \mathbf{r}(\theta) V(p) & U^\dagger(q) V^*(q) \end{pmatrix} \right], \quad (\text{K.6})$$

where the pfaffian of a symplectic matrix and Bloch-Messiah-Zumino's decompositions [43] of the Bogoliubov transformations of the left and (unrotated) right states have been

invoked. In Eq. (K.6), $2n$ denotes the dimension of \mathcal{H}_1 . This expression is however not numerically stable as it amounts to taking the ratio of two vanishing quantities. A way to circumvent this difficulty has been proposed in Ref. [176], but a simpler alternative consists of rescaling the matrix before evaluating the pfaffian. For any $2n \times 2n$ skew-symmetric matrix A and real scalar λ , one has

$$\text{pf}(\lambda A) = \lambda^n \text{pf}(A). \quad (\text{K.7})$$

Therefore, Eq. (K.6) can be rewritten as

$$\langle \Phi(p) | \Phi(q; \theta) \rangle = (-1)^n \det(C^*(p)) \det(C(q)) \text{pf} \left[\frac{1}{\sqrt[n]{\prod_k v_k(p) v_k(q)}} \begin{pmatrix} V(p)^T U(p) & V^T(p) \mathbf{r}^T(\theta) V^*(q) \\ -V(q)^\dagger \mathbf{r}(\theta) V(p) & U^\dagger(q) V^*(q) \end{pmatrix} \right] \quad (\text{K.8})$$

which is well-behaved numerically. The numerical library Pfpack [177] is used to compute the pfaffian.

Appendix L.

Anti-symmetry reduction

From a technical viewpoint, and as extensively explained in Chapter 2, PGCM-PT(2) calculations rely on solving a large-scale linear problem of the form

$$\mathbf{M}\mathbf{a} = -\mathbf{h}_1. \quad (\text{L.1})$$

The linear problem relates to excitations I of several non-orthogonal Hartree-Fock-Bogoliubov vacua, each of which is defined by a set of quasi-particle creations, i.e. a rank- n excitation is defined through a set of n quasi-particle labels $I \sim (k_{i_1}, \dots, k_{i_n})$. Correspondingly, the problem is initially expressed in terms of unrestricted sets of quasi-particle indices. Still, anti-commutation relations of quasi-particle creation operators imply that \mathbf{M} , \mathbf{a} and \mathbf{h}_1 are anti-symmetric with respect to the permutations of quasi-particle indices, which can be exploited to reduce the effective dimensionality of the linear system.

Given a rank- n excitation $I \sim (k_{i_1}, \dots, k_{i_n})$ on a given Bogoliubov state, the set $\mathcal{I} \equiv \{\tau(I)\}_{\tau \in \mathcal{S}_n}$ of $|\mathcal{I}| \equiv n!$ permutations of the quasi-particle indices of I is considered. For a pair (I, J) of excitations and two permutations (τ, τ') applicable on I and J , the antisymmetry properties at play read as

$$M_{pIqJ} = \epsilon(\tau)\epsilon(\tau')M_{p\tau(I)q\tau'(J)}, \quad (\text{L.2a})$$

$$a^J(q) = \epsilon(\tau)a^{\tau(J)}(q), \quad (\text{L.2b})$$

$$h_1^I(p) = \epsilon(\tau')h_1^{\tau'(I)}(p), \quad (\text{L.2c})$$

where $\epsilon(\tau)$ denotes the signature of the permutation τ . First, these antisymmetry properties trivially imply that excitations with repeated quasi-particle indices can be excluded from the basis. Second, the set of excitations \mathcal{I} corresponding to one another via a change of the quasi-particle ordering can all be tracked through the one representative \bar{I} of \mathcal{I} characterized by a strictly increasing ordering of the quasi-particle indices $k_1 < \dots < k_n$. Writing Eq. (L.1) for such an external ordered excitation \bar{I}

$$\sum_q \sum_{\mathcal{J}} \sum_{J \in \mathcal{J}} M_{p\bar{I}qJ} a^J(q) = -h_1^{\bar{I}}(p), \quad (\text{L.3})$$

the internal sum is split such that, with the help of Eq. (L.2), $|\mathcal{J}|$ equivalent terms are generated to eventually deliver the reduced form

$$\sum_q \sum_{\mathcal{J}} |\mathcal{J}| M_{p\bar{I}q\bar{J}} a^{\bar{J}}(q) = -h_1^{\bar{I}}(p). \quad (\text{L.4})$$

In order to maintain the hermiticity of the reduced matrix one further left-multiplies the equation by $\sqrt{|\mathcal{I}|}$ such that the final form

$$\sum_q \sum_{\mathcal{J}} \sqrt{|\mathcal{J}|} \sqrt{|\mathcal{I}|} M_{p\bar{I}q\bar{J}} \sqrt{|\mathcal{J}|} a^{\bar{J}}(q) = -\sqrt{|\mathcal{I}|} h_1^{\bar{I}}(p), \quad (\text{L.5})$$

naturally leads to a trivial redefinition of the reduced matrix and vectors through the inclusion of the combinatorial factors. In the following, the above reduction process is assumed such that the effective working basis only includes excitations characterized by quasi-particle indices in a strictly increasing order.

Appendix M.

Solving the linear problem

Finding the numerical solution of Eq. (L.1) (or equivalently its reduced version given Eq. (L.5)) is delicate due to the non-orthogonality of the many-body states used to represent it. Thus, a careful handling of zeros in the norm eigenvalues is typically necessary to avoid instabilities in the resolution of the equation. Different methods are progressively introduced below to eventually motivate the use of the iterative MINRES-QLP algorithm.

M.1. Exact SVD-based solution

The pedestrian way to solve the linear system can be summarized in three steps: diagonalize the norm matrix to transform the equation into an orthonormal basis, diagonalize the Hamiltonian matrix in that basis and finally invert the problem. This strategy is essentially similar to the one at play in PGCM to solve HWG equation (see App. J).

The norm matrix (see Chap. 2) is first decomposed by projecting on the range of \mathbf{N}

$$\mathbf{N} = \mathbf{X}\mathbf{I}\mathbf{X}^\dagger, \quad (\text{M.1})$$

where \mathbf{X} is unitary. \mathbf{M} , \mathbf{a} and \mathbf{h}_1 are transformed into the resulting orthogonal basis

$$\tilde{\mathbf{M}} \equiv \mathbf{X}\mathbf{M}\mathbf{X}^\dagger, \quad (\text{M.2a})$$

$$\tilde{\mathbf{a}} \equiv \mathbf{X}^\dagger \mathbf{a}, \quad (\text{M.2b})$$

$$\tilde{\mathbf{h}}_1 \equiv \mathbf{X}^\dagger \mathbf{h}_1, \quad (\text{M.2c})$$

such that the linear problem equivalently reads

$$\tilde{\mathbf{M}}\tilde{\mathbf{a}} = -\tilde{\mathbf{h}}_1. \quad (\text{M.3})$$

The solution of this system is then found by diagonalizing $\tilde{\mathbf{M}}$

$$\Delta = \mathbf{Y}^\dagger \tilde{\mathbf{M}} \mathbf{Y}, \quad (\text{M.4})$$

such that, similarly to canonical MBPT, the system is inverted in the basis where $\tilde{\mathbf{M}}$ is diagonal to obtain the second-order energy under the form

$$E^{(2)} = -\mathbf{h}_1^\dagger \mathbf{X} \mathbf{Y} \Delta^{-1} \mathbf{Y}^\dagger \mathbf{X}^\dagger \mathbf{h}_1. \quad (\text{M.5})$$

In principle, the projection on the range of \mathbf{N} is not necessary to solve the system. However, in numerical applications, the coupling between spurious eigenvalues of \mathbf{N} and large eigenvalues of \mathbf{M} can arise such that the explicit removal of the redundancies is often necessary. However, the full diagonalization is not applicable to the large matrices

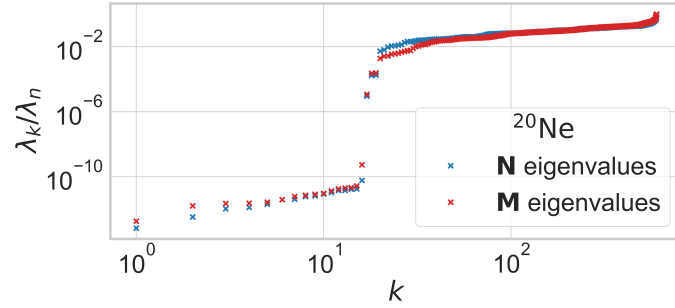


Figure M.1. (Color online) Distribution of eigenvalues of \mathbf{N} and \mathbf{M} matrices for ^{20}Ne . The calculation is performed with a two-body χEFT Hamiltonian, $\lambda_{\text{srg}} = 1.88\text{fm}^{-1}$, $\hbar\omega = 20\text{MeV}$ and $e_{\text{max}} = 2$.

encountered in realistic PGCM-PT(2) calculations (contrary to the PGCM step where the typical dimensions at play allow for such a strategy) such that other methods need to be designed to solve the problem.

As an example, the distribution of eigenvalues of matrices \mathbf{N} and \mathbf{M} obtained through a PHFB-PT(2) calculation of ^{20}Ne in a small model-space is displayed in Fig. M.1. Two observations can be made

- The distributions of eigenvalues of the two matrices are very close up to a scaling factor. In particular, and as expected, their (numerical) kernel has the same dimension.
- The kernels dimension is small compared to the matrices dimension, and all eigenvalues have the same magnitude. This prevents from using truncated SVD approaches in larger model spaces.

Although the GCM mixing enlarges the kernel of the PGCM-PT(2) matrices compared to PHFB-PT(2) due to the partial linear dependencies of the added HFB states, there is still a large number of independent configurations.

M.2. QLP decomposition

Before introducing iterative methods, one may introduce an intermediate method effectively removing spurious eigenvalues without paying the price of fully diagonalizing the norm and Hamiltonian matrices. Indeed pivoted QR [178] and QLP [179] factorizations may be used to reach the range of symmetric matrices without resorting to a full diagonalization.

M.2.1. Pivoted QR

Let us consider an arbitrary $n \times m$ complex matrix A . A can be decomposed according to

$$AD = QR, \quad (\text{M.6})$$

where D is a permutation of the columns of A , Q is a unitary matrix, and R is an upper triangular matrix. The permutation D is used to sort the diagonal entries of R in decreasing order of magnitude. This way, the kernel of A corresponds to the last columns of R with diagonal entries 0.

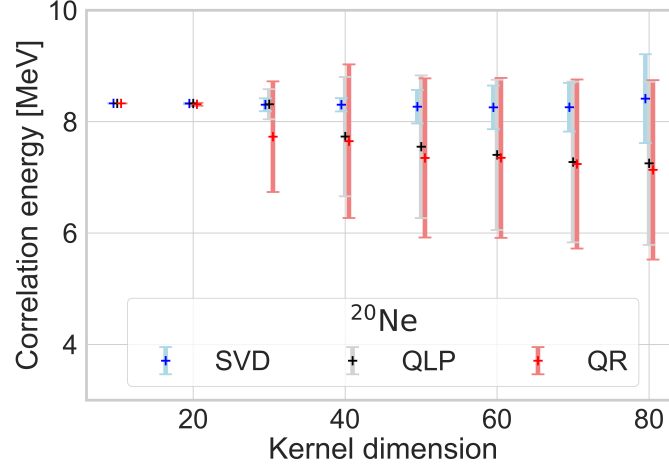


Figure M.2. (Color online) PHFB-PT correlation energy of ^{20}Ne obtained for SVD, QR and QLP decompositions as function of the size of the excluded kernel in the decomposition. The calculation is performed with a two-body χEFT Hamiltonian, $\lambda_{\text{srg}} = 1.88\text{fm}^{-1}$, $\hbar\omega = 20\text{MeV}$ and $e_{\text{max}} = 2$.

M.3. Pivoted QLP

Performing two successive pivoted QR decompositions allows to further decompose A into the form

$$D'AD = QLP \quad (\text{M.7})$$

where D, D' are permutation matrices, Q, P are unitary matrices and L is a lower triangular matrix. In particular, L takes the block-diagonal form

$$L = \begin{pmatrix} \tilde{L} & 0 \\ 0 & 0 \end{pmatrix}, \quad (\text{M.8})$$

such that Q and P naturally block factorize A into a full-rank part and its null-space.

M.3.1. Application

In the case of present interest, pivoted QR/QLP factorizations can either be used directly on \mathbf{M} to solve Eq. (L.1) or on the norm matrix in order to remove redundancies in the basis. In both cases, the symmetry of the matrices guarantees that the range and the kernel of both matrices are in direct sum. QLP factorization can therefore be seen as a way to reexpress the original problem in the range of \mathbf{M} or \mathbf{N} . In practical applications, a tolerance is used (as with SVD) to numerically discard small eigenvalues and disentangle the numerical kernel from the numerical range. The QLP factorization, although twice more expansive than the single QR decomposition, is found to be more stable and to better discard spurious eigenvalues.

Figure M.2 shows a comparison of SVD, QR and QLP decompositions in a PHFB-PT(2) calculation. The three of them are in very good agreement when nearly all the space is kept in the calculation. However, truncating along the magnitude of the diagonal elements of the decomposition deteriorate the results. While the SVD is by far the most reliable method, the QLP decomposition significantly improves the correlation energy with respect

to the simpler QR decomposition and reduces the corresponding error. The reduced cost of QLP/QR decompositions compared to SVD, especially in their sparse version, make them very profitable.

M.4. From QLP to MINRES-QLP algorithm

The QLP decomposition introduced above is still not applicable to very large matrices due to the runtime and memory requirements. An alternative solution is to use an iterative method, preferentially one that exploits the symmetry of the input matrix. Among various available solvers, the MINRES algorithm [180] finds the minimum length solution to $\|\mathbf{M}\mathbf{a} + \mathbf{h}_1\|$ via QR factorizations in the Krylov space of \mathbf{M} . In case of ill-conditioned problems, QR factorizations are replaced by QLP factorizations, the corresponding algorithm being coined as MINRES-QLP [181].

The benefit of iterative solvers compared to exact decompositions is that the QR (resp. QLP) factorization is performed in the Krylov subspace of the matrix instead of the whole matrix itself. At iteration k , the problem is of dimension $k \times k$, k being usually kept much smaller than the original matrix dimensions. This results both in a runtime and memory saving, at the cost of solving the system only approximately.

M.5. Preconditioning of the linear system

The number of iterations required by the solvers strongly depends on the distribution of eigenvalues of the linear system under consideration. Typically, systems where the eigenvalues are clustered will have a faster convergence than systems with a spread spectrum. The spread of the eigenvalues can be altered with preconditioning techniques that amounts to finding equivalent systems with different (generally much smaller) condition numbers.

In this section, the compatible symmetric system

$$\mathbf{M}\mathbf{x} = -\mathbf{h}_1, \quad (\text{M.9})$$

is considered. Let $\mathbf{A} = \mathbf{C}\mathbf{C}^T$ be a positive definite matrix. The solution of the initial system can be deduced from the solution of the preconditioned system

$$\mathbf{C}^{-1}\mathbf{M}\mathbf{C}^{-T}\mathbf{y} = -\mathbf{C}^{-1}\mathbf{h}_1. \quad (\text{M.10})$$

Whereas various techniques are available to build an appropriate matrix \mathbf{A} , designing efficient preconditioners is still an active field of research [182]. There is no perfect preconditioner, and finding the trade-off between effectiveness and computational cost heavily relies on heuristic. Furthermore, for systems only known up to a given precision, preconditioners can artificially magnify eigenvalues that are numerically close to zero. Thus, a slower convergence with the possibility to stop the iterations before the appearance of spurious divergences might be preferable. Eventually, solving simultaneously several equivalent systems can help better identify systems where the solution is harder to find and discrepancies between different solutions can be used as uncertainty estimates in the resolution.

M.5.1. Matrix scaling

Matrix scaling is a subcase of preconditioning where the preconditioner is a diagonal matrix $\mathbf{A} \equiv \mathbf{D}$ such that the equivalent system reads

$$\mathbf{D}^{-\frac{1}{2}} \mathbf{M} \mathbf{D}^{-\frac{1}{2}} \mathbf{y} = -\mathbf{D}^{-\frac{1}{2}} \mathbf{h}_1. \quad (\text{M.11})$$

If the scaled matrix

$$\tilde{\mathbf{M}} \equiv \mathbf{D} \mathbf{M} \mathbf{D} \quad (\text{M.12})$$

is better conditioned than \mathbf{M} , then the solution to the initial system can be found in less iterations. For a diagonally dominant matrix \mathbf{M} , scaling the matrix with its own diagonal elements will reduce its condition number. The binormalization method detailed in Ref. [183] amounts to scaling all rows and columns to unit norm and can deliver significantly better results at low cost. A stochastic matrix-free variant [184] allows one to efficiently apply this method for abstract linear operators that are not necessarily defined explicitly by a matrix-vector product. Below, the stochastic binormalization preconditioner is denoted as SBIN.

M.5.2. Incomplete Cholesky decomposition

For a sparse positive definite matrix \mathbf{N} , an approximate Cholesky factorization preserving the sparsity pattern of the original matrix can be computed as

$$\mathbf{N} \sim \mathbf{L} \mathbf{L}^T, \quad (\text{M.13})$$

with \mathbf{L} a (sparse) lower triangular matrix. A variant of Cholesky factorization applicable to positive indefinite matrices can be applied directly on the norm matrix \mathbf{N} . Since \mathbf{N} and \mathbf{M} have similar eigenvalue spread, eigenvalues of the system preconditioned with $\mathbf{L} \mathbf{L}^T$ will be much more clustered than those of the original system. Below, the incomplete Cholesky preconditioner is denoted as IC0.

M.5.3. Norm preconditioning

In some cases, spurious eigenvalues in the linear system can couple to physical modes and prevent any convergence of the iterative solvers. In this case, clustering the eigenvalues via preconditioning techniques is counterproductive as spurious modes are given an equivalent amplitude to physical ones. When this happens, it is preferable to amplify the separation of scale between numerically small and large eigenvalues. Instead of manually removing redundancies in the norm matrix, there exists a simple way to reach the image of \mathbf{N} without resorting to a decomposition. Instead of solving

$$\mathbf{M} \mathbf{a} = -\mathbf{h}_1, \quad (\text{M.14})$$

one directly solves for $\mathbf{N}^{-1} \mathbf{a}$ inside the range of \mathbf{N} via

$$\mathbf{N} \mathbf{M} \mathbf{N} (\mathbf{N}^{-1} \mathbf{a}) = -\mathbf{N} \mathbf{h}_1, \quad (\text{M.15})$$

Even if \mathbf{N} is singular, the fact that \mathbf{h}_1 and \mathbf{a} live in the range of \mathbf{N} by construction ensures that $\mathbf{N}^{-1} \mathbf{a}$ is well-defined. The procedure ensures that small numerical eigenvalues of \mathbf{N} , originating from colinear many-body basis vectors, are tamed down in $\mathbf{N} \mathbf{M} \mathbf{N}$. Furthermore,

numerical errors in \mathbf{h}_1 are additionally suppressed. Of course, in exact arithmetic, the two systems are equivalent. This method corresponds in fact to preconditioning the system with \mathbf{N}^{-2} . As mentioned, this slows down the convergence of the iterative procedure and must be kept for cases where the direct resolution or the complex shift method (see below) do not provide accurate solutions. Below, the norm precondition is denoted as **NMN**.

M.6. Error evaluation

Iterative methods may require a large number of iterations or even diverge due to numerical errors. In this section, a conservative error bound to estimate the error on the computed second-order energy is advocated.

Given an approximate resolution of the system

$$\mathbf{M}\mathbf{a} = -\mathbf{h}_1 + \mathbf{b}, \quad (\text{M.16})$$

the second-order energy evaluated with Hylleraas' functional reads

$$\begin{aligned} E^{(2)} &= \mathbf{a}^\dagger \mathbf{M}\mathbf{a} + \mathbf{h}_1^\dagger \mathbf{a} + \mathbf{a}^\dagger \mathbf{h}_1 \\ &= \mathbf{a}^\dagger \mathbf{b} + \mathbf{h}_1^\dagger \mathbf{a}. \end{aligned} \quad (\text{M.17})$$

The difference in the second-order energy evaluated directly or via Hylleraas' functional reads

$$\delta E^{(2)} = \mathbf{a}^\dagger (\mathbf{M}\mathbf{a} + \mathbf{h}_1). \quad (\text{M.18})$$

A conservative error estimate on the second-order energy can thus be expressed as

$$|\delta E|^{(2)} \equiv \|\mathbf{a}\| \|\mathbf{M}\mathbf{a} + \mathbf{h}_1\|. \quad (\text{M.19})$$

The quantity $|\delta E|^{(2)}$ vanishes for an exact resolution and grows whenever $\|\mathbf{a}\|$ becomes too large, which generally occurs if \mathbf{M} is badly conditioned. When the norm-preconditioning is used, the error estimate is obtained as

$$|\delta E|^{(2)} \equiv \|\mathbf{N}^{-1}\mathbf{a}\| \|\mathbf{NMN}(\mathbf{N}^{-1}\mathbf{a}) + \mathbf{N}\mathbf{h}_1\|. \quad (\text{M.20})$$

M.7. Stopping condition of iterative solver

MINRES-QLP already implements by default its own stopping criterion based on the relative norm of the residuals

$$\frac{\|\mathbf{M}\mathbf{a} + \mathbf{h}_1\|}{\|\mathbf{a}\|}. \quad (\text{M.21})$$

In the present case, elements of \mathbf{M} and \mathbf{h}_1 are obtained after several computational steps such that round-off and discretization errors will alter the quality of the input matrices. Furthermore, a threshold on the magnitude of the matrix elements of \mathbf{M} is employed to enforce the sparsity of the matrix. As such, iterations should be stopped when the residual errors are of the same order as the precision of the input matrix elements.

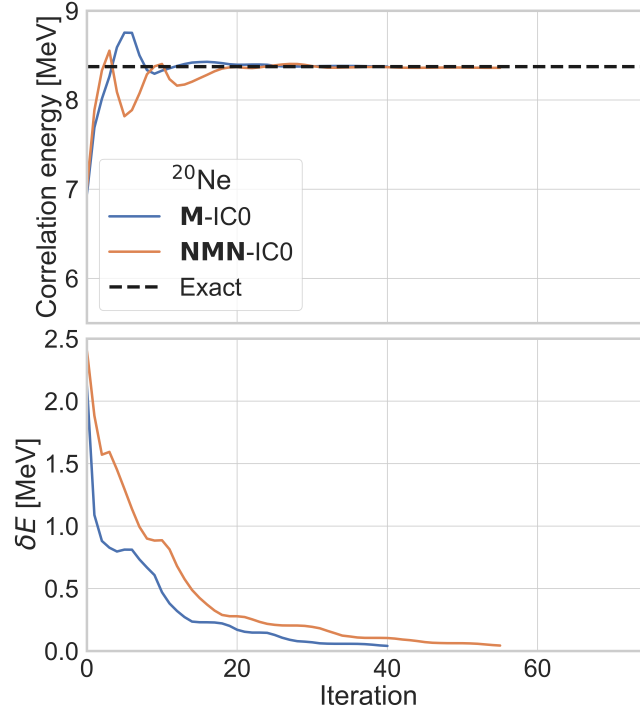


Figure M.3. (Color online) Correlation energy (top) and respective error (bottom) at each MINRES-QLP iteration for the ground state of ^{20}Ne for various systems and preconditioning techniques. Exact solution is obtained via SVD. The calculation is performed with a two-body χEFT Hamiltonian, $\lambda_{\text{srg}} = 1.88\text{fm}^{-1}$, $\hbar\omega = 20\text{MeV}$ and $e_{\text{max}} = 2$.

M.8. Illustration of iterative solvers

In order to illustrate the use of iterative solvers and preconditioning techniques, results obtained in ^{20}Ne with $e_{\text{max}} = 2$ are shown in Fig. M.3. The IC0 preconditioning significantly reduces the number of iterations before reaching the converged value. Contrarily, the norm preconditioning tends to spread the eigenvalues of the system and therefore slows down the convergence. On a well-behaved system, applying the IC0 to the original matrix is the method of choice. On the contrary, whenever spurious eigenvalues prevent any convergence of the iterative process, the IC0 preconditioning amplifies the problem. Such a case is shown Fig. M.4 for the ground state of ^{18}O . In that case, applying the norm preconditioning is necessary to converge the system to the SVD solution.

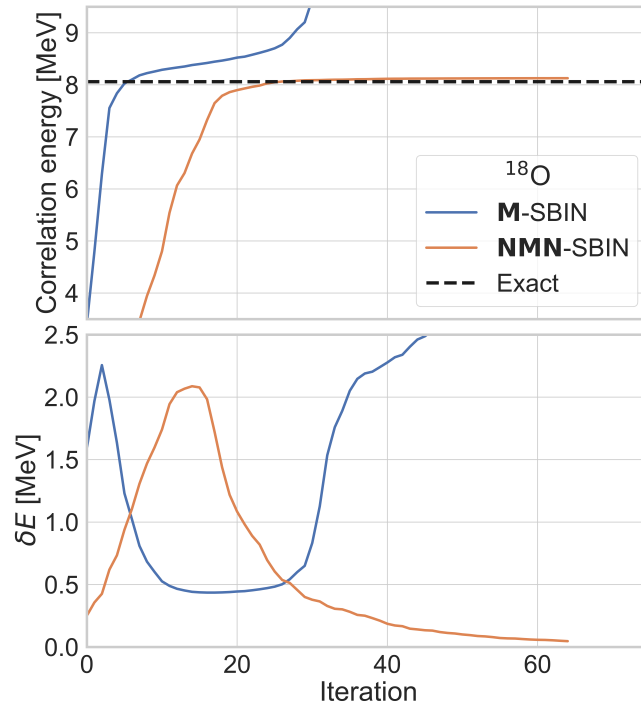


Figure M.4. (Color online) Correlation energy (top) and respective error (bottom) at each MINRES-QLP iteration for the ground state of ^{18}O for various systems and preconditioning techniques. The exact solution is obtained via SVD. The calculation is performed with a two-body χEFT Hamiltonian, $\lambda_{\text{srg}} = 1.88\text{fm}^{-1}$, $\hbar\omega = 20\text{MeV}$ and $e_{\text{max}} = 2$.

Appendix N.

Complex shift

N.1. Motivations

As it appears in Eq. (M.5), the second-order energy relies on the invertibility of Δ to generate non-zero energy denominators. However, the eigenvalues of Δ can vanish, making the calculation of the second-order energy unstable if not ill-defined. Multi-reference methods are indeed susceptible to this so-called intruder-state problem [65, 185].

One way to regularize these zeros is to introduce a diagonal imaginary shift in the eigenbasis of \mathbf{M} . The eigenvalues are thus replaced by

$$\bar{\Delta} \equiv \Delta + i\gamma I, \quad (\text{N.1})$$

or, equivalently, working in the original basis

$$\bar{\mathbf{M}} \equiv \mathbf{M} + i\gamma \mathbf{N}, \quad (\text{N.2})$$

which actually corresponds to adding such a term to the unperturbed Hamiltonian H_0 . The imaginary shift moves zero eigenvalues of Δ into the complex plane and provides a robust way to remove intruder-states' divergences.

In this context, the second-order energy is eventually evaluated using the real part of the Hylleraas functional

$$E^{(2)} = \Re \left[\mathbf{a}^\dagger \bar{\mathbf{M}} \mathbf{a} + \mathbf{a}^\dagger \mathbf{h}_1 + \mathbf{h}_1^\dagger \mathbf{a} \right]. \quad (\text{N.3})$$

N.2. Implementation in real arithmetic

Although an extension of MINRES-QLP has been developed to handle complex symmetric matrices [186, 187], it is possible, due to the specificity of PGCM-PT(2), to rewrite the complex system into a larger real system and use directly the MINRES-QLP algorithm. The system

$$(\mathbf{M} + i\gamma \mathbf{N})(\mathbf{a} + i\mathbf{b}) = -\mathbf{h}_1 \quad (\text{N.4})$$

is recast into a blockwise 2x2 real symmetric system

$$\begin{pmatrix} \mathbf{M} & -\gamma \mathbf{N} \\ -\gamma \mathbf{N} & -\mathbf{M} \end{pmatrix} \begin{pmatrix} \mathbf{a} \\ \mathbf{b} \end{pmatrix} = \begin{pmatrix} -\mathbf{h}_1 \\ \mathbf{0} \end{pmatrix}. \quad (\text{N.5})$$

Since the matrices are real by default after projection, implementing the imaginary shift via an augmented real system is profitable to make use of the MINRES-QLP real symmetric solver.

Note that preconditioning techniques such as SBIN and N-IC0 are still applicable with the augmented system.

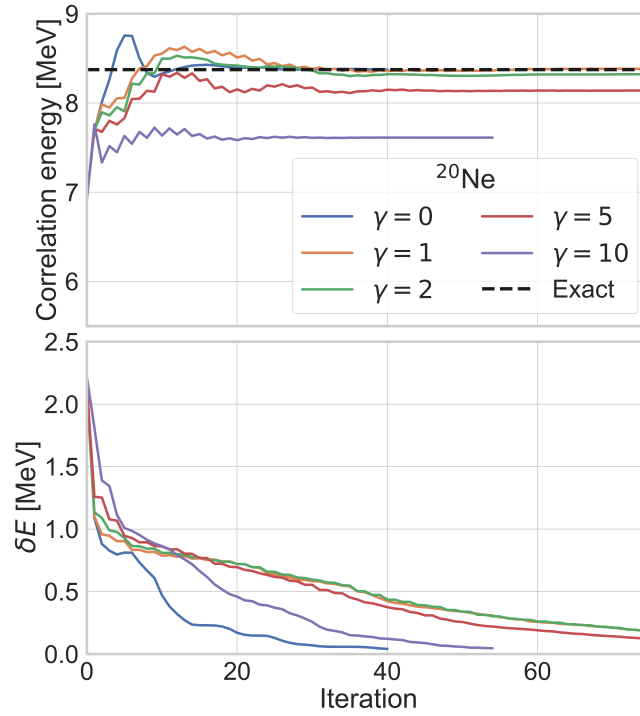


Figure N.1. (Color online) Correlation energy (top panel) and corresponding estimated error for different values of the complex shift γ as a function of the number of MINRES-QLP iterations in ^{20}Ne . The calculation is performed with a two-body χEFT Hamiltonian, $\lambda_{\text{srg}} = 1.88\text{fm}^{-1}$, $\hbar\omega = 20\text{MeV}$ and $e_{\text{max}} = 2$.

N.3. Example

Pursuing with the ^{20}Ne test case ($e_{\text{max}} = 2$), the effect of the complex shifts on the MINRES-QLP iterations with the IC0 preconditioning is illustrated in Fig. N.1. In general, the complex shift tends to lower the correlation energy (the correlation energy vanishes in the limit of an infinite shift), which thus induces a bias that must be monitored. Eventually, the larger the complex shift, the faster the convergence of the iterative procedure (towards a biased result).

As shown in Fig. M.4, the linear problem is not solvable directly in ^{18}O such that the norm preconditioning must be used. It is possible to combine it with the complex shift, as pictured in Fig. N.2 with an additional SBIN preconditioning. Unlike in ^{20}Ne , the complex shift with the norm preconditioning decreases the convergence speed. Note that the complex shift without norm preconditioning is also possible, but does only lead to a stabilization of the result before the occurrence of a divergence.

In practical applications, the optimal shift is a function of the interaction, the model space and the system under consideration. As the model space is enlarged, encountering small eigenvalues becomes more probable and the complex shift becomes necessary to smear out the contaminations. A shift $\gamma \in [10, 20]$ MeV is well suited to remove spurious behaviors, with an estimated error lying around 4% on the correlation energy as can be seen in Fig. N.3. The difference between the results obtained with $\gamma = 15$ MeV and

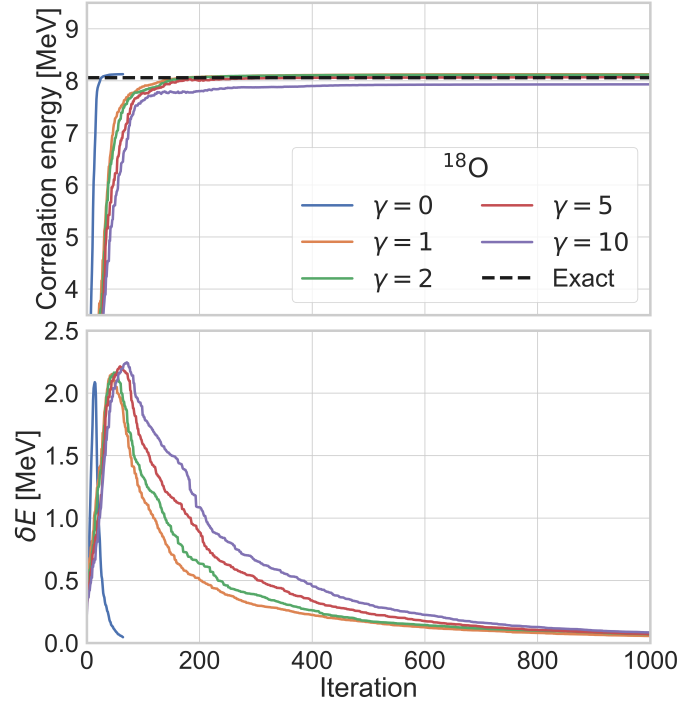


Figure N.2. (Color online) Correlation energy (top panel) and corresponding estimated error for different values of the complex shift γ as a function of the number of MINRES-QLP iterations in ^{18}O . The calculation is performed with a two-body χEFT Hamiltonian, $\lambda_{\text{srg}} = 1.88\text{fm}^{-1}$, $\hbar\omega = 20\text{MeV}$ and $e_{\text{max}} = 2$.

$\gamma = 4\text{MeV}$ is used to estimate the bias due to the shift. Note that PHFB-PT(2) is more sensitive to intruder states problem than PGCM-PT(2), hence the need to employ a larger shift to smooth out singularities on the energy curve. In practice, it is essential to use the same shift for all quantum states of a given nucleus for the bias on absolute binding energies to be consistent and to largely cancel out in the excitation spectrum. The development of an extrapolation method to correct for the bias due to the complex shift is left to a future study.

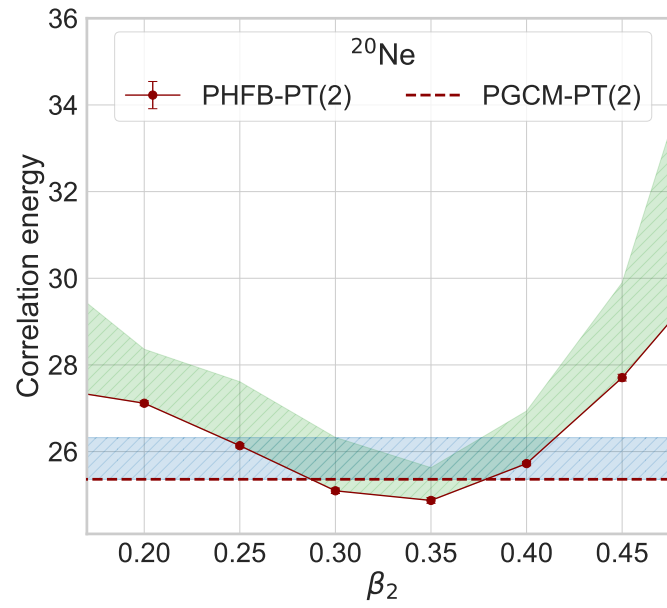


Figure N.3. (Color online) Correlation energy in ^{20}Ne for a complex shift $\gamma = 15$ MeV. Error bars associated to the effect of the shift correspond to the correlation energy with $\gamma = 4$ MeV. The calculation is performed with a two-body χEFT Hamiltonian, $\lambda_{\text{srg}} = 1.88\text{fm}^{-1}$, $\hbar\omega = 20\text{MeV}$ and $e_{\text{max}} = 2$.

Appendix O.

Discussion on numerics

O.1. Complexity

Each method to solve the A-body Schrodinger equation comes with its numerical complexity and storage requirement. For a given basis size N of the one-body Hilbert space the naive runtime and storage complexity of the methods is given as a polynomial in N in Tab. O.1. These asymptotic values are to be revised when making use of symmetries (like spherical or axial symmetry, that reduce the size of the many-body tensors at play), and prefactors (ignored here) may play a significant role. However, it gives a fair idea of the asymptotic of the method. As an example, the computational cost of each individual matrix element at play in PGCM-PT(2), requiring 1000 vectorized elementary operations, makes the building of the matrix the most time-consuming step in the calculation, i.e. the computation of the N^8 matrix elements dictates the overall complexity given that the (approximate) sparsity of the matrix makes the cost of the linear system resolution to be subleading. Similarly, even if BMBPT(3) has the same storage cost as HFB in principle, symmetry properties of the density matrices are used to drastically reduce the number of matrix elements needed at the HFB level. In general, the nominal complexity and storage requirement have to be balanced with the possible optimizations (vectorization, parallelization, compression techniques) that depend on the method and can play a decisive role in practical applications. Also, shape mixing through PGCM scales quadratically with the number of reference states, i.e. a PGCM (resp. PGCM-PT(2)) calculations with 10 states is 100 times costlier than a PHFB (resp. PHFB-PT(2)) calculation.

A selection of runtimes as a function of the one-body basis dimension is displayed in Fig. O.1. Symmetry properties lower the effective complexity to $O(N^4)$ for BMBPT(2,3) and PHFB, the main differences residing in the prefactor that is logically larger for BMBPT(3). Note that the normal ordering of the Hamiltonian and the transformation to the quasi-particle basis is included into the runtime estimate.

Method	HFB	PGCM	BMBPT(2)	BMBPT(3)	PGCM-PT(2)	FCI
Runtime	$O(N^4)$	$O(n_{\text{proj}} n_{\text{gcm}}^2 N^4)$	$O(N^5)$	$O(N^6)$	$O(n_{\text{proj}} n_{\text{gcm}}^2 N^8)$	$O(N^A)$
Storage	$O(N^4)$	$O(N^4)$	$O(N^4)$	$O(N^4)$	$O(n_{\text{gcm}}^2 N^8)$	$O(N^A)$

Table O.1. Runtime complexity and storage requirements for various resolution methods of the many-body problem. n_{proj} denotes the number of gauge angles used for projections and n_{gcm} the number of states used in the mixing.

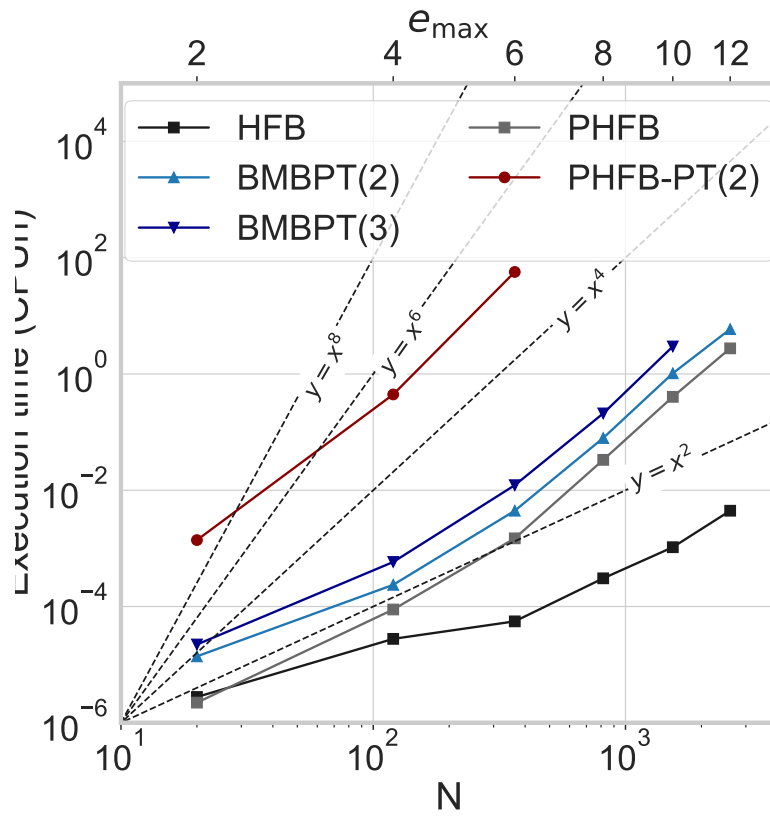


Figure O.1. Timing of many-body methods as a function of the basis size of the one body Hilbert space. Projections are performed on J with 24 gauge angles.

O.2. Complexity reduction in PGCM-PT(2)

The multi-reference PGCM-PT(2) calculation is, in its naive formulation, significantly costlier than its single-reference counterparts. This is mainly due to the redundancies in the visited Hilbert space: many projected quasi-particle configurations play little to no role in the correlation energy or are redundant. This is even more true for large scale applications where the multi-reference unperturbed state mixes many product HF(B) states. The idea is therefore to reduce the dimensionality of the problem by controlling the number of configurations. This has been recently employed in nuclear physics [161] and quantum chemistry [188]. In particular, the application of importance truncation techniques in the context of non perturbative methods [160] show promising results that should be applicable to the present problem.

Several procedures, some of which are left to be implemented, to reduce the number of configurations in a controlled way are now briefly introduced.

O.2.1. Norm-based importance truncation

Exact arithmetic

The norm of a projected configuration is

$$n^I(p) \equiv \langle \Omega^I(p) | \Omega^I(p) \rangle \in [0, 1] \quad (\text{O.1})$$

such that a configuration I for which $n^I(p) = 0$ verifies

$$|\Omega^I(p)\rangle = 0. \quad (\text{O.2})$$

Trivially, a null vector does not contribute to the linear system and can be safely removed from the calculation.

Approximate zeros

Given a threshold $\epsilon_n > 0$, the norm-based importance-truncated problem is introduced by removing configurations I verifying $n^I(p) < \epsilon_n$. The exact problem is obtained in the limit $\epsilon_n = 0$. For now, this is the only method that has been implemented to discard configurations in ^{18}O at $e_{\text{max}} = 6$. Although the number of configurations was divided by two (from 1000000 to 500000) by only keeping configurations whose norm reaches 2% of the maximal value, the induced error was shown to be less than 1%. A systematic study of the results obtained via this procedure still remains to be performed.

O.2.2. Hamiltonian-based importance truncation

Exact arithmetic

The Hamiltonian vector element of a projected configuration reads

$$h_1^I(p) \equiv \langle \Omega^I(p) | H_1 | \Theta^{(0)} \rangle. \quad (\text{O.3})$$

A configuration I for which $h_1^I(p) = 0$ does not contribute to the linear system nor to the second-order energy such that it can be safely removed from the calculation.

Approximate zeros

Given a threshold $\epsilon_h > 0$, the hamiltonian-based importance-truncated problem is introduced by removing configurations I verifying $|h_1^I(p)| < \epsilon_h$. The exact problem is obtained in the limit $\epsilon_h = 0$.

O.2.3. Energy-based importance truncation

The contribution of a configuration I associated with the vacuum $|\Phi(q)\rangle$ to the second-order correlation energy reads as

$$e^{(2)I}(q) = h_1^{I*}(q)a^I(q). \quad (\text{O.4})$$

A configuration I for which $e^{(2)I}(q) = 0$ does not contribute to the correlation energy. However, this configuration might contribute to the system and influence the value of the other coefficients $a^J(q')$. Removing configurations based on their contribution to the correlation energy (estimated by using the SR-BMBPT evaluation of $a^I(q)$) corresponds to the method advocated in Refs. [160, 161] and is expected to lead to a critical gain without altering significantly the end result.

O.2.4. Incremental building of the basis

Besides the importance of a given configuration, it could be also interesting to optimize the building of the matrix by removing redundant configurations from the outset. A procedure for PGCM calculations proposed in Ref. [189] could be adapted to a the PGCM-PT(2) matrix. Although it is not possible to apply it directly to a large matrix, it is possible to subdivide the original matrix and to incrementally build a non-degenerate configuration space

Appendix P.

On the numerical implementation

A schematic representations of the developments of the modules in the numerical implementation is provided Fig. P.1.

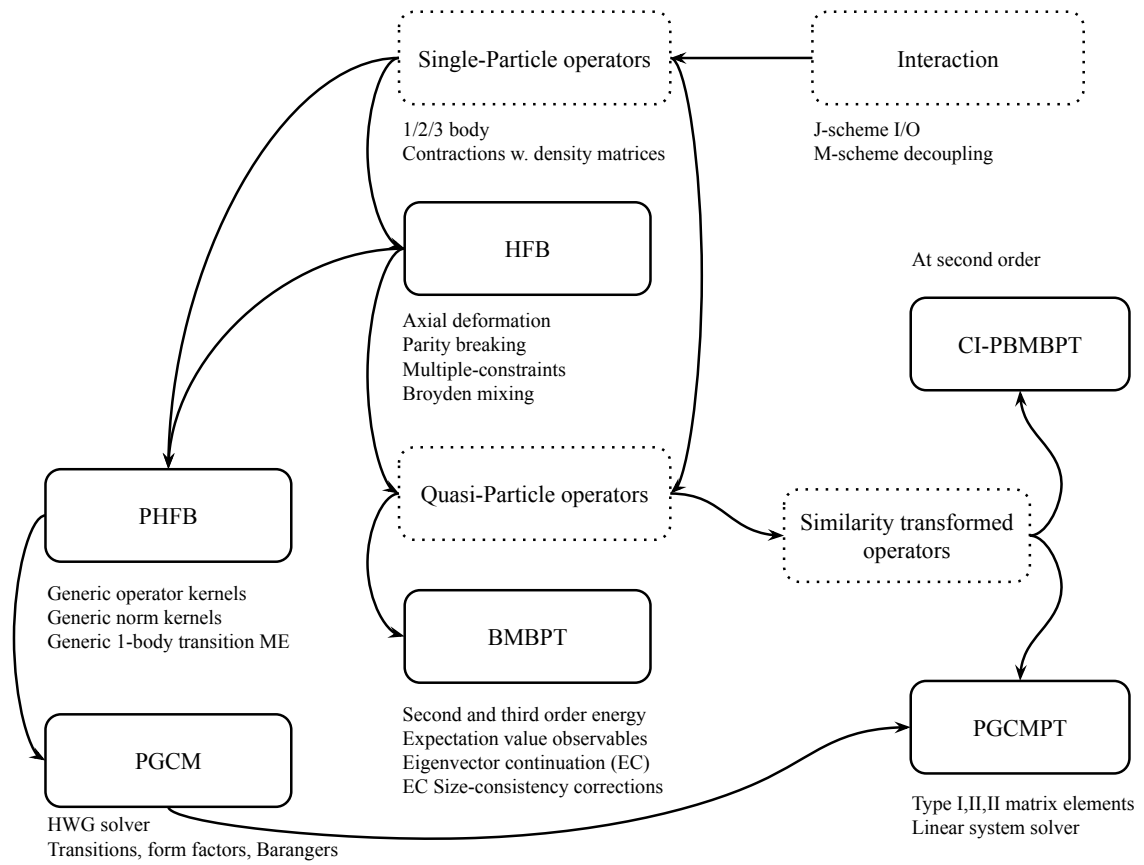


Figure P.1. Schematic representation of the structure of the numerical implementation.

Résumé en français

Le problème à A corps nucléaire

La description théorique des systèmes nucléaires reste, à ce jour, toujours un sujet de recherche actif. Bien que les progrès expérimentaux aient apporté une description toujours plus fine de la vaste gamme de phénomènes à l'œuvre dans les noyaux atomiques, on manque encore d'une description unifiée de l'ensemble de la carte des noyaux. Aujourd'hui, il semble que la meilleure piste pour construire une théorie unifiée prend forme comme une superposition de théories effectives des champs (EFT) successives, qui permettent de décrire de façon cohérente les différentes échelles d'énergies en jeu. Pour les noyaux de basse énergie, la version la plus élémentaire d'une telle EFT, la théorie effective des champs chirale (χ EFT) décrit le noyau auto-lié comme une collection de N neutrons et Z protons ponctuels en interaction forte. Dans ce modèle on résout l'équation de Schrödinger à A corps en partant d'un Hamiltonien dérivé à partir d'une expansion chirale.

Ainsi, le premier obstacle à la résolution d'un problème à N corps nucléaire provient de la complexité de l'interaction entre nucléons, découlant elle-même de l'interaction résiduelle entre les quarks et gluons composant les nucléons. On a longtemps cru que le fait que la chromodynamique quantique (QCD) ne soit pas perturbative à basse énergie empêcherait d'en faire un développement utilisable en pratique. En parallèle, les calculs non perturbatifs sur réseau n'ont pas permis, pour l'instant, de fournir une interaction utilisable pour les noyaux. Si ça ne suffisait pas, la répulsion de courte portée entre nucléons est à l'origine de divergences ultraviolettes (UV), tandis que le deuteron (faiblement lié) et le di-neutron (virtuel) génèrent des divergences infrarouges (IR). Ces deux phénomènes, fondamentalement différents, doivent être traités séparément pour résoudre le problème de structure nucléaire. Enfin, si les nucléons sont pris ponctuels dans le cadre de la χ EFT, leur structure interne est tout de même à l'origine de forces à deux, trois, quatre, ... jusqu'à A corps qui, en théorie, doivent être pris en compte pour avoir une résolution exacte du problème à A corps.

En plus de la construction du Hamiltonien, cette résolution fait face à un second problème. La vaste majorité des noyaux atomiques, qui peuvent contenir jusqu'à environ 300 nucléons, contiennent beaucoup trop de nucléons pour permettre une résolution exacte de l'équation de Schrödinger à A corps. De plus, les différentes échelles en jeu dans les noyaux, qui comprennent à la fois des excitations individuelles de courte portée (responsables par exemple des énergies de liaison absolues) mais aussi des corrélations de longue portée associées à des phénomènes collectifs (à l'origine de la physique de l'appariement, de la rotation et de la vibration), sans parler des phénomènes comme les désintégrations radioactives ou les réactions, rendent encore plus difficile l'élaboration d'un modèle unifié. À ce jour, plus de 3400 noyaux stables vis à vis de l'interaction forte ont été observés, et un millier d'autres ont été prédits par la théorie.

Les premières tentatives pour contourner ces difficultés ont promu l'utilisation de modèles macroscopiques. Par exemple, des modèles semi-classiques comme le modèle de la goutte liquide (LDM), même s'ils ne proposent qu'une description sommaire du noyau, ont été

et sont toujours utilisés dans des calculs où les mécanismes de structure fine ne sont pas nécessaires en première approximation. Cependant, l'inclusion des effets de structure fine sont nécessaires dès que l'on recherche une théorie prédictive et suffisamment précise. Parmi ces approches, la fonctionnelle de la densité de l'énergie (EDF) est parvenue, au fil de ces dernières décennies, à apporter une description empirique des corrélations de courte et de longue portée dans tous les noyaux (connus ou pas). Mais le caractère phénoménologique de l'interaction en jeu, qui ne repose pas sur hiérarchie bien définie entre les différents termes, manque toujours d'une formulation systématique. Malgré les progrès constants des ressources de calcul, ceci ne permet pas d'envisager une route claire vers l'amélioration de cette méthode.

Dans ce contexte, les méthodes d'expansion *ab initio*, employées dans le cadre des χ EFT, approximent la solution exacte de l'équation de Schrödinger comme une série tronquée, ce qui permet d'identifier et de propager les incertitudes aux différents niveaux de la théorie jusqu'aux observables finales. Les méthodes *ab initio* partagent toutes un certain nombre de caractéristiques

- Les nucléons sont considérés comme des degrés de liberté ponctuels élémentaires. En conséquence, les phénomènes nucléaires collectifs doivent émerger des corrélations entre les nucléons en interaction.
- L'hamiltonien est dérivé de manière consistante à partir de la théorie sous-jacente, la QCD. Actuellement, ceci est fait en utilisant la χ EFT pour développer les éléments de matrice du hamiltonien dans une suite d'approximation successives compatibles avec les symétries de la QCD.
- La solution de l'équation de Schrödinger est développée de manière systématique, chaque ordre de la théorie corrigeant le précédent pour se rapprocher de la solution exacte.
- Les erreurs provenant de chaque étape de la résolution (du hamiltonien, du développement, des approximations numériques doivent être estimées et propagées jusqu'aux observables d'intérêt.

En ce sens, les méthodes *ab initio* diffèrent des approches plus phénoménologiques pour lesquelles il est difficile voire impossible d'évaluer les erreurs de façon rigoureuse. Il y a une vingtaine d'années, ces méthodes étaient implémentées uniquement dans le cadre d'approches quasi-exactes, e.g. Fadeev Yakubovski, les fonctions de Green Monte-Carlo, le modèle en couche sans coeur (NCSM). Ainsi, elles étaient limitées aux noyaux légers à cause de la complexité du problème, exponentielle en fonction du nombre de particules A . Grâce à la formalisation concomitante de méthodes de pré-traitement de l'interaction (qui enlèvent les divergences UV) et de méthodes d'expansion qui construisent une solution approchée de l'équation de Schrödinger, des méthodes de résolution de complexité polynomiales ont été développées avec succès au cours de ces 15 dernières années pour donner une description des systèmes nucléaires de masse moyenne.

Méthodes d'expansion *ab initio*

Les méthodes d'expansion ont pour but d'ajouter des corrélations par dessus un état de référence bien choisi qui constitue un bon point de départ pour aller vers la solution exacte.

Même si ces méthodes d'expansion capturent toutes les corrélations dans leur limite exacte, elles tendent (par construction) à se concentrer sur les corrélations de courte portée (i.e. les corrélations dynamiques), et ne parviennent pas, en général, à incorporer de manière efficace les corrélations résiduelles de longue portée (i.e. les corrélations statiques) qui sont particulièrement importantes dans les noyaux à couche ouverte. Cette distinction entre corrélations statiques et dynamiques, même si elle est partiellement arbitraire, se révèle très utile et pertinente en pratique, et l'inclusion simultanée des deux types de corrélations est à ce jour un défi important des méthodes *ab initio*.

Expansion à un état de référence dans les noyaux à couche fermée

Dans les noyaux à couche fermée, la physique collective de longue portée n'est pas réellement nécessaire pour la description de l'état fondamental. Il est donc suffisant de traiter uniquement les corrélations dynamiques. Dans ce cas, les méthodes d'expansions construites par dessus un unique déterminant de Slater de référence (SR), lui même généralement optimisé via un calcul de champ moyen Hartree-Fock (HF), capturent les corrélations dynamiques via des excitations particule-trou. La fonction d'onde totale du système $|\Psi\rangle$ est donc écrite comme un opérateur de corrélation Ω agissant sur l'état de référence $|\Phi\rangle$

$$|\Psi\rangle = \Omega|\Phi\rangle.$$

Ainsi, l'opérateur Ω corréle l'état de référence vers la solution exacte du système. Le premier exemple est la théorie de perturbation à A corps (MBPT), dans laquelle Ω est développé en une série perturbative. Cette méthode a observé un regain d'intérêt ces dernières années grâce au pré-traitement de l'interaction via les méthodes du groupe de transformation similaire (SRG) qui permettent de rendre la série perturbative convergente. En parallèle, des méthodes d'expansion perturbatives ont aussi été développées. Les méthodes des clusters couplés (CC), du groupe de transformation similaire dans le milieu (IMSRG) ou de la fonction de Green auto-cohérente (SCGF) resument toutes (à leur façon) des sous-ensembles de diagrammes perturbatifs à tous les ordres. Ainsi, ils permettent d'avoir un résultat plus précis pour un coût donné.

Toutes ces méthodes donnent des résultats compatibles entre elles et avec les calculs exacts NCSM. Elles ont été capables d'étendre la portée des calculs *ab initio* jusqu'à des systèmes contenant $A \sim 130$ nucléons.

Approches multi-références et corrélations statiques

L'application des méthodes d'expansion pose des problèmes dans les systèmes à couche ouverte, où les dégénérescences de l'état de référence déterminantal (par rapport aux excitations particules-trous) sont à l'origine de singularités dans l'expansion. Cette difficulté est déjà connue dans le cadre des EDFs phénoménologiques, où la description qualitative des noyaux à couche ouverte par des méthodes de champ moyen conservant la symétrie se détériore rapidement lorsqu'on s'éloigne des fermetures de couche. Ces dégénérescences sont en fait à l'origine de corrélations fortes de longue portée près du niveau de Fermi, qui peuvent être capturées aisément si on complexifie l'état de référence. Au lieu d'imposer un état de référence uni-déterminantal conservant la symétrie, une combinaison linéaire optimale d'états produits généralisés peut être utilisée avec succès comme état de départ.

Dans les approches EDF, l'état multi-référence est construit en deux étapes distinctes. Premièrement, le déterminant conservant les symétries de l'interaction est remplacé par un état de référence à symétrie brisée. Cet état reste un état produit (proche de l'image de particules indépendantes) mais peut être déformé spatialement ou briser la symétrie du nombre de particules. Comme les noyaux sont des systèmes quantiques mésoscopiques, les vrais états propres du hamiltonien doivent impérativement avoir de bons nombres quantiques de symétrie. C'est pourquoi, dans un second temps, on doit projeter l'état de référence sur les bonnes symétries, ceci étant obtenu en faisant une combinaison linéaire incluant les partenaires tournés de l'état initial. Ainsi, on peut prendre en compte naturellement la physique de la rotation (et / ou de l'appariement). La physique vibrationnelle est prise en compte dans une dernière étape qui mélange différents états projetés différents par la nature de la brisure de symétrie de l'état sous-jacent. Cette approche porte le nom de méthode de la coordonnée génératrice projetée (PGCM).

Poursuivant la même logique, l'état non perturbé en jeu dans les méthodes d'expansion *ab initio* peut être autorisé à briser des symétries dans le but de lever les dégénérescences, de sorte que l'expansion soit faite directement par-dessus cet état de référence à symétrie brisée. Cette approche a été implémentée pour la symétrie du nombre de particules via la théorie de perturbation de Bogoliubov (BMBPT), les fonctions de Green auto-cohérences de Gorkov (GSCGF), et les clusters couplés de Bogoliubov (BCC), ainsi que pour la symétrie de rotation via CC. La description des propriétés du fondamental des noyaux de masse moyenne n'a pas à rougir face à des approches plus phénoménologiques. Cependant, comme en EDF, la brisure de symétrie ne peut être qu'une étape intermédiaire du calcul et ces symétries doivent être restaurées. Cependant, la restauration devient non triviale au-delà du champ moyen, et a été formulée assez récemment pour les expansions (perturbatives ou non). Les clusters couplés de Bogoliubov projetés (PBCC) ont été implémentés avec succès pour des hamiltoniens schématisés, mais aucune implémentation réaliste n'est disponible à ce jour, et les premières tentatives dans ce sens sont restées infructueuses jusqu'à maintenant.

Une autre stratégie possible est d'ajouter des corrélations dynamiques directement par-dessus un état de référence incorporant les corrélations statiques. Dans cette ligne d'idée, l'approche d'IMSRG multi-référence (MR-IMSRG) a été développée en physique nucléaire, et les clusters-couplés multi-référence (MR-CC) en chimie quantique. En parallèle, la théorie de perturbation multi-configurationnelle (MCPT) corrige en perturbation un état de référence issu d'un calcul NCSM. Cependant, MR-IMSRG n'est pas une méthode de résolution à proprement parler mais doit plus être comprise comme une méthode de pré-traitement du hamiltonien, tandis que MCPT nécessite un calcul NCSM préliminaire, qui devient vite prohibitif au-delà des noyaux légers. En chimie quantique, une autre méthode de perturbation multi-référence basée sur un mélange non-orthogonal de déterminants de Slater a été proposée et implémentée récemment. Cette méthode parvient, sans ce contexte, à capturer avec succès les corrélations de longue portée dans les systèmes fortement corrélés.

Développements de la thèse

Ce travail de thèse s'est basé sur les avancées récentes en chimie quantique dans le but de

- Formaliser une théorie de perturbation multi-référence basée sur un état non perturbé mélange non-orthogonal d'états produits de Bogoliubov projetés, dans le but de capturer de manière consistante les corrélations statiques et dynamiques dans un

contexte *ab initio*.

- Implémenter le premier ordre du formalisme et l'utiliser pour une étude systématique de la spectroscopie de basse énergie dans la chaîne des naons.
- Implémenter le deuxième ordre de la théorie dans un espace de taille réduite pour déterminer les performances de la méthodes avec des hamiltoniens réalistes.
- Formaliser, implémenter et tester une méthode de réduction de rang d'opérateurs conservant la symétrie, dans le but de réabsorber efficacement les effets dans interactions à trois corps dans une interaction effective à deux corps (au prix de l'introduction d'une erreur contrôlée dans les observables finales).

Définitions et éléments de l'algèbre de Bogoliubov

Dans le Chapitre 1, les notations et éléments de formalisme essentiels aux chapitres suivants sont introduits. Après avoir rappelé l'équation de Schrödinger que l'on cherche à résoudre, une base de l'espace de Fock est définie sur laquelle les opérateurs sont développés. Enfin, les états de produits de Bogoliubov sont définis, ainsi que les transformations entre différents états différant par leur déformation q ou par leur orientation θ .

Formalisme PGCM-PT

Le formalisme générique de la théorie de perturbation est introduit dans le Chapitre 2. En particulier, on y insiste sur l'importance du choix de l'état de référence et du partitionnement du problème dans une théorie de perturbation. Le cas particulier d'un état de référence PGCM, qui mélange des états produits projetés différant par leur déformation intrinsèque, est discuté en détail. On y donne les dérivations spécifiques ainsi que les formules utilisables dans une implémentation pratique. Un des grands avantages de la théorie de perturbation basée sur un état PGCM (PGCM-PT) est la possibilité de traiter sur un pied d'égalité tous les états rotationnels. À l'heure actuelle, l'extension aux états vibrationnels n'est pas encore formalisée mais est envisagée dans un futur proche.

Interaction *in medium*

Le principal facteur limitant des méthodes *ab initio* à l'heure actuelle réside dans la partie purement 3 corps de l'interaction. En effet, les éléments de matrice à 3 corps nécessitent de grandes capacités de stockage (même en conservant la symétrie sphérique), tandis que le traitement exact du 3 corps augmente de façon importante le coût d'un calcul. Dans ce contexte, et en s'inspirant des méthodes déjà disponibles dans les noyaux à couche fermée, une nouvelle méthode d'approximation de la partie 3 corps de l'interaction a été proposée, implémentée et testée dans le Chapitre 3. La qualité de cette approximation a été vérifiée dans une large variété de systèmes (à couche fermée et ouverte) et pour différentes méthodes de résolution. La méthode de réduction de rang, qui moyenne la partie à 3 corps en une interaction effective à 2 corps, est précise, universelle, simple à implémenter et robuste. Ces caractéristiques en font une des routes possibles vers les noyaux de masse plus importante, notamment car elle est déjà formulée pour des interactions comprenant, par exemple, des termes à 4 corps, le jour où elles deviendront disponibles pour des calculs pratiques.

PGCM: Résultats

Le Chapitre 4 s'est intéressé au premier ordre de la théorie formalisée dans le Chapitre 2. Des calculs systématiques de la chaîne des néons ont été produits avec des interactions chirales de nouvelle génération. En particulier, l'étude approfondie du ^{20}Ne a montré que le premier ordre de la théorie, bien que manquant certaines corrélations dynamiques, donne une bonne description de la spectroscopie de basse énergie avec un bon accord avec les données expérimentales pour peu que les bons degrés de liberté collectifs (e.g. quadrupolaires et octupolaires) soient pris en compte. En particulier, l'émergence de structures en agrégats associées avec des fluctuations de forces octupolaires dans le ^{20}Ne a montré le pouvoir prédictif de la PGCM dans un contexte *ab initio*. Dans une seconde étape, les systématiques de la chaîne ont été comparées avec des résultats IM-NCSM quasi-exacts. Même si la description globale est satisfaisante, il est clair que certaines corrélations manquent dans les noyaux riches en neutron, ce qui appelle à un état de référence PGCM plus riche (incorporant plus de coordonnées collectives) ou l'ajout de corrélations dynamiques par dessus la solution PGCM.

PGCM-PT(2): Résultats

C'est précisément l'objectif du Chapitre 5 que de compléter l'état PGCM avec des corrélations dynamiques en utilisant le formalisme introduit Chapitre 2. Tandis que l'état de référence capture par construction les corrélations collectives de longue portée, la méthode de perturbation dépendant de l'état corrige cet état de manière consistante avec des excitations élémentaires de bas rang. Au final, la méthode a été appliquée en conjonction avec des interactions issues d'hamiltoniens préprocessés avec une transformation MR-IMSRG. Dans ce cas, les ces corrélations dynamiques ont réussi à corriger les énergies absolues, mais aussi les spectres PGCM qui ont tendance à être artificiellement dilatés par l'évolution MR-IMSRG.

Conclusion

Cette thèse indique finalement qu'une description précise et complète des noyaux de masse moyenne et lourde devra probablement reposer sur trois leviers complémentaires, dont l'interaction doit encore être étudiée plus en détail dans les années à venir:

1. Le prétraitement de l'hamiltonien via, par exemple, des méthodes MR-IMSRG pour capturer de façon efficace la majeure partie des corrélations dynamiques.
2. L'utilisation d'un état perturbé multi-référence (e.g. obtenu via PGCM) qui capture les corrélations collectives de longue portée via une diagonalisation de faible dimensionalité.
3. Les premiers ordres d'une méthode d'expansion additionnelle par dessus l'état de référence, e.g. via le formalisme PGCM-PT, pour capturer les corrélations dynamiques restantes.

Chacune de ces étapes est elle-même flexible et sujette à amélioration, et leur combinaison reste à être optimisée. Premièrement, le prétraitement est une fonction du paramètre de développement qui doit être optimisé pour capturer des corrélations dynamiques sans briser l'unitarité. Ensuite, la PGCM dépend du choix des coordonnées collectives qui doivent

être assez riches pour capturer efficacement tout la physique non perturbative de longue portée. Enfin, si PGCM-PT est formulé à tous les ordres, on veut naturellement le garder à un ordre réduit pour garder un coût tractable.

Tandis que cette thèse a posé les fondations d'un tel schéma de calcul, les études à venir vont permettre de mieux comprendre le jeu des corrélations dans les méthodes *ab initio*. Par exemple, la description de noyaux montrant un fort caractère de mélange de forme serait un objectif intéressant à atteindre dans les prochaines années.

List of Figures

2.1.	(color online) Schematic illustration of the workflow of expansion many-body methods based on a given input Hamiltonian H . While the unperturbed state must be capable of capturing so-called static correlations (if any), the expansion on top of it typically focuses on grasping so-called dynamical correlations (either perturbatively or non-perturbatively).	20
2.2.	(color online) Schematic representation of the HFB PES $\mathbf{H}^{00}(q; \theta)$ in the two-dimensional plane associated with the order parameter $\varrho = qe^{i\theta}$ of the (intermediately broken) symmetry. Light (dark) blue circles represent configurations along the q (θ) direction. Left (right) panel: system characterized by a symmetry-conserving (-breaking) minimum.	28
2.3.	(color online) Schematic energetic representation as a function of the norm q of the order parameter of the considered symmetry of excited Bogoliubov states $\{ \Phi^I(q)\rangle; q \in \text{set and } I \in \text{S,D,T}, \dots\}$ employed to expand $ \Theta^{(1)}\rangle$. The (red) dotted curve represents the constrained HFB energy $\mathbf{H}^{00}(q; 0)$ associated with the vacua $B_q = \{ \Phi(q)\rangle; q \in \text{set}\}$ entering the unperturbed PGCM state $ \Theta^{(0)}\rangle$. Left (right) panel: system characterized by a symmetry-conserving (-breaking) minimum of $\mathbf{H}^{00}(q; 0)$. In single-reference methods, the problematic gapless symmetry-conserving solution encountered in open-shell nuclei is replaced by a gentle gap-full one by allowing the unperturbed state to spontaneously break the symmetry.	34
2.4.	(color online) Schematic representation of the existing options to define the partitioning and unperturbed state at the heart of expansion many-body methods. Standard single-reference symmetry-conserving schemes appear as particular limits of more general choices, i.e. single-reference symmetry-breaking schemes that are themselves limits of the multi-reference symmetry-conserving scheme introduced in the present work. Moving up in generality allows one to tackle stronger static correlations, which effectively enlarge the classes of nuclei that can be accessed in a controlled fashion. . .	37
3.1.	Error (in %) of dHFB ground-state energies obtained with $H^{2B}[\rho]$ for the various test one-body density matrices. The error corresponding to the use of ρ^{sHOSD} for ^{40}Mg amounts to 2.6% and lies outside the figure. Calculations were performed with $e_{\text{max}} = 8$, $e_{3\text{max}} = 12$ and $\lambda_{\text{srg}} = 1.88 \text{ fm}^{-1}$	53
3.2.	Upper panel: dHFB total energy curve of ^{20}Ne as a function of the axial quadrupole deformation computed with the full H . Lower panel: Error (in %) in the total energy curve when using $H^{2B}[\rho]$ with the various test one-body density matrices. Calculations are performed with $e_{\text{max}} = 8$, $e_{3\text{max}} = 10$ and $\lambda_{\text{srg}} = 1.88 \text{ fm}^{-1}$	55
3.3.	Contributions of the various components of $H^{2B}[\rho]$ and H to the dHFB energy. Upper panel: ^{16}O . Lower panel: ^{20}Ne . Calculations are performed with $e_{\text{max}} = 6$ and $e_{3\text{max}} = 6$	57

3.4.	Difference of dMBPT(3) ground-state energies (in %) obtained with $H^{2B}[\rho]$ and within the PNO2B approximation of H for the various test one-body density matrices. Calculations are performed with $e_{\max} = 8$, $e_{3\max} = 12$ and $\lambda_{\text{srg}} = 1.88 \text{ fm}^{-1}$	58
3.5.	Results of PHFB calculations with H and $H^{2B}[\rho]$ for several test one-body density matrices ρ . Left and right panels display results obtained for $e_{3\max} = 8$ and 12, respectively, at fixed $e_{\max} = 8$. Upper panel: absolute energies of lowest $J^{\Pi} = 0^+, 2^+, 4^+$ states to which the dHFB energy obtained from H in each nucleus is subtracted. Lower panel: ground-state root-mean-square matter radii. Calculations are performed with $\lambda_{\text{srg}} = 1.88 \text{ fm}^{-1}$	60
3.6.	Same as Fig. 3.5 for ^{20}Ne (left) and ^{30}Ne (right) for $e_{\max} = 8$ and 10 at fixed $e_{3\max} = 10$	62
3.7.	Same as Fig. 3.6 but for two values of the SRG parameter λ_{srg} . Calculations are performed with $e_{\max} = 8$ and $e_{3\max} = 12$	63
3.8.	Low-lying PHFB excitation spectra of doubly open-shell nuclei. Reference results calculated from H are compared to those computed from $H^{2B}[\rho]$ using the various one-body test density matrices. Calculations are performed with $e_{\max} = 8$, $e_{3\max} = 12$ and $\lambda_{\text{srg}} = 1.88 \text{ fm}^{-1}$	64
3.9.	Same as the bottom panel of Fig. 3.2 for $J^{\Pi} = 0^+, 2^+, 4^+$ PHFB states.	65
3.10.	Low-lying part of the PGCM ground-state rotational band of ^{20}Ne . Reference results calculated from H are compared to those computed from $H^{2B}[\rho]$ using various test one-body density matrices. Each energy level is displayed along with the magnetic dipole (below) and electric quadrupole (above) moments of the associated state. B(E2) transitions strengths are displayed using red arrows. Calculations are performed with $e_{\max} = 8$, $e_{3\max} = 10$ and $\lambda_{\text{srg}} = 1.88 \text{ fm}^{-1}$	66
3.11.	Same as Fig. 3.10 for ^{30}Ne	67
3.12.	Electric isovector dipole strength of ^{16}O as a function of the excitation energy (upper panel). Reference results calculated from H are compared to those computed from $H^{2B}[\rho]$ using ρ^{sHFB} . The relative deviation from the strength computed with the exact Hamiltonian is displayed as a function of the excitation energy in the lower panel. Calculations are performed with $e_{\max} = 8$, $e_{3\max} = 10$ and $\lambda_{\text{srg}} = 1.88 \text{ fm}^{-1}$	68
3.13.	Same as Fig. 3.12 for ^{20}Ne	69
3.14.	Ground-state energy error $\Delta E_{\Psi}^{2B}[\rho]$ associated with the use of $H^{2B}[\rho]$ as a function of the distance $\ \rho - \rho^{\Psi}\ $ between the test one-body density matrix ρ and the actual ground-state one ρ^{Ψ} in log-log scale. Left panel: sHF ($J^{\Pi} = 0^+$) solution for ^{16}O . Right panel: PHFB ($J^{\Pi} = 0^+$) solution for ^{20}Ne . Data points are for physical and randomly-sampled test one-body density matrices. For the latter, the color scale characterizes their von Neumann entropy. The dashed-dotted lines denote the cubic envelop extracted from the left panel and reported on the right panel. Calculations are performed for $e_{\max} = 6$ and $e_{3\max} = 6$	71

-
- 4.1. Dependence of PHFB results in ^{20}Ne (left column) and ^{28}Ne (right column) on the employed HO model space. Results are plotted as a function of $\hbar\omega$ for various values of e_{max} . The dashed lines denote extrapolated values whereas the grey band provides the associated uncertainty. The first row (panels (a) and (b)) focuses on the first 2^+ absolute energy whereas the second (panels (c) and (d)) and third (panels (e) and (f)) rows provide the ground-state energy and associated rms charge radius. Calculations employ the $\text{N}^3\text{LO } \chi\text{EFT}$ Hamiltonian with $\lambda_{\text{srg}} = 1.88 \text{ fm}^{-1}$ 84
- 4.2. (Color online) Constrained HFB TES of ^{20}Ne in the axial (β_2, β_3) plane. The (red) full line indicates the lowest-energy path, with the arrow positioned at the minimum of the TES. The (red) dots characterize the set of HFB states used in the subsequent PGCM calculation. Calculations employ the $\text{N}^3\text{LO } \chi\text{EFT}$ Hamiltonian with $\lambda_{\text{srg}} = 1.88 \text{ fm}^{-1}$ 85
- 4.3. (Color online) Projected HFB TES of ^{20}Ne in the axial (β_2, β_3) plane for spin-parity values $J^\pi = 0^+, 1^-, 2^+, \dots, 7^-$. In each case, the minimum of the TES is indicated by a (red) star. Calculations employ the $\text{N}^3\text{LO } \chi\text{EFT}$ Hamiltonian with $\lambda_{\text{srg}} = 1.88 \text{ fm}^{-1}$ 86
- 4.4. (Color online) Collective PGCM wave-functions in the axial (β_2, β_3) plane of low-lying positive- and negative-parity states. Calculations employ the $\text{N}^3\text{LO } \chi\text{EFT}$ Hamiltonian with $\lambda_{\text{srg}} = 1.88 \text{ fm}^{-1}$ 87
- 4.5. (Color online) Low-lying positive- and negative-parity bands in ^{20}Ne . The intra-band $E2$ transition strengths (in e^2fm^4) are indicated along vertical arrows whereas a selection of $E3$ transition strengths (in e^3fm^6) are indicated along oblique lines. Panel (a): PGCM results obtained by restricting the mixing to the quadrupole axial degree of freedom. Panel (b): PHFB results based on the HFB configuration corresponding to the minimum of the 0^+ TES located at $(\beta_2 = 0.75, \beta_3 = 0.53)$ (see Fig. 4.3). Panel (c): PGCM results obtained using the set of points in the axial (β_2, β_3) plane displayed in Fig. 4.2. Panel (d): IM-NCSM results. Panel (e): experimental data. PGCM results in panel (c) display model-space (black box) plus χEFT (pink band) uncertainties. IM-NCSM results in panel (d) display total many-body (black box) plus χEFT (pink band) uncertainties. The $\text{N}^3\text{LO } \chi\text{EFT}$ Hamiltonian with $\lambda_{\text{srg}} = 1.88 \text{ fm}^{-1}$ ($\lambda_{\text{srg}} = 2.23 \text{ fm}^{-1}$) is employed in PGCM (IM-NCSM) calculations. 88
- 4.6. (Color online) Point matter distribution of ^{20}Ne in the x-y plane corresponding to three constrained HFB configurations located at (i) $(\beta_2 = 0.7, \beta_3 = 0)$, (ii) $(\beta_2 = 0.7, \beta_3 = 0.9)$ and (iii) $(\beta_2 = 1.2, \beta_3 = 1.2)$ in the axial (β_2, β_3) plane. Calculations employ the $\text{N}^3\text{LO } \chi\text{EFT}$ Hamiltonian with $\lambda_{\text{srg}} = 1.88 \text{ fm}^{-1}$ 89
- 4.7. (Color online) Spherical HFB, PGCM and experimental ^{20}Ne ground-state charge density distributions in linear (upper panel) and logarithmic (lower panel) scales. Calculations employ the $\text{N}^3\text{LO } \chi\text{EFT}$ Hamiltonian with $\lambda_{\text{srg}} = 1.88 \text{ fm}^{-1}$ 90
- 4.8. (Color online) HFB TES of $^{18-32}\text{Ne}$ in the axial (β_2, β_3) plane. The (red) dots characterize in each case the set of HFB states used in the subsequent PGCM calculations. Calculations employ the $\text{N}^3\text{LO } \chi\text{EFT}$ Hamiltonian with $\lambda_{\text{srg}} = 1.88 \text{ fm}^{-1}$ 91

- 4.9. (Color online) Absolute ground-state energies (upper panel) and two-neutron separation energies (lower panel) along the Ne isotopic chain. Results from HFB, PGCM, BMBPT and IM-NCSM calculations are compared to experimental data. The N³LO χ EFT Hamiltonian with $\lambda_{\text{srg}} = 1.88 \text{ fm}^{-1}$ ($\lambda_{\text{srg}} = 2.23 \text{ fm}^{-1}$) is employed in IM-NCSM calculations. BMBPT calculations are performed with $e_{\text{max}} = 10$ 92
- 4.10. (Color online) Evolution of neutron (upper panels) and proton (lower panels) Baranger's single-particle spectra of the 0^+ ground-state in $^{18-32}\text{Ne}$. Results from spherical HFB (left column) and PGCM (right column) calculations in the axial (β_2, β_3) plane are shown. Black dots denote the last occupied orbital associated with a naive filling of the shells. Calculations employ the N³LO χ EFT Hamiltonian with $\lambda_{\text{srg}} = 1.88 \text{ fm}^{-1}$ 93
- 4.11. (Color online) Theoretical (HFB, PGCM, BMBPT, IM-NCSM) and experimental ground-state rms charge radius along the Neon isotopic chain. HFB and BMBPT results correspond to the HFB minimum in the axial (β_2, β_3) plane. PGCM calculations are performed over the axial (β_2, β_3) plane. The N³LO χ EFT Hamiltonian with $\lambda_{\text{srg}} = 1.88 \text{ fm}^{-1}$ ($\lambda_{\text{srg}} = 2.23 \text{ fm}^{-1}$) is employed in IM-NCSM calculations. BMBPT calculations are performed with $e_{\text{max}} = 10$ 95
- 4.12. (Color online) Low-lying spectroscopy in $^{18-32}\text{Ne}$. First $\Delta E_1^{2^+}$ and $\Delta E_1^{4^+}$ excitation energies (upper panel) and their ratio $\Delta E_1^{4^+}/\Delta E_1^{2^+}$ (lower panel). PGCM results with model-space (black box) plus χ EFT (pink band) uncertainties and IM-NCSM results with total many-body (black box) plus χ EFT (pink band) uncertainties are compared to experimental data. The N³LO χ EFT Hamiltonian with $\lambda_{\text{srg}} = 1.88 \text{ fm}^{-1}$ ($\lambda_{\text{srg}} = 2.23 \text{ fm}^{-1}$) is employed in PGCM (IM-NCSM) calculations. 97
- 4.13. (Color online) Low-lying spectroscopy in $^{18-32}\text{Ne}$ from sd valence-space calculations. First $\Delta E_1^{2^+}$ and $\Delta E_1^{4^+}$ excitation energies (upper panel) and their ratio $\Delta E_1^{4^+}/\Delta E_1^{2^+}$ (lower panel). PGCM results obtained by mixing states along the axial quadrupole coordinate are compared to experimental data and to full configuration interaction (FCI) results as well as to PGCM results obtained by adding the triaxial quadrupole coordinate. 98
- 4.14. (Color online) First two positive-parity bands in $^{20,24,30}\text{Ne}$. The $E2$ transition strengths (in e^2fm^4) are indicated along vertical arrows. Panel (a): PGCM results obtained using HFB configurations in the axial (β_2, β_3) plane. Panel (b): PGCM results obtained adding triaxially deformed HFB configurations. Panel (c): IM-NCSM results. Panel (d): experimental data. PGCM results in panel (a) display model-space (black box) plus χ EFT (pink band) uncertainties. IM-NCSM results in panel (c) display total many-body (black box) plus χ EFT (pink band) uncertainties. The N³LO χ EFT Hamiltonian with $\lambda_{\text{srg}} = 1.88 \text{ fm}^{-1}$ ($\lambda_{\text{srg}} = 2.23 \text{ fm}^{-1}$) is employed in PGCM (IM-NCSM) calculations. 100
- 4.15. (Color online) Average neutron natural orbital occupations (including the $2j + 1$ degeneracy factor) for the first two PGCM 0^+ states of $^{18-32}\text{Ne}$. Calculations employ the N³LO χ EFT Hamiltonian with $\lambda_{\text{srg}} = 1.88 \text{ fm}^{-1}$. . . 101

4.16. (Color online) Adaptation of the lower panel of Fig. 4.14 via the addition of the axial PGCM results obtained from the N ³ LO χ EFT Hamiltonian $\lambda_{\text{srg}} = 2.23 \text{ fm}^{-1}$	102
4.17. (Color online) Theoretical (PGCM, IM-NCSM) and experimental electromagnetic moments along the Neon isotopic chain. Upper panel: reduced electric quadrupole transition $B(E2 : 2_1^+ \rightarrow 0_1^+)$ to which is added the PGCM $B(E2 : 2_2^+ \rightarrow 0_2^+)$ value in ³⁰ Ne. Middle panel: spectroscopic electric quadrupole moment of the first 2^+ state. Lower panel: spectroscopic magnetic dipole moment of the first 2^+ and 4^+ states. PGCM calculations are performed in the axial (β_2, β_3) plane. The N ³ LO χ EFT Hamiltonian with $\lambda_{\text{srg}} = 1.88 \text{ fm}^{-1}$ ($\lambda_{\text{srg}} = 2.23 \text{ fm}^{-1}$) is employed in PGCM (IM-NCSM) calculations.	103
5.1. (color online) Schematic workflow of expansion many-body methods (vertical axis) versus potential pre-processings of the Hamiltonian (horizontal axis). Unitary vacuum (in-medium) similarity renormalization group transformations denote a nucleus-independent (nucleus-dependent) pre-processing of the Hamiltonian.	106
5.2. (Color online) Ground-state energy of ¹⁶ O as a function of r_{rms} of the (underlying) HF vacua. Calculations are performed with $\hbar\omega = 20 \text{ MeV}$ and $e_{\text{max}} = 4$ as well as with the two-body part of the N ³ LO χ EFT Hamiltonian evolved to $\lambda_{\text{vsrg}} = 1.88 \text{ fm}^{-1}$	109
5.3. (Color online) Upper panel: collective ground-state GCM wave-function probability distribution $(\tilde{f}_{01}^+(r_{\text{rms}}) ^2)$ in ¹⁶ O as a function of the rms radius of the underlying HF vacua. Lower panel: contributions to GCM $(e_0^{(0+1)}(r_{\text{rms}}))$ and GCM-PT(2) $(e_S^{(2)}(r_{\text{rms}}) + e_S^{(2)}(r_{\text{rms}}))$ ground-state energies as a function of r_{rms} . GCM-PT(2) contributions are split into single (one-particle/one-hole) and double (two-particle/two-hole) excitations. Calculations are performed with $\hbar\omega = 20 \text{ MeV}$ and $e_{\text{max}} = 4$ as well as with the two-body part of the N ³ LO χ EFT Hamiltonian evolved to $\lambda_{\text{vsrg}} = 1.88 \text{ fm}^{-1}$	110
5.4. Ground-state energy of ¹⁸ O as a function of the pairing constraint δ calculated from various many-body methods with $\hbar\omega = 20 \text{ MeV}$ and $e_{\text{max}} = 4$. The two-body part of the N ³ LO χ EFT Hamiltonian evolved to $\lambda_{\text{vsrg}} = 1.88 \text{ fm}^{-1}$ is employed.	112
5.5. (Color online) Upper panel: collective ground-state PGCM wave-function probability distribution $(\tilde{f}_{01}^+(\delta) ^2)$ in ¹⁸ O as a function of the pairing constraint δ characterizing the underlying HFB vacua. Lower panel: contributions to the PGCM $(e_0^{(0+1)}(\delta))$ ground-state energy and to the PGCM-PT(2) $(e_S^{(2)}(\delta) + e_S^{(2)}(\delta))$ correlation energy. The latter is split into single (two quasi-particle) and double (four quasi-particle) contributions. Calculations are performed with $\hbar\omega = 20 \text{ MeV}$ and $e_{\text{max}} = 4$, using the two-body part of the N ³ LO χ EFT Hamiltonian evolved to $\lambda_{\text{vsrg}} = 1.88 \text{ fm}^{-1}$	113
5.6. Ground-state energy of ²⁰ Ne as a function of the axial quadrupole deformation β_2 of the (underlying) HFB states. Calculations are performed with $\hbar\omega = 20 \text{ MeV}$ and $e_{\text{max}} = 4$ using the two-body part of the N ³ LO χ EFT Hamiltonian evolved to $\lambda_{\text{vsrg}} = 1.88 \text{ fm}^{-1}$	114

5.7.	(Color online) Upper panel: collective ground-state PGCM wave-function probability distribution ($ \tilde{f}^{0+}_1(\beta_2) ^2$) in ^{20}Ne as a function of the axial quadrupole deformation (β_2) of the underlying HFB vacua. Lower panel: contributions to PGCM ($e_0^{(0+1)}(\beta_2)$) and PGCM-PT(2) ($e_S^{(2)}(\beta_2) + e_S^{(2)}(\beta_2)$) ground-state energies as a function of the axial quadrupole deformation (β_2) of the underlying HFB vacua. The PGCM-PT(2) contributions are split into singles (two quasi-particle) and doubles (four quasi-particle) contributions. Calculations are performed with $\hbar\omega = 20$ MeV and $e_{\text{max}} = 4$ using the two-body part of the N^3LO χEFT Hamiltonian evolved to $\lambda_{\text{vsrg}} = 1.88 \text{ fm}^{-1}$.	115
5.8.	(Color online) Excitation energy in ^{20}Ne as a function of the axial quadrupole deformation (β_2) of the underlying HFB vacua. Top panel: first 4^+ state. Bottom panel: first 2^+ state. Calculations are performed with $\hbar\omega = 20$ MeV and $e_{\text{max}} = 4$ using the two-body part of the N^3LO χEFT Hamiltonian evolved to $\lambda_{\text{vsrg}} = 1.88 \text{ fm}^{-1}$.	116
5.9.	Absolute energies of the first 0^+ , 2^+ and 4^+ states in ^{20}Ne computed via PGCM, PGCM-PT(2) and FCI. Calculations are performed with $\hbar\omega = 20$ MeV and $e_{\text{max}} = 4$ as well as with the two-body part of the N^3LO χEFT Hamiltonian evolved to $\lambda_{\text{vsrg}} = 1.88 \text{ fm}^{-1}$.	118
5.10.	(Color online) Absolute binding energy of ^{18}O as a function of the flow parameter s associated with the MR-IMSRG pre-processing of the Hamiltonian. Calculations are performed with $\hbar\omega = 16\text{MeV}$ and $e_{\text{max}} = 6$.	120
5.11.	(Color online) Correlation energy, i.e. difference to the canonical HFB result, in ^{18}O as a function of the flow parameter s associated with the MR-IMSRG pre-processing of the Hamiltonian. Calculations are performed with $\hbar\omega = 16\text{MeV}$ and $e_{\text{max}} = 6$.	121
5.12.	(Color online) $J^\pi = 0^+, 2^+, 4^+$ PHFB TECs in ^{20}Ne as a function of the axial quadrupole deformation β_2 for $s = 0$ (upper panel), $s = 10$ (middle panel) and $s = 20$ (lower panel). Calculations are performed with $\hbar\omega = 20\text{MeV}$ and $e_{\text{max}} = 6$.	123
5.13.	(Color online) Absolute PGCM and PGCM-PT(2) binding energies of ^{20}Ne as a function of the MR-IMSRG flow parameter s . Calculations are performed with $\hbar\omega = 20\text{MeV}$ and $e_{\text{max}} = 6$.	124
5.14.	(Color online) 2^+_1 (bottom row) and 4^+_1 (top row) excitation energies as a function of β_2 for $s = 0$ (left column), $s = 10$ (middle column) and $s = 20$ (right column). Calculations are performed with $\hbar\omega = 20\text{MeV}$ and $e_{\text{max}} = 6$.	125
5.15.	(Color online) Low lying spectrum of ^{20}Ne as a function of the MR-IMSRG flow parameter. Calculations are performed with $\hbar\omega = 20\text{MeV}$ and $e_{\text{max}} = 6$.	126
5.16.	(Color online) Absolute binding energy of ^{20}Ne 0^+ ground state for different order of the theory as a function of the MR-IMSRG flow. Calculations are performed with $\hbar\omega = 20\text{MeV}$ and $e_{\text{max}} = 6$.	127
M.1.	(Color online) Distribution of eigenvalues of \mathbf{N} and \mathbf{M} matrices for ^{20}Ne . The calculation is performed with a two-body χEFT Hamiltonian, $\lambda_{\text{srg}} = 1.88\text{fm}^{-1}$, $\hbar\omega = 20\text{MeV}$ and $e_{\text{max}} = 2$.	174
M.2.	(Color online) PHFB-PT correlation energy of ^{20}Ne obtained for SVD, QR and QLP decompositions as function of the size of the excluded kernel in the decomposition. The calculation is performed with a two-body χEFT Hamiltonian, $\lambda_{\text{srg}} = 1.88\text{fm}^{-1}$, $\hbar\omega = 20\text{MeV}$ and $e_{\text{max}} = 2$.	175

M.3.	(Color online) Correlation energy (top) and respective error (bottom) at each MINRES-QLP iteration for the ground state of ^{20}Ne for various systems and preconditioning techniques. Exact solution is obtained via SVD. The calculation is performed with a two-body χEFT Hamiltonian, $\lambda_{\text{srg}} = 1.88\text{fm}^{-1}$, $\hbar\omega = 20\text{MeV}$ and $e_{\text{max}} = 2$	179
M.4.	(Color online) Correlation energy (top) and respective error (bottom) at each MINRES-QLP iteration for the ground state of ^{18}O for various systems and preconditioning techniques. The exact solution is obtained via SVD. The calculation is performed with a two-body χEFT Hamiltonian, $\lambda_{\text{srg}} = 1.88\text{fm}^{-1}$, $\hbar\omega = 20\text{MeV}$ and $e_{\text{max}} = 2$	180
N.1.	(Color online) Correlation energy (top panel) and corresponding estimated error for different values of the complex shift γ as a function of the number of MINRES-QLP iterations in ^{20}Ne . The calculation is performed with a two-body χEFT Hamiltonian, $\lambda_{\text{srg}} = 1.88\text{fm}^{-1}$, $\hbar\omega = 20\text{MeV}$ and $e_{\text{max}} = 2$	182
N.2.	(Color online) Correlation energy (top panel) and corresponding estimated error for different values of the complex shift γ as a function of the number of MINRES-QLP iterations in ^{18}O . The calculation is performed with a two-body χEFT Hamiltonian, $\lambda_{\text{srg}} = 1.88\text{fm}^{-1}$, $\hbar\omega = 20\text{MeV}$ and $e_{\text{max}} = 2$	183
N.3.	(Color online) Correlation energy in ^{20}Ne for a complex shift $\gamma = 15\text{ MeV}$. Error bars associated to the effect of the shift correspond to the correlation energy with $\gamma = 4\text{ MeV}$. The calculation is performed with a two-body χEFT Hamiltonian, $\lambda_{\text{srg}} = 1.88\text{fm}^{-1}$, $\hbar\omega = 20\text{MeV}$ and $e_{\text{max}} = 2$	184
O.1.	Timing of many-body methods as a function of the basis size of the one body Hilbert space. Projections are performed on J with 24 gauge angles.	186
P.1.	Schematic representation of the structure of the numerical implementation.	190

List of Tables

3.1.	Average difference (in %) between ground-state dHFB energies computed with $H^{2B}[\rho]$ and H for different sub-categories in the test panel and the various test one-body density matrices. The neutron-rich subcategory encompasses ^{30}Ne , ^{40}Mg and ^{48}Ar . See Eq. (3.21a) for the definition of the cost function. Calculations are performed with $e_{\text{max}} = 8$, $e_{3\text{max}} = 12$ and $\lambda_{\text{srg}} = 1.88 \text{ fm}^{-1}$	54
3.2.	Average difference (in %) of ground-state dMBPT(3) energies obtained with $H^{2B}[\rho]$ and within the PNO2B approximation of H for different sub-categories in the test panel and the various test one-body density matrices. The neutron-rich subcategory encompasses ^{30}Ne , ^{40}Mg and ^{48}Ar . See Eq. (3.21c) for details on the cost function. Calculations are performed with $e_{\text{max}} = 8$, $e_{3\text{max}} = 12$ and $\lambda_{\text{srg}} = 1.88 \text{ fm}^{-1}$	58
3.3.	Average error (in %) on absolute PHFB energies of low-lying $J^\pi = 0^+, 2^+, 4^+$ and 6^+ states for different sub-categories in the test panel and the various test one-body density matrices. Calculations are performed with $e_{3\text{max}} = 8$, $e_{3\text{max}} = 12$ and $\lambda_{\text{srg}} = 1.88 \text{ fm}^{-1}$. See Eq. (3.21b) for details on the cost function.	61
3.4.	Average error (in %) on PHFB low-lying excitation energies computed from $H^{2B}[\rho]$ for various sub-categories of nuclei and test one-body density matrices. See Eq. (3.22) for details on the cost function. Calculations are performed with $e_{\text{max}} = 8$, $e_{3\text{max}} = 12$ and $\lambda_{\text{srg}} = 1.88 \text{ fm}^{-1}$	65
3.5.	Average error (in %) on PGCM excitation energies and spectroscopic observables computed from $H^{2B}[\rho]$ in ^{20}Ne and ^{30}Ne for various test one-body density matrices. See Eq. (3.21d) for details on the cost function. Calculations are performed with $e_{\text{max}} = 8$, $e_{3\text{max}} = 10$ and $\lambda_{\text{srg}} = 1.88 \text{ fm}^{-1}$	67
3.6.	Average relative error (in %) on dQRPA excitation energies and on the total photo-emission cross section computed from $H^{2B}[\rho]$ in ^{16}O and ^{20}Ne for various test one-body density matrices. Calculations are performed with $e_{\text{max}} = 8$, $e_{3\text{max}} = 10$ and $\lambda_{\text{srg}} = 1.88 \text{ fm}^{-1}$	70
4.1.	Percentage of variation of selected PGCM results along the Neon isotopic chain for $\lambda_{\text{srg}} \in [1.88, 2.23] \text{ fm}^{-1}$	102
I.1.	Proton and neutron parameters entering the Gaussian expansion (I.2). Taken from Ref. [170]. The resulting mean-square charge radii are also reported.	164
O.1.	Runtime complexity and storage requirements for various resolution methods of the many-body problem. n_{proj} denotes the number of gauge angles used for projections and n_{gcm} the number of states used in the mixing.	185

Bibliography

- [1] N. Ishii, S. Aoki, and T. Hatsuda. “Nuclear Force from Lattice QCD”. In: *Physical Review Letters* 99.2 (2007), p. 022001. ISSN: 0031-9007. DOI: [10.1103/PhysRevLett.99.022001](https://doi.org/10.1103/PhysRevLett.99.022001). URL: <https://link.aps.org/doi/10.1103/PhysRevLett.99.022001>.
- [2] S. Aoki et al. “Lattice quantum chromodynamical approach to nuclear physics”. In: *Progress of Theoretical and Experimental Physics* 2012.1 (2012), 1A105–. ISSN: 2050-3911. DOI: [10.1093/ptep/pts010](https://doi.org/10.1093/ptep/pts010). URL: <https://academic.oup.com/ptep/article-lookup/doi/10.1093/ptep/pts010>.
- [3] U. van Kolck. “Few-Nucleon Systems in a Quirky World”. In: *Few-Body Systems* 56.11-12 (2015), pp. 745–752. ISSN: 0177-7963. DOI: [10.1007/s00601-015-0980-1](https://doi.org/10.1007/s00601-015-0980-1). URL: <http://link.springer.com/10.1007/s00601-015-0980-1>.
- [4] G. Audi et al. “The NUBASE2016 evaluation of nuclear properties”. In: *Chinese Physics C* 41.3 (2017), p. 030001. ISSN: 1674-1137. DOI: [10.1088/1674-1137/41/3/030001](https://doi.org/10.1088/1674-1137/41/3/030001). URL: <http://stacks.iop.org/1674-1137/41/i=3/a=030001?key=crossref.05045a4e9903d0710551e7df47cdd312>.
- [5] G. Royer and C. Gautier. “Coefficients and terms of the liquid drop model and mass formula”. In: *Physical Review C* 73.6 (2006), p. 067302. ISSN: 0556-2813. DOI: [10.1103/PhysRevC.73.067302](https://doi.org/10.1103/PhysRevC.73.067302). URL: <https://link.aps.org/doi/10.1103/PhysRevC.73.067302>.
- [6] Michael Bender, Paul-Henri Heenen, and Paul-Gerhard Reinhard. “Self-consistent mean-field models for nuclear structure”. In: *Reviews of Modern Physics* 75.1 (2003), pp. 121–180. ISSN: 0034-6861. DOI: [10.1103/RevModPhys.75.121](https://doi.org/10.1103/RevModPhys.75.121). URL: <https://link.aps.org/doi/10.1103/RevModPhys.75.121>.
- [7] T. Duguet. “The Nuclear Energy Density Functional Formalism”. In: Springer, Berlin, Heidelberg, 2014, pp. 293–350. DOI: [10.1007/978-3-642-45141-6_7](https://doi.org/10.1007/978-3-642-45141-6_7). URL: http://link.springer.com/10.1007/978-3-642-45141-6_7.
- [8] E. Epelbaum, H.-W. Hammer, and Ulf-G. Meißner. “Modern theory of nuclear forces”. In: *Reviews of Modern Physics* 81.4 (2009), pp. 1773–1825. ISSN: 0034-6861. DOI: [10.1103/RevModPhys.81.1773](https://doi.org/10.1103/RevModPhys.81.1773). URL: <https://link.aps.org/doi/10.1103/RevModPhys.81.1773>.
- [9] H.-W. Hammer, Sebastian König, and U. van Kolck. “Nuclear effective field theory: Status and perspectives”. In: *Rev. Mod. Phys.* 92 (2 June 2020), p. 025004. DOI: [10.1103/RevModPhys.92.025004](https://doi.org/10.1103/RevModPhys.92.025004). URL: <https://link.aps.org/doi/10.1103/RevModPhys.92.025004>.
- [10] R. Machleidt and F. Sammarruca. “Can chiral EFT give us satisfaction?” In: *Eur. Phys. J. A* 56.3 (2020), p. 95. DOI: [10.1140/epja/s10050-020-00101-3](https://doi.org/10.1140/epja/s10050-020-00101-3). arXiv: 2001.05615 [nucl-th].

- [11] J.L. Friar et al. “Triton calculations with the new Nijmegen potentials”. In: *Physics Letters B* 311.1-4 (1993), pp. 4–8. ISSN: 0370-2693. DOI: [10.1016/0370-2693\(93\)90523-K](https://doi.org/10.1016/0370-2693(93)90523-K). URL: <https://www.sciencedirect.com/science/article/abs/pii/S037026939390523K>.
- [12] W. Glöckle and H. Kamada. “Alpha-particle binding energies for realistic nucleon-nucleon interactions”. In: *Physical Review Letters* 71.7 (1993), pp. 971–974. ISSN: 0031-9007. DOI: [10.1103/PhysRevLett.71.971](https://doi.org/10.1103/PhysRevLett.71.971). URL: <https://link.aps.org/doi/10.1103/PhysRevLett.71.971>.
- [13] A. Nogga et al. “Triton binding energies for modern NN forces and the π - π exchange three-nucleon force”. In: *Physics Letters B* 409.1-4 (1997), pp. 19–25. ISSN: 0370-2693. DOI: [10.1016/S0370-2693\(97\)00841-1](https://doi.org/10.1016/S0370-2693(97)00841-1). URL: <https://www.sciencedirect.com/science/article/abs/pii/S0370269397008411>.
- [14] B. S. Pudliner et al. “Quantum Monte Carlo calculations of nuclei with $A < 7$ ”. In: *Physical Review C* 56.4 (1997), pp. 1720–1750. ISSN: 0556-2813. DOI: [10.1103/PhysRevC.56.1720](https://doi.org/10.1103/PhysRevC.56.1720). URL: <https://link.aps.org/doi/10.1103/PhysRevC.56.1720>.
- [15] R.B. Wiringa. “Quantum Monte Carlo calculations for light nuclei”. In: *Nuclear Physics A* 631 (1998), pp. 70–90. ISSN: 0375-9474. DOI: [10.1016/S0375-9474\(98\)00016-5](https://doi.org/10.1016/S0375-9474(98)00016-5). URL: <https://www.sciencedirect.com/science/article/abs/pii/S0375947498000165>.
- [16] R. B. Wiringa et al. “Quantum Monte Carlo calculations of $A = 8$ nuclei”. In: *Physical Review C* 62.1 (2000), p. 014001. ISSN: 0556-2813. DOI: [10.1103/PhysRevC.62.014001](https://doi.org/10.1103/PhysRevC.62.014001). URL: <https://link.aps.org/doi/10.1103/PhysRevC.62.014001>.
- [17] P. Navrátil and B. R. Barrett. “Shell-model calculations for the three-nucleon system”. In: *Physical Review C* 57.2 (1998), pp. 562–568. ISSN: 0556-2813. DOI: [10.1103/PhysRevC.57.562](https://doi.org/10.1103/PhysRevC.57.562). URL: <https://link.aps.org/doi/10.1103/PhysRevC.57.562>.
- [18] P. Navrátil and B. R. Barrett. “Large-basis shell-model calculations for p -shell nuclei”. In: *Physical Review C* 57.6 (1998), pp. 3119–3128. ISSN: 0556-2813. DOI: [10.1103/PhysRevC.57.3119](https://doi.org/10.1103/PhysRevC.57.3119). URL: <https://link.aps.org/doi/10.1103/PhysRevC.57.3119>.
- [19] P. Navrátil, G. P. Kamuntavičius, and B. R. Barrett. “Few-nucleon systems in a translationally invariant harmonic oscillator basis”. In: *Physical Review C* 61.4 (2000), p. 044001. ISSN: 0556-2813. DOI: [10.1103/PhysRevC.61.044001](https://doi.org/10.1103/PhysRevC.61.044001). URL: <https://link.aps.org/doi/10.1103/PhysRevC.61.044001>.
- [20] S. Quaglioni and P. Navrátil. “Ab initio no-core shell model and microscopic reactions: Recent achievements”. In: *Few-Body Systems* 44.1-4 (2008), pp. 337–339. ISSN: 0177-7963. DOI: [10.1007/s00601-008-0322-7](https://doi.org/10.1007/s00601-008-0322-7). URL: <http://link.springer.com/10.1007/s00601-008-0322-7>.
- [21] Petr Navrátil et al. “Recent developments in no-core shell-model calculations”. In: *Journal of Physics G: Nuclear and Particle Physics* 36.8 (2009), p. 083101. ISSN: 0954-3899. DOI: [10.1088/0954-3899/36/8/083101](https://doi.org/10.1088/0954-3899/36/8/083101). URL: <http://stacks.iop.org/0954-3899/36/i=8/a=083101?key=crossref.6a3adac3ac4b1686ba805c2214de955f>.

- [22] S. K. Bogner, R. J. Furnstahl, and A. Schwenk. “From low-momentum interactions to nuclear structure”. In: *Prog. Part. Nucl. Phys.* 65 (2010), pp. 94–147. DOI: [10.1016/j.pnpnp.2010.03.001](https://doi.org/10.1016/j.pnpnp.2010.03.001).
- [23] Jeffrey Goldstone. “Derivation of the Brueckner many-body theory”. In: *Proceedings of the Royal Society of London. Series A. Mathematical and Physical Sciences* 239.1217 (1957), pp. 267–279. DOI: [10.1098/rspa.1957.0037](https://doi.org/10.1098/rspa.1957.0037). URL: <http://www.royalsocietypublishing.org/doi/10.1098/rspa.1957.0037>.
- [24] N.M. Hugenholtz. “Perturbation theory of large quantum systems”. In: *Physica* 23.1-5 (1957), pp. 481–532. ISSN: 0031-8914. DOI: [10.1016/S0031-8914\(57\)92950-6](https://doi.org/10.1016/S0031-8914(57)92950-6). URL: <https://www.sciencedirect.com/science/article/pii/S0031891457929506>.
- [25] Isaiah Shavitt and Rodney J. Bartlett. *Many-body methods in chemistry and physics : MBPT and coupled-cluster theory*. Cambridge University Press, 2009, p. 532. ISBN: 052181832X. URL: <https://books.google.fr/books?hl=fr%7B%5C%7Dlr=%7B%5C%7Ddid=SWw6ac1NHZYC%7B%5C%7Ddoi=fnd%7B%5C%7Dpg=PR1%7B%5C%7Ddq=Many+body+methods+in+chemistry+and+physics%7B%5C%7Ddots=qZTjEc5JQw%7B%5C%7Dsig=fCTgkJ%7B%5C%7DXj84m2KYY1CXC0Xx5G5E%7B%5C%7Dv=onepage%7B%5C%7Dq=Many%20body%20methods%20in%20chemistry%20and%20physics%7B%5C%7Ddf=false>.
- [26] Alexander Tichai et al. “Hartree–Fock many-body perturbation theory for nuclear ground-states”. In: *Physics Letters B* 756 (2016), pp. 283–288. ISSN: 0370-2693. DOI: [10.1016/J.PHYSLETB.2016.03.029](https://doi.org/10.1016/J.PHYSLETB.2016.03.029). URL: <https://www.sciencedirect.com/science/article/pii/S0370269316002008>.
- [27] B. S. Hu et al. “Ab initio nuclear many-body perturbation calculations in the Hartree-Fock basis”. In: *Physical Review C* 94.1 (2016), p. 014303. ISSN: 2469-9985. DOI: [10.1103/PhysRevC.94.014303](https://doi.org/10.1103/PhysRevC.94.014303). URL: <https://link.aps.org/doi/10.1103/PhysRevC.94.014303>.
- [28] Alexander Tichai et al. “Open-shell nuclei from No-Core Shell Model with perturbative improvement”. In: *Physics Letters B* 786 (2018), pp. 448–452. ISSN: 0370-2693. DOI: [10.1016/J.PHYSLETB.2018.10.029](https://doi.org/10.1016/J.PHYSLETB.2018.10.029). URL: <https://www.sciencedirect.com/science/article/pii/S0370269318307986>.
- [29] K. Kowalski et al. “Coupled Cluster Calculations of Ground and Excited States of Nuclei”. In: *Physical Review Letters* 92.13 (2004), p. 132501. ISSN: 0031-9007. DOI: [10.1103/PhysRevLett.92.132501](https://doi.org/10.1103/PhysRevLett.92.132501). URL: <https://link.aps.org/doi/10.1103/PhysRevLett.92.132501>.
- [30] Rodney J. Bartlett and Monika Musiał. “Coupled-cluster theory in quantum chemistry”. In: *Reviews of Modern Physics* 79.1 (2007), pp. 291–352. ISSN: 0034-6861. DOI: [10.1103/RevModPhys.79.291](https://doi.org/10.1103/RevModPhys.79.291). URL: <https://link.aps.org/doi/10.1103/RevModPhys.79.291>.
- [31] G. Hagen et al. “<i>Ab initio</i> coupled-cluster approach to nuclear structure with modern nucleon-nucleon interactions”. In: *Physical Review C* 82.3 (2010), p. 034330. ISSN: 0556-2813. DOI: [10.1103/PhysRevC.82.034330](https://doi.org/10.1103/PhysRevC.82.034330). URL: <https://link.aps.org/doi/10.1103/PhysRevC.82.034330>.

- [32] Piotr Piecuch, Jeffrey R. Gour, and Marta Włoch. “Left-eigenstate completely renormalized equation-of-motion coupled-cluster methods: Review of key concepts, extension to excited states of open-shell systems, and comparison with electron-attached and ionized approaches”. In: *International Journal of Quantum Chemistry* 109.14 (2009), pp. 3268–3304. ISSN: 00207608. DOI: [10.1002/qua.22367](https://doi.org/10.1002/qua.22367). URL: <http://doi.wiley.com/10.1002/qua.22367>.
- [33] Sven Binder et al. “Extension of coupled-cluster theory with a noniterative treatment of connected triply excited clusters to three-body Hamiltonians”. In: *Physical Review C* 88.5 (2013), p. 054319. ISSN: 0556-2813. DOI: [10.1103/PhysRevC.88.054319](https://doi.org/10.1103/PhysRevC.88.054319). URL: <https://link.aps.org/doi/10.1103/PhysRevC.88.054319>.
- [34] K. Tsukiyama, S. K. Bogner, and A. Schwenk. “In-Medium Similarity Renormalization Group For Nuclei”. In: *Physical Review Letters* 106.22 (2011), p. 222502. ISSN: 0031-9007. DOI: [10.1103/PhysRevLett.106.222502](https://doi.org/10.1103/PhysRevLett.106.222502). URL: <https://link.aps.org/doi/10.1103/PhysRevLett.106.222502>.
- [35] H. Hergert et al. “In-medium similarity renormalization group with chiral two- plus three-nucleon interactions”. In: *Physical Review C* 87.3 (2013), p. 034307. ISSN: 0556-2813. DOI: [10.1103/PhysRevC.87.034307](https://doi.org/10.1103/PhysRevC.87.034307). URL: <https://link.aps.org/doi/10.1103/PhysRevC.87.034307>.
- [36] T. D. Morris, N. M. Parzuchowski, and S. K. Bogner. “Magnus expansion and in-medium similarity renormalization group”. In: *Physical Review C* 92.3 (2015), p. 034331. ISSN: 0556-2813. DOI: [10.1103/PhysRevC.92.034331](https://doi.org/10.1103/PhysRevC.92.034331). URL: <https://link.aps.org/doi/10.1103/PhysRevC.92.034331>.
- [37] H. Hergert et al. “The In-Medium Similarity Renormalization Group: A novel ab initio method for nuclei”. In: *Physics Reports* 621 (2016), pp. 165–222. ISSN: 0370-1573. DOI: [10.1016/J.PHYSREP.2015.12.007](https://doi.org/10.1016/J.PHYSREP.2015.12.007). URL: <https://www.sciencedirect.com/science/article/abs/pii/S0370157315005414>.
- [38] W.H. Dickhoff and C. Barbieri. “Self-consistent Green’s function method for nuclei and nuclear matter”. In: *Progress in Particle and Nuclear Physics* 52.2 (2004), pp. 377–496. ISSN: 0146-6410. DOI: [10.1016/J.PPNP.2004.02.038](https://doi.org/10.1016/J.PPNP.2004.02.038). URL: <https://www.sciencedirect.com/science/article/pii/S0146641004000535>.
- [39] A. Cipollone, C. Barbieri, and P. Navrátil. “Chiral three-nucleon forces and the evolution of correlations along the oxygen isotopic chain”. In: *Physical Review C* 92.1 (2015), p. 014306. ISSN: 0556-2813. DOI: [10.1103/PhysRevC.92.014306](https://doi.org/10.1103/PhysRevC.92.014306). URL: <https://link.aps.org/doi/10.1103/PhysRevC.92.014306>.
- [40] Arianna Carbone et al. “Self-consistent Green’s functions formalism with three-body interactions”. In: *Physical Review C* 88.5 (2013), p. 054326. ISSN: 0556-2813. DOI: [10.1103/PhysRevC.88.054326](https://doi.org/10.1103/PhysRevC.88.054326). URL: <https://link.aps.org/doi/10.1103/PhysRevC.88.054326>.
- [41] H. Hergert. “A Guided Tour of *ab initio* Nuclear Many-Body Theory”. In: *Front. in Phys.* 8 (2020), p. 379. DOI: [10.3389/fphy.2020.00379](https://doi.org/10.3389/fphy.2020.00379). arXiv: [2008.05061](https://arxiv.org/abs/2008.05061) [nucl-th].
- [42] T. Miyagi et al. *Converged ab initio calculations of heavy nuclei*. 2021. arXiv: [2104.04688](https://arxiv.org/abs/2104.04688) [nucl-th].
- [43] Peter Ring and Peter Schuck. *The nuclear many-body problem*. Springer-Verlag, 1980, p. 716. ISBN: 9783540212065.

- [44] Pierre Arthuis. “Bogoliubov Many-Body Perturbation Theory for Nuclei : Systematic Generation and Evaluation of Diagrams and First ab initio Calculations”. 2018. URL: <https://www.theses.fr/2018SACLS304>.
- [45] P. Arthuis et al. “ADG: Automated generation and evaluation of many-body diagrams I. Bogoliubov many-body perturbation theory”. In: *Computer Physics Communications* (2018). ISSN: 0010-4655. DOI: [10.1016/J.CPC.2018.11.023](https://doi.org/10.1016/J.CPC.2018.11.023). URL: <https://www.sciencedirect.com/science/article/pii/S0010465518304156>.
- [46] A. Tichai et al. “Bogoliubov many-body perturbation theory for open-shell nuclei”. In: *Physics Letters B* 786 (2018), pp. 195–200. ISSN: 0370-2693. DOI: [10.1016/J.PHYSLETB.2018.09.044](https://doi.org/10.1016/J.PHYSLETB.2018.09.044). URL: <https://www.sciencedirect.com/science/article/pii/S0370269318307457>.
- [47] P. Demol et al. “Bogoliubov many-body perturbation theory under constraint”. In: *Annals Phys.* 424 (2021), p. 168358. DOI: [10.1016/j.aop.2020.168358](https://doi.org/10.1016/j.aop.2020.168358).
- [48] V. Somà, T. Duguet, and C. Barbieri. “Ab initio self-consistent Gorkov-Green’s function calculations of semimagic nuclei: Formalism at second order with a two-nucleon interaction”. In: *Physical Review C* 84.6 (2011), p. 064317. ISSN: 0556-2813. DOI: [10.1103/PhysRevC.84.064317](https://doi.org/10.1103/PhysRevC.84.064317). URL: <https://link.aps.org/doi/10.1103/PhysRevC.84.064317>.
- [49] V. Somà, C. Barbieri, and T. Duguet. “Ab initio Gorkov-Green’s function calculations of open-shell nuclei”. In: *Physical Review C* 87.1 (2013), p. 011303. ISSN: 0556-2813. DOI: [10.1103/PhysRevC.87.011303](https://doi.org/10.1103/PhysRevC.87.011303). URL: <https://link.aps.org/doi/10.1103/PhysRevC.87.011303>.
- [50] V. Somà et al. “Chiral two- and three-nucleon forces along medium-mass isotope chains”. In: *Physical Review C* 89.6 (2014), p. 061301. ISSN: 0556-2813. DOI: [10.1103/PhysRevC.89.061301](https://doi.org/10.1103/PhysRevC.89.061301). URL: <https://link.aps.org/doi/10.1103/PhysRevC.89.061301>.
- [51] A. Signoracci et al. “Ab initio Bogoliubov coupled cluster theory for open-shell nuclei”. In: *Physical Review C* 91.6 (2015), p. 064320. DOI: [10.1103/PhysRevC.91.064320](https://doi.org/10.1103/PhysRevC.91.064320). URL: <https://journals.aps.org/prc/abstract/10.1103/PhysRevC.91.064320>.
- [52] S. J. Novario et al. “Charge radii of exotic neon and magnesium isotopes”. In: *Physical Review C* 102.5 (2020). ISSN: 2469-9993. DOI: [10.1103/physrevc.102.051303](https://doi.org/10.1103/physrevc.102.051303). URL: <http://dx.doi.org/10.1103/PhysRevC.102.051303>.
- [53] Thomas Duguet and A Signoracci. “Symmetry broken and restored coupled-cluster. Global gauge symmetry and particle number”. In: *Journal of Physics G, Nuclear and Particle Physics* 44.1 (2016). ISSN: 0954-3899. DOI: [10.1088/0954-3899/44/1/015103](https://doi.org/10.1088/0954-3899/44/1/015103). URL: <https://lirias.kuleuven.be/290803?limo=0>.
- [54] Julien Ripoché. “Projected Bogoliubov Many-Body Perturbation Theory : Overcoming formal and technical challenges”. 2019SACLS325. PhD thesis. 2019. URL: <http://www.theses.fr/2019SACLS325/document>.
- [55] Yiheng Qiu et al. “Projected coupled cluster theory”. In: *The Journal of Chemical Physics* 147.6 (2017), p. 064111. ISSN: 0021-9606. DOI: [10.1063/1.4991020](https://doi.org/10.1063/1.4991020). URL: <http://aip.scitation.org/doi/10.1063/1.4991020>.

- [56] Y. Qiu et al. “Particle-number projected Bogoliubov-coupled-cluster theory: Application to the pairing Hamiltonian”. In: *Physical Review C* 99.4 (2019), p. 044301. ISSN: 2469-9985. DOI: [10.1103/PhysRevC.99.044301](https://doi.org/10.1103/PhysRevC.99.044301). URL: <https://link.aps.org/doi/10.1103/PhysRevC.99.044301>.
- [57] H. Hergert et al. “Ab initio multireference in-medium similarity renormalization group calculations of even calcium and nickel isotopes”. In: *Physical Review C* 90.4 (2014), p. 041302. ISSN: 0556-2813. DOI: [10.1103/PhysRevC.90.041302](https://doi.org/10.1103/PhysRevC.90.041302). URL: <https://link.aps.org/doi/10.1103/PhysRevC.90.041302>.
- [58] Takashi Tsuchimochi and Seiichiro L. Ten-no. “Second-Order Perturbation Theory with Spin-Symmetry-Projected Hartree-Fock”. In: *Journal of Chemical Theory and Computation* 15.12 (2019). PMID: 31661264, pp. 6688–6702. DOI: [10.1021/acs.jctc.9b00897](https://doi.org/10.1021/acs.jctc.9b00897). eprint: <https://doi.org/10.1021/acs.jctc.9b00897>. URL: <https://doi.org/10.1021/acs.jctc.9b00897>.
- [59] Hugh G. A. Burton and Alex J. W. Thom. “Reaching Full Correlation through Nonorthogonal Configuration Interaction: A Second-Order Perturbative Approach”. In: *Journal of Chemical Theory and Computation* 16.9 (2020), pp. 5586–5600. ISSN: 1549-9626. DOI: [10.1021/acs.jctc.0c00468](https://doi.org/10.1021/acs.jctc.0c00468). URL: <http://dx.doi.org/10.1021/acs.jctc.0c00468>.
- [60] Alexander Tichai, Robert Roth, and Thomas Duguet. “Many-Body Perturbation Theories for Finite Nuclei”. In: *Front. Phys.* 8 (2020), p. 164. DOI: [10.3389/fphy.2020.00164](https://doi.org/10.3389/fphy.2020.00164).
- [61] J. Ripoche, A. Tichai, and T. Duguet. “Normal-ordered k-body approximation in particle-number-breaking theories”. In: *The European Physical Journal A* 56.2 (2020). ISSN: 1434-601X. DOI: [10.1140/epja/s10050-020-00045-8](https://doi.org/10.1140/epja/s10050-020-00045-8). URL: <http://dx.doi.org/10.1140/epja/s10050-020-00045-8>.
- [62] I. Mayer. *Simple Theorems, Proofs, and Derivations in Quantum Chemistry*. Springer Science, 2003. DOI: [ISBN978-1-4419-3389-8](https://doi.org/10.1007/978-1-4419-3389-8).
- [63] G. F. Bertsch and L. M. Robledo. “Symmetry Restoration in Hartree-Fock-Bogoliubov Based Theories”. In: *Phys. Rev. Lett.* 108 (4 2012), p. 042505. DOI: [10.1103/PhysRevLett.108.042505](https://doi.org/10.1103/PhysRevLett.108.042505). URL: <https://link.aps.org/doi/10.1103/PhysRevLett.108.042505>.
- [64] B. Bally and T. Duguet. “Norm overlap between many-body states: Uncorrelated overlap between arbitrary Bogoliubov product states”. In: *Physical Review C* 97.2 (2018), p. 024304. ISSN: 2469-9985. DOI: [10.1103/PhysRevC.97.024304](https://doi.org/10.1103/PhysRevC.97.024304). URL: <https://link.aps.org/doi/10.1103/PhysRevC.97.024304>.
- [65] H. G. A. Burton and A. J. W. Thom. In: *J. Chem. Theory Comput.* 16.4 (2020), p. 5586.
- [66] Thomas M. Henderson et al. “Quasiparticle coupled cluster theory for pairing interactions”. In: *Physical Review C* 89.5 (2014), p. 054305. ISSN: 0556-2813. DOI: [10.1103/PhysRevC.89.054305](https://doi.org/10.1103/PhysRevC.89.054305). URL: <https://link.aps.org/doi/10.1103/PhysRevC.89.054305>.
- [67] V. Somà et al. “Moving away from singly-magic nuclei with Gorkov Green’s function theory”. In: *Eur. Phys. J. A* 57.4 (2021), p. 135. DOI: [10.1140/epja/s10050-021-00437-4](https://doi.org/10.1140/epja/s10050-021-00437-4). arXiv: 2009.01829 [nucl-th].

- [68] A. Tichai et al. “ADG: Automated generation and evaluation of many-body diagrams III. Bogoliubov in-medium similarity renormalization group formalism”. In: (2021). arXiv: [2102.10889 \[nucl-th\]](#).
- [69] T Duguet. “Symmetry broken and restored coupled-cluster theory: I. Rotational symmetry and angular momentum”. In: *Journal of Physics G: Nuclear and Particle Physics* 42.2 (2015), p. 025107. ISSN: 0954-3899. DOI: [10.1088/0954-3899/42/2/025107](#). URL: <http://stacks.iop.org/0954-3899/42/i=2/a=025107?key=crossref.a2cb33fa61e89b318f16fbb49b5cd7aa>.
- [70] P. Arthuis et al. “ADG : Automated generation and evaluation of many-body diagrams II. Particle-number projected Bogoliubov many-body perturbation theory”. In: *Comput. Phys. Commun.* 261 (2021), p. 107677. DOI: [10.1016/j.cpc.2020.107677](#). arXiv: [2007.01661 \[nucl-th\]](#).
- [71] R. Peierls. In: *Proc. R. Soc. Lond.* A333 (1973), p. 157.
- [72] B. Atalay, A. Mann, and R. Peierls. In: *Proc. R. Soc. Lond.* A335 (1973), p. 251.
- [73] B. I. Atalay, D. M. Brink, and A. Mann. In: *Nucl. Phys.* A218 (1974), p. 461.
- [74] B.I. Atalay and A. Mann. In: *Nucl. Phys.* A238 (1975), p. 70.
- [75] B.I. Atalay, A. Mann, and A. Zelicoff. In: *Nucl. Phys.* A295 (1978), p. 204.
- [76] H. B. Schlegel. “Potential energy curves using unrestricsted Moller Plesset perturbation theory with spin annihilation”. In: *J. Chem. Phys.* 84 (1986), p. 4530.
- [77] H. B. Schlegel. “Moller Plesset perturbation theory with spin annihilation”. In: *J. Phys. Chem.* 92 (1988), p. 3075.
- [78] P. J. Knowles and N. C. Hardy. “Projected unrestricted Moller-Plesset second order energies”. In: *J. Chem. Phys.* 88 (1988), p. 6991.
- [79] P.-O. Lowdin. In: *Phys. Rev.* 97 (1955), p. 1509.
- [80] Z. H. Sun et al. Unpublished. 2021.
- [81] M. Baranger. In: *Nucl. Phys. A* 149 (1970), p. 225.
- [82] T. Duguet et al. “Nonobservable nature of the nuclear shell structure: Meaning, illustrations, and consequences”. In: *Phys. Rev. C* 92.3 (2015), p. 034313. DOI: [10.1103/PhysRevC.92.034313](#). arXiv: [1411.1237 \[nucl-th\]](#).
- [83] T. Duguet et al. “Pairing correlations. I. Description of odd nuclei in mean-field theories”. In: *Phys. Rev. C* 65 (1 2001), p. 014310. DOI: [10.1103/PhysRevC.65.014310](#). URL: <https://link.aps.org/doi/10.1103/PhysRevC.65.014310>.
- [84] S. Perez-Martin and L. M. Robledo. “Microscopic justification of the equal filling approximation”. In: *Phys. Rev. C* 78 (1 2008), p. 014304. DOI: [10.1103/PhysRevC.78.014304](#). URL: <https://link.aps.org/doi/10.1103/PhysRevC.78.014304>.
- [85] Hugh G. A. Burton. “Generalized nonorthogonal matrix elements: Unifying Wick’s theorem and the Slater–Condon rules”. In: *The Journal of Chemical Physics* 154.14 (2021), p. 144109. DOI: [10.1063/5.0045442](#). eprint: <https://doi.org/10.1063/5.0045442>. URL: <https://doi.org/10.1063/5.0045442>.
- [86] B. O. Roos and K. Andersson. In: *Chem. Phys. Lett.* 245 (1995), p. 215.
- [87] N. Forsberg and P.-A. Malmqvist. In: *Chem. Phys. Lett.* 274 (1997), p. 196.

- [88] Robert Roth et al. “Medium-Mass Nuclei with Normal-Ordered Chiral $NN + 3N$ Interactions”. In: *Physical Review Letters* 109.5 (2012), p. 052501. ISSN: 0031-9007. DOI: [10.1103/PhysRevLett.109.052501](https://doi.org/10.1103/PhysRevLett.109.052501). URL: <https://link.aps.org/doi/10.1103/PhysRevLett.109.052501>.
- [89] Eskendr Gebrerufael, Angelo Calci, and Robert Roth. “Open-shell nuclei and excited states from multireference normal-ordered Hamiltonians”. In: *Physical Review C* 93.3 (2016), p. 031301. ISSN: 2469-9985. DOI: [10.1103/PhysRevC.93.031301](https://doi.org/10.1103/PhysRevC.93.031301). URL: <https://link.aps.org/doi/10.1103/PhysRevC.93.031301>.
- [90] A. Dyhdalo, S. K. Bogner, and R. J. Furnstahl. “Estimates and power counting in uniform nuclear matter with softened interactions”. In: *Phys. Rev. C* 96.5 (2017), p. 054005. DOI: [10.1103/PhysRevC.96.054005](https://doi.org/10.1103/PhysRevC.96.054005).
- [91] G. C. Wick. “The Evaluation of the Collision Matrix”. In: *Physical Review* 80.2 (1950), pp. 268–272. ISSN: 0031-899X. DOI: [10.1103/PhysRev.80.268](https://doi.org/10.1103/PhysRev.80.268). URL: <https://link.aps.org/doi/10.1103/PhysRev.80.268>.
- [92] S. J. Novario et al. “Charge radii of exotic neon and magnesium isotopes”. In: *Phys. Rev. C* 102 (5 2020), p. 051303. DOI: [10.1103/PhysRevC.102.051303](https://doi.org/10.1103/PhysRevC.102.051303). URL: <https://link.aps.org/doi/10.1103/PhysRevC.102.051303>.
- [93] J.M. Yao et al. “Ab Initio Treatment of Collective Correlations and the Neutrinoless Double Beta Decay of ^{48}Ca ”. In: *Phys. Rev. Lett.* 124.23 (2020), p. 232501. DOI: [10.1103/PhysRevLett.124.232501](https://doi.org/10.1103/PhysRevLett.124.232501).
- [94] Werner Kutzelnigg and Debashis Mukherjee. “Normal order and extended Wick theorem for a multiconfiguration reference wave function”. In: *The Journal of Chemical Physics* 107.2 (1997), pp. 432–449. ISSN: 0021-9606. DOI: [10.1063/1.474405](https://doi.org/10.1063/1.474405). URL: <http://aip.scitation.org/doi/10.1063/1.474405>.
- [95] S. R. Stroberg et al. “Nucleus-Dependent Valence-Space Approach to Nuclear Structure”. In: *Physical Review Letters* 118.3 (2017), p. 032502. ISSN: 0031-9007. DOI: [10.1103/PhysRevLett.118.032502](https://doi.org/10.1103/PhysRevLett.118.032502). URL: <https://link.aps.org/doi/10.1103/PhysRevLett.118.032502>.
- [96] Liguo Kong, Marcel Nooijen, and Debashis Mukherjee. “An algebraic proof of generalized Wick theorem”. In: *The Journal of Chemical Physics* 132.23 (2010), p. 234107. ISSN: 0021-9606. DOI: [10.1063/1.3439395](https://doi.org/10.1063/1.3439395). URL: <http://aip.scitation.org/doi/10.1063/1.3439395>.
- [97] B. Bally and M. Bender. “Projection on particle number and angular momentum: Example of triaxial Bogoliubov quasiparticle states”. In: *Phys. Rev. C* 103 (2 2021), p. 024315. DOI: [10.1103/PhysRevC.103.024315](https://doi.org/10.1103/PhysRevC.103.024315). URL: <https://link.aps.org/doi/10.1103/PhysRevC.103.024315>.
- [98] Takashi Nakatsukasa, Tsunenori Inakura, and Kazuhiro Yabana. “Finite amplitude method for the solution of the random-phase approximation”. In: *Phys. Rev. C* 76 (2 2007), p. 024318. DOI: [10.1103/PhysRevC.76.024318](https://doi.org/10.1103/PhysRevC.76.024318). URL: <https://link.aps.org/doi/10.1103/PhysRevC.76.024318>.
- [99] Y. Beaujeault-Taudière et al. Unpublished. 2021.
- [100] M. Frosini et al. “In-medium k -body reduction of n -body operators: A flexible symmetry-conserving approach based on the sole one-body density matrix”. In: *Eur. Phys. J. A* 57.4 (2021), p. 151. DOI: [10.1140/epja/s10050-021-00458-z](https://doi.org/10.1140/epja/s10050-021-00458-z). arXiv: [2102.10120](https://arxiv.org/abs/2102.10120) [nucl-th].

- [101] B. Jancovici and D. H. Schiff. In: *Nucl. Phys.* 58 (1964), p. 678.
- [102] E. Khan et al. “Two-neutron transfer in nuclei close to the drip line”. In: *Phys. Rev. C* 69 (1 2004), p. 014314. DOI: [10.1103/PhysRevC.69.014314](https://link.aps.org/doi/10.1103/PhysRevC.69.014314). URL: <https://link.aps.org/doi/10.1103/PhysRevC.69.014314>.
- [103] B. Avez, C. Simenel, and Ph. Chomaz. “Pairing vibrations study with the time-dependent Hartree-Fock-Bogoliubov theory”. In: *Phys. Rev. C* 78 (4 2008), p. 044318. DOI: [10.1103/PhysRevC.78.044318](https://link.aps.org/doi/10.1103/PhysRevC.78.044318). URL: <https://link.aps.org/doi/10.1103/PhysRevC.78.044318>.
- [104] J.M. Yao et al. “Generator-coordinate reference states for spectra and $0\nu\beta\beta$ decay in the in-medium similarity renormalization group”. In: *Phys. Rev. C* 98.5 (2018), p. 054311. DOI: [10.1103/PhysRevC.98.054311](https://link.aps.org/doi/10.1103/PhysRevC.98.054311).
- [105] T. Duguet, B. Bally, and A. Tichai. “Zero-pairing limit of Hartree-Fock-Bogoliubov reference states”. In: *Phys. Rev. C* 102.5 (2020), p. 054320. DOI: [10.1103/PhysRevC.102.054320](https://link.aps.org/doi/10.1103/PhysRevC.102.054320). arXiv: [2006.02871](https://arxiv.org/abs/2006.02871) [nucl-th].
- [106] M. R. Strayer, W. H. Bassichis, and A. K. Kerman. “Correlation Effects in Nuclear Densities”. In: *Physical Review C* 8.4 (1973), pp. 1269–1274. ISSN: 0556-2813. DOI: [10.1103/PhysRevC.8.1269](https://link.aps.org/doi/10.1103/PhysRevC.8.1269). URL: <https://link.aps.org/doi/10.1103/PhysRevC.8.1269>.
- [107] J. Hoppe et al. “Natural orbitals for many-body expansion methods”. In: *Phys. Rev. C* 103.1 (2021), p. 014321. DOI: [10.1103/PhysRevC.103.014321](https://link.aps.org/doi/10.1103/PhysRevC.103.014321).
- [108] D. R. Entem and R. Machleidt. “Accurate charge-dependent nucleon-nucleon potential at fourth order of chiral perturbation theory”. In: *Physical Review C* 68.4 (2003), p. 041001. ISSN: 0556-2813. DOI: [10.1103/PhysRevC.68.041001](https://link.aps.org/doi/10.1103/PhysRevC.68.041001). URL: <https://link.aps.org/doi/10.1103/PhysRevC.68.041001>.
- [109] R. Machleidt and D. R. Entem. “Chiral effective field theory and nuclear forces”. In: *Physics Reports* 503.1 (2011), pp. 1–75. ISSN: 0370-1573. DOI: <https://doi.org/10.1016/j.physrep.2011.02.001>. URL: <http://www.sciencedirect.com/science/article/pii/S0370157311000457>.
- [110] P. Navrátil. “Local three-nucleon interaction from chiral effective field theory”. In: *Few-Body Systems* 41.3 (2007), pp. 117–140. ISSN: 1432-5411. DOI: [10.1007/s00601-007-0193-3](https://doi.org/10.1007/s00601-007-0193-3). URL: <http://dx.doi.org/10.1007/s00601-007-0193-3>.
- [111] Robert Roth et al. “Similarity-Transformed Chiral $NN + 3N$ Interactions for the Ab Initio Description of ^{12}C and ^{16}O ”. In: *Phys. Rev. Lett.* 107 (7 2011), p. 072501. DOI: [10.1103/PhysRevLett.107.072501](https://link.aps.org/doi/10.1103/PhysRevLett.107.072501). URL: <https://link.aps.org/doi/10.1103/PhysRevLett.107.072501>.
- [112] Robert Roth et al. “Evolved chiral $NN + 3N$ Hamiltonians for ab initio nuclear structure calculations”. In: *Phys. Rev. C* 90 (2 2014), p. 024325. DOI: [10.1103/PhysRevC.90.024325](https://link.aps.org/doi/10.1103/PhysRevC.90.024325). URL: <https://link.aps.org/doi/10.1103/PhysRevC.90.024325>.
- [113] V. Somà et al. “Novel chiral Hamiltonian and observables in light and medium-mass nuclei”. In: *Phys. Rev. C* 101.1 (2020), p. 014318. DOI: [10.1103/PhysRevC.101.014318](https://link.aps.org/doi/10.1103/PhysRevC.101.014318).
- [114] D. Rozpedzik et al. “A First estimation of chiral four-nucleon force effects in He-4 ”. In: *Acta Phys. Polon. B* 37 (2006), pp. 2889–2904.

- [115] T. Krüger et al. “Neutron matter from chiral effective field theory interactions”. In: *Phys. Rev. C* 88 (2013), p. 025802. DOI: [10.1103/PhysRevC.88.025802](https://doi.org/10.1103/PhysRevC.88.025802).
- [116] N. Kaiser and R. Milkus. “Reducible chiral four-body interactions in nuclear matter”. In: *Eur. Phys. J. A* 52.1 (2016), p. 4. DOI: [10.1140/epja/i2016-16004-7](https://doi.org/10.1140/epja/i2016-16004-7).
- [117] Hermann Krebs. “Nuclear Currents in Chiral Effective Field Theory”. In: *Eur. Phys. J. A* 56.9 (2020), p. 234. DOI: [10.1140/epja/s10050-020-00230-9](https://doi.org/10.1140/epja/s10050-020-00230-9).
- [118] T. Niksic, D. Vretenar, and P. Ring. “Relativistic Nuclear Energy Density Functionals: Mean-Field and Beyond”. In: *Prog. Part. Nucl. Phys.* 66 (2011), pp. 519–548. DOI: [10.1016/j.ppnp.2011.01.055](https://doi.org/10.1016/j.ppnp.2011.01.055). arXiv: [1102.4193](https://arxiv.org/abs/1102.4193) [nucl-th].
- [119] L. M. Robledo, T. R. Rodríguez, and R. R. Rodríguez-Guzmán. “Mean field and beyond description of nuclear structure with the Gogny force: A review”. In: *J. Phys. G* 46.1 (2019), p. 013001. DOI: [10.1088/1361-6471/aadebd](https://doi.org/10.1088/1361-6471/aadebd). arXiv: [1807.02518](https://arxiv.org/abs/1807.02518) [nucl-th].
- [120] J. Dobaczewski et al. “Particle-Number Projection and the Density Functional Theory”. In: *Phys. Rev. C* 76 (2007), p. 054315. DOI: [10.1103/PhysRevC.76.054315](https://doi.org/10.1103/PhysRevC.76.054315). arXiv: [0708.0441](https://arxiv.org/abs/0708.0441) [nucl-th].
- [121] T. Duguet et al. “Particle-Number Restoration within the Energy Density Functional formalism: Are terms depending on non-integer powers of the density matrices viable?” In: *Phys. Rev. C* 79 (2009), p. 044320. DOI: [10.1103/PhysRevC.79.044320](https://doi.org/10.1103/PhysRevC.79.044320). arXiv: [0809.2049](https://arxiv.org/abs/0809.2049) [nucl-th].
- [122] M. Bender, T. Duguet, and D. Lacroix. “Particle-number restoration within the energy density functional formalism”. In: *Physical Review C* 79.4 (2009), p. 044319. ISSN: 0556-2813. DOI: [10.1103/PhysRevC.79.044319](https://doi.org/10.1103/PhysRevC.79.044319). URL: <https://link.aps.org/doi/10.1103/PhysRevC.79.044319>.
- [123] D. Lacroix, T. Duguet, and M. Bender. “Configuration mixing within the energy density functional formalism: Removing spurious contributions from nondiagonal energy kernels”. In: *Physical Review C* 79.4 (2009), p. 044318. ISSN: 0556-2813. DOI: [10.1103/PhysRevC.79.044318](https://doi.org/10.1103/PhysRevC.79.044318). URL: <https://link.aps.org/doi/10.1103/PhysRevC.79.044318>.
- [124] Zao-Chun Gao, Mihai Horoi, and Y. S. Chen. “Variation after projection with a triaxially deformed nuclear mean field”. In: *Phys. Rev. C* 92.6 (2015), p. 064310. DOI: [10.1103/PhysRevC.92.064310](https://doi.org/10.1103/PhysRevC.92.064310). arXiv: [1509.03058](https://arxiv.org/abs/1509.03058) [nucl-th].
- [125] C. F. Jiao, J. Engel, and J. D. Holt. “Neutrinoless double-beta decay matrix elements in large shell-model spaces with the generator-coordinate method”. In: *Phys. Rev. C* 96.5 (2017), p. 054310. DOI: [10.1103/PhysRevC.96.054310](https://doi.org/10.1103/PhysRevC.96.054310). arXiv: [1707.03940](https://arxiv.org/abs/1707.03940) [nucl-th].
- [126] Noritaka Shimizu et al. “Generator-coordinate methods with symmetry-restored Hartree-Fock-Bogoliubov wave functions for large-scale shell-model calculations”. In: *Phys. Rev. C* 103.6 (2021), p. 064302. DOI: [10.1103/PhysRevC.103.064302](https://doi.org/10.1103/PhysRevC.103.064302).
- [127] B. Bally, A. Sánchez-Fernández, and T. R. Rodríguez. “Variational approximations to exact solutions in shell-model valence spaces: calcium isotopes in the pf-shell”. In: *Phys. Rev. C* 100.4 (2019), p. 044308. DOI: [10.1103/PhysRevC.100.044308](https://doi.org/10.1103/PhysRevC.100.044308). arXiv: [1907.05493](https://arxiv.org/abs/1907.05493) [nucl-th].

- [128] Adrián Sánchez-Fernández, Benjamin Bally, and Tomás R. Rodríguez. “Variational approximations to exact solutions in shell-model valence spaces: systematic calculations in the *sd*-shell”. In: (2021). arXiv: [2106.08841 \[nucl-th\]](#).
- [129] Heiko Hergert et al. “In-Medium Similarity Renormalization Group Approach to the Nuclear Many-Body Problem”. In: *In-Medium Similarity Renormalization Group Approach to the Nuclear Many-Body Problem*. Springer, Cham, 2017, pp. 477–570. DOI: [10.1007/978-3-319-53336-0_10](#). URL: http://link.springer.com/10.1007/978-3-319-53336-0%7B%5C_%7D10.
- [130] Thomas H  ther et al. “Family of chiral two- plus three-nucleon interactions for accurate nuclear structure studies”. In: *Physics Letters B* 808 (2020), p. 135651. ISSN: 0370-2693. DOI: [10.1016/j.physletb.2020.135651](#). URL: <http://dx.doi.org/10.1016/j.physletb.2020.135651>.
- [131] Evgeny Epelbaum. “Towards high-precision nuclear forces from chiral effective field theory”. In: *6th International Conference Nuclear Theory in the Supercomputing Era*. 2019. arXiv: [1908.09349 \[nucl-th\]](#).
- [132] R. Machleidt and F. Sammarruca. “Can chiral EFT give us satisfaction?” In: *Eur. Phys. J. A* 56.3 (2020), p. 95. DOI: [10.1140/epja/s10050-020-00101-3](#). arXiv: [2001.05615 \[nucl-th\]](#).
- [133] David Lawrence Hill and John Archibald Wheeler. “Nuclear Constitution and the Interpretation of Fission Phenomena”. In: *Phys. Rev.* 89 (5 1953), pp. 1102–1145. DOI: [10.1103/PhysRev.89.1102](#). URL: <https://link.aps.org/doi/10.1103/PhysRev.89.1102>.
- [134] James J. Griffin and John A. Wheeler. “Collective Motions in Nuclei by the Method of Generator Coordinates”. In: *Phys. Rev.* 108 (2 1957), pp. 311–327. DOI: [10.1103/PhysRev.108.311](#). URL: <https://link.aps.org/doi/10.1103/PhysRev.108.311>.
- [135] B. Bally, A. S  nchez-Fern  ndez, and T. R. Rodr  guez. “Symmetry-projected variational calculations with the numerical suite TAURUS: I. Variation after particle-number projection”. In: *Eur. Phys. J. A* 57.2 (2021). [Erratum: *Eur.Phys.J.A* 57, 124 (2021)], p. 69. DOI: [10.1140/epja/s10050-021-00369-z](#). arXiv: [2010.14169 \[nucl-th\]](#).
- [136] B. Bally, A. S  nchez-Fern  ndez, and T. R. Rodr  guez. Unpublished. 2021.
- [137] B. Bally. “Private communication.” 2021.
- [138] R. Roth. “Private communication.” 2021.
- [139] Eskendr Gebrerufael et al. “Ab initio Description of Open-Shell Nuclei: Merging No-Core Shell Model and In-Medium Similarity Renormalization Group”. In: *Physical Review Letters* 118.15 (2017), p. 152503. ISSN: 0031-9007. DOI: [10.1103/PhysRevLett.118.152503](#). URL: <http://link.aps.org/doi/10.1103/PhysRevLett.118.152503>.
- [140] R. J. Furnstahl, G. Hagen, and T. Papenbrock. “Corrections to nuclear energies and radii in finite oscillator spaces”. In: *Phys. Rev. C* 86 (2012), p. 031301. DOI: [10.1103/PhysRevC.86.031301](#). arXiv: [1207.6100 \[nucl-th\]](#).

- [141] E.F. Zhou et al. “Anatomy of molecular structures in ^{20}Ne ”. In: *Physics Letters B* 753 (2016), pp. 227–231. ISSN: 0370-2693. DOI: <https://doi.org/10.1016/j.physletb.2015.12.028>. URL: <https://www.sciencedirect.com/science/article/pii/S0370269315009764>.
- [142] P. Marević et al. “Quadrupole and octupole collectivity and cluster structures in neon isotopes”. In: *Physical Review C* 97.2 (2018). ISSN: 2469-9993. DOI: [10.1103/PhysRevC.97.024334](https://doi.org/10.1103/PhysRevC.97.024334). URL: <http://dx.doi.org/10.1103/PhysRevC.97.024334>.
- [143] Petar Marević. “Towards a unified description of quantum liquid and cluster states in atomic nuclei within the relativistic energy density functional framework”. 2018SACLS358. PhD thesis. 2018. URL: <http://www.theses.fr/2018SACLS358/document>.
- [144] P. A. Butler and W. Nazarewicz. “Intrinsic reflection asymmetry in atomic nuclei”. In: *Rev. Mod. Phys.* 68 (2 1996), pp. 349–421. DOI: [10.1103/RevModPhys.68.349](https://doi.org/10.1103/RevModPhys.68.349). URL: <https://link.aps.org/doi/10.1103/RevModPhys.68.349>.
- [145] Hisashi Horiuchi and Kiyomi Ikeda. “A Molecule-like Structure in Atomic Nuclei of $^{16}\text{O}^*$ and ^{10}Ne ”. In: *Progress of Theoretical Physics* 40.2 (1968), pp. 277–287. ISSN: 0033-068X. DOI: [10.1143/PTP.40.277](https://doi.org/10.1143/PTP.40.277). eprint: <https://academic.oup.com/ptp/article-pdf/40/2/277/5305544/40-2-277.pdf>. URL: <https://doi.org/10.1143/PTP.40.277>.
- [146] S. Marcos, H. Flocard, and P.H. Heenen. “Influence of left-right asymmetry degrees of freedom in self-consistent calculations of ^{20}Ne ”. In: *Nuclear Physics A* 410.1 (1983), pp. 125–136. ISSN: 0375-9474. DOI: [https://doi.org/10.1016/0375-9474\(83\)90405-0](https://doi.org/10.1016/0375-9474(83)90405-0). URL: <https://www.sciencedirect.com/science/article/pii/0375947483904050>.
- [147] W. Nazarewicz and J. Dobaczewski. “Dynamical symmetries, multiclustering, and octupole susceptibility in superdeformed and hyperdeformed nuclei”. In: *Phys. Rev. Lett.* 68 (2 1992), pp. 154–157. DOI: [10.1103/PhysRevLett.68.154](https://doi.org/10.1103/PhysRevLett.68.154). URL: <https://link.aps.org/doi/10.1103/PhysRevLett.68.154>.
- [148] D. S. Ahn et al. “Location of the Neutron Dripline at Fluorine and Neon”. In: *Phys. Rev. Lett.* 123 (21 2019), p. 212501. DOI: [10.1103/PhysRevLett.123.212501](https://doi.org/10.1103/PhysRevLett.123.212501). URL: <https://link.aps.org/doi/10.1103/PhysRevLett.123.212501>.
- [149] T. Duguet and G. Hagen. “Ab-initio approach to effective single-particle energies in doubly closed shell nuclei”. In: *Phys. Rev. C* 85 (2012), p. 034330. DOI: [10.1103/PhysRevC.85.034330](https://doi.org/10.1103/PhysRevC.85.034330). arXiv: [1110.2468](https://arxiv.org/abs/1110.2468) [nucl-th].
- [150] G. Hagen. private communication. 2021.
- [151] T. R. Rodríguez. “Private communication.” 2021.
- [152] B. A. Brown and W. A. Richter. In: *Phys. Rev. C* 74 (2006), p. 034315.
- [153] H Hergert. “In-medium similarity renormalization group for closed and open-shell nuclei”. In: *Physica Scripta* 92.2 (2017), p. 023002. DOI: [10.1088/1402-4896/92/2/023002](https://doi.org/10.1088/1402-4896/92/2/023002). URL: <http://stacks.iop.org/1402-4896/92/i=2/a=023002?key=crossref.e2806985ff1c4cb0faed70a3cb76ec7f>.

- [154] Bence Ladóczki, Motoyuki Uejima, and Seiichiro L. Ten-no. “Third-order Epstein–Nesbet perturbative correction to the initiator approximation of configuration space quantum Monte Carlo”. In: *The Journal of Chemical Physics* 153.11 (2020), p. 114112. DOI: [10.1063/5.0022101](https://doi.org/10.1063/5.0022101). eprint: <https://doi.org/10.1063/5.0022101>. URL: <https://doi.org/10.1063/5.0022101>.
- [155] Marc Dvorak and Patrick Rinke. “Dynamic al configuration interaction: Quantum embedding that combines wave functions and Green’s functions”. In: *Phys. Rev. B* 99 (11 Mar. 2019), p. 115134. DOI: [10.1103/PhysRevB.99.115134](https://link.aps.org/doi/10.1103/PhysRevB.99.115134). URL: <https://link.aps.org/doi/10.1103/PhysRevB.99.115134>.
- [156] K. Hebeler et al. “Improved nuclear matter calculations from chiral low-momentum interactions”. In: *Phys. Rev. C* 83 (3 Mar. 2011), p. 031301. DOI: [10.1103/PhysRevC.83.031301](https://link.aps.org/doi/10.1103/PhysRevC.83.031301). URL: <https://link.aps.org/doi/10.1103/PhysRevC.83.031301>.
- [157] H. Hergert. “Private communication.” 2021.
- [158] H. Hergert et al. “Nuclear Structure from the In-Medium Similarity Renormalization Group”. In: *Journal of Physics: Conference Series* 1041.1 (2018), p. 012007. ISSN: 1742-6596. DOI: [10.1088/1742-6596/1041/1/012007](https://iopscience.iop.org/article/10.1088/1742-6596/1041/1/012007/meta). URL: <https://iopscience.iop.org/article/10.1088/1742-6596/1041/1/012007/meta>.
- [159] A. Belley et al. “*AbInitio* Neutrinoless Double-Beta Decay Matrix Elements for ^{48}Ca , ^{76}Ge , and ^{82}Se ”. In: *Phys. Rev. Lett.* 126.4 (2021), p. 042502. DOI: [10.1103/PhysRevLett.126.042502](https://doi.org/10.1103/PhysRevLett.126.042502).
- [160] Andrea Porro et al. *Importance truncation in non-perturbative many-body techniques*. 2021. arXiv: [2103.14544](https://arxiv.org/abs/2103.14544) [nucl-th].
- [161] A. Tichai, J. Ripoché, and T. Duguet. “Pre-processing the nuclear many-body problem”. In: *The European Physical Journal A* 55.6 (2019), p. 90. ISSN: 1434-6001. DOI: [10.1140/epja/i2019-12758-6](http://link.springer.com/10.1140/epja/i2019-12758-6). URL: <http://link.springer.com/10.1140/epja/i2019-12758-6>.
- [162] V. Somà, C. Barbieri, and T. Duguet. “Ab initio self-consistent Gorkov-Green’s function calculations of semi-magic nuclei: Numerical implementation at second order with a two-nucleon interaction”. In: *Physical Review C* 89.2 (2014), p. 024323. ISSN: 0556-2813. DOI: [10.1103/PhysRevC.89.024323](https://link.aps.org/doi/10.1103/PhysRevC.89.024323). URL: <https://link.aps.org/doi/10.1103/PhysRevC.89.024323>.
- [163] J. L. Egido and L. M. Robledo. In: *Nucl. Phys.* A524 (1991), p. 65.
- [164] D A Varshalovich, A N Moskalev, and V K Khersonskii. *Quantum Theory of Angular Momentum*. WORLD SCIENTIFIC, 1988. ISBN: 978-9971-5-0107-5. DOI: [10.1142/0270](https://www.worldscientific.com/worldscibooks/10.1142/0270). URL: <https://www.worldscientific.com/worldscibooks/10.1142/0270>.
- [165] K. Hara and S. Iwasaki. “On the quantum number projection: (I). General theory”. In: *Nuclear Physics A* 332.1-2 (1979), pp. 61–68. ISSN: 0375-9474. DOI: [10.1016/0375-9474\(79\)90094-0](https://www.sciencedirect.com/science/article/abs/pii/0375947479900940). URL: <https://www.sciencedirect.com/science/article/abs/pii/0375947479900940>.
- [166] Luis M. Robledo. “The sign of the overlap of HFB wave functions”. In: *Phys. Rev. C* 79 (2009), p. 021302.
- [167] D. Mazziotti. In: *Chem. Phys. Lett.* 289 (1998), p. 419.
- [168] D. Mazziotti. In: *Int. J. Quantum Chem.* 70 (1998), p. 557.

- [169] W. Bertozzi et al. “Contributions of neutrons to elastic electron scattering from nuclei”. In: *Phys. Lett. B* 41 (1972), pp. 408–414. DOI: [10.1016/0370-2693\(72\)90662-4](https://doi.org/10.1016/0370-2693(72)90662-4).
- [170] Harish Chandra and Gerhard Sauer. “Relativistic corrections to the elastic electron scattering from ^{208}Pb ”. In: *Phys. Rev. C* 13 (1 1976), pp. 245–252. DOI: [10.1103/PhysRevC.13.245](https://doi.org/10.1103/PhysRevC.13.245). URL: <https://link.aps.org/doi/10.1103/PhysRevC.13.245>.
- [171] B.A. Brown, S.E. Massen, and P.E. Hodgson. “The charge distributions of the oxygen and calcium isotopes”. In: *Phys. Lett. B* 85 (1979), pp. 167–171. DOI: [10.1016/0370-2693\(79\)90569-0](https://doi.org/10.1016/0370-2693(79)90569-0).
- [172] Peter J. Mohr, Barry N. Taylor, and David B. Newell. “CODATA recommended values of the fundamental physical constants: 2010*”. In: *Rev. Mod. Phys.* 84 (4 2012), p. 1527.
- [173] Peter J. Mohr, David B. Newell, and Barry N. Taylor. “CODATA recommended values of the fundamental physical constants: 2014”. In: *Rev. Mod. Phys.* 88 (3 2016), p. 035009. DOI: [10.1103/RevModPhys.88.035009](https://doi.org/10.1103/RevModPhys.88.035009). URL: <https://link.aps.org/doi/10.1103/RevModPhys.88.035009>.
- [174] J. W. Negele. “Structure of Finite Nuclei in the Local-Density Approximation”. In: *Phys. Rev. C* 1 (4 1970), pp. 1260–1321. DOI: [10.1103/PhysRevC.1.1260](https://doi.org/10.1103/PhysRevC.1.1260). URL: <https://link.aps.org/doi/10.1103/PhysRevC.1.1260>.
- [175] G. Hagen, T. Papenbrock, and D. J. Dean. “Solution of the Center-Of-Mass Problem in Nuclear Structure Calculations”. In: *Phys. Rev. Lett.* 103 (6 2009), p. 062503. DOI: [10.1103/PhysRevLett.103.062503](https://doi.org/10.1103/PhysRevLett.103.062503). URL: <https://link.aps.org/doi/10.1103/PhysRevLett.103.062503>.
- [176] B. G. Carlsson and J. Rotureau. “New and Practical Formulation for Overlaps of Bogoliubov Vacua”. In: *Physical Review Letters* 126.17 (2021). ISSN: 1079-7114. DOI: [10.1103/physrevlett.126.172501](https://doi.org/10.1103/physrevlett.126.172501). URL: <http://dx.doi.org/10.1103/PhysRevLett.126.172501>.
- [177] M. Wimmer. “Algorithm 923”. In: *ACM Transactions on Mathematical Software* 38.4 (2012), pp. 1–17. ISSN: 1557-7295. DOI: [10.1145/2331130.2331138](https://doi.org/10.1145/2331130.2331138). URL: <http://dx.doi.org/10.1145/2331130.2331138>.
- [178] P. Businger and G. H. Golub. “Linear Least Squares Solutions by Housholder Transformations”. In: *Linear Algebra*. Ed. by F. L. Bauer. Berlin, Heidelberg: Springer Berlin Heidelberg, 1971, pp. 111–118. ISBN: 978-3-662-39778-7. DOI: [10.1007/978-3-662-39778-7_8](https://doi.org/10.1007/978-3-662-39778-7_8). URL: https://doi.org/10.1007/978-3-662-39778-7_8.
- [179] G. W. Stewart. “The QLP Approximation to the Singular Value Decomposition”. In: *SIAM Journal on Scientific Computing* 20.4 (1999), pp. 1336–1348. DOI: [10.1137/S1064827597319519](https://doi.org/10.1137/S1064827597319519). eprint: <https://doi.org/10.1137/S1064827597319519>. URL: <https://doi.org/10.1137/S1064827597319519>.
- [180] C. C. Paige and M. A. Saunders. “Solution of Sparse Indefinite Systems of Linear Equations”. In: *SIAM Journal on Numerical Analysis* 12.4 (1975), pp. 617–629. DOI: [10.1137/0712047](https://doi.org/10.1137/0712047). eprint: <https://doi.org/10.1137/0712047>. URL: <https://doi.org/10.1137/0712047>.

-
- [181] Sou-Cheng T. Choi, Christopher C. Paige, and Michael A. Saunders. “MINRES-QLP: A Krylov Subspace Method for Indefinite or Singular Symmetric Systems”. In: *SIAM Journal on Scientific Computing* 33.4 (Jan. 2011), pp. 1810–1836. ISSN: 1095-7197. DOI: [10.1137/100787921](https://doi.org/10.1137/100787921). URL: <http://dx.doi.org/10.1137/100787921>.
- [182] A. J. Wathen. “Preconditioning”. In: *Acta Numerica* 24 (2015), pp. 329–376. DOI: [10.1017/S0962492915000021](https://doi.org/10.1017/S0962492915000021).
- [183] Oren Livne and Gene Golub. “Scaling by Binormalization”. In: *Numerical Algorithms* 35 (Jan. 2004), pp. 97–120. DOI: [10.1023/B:NUMA.0000016606.32820.69](https://doi.org/10.1023/B:NUMA.0000016606.32820.69).
- [184] A. Bradley. “Algorithms for the Equilibration of Matrices and Their Application to Limited-Memory Quasi-Newton Methods”. 2010.
- [185] Niclas Forsberg and Per-Åke Malmqvist. “Multiconfiguration perturbation theory with imaginary level shift”. In: *Chemical Physics Letters* 274.1 (1997), pp. 196–204. ISSN: 0009-2614. DOI: [https://doi.org/10.1016/S0009-2614\(97\)00669-6](https://doi.org/10.1016/S0009-2614(97)00669-6). URL: <https://www.sciencedirect.com/science/article/pii/S0009261497006696>.
- [186] Sou-Cheng T. Choi. “Minimal Residual Methods for Complex Symmetric, Skew Symmetric, and Skew Hermitian Systems”. In: *arXiv e-prints*, arXiv:1304.6782 (Apr. 2013), arXiv:1304.6782. arXiv: [1304.6782](https://arxiv.org/abs/1304.6782) [cs.MS].
- [187] Sou-Cheng and Choi. *CS-MINRES-QLP, version 1" [Matlab/GNU-Octave Software]*. 2013.
- [188] Yann Garniron et al. “Selected configuration interaction dressed by perturbation”. In: *The Journal of Chemical Physics* 149.6 (Aug. 2018), p. 064103. ISSN: 1089-7690. DOI: [10.1063/1.5044503](https://doi.org/10.1063/1.5044503). URL: <http://dx.doi.org/10.1063/1.5044503>.
- [189] A. M Romero et al. *Application of efficient generator-coordinate subspace-selection algorithm to neutrinoless double- β decay*. 2021. arXiv: [2105.03471](https://arxiv.org/abs/2105.03471) [nucl-th].

Titre: Description ab initio des noyaux à double couches ouvertes via une nouvelle méthode de résolution du problème quantique à N corps

Mots clés: Systèmes à N corps, structure nucléaire, méthodes numériques

Résumé: Les noyaux atomiques sont des systèmes liés de nucléons en interaction dont la description unifiée pose encore des problèmes théoriques à l'heure actuelle à cause de la grande diversité dans la phénoménologie émergeant dans les systèmes nucléaires. En plus des excitations individuelles responsables des énergies de liaison absolues et des énergies de séparation entre noyaux, des corrélations de longue portée avec un grand degré de collectivité jouent dans rôle majeur dans les propriétés macroscopiques du noyau et sont essentielles pour la comparaison avec l'expérience. Dans cette thèse, on s'intéresse aux modèles microscopiques où le noyau est décrit comme une collection de nucléons ponctuels en interaction forte. On rentre donc dans le domaine du problème à N corps quantique.

Deux approches complémentaires existent pour résoudre ce problème, qui diffèrent par la nature de l'interaction. La méthode de la fonctionnelle de la densité de l'énergie (EDF) utilise une interaction phénoménologique dépendant du système qui capture facilement les corrélations de courte portée au niveau du champ moyen. La physique de longue portée doit être capturée au-delà du champ moyen

via des méthodes multi référence. À l'inverse les méthodes ab-initio partent d'une interaction réaliste dérivée (via la théorie effective des champs chirale) à partir de la physique sous-jacente, l'interaction forte, c'est-à-dire la chromodynamique quantique. La solution du problème à N corps est donc bien plus difficile obtenir mais les résultats qui ressortent sont plus fiables et systématiquement améliorables.

Dans cette thèse une nouvelle théorie de perturbation multi référence est introduite pour résoudre le problème à N corps à partir d'interactions chirales. Ce nouveau formalisme inclue de façon cohérente les corrélations de courte et longue portée. Le premier ordre de la théorie, directement adapté du savoir-faire EDF au contexte ab-initio, est comparé dans des calculs à grande échelle à d'autres méthodes et appliqué à la chaîne de Néons. Le second ordre (nouvellement formulé) est implémenté dans des bases de taille réduite pour s'assurer de la qualité de la méthode et le comparer avec des méthodes de perturbation à une référence déjà existantes. Ce nouveau formalisme est très prometteur pour la description unifiée des états fondamentaux excités des noyaux à couche fermées comme à couches ouvertes.

Title: Ab initio description of doubly-open shell nuclei via a novel resolution method of the quantum many-body problem

Keywords: Many-body problem, nuclear structure, numerical methods

Abstract: Nuclei are self bound systems of interacting nucleons, whose unified description is made intricate by the very diverse phenomenology emerging in nuclear systems. Besides individual excitations responsible for absolute binding energies and separation energies between nuclei, long range correlations with a high degree of collectivity play a major role in macroscopic properties of nuclei and are essential for comparison with experimental measurements. In this thesis, the focus is put on microscopic models where the nucleus is described as a collection of point-like nucleons in strong interactions, falling into the realm of the quantum many-body problem.

Two approaches exist to solve this problem, differing by the very nature of the interaction. Energy Density Functional (EDF) uses a phenomenological system-dependent Hamiltonian easily encompassing short-range correlations at the mean-field level, leaving long-range physics to be captured beyond the mean-field via multi-reference methods. On the contrary, ab initio

methods start from a realistic interaction rooted (through chiral Effective Field Theory) into the underlying theory of the strong force, i.e. quantum chromo-dynamics, making the solution of the many-body problem much more difficult to compute but providing results that are more reliable and systematically improvable.

In the present work, a new multi-reference perturbation theory to solve the many-body problem starting from chiral interactions is formalized in order to include coherently long and short range correlations in both closed- and open-shell nuclei. The first order of this theory, directly adapted from the EDF know-how to the ab initio context, is benchmarked in large scale calculations against other methods, and applied to the Neon chain. The second - newly formalized - order of the theory is implemented in small-scale model spaces to assess the quality of the method and compared with available single-reference perturbative expansions. The novel formalism shows great promises to describe ground and excited states of closed and open-shell nuclei.